Tunable Silicon integrated photonics based on functional materials

Submitted by

Joaquin Faneca Ruedas

to the

University of Exeter as a Thesis for the Degree of Doctor of Philosophy in Engineering

in July 2020

I certify that all material in this thesis which is not my own work has been identified and that any material that has previously been submitted and approved for the award of a degree by this or any other University has been acknowledged.

Signature: .....

I would like to dedicate this thesis to my loving parents and my brother. Especially to my mum, Carmen Ruedas Ariza, who has taught me how to overcome all the different difficulties in life, how to always be humble, and how difficult it is to achieve something. To my brother, who has taught me how to grow up to be a good person. I would like to dedicate this thesis to my aunts and uncles; Sacaramentos, Ana, Manuel and Curri for all the support they have given me when I was studying for my degree, also to my cousins Victor and Maria.

Declaration

I hereby declare that except where specific reference is made to the work of others, the contents of this dissertation are original and have not been submitted in whole or in part for consideration for any other degree or qualification in this, or any other university. This dissertation is my own work and contains nothing which is the outcome of work done in collaboration with others, except as specified in the text and Acknowledgements.

Joaquin Faneca
November 2020

Acknowledgements

I would like to acknowledge financial support from the Engineering and Physical Sciences Research Council (EPSRC) of the United Kingdom, and all the people that contribute to its existence, for the financial support during my studies. I thank also all the people in the Centre for Doctoral Training in Metamaterials at the University of Exeter for making possible this great experience. I thank Adrian Janssen and the support provided by LUMENTUM that has made this work possible. My most sincere gratitude to my supervisor, Prof. Anna Baldycheva, for placing her confidence in me for this project. Thank you for your helpful advice, for your patience and for the insight I gained during all these years of work. Thank you also to Prof. C. David Wright for his help, support and guidance as second supervisor. I can say that I was truly fortunate to have you as supervisors. I would like also to thank Prof. Frederic Y. Gardes, who has transferred to me his passion for engineering, I would like to thank him for his support and the confidence placed in me, the help he has provided me since he met me and how to be honest, humble and professional at the same time. Frederic, thank you for everything. I would also like to express my gratitude to all members of the research group at the University of Exeter and at the University of Southampton, to the ones that are still here and the ones that have moved away, for all the discussions and help during the development of this thesis. I greatly enjoyed learning and working with all of you. Special thanks to Dr. Thalia Dominguez Bucio, Dr. Lorenzo Mastonardi and Stefan Illie for their help in the development of the photonic integrated devices, fabrication and near infrared measurements set-up. Dr. Ben Hogan for the liquid crystal and 2D materials discussions, and Dr. Santiago Garcia Carrillo and Dr Carlota Ruiz de Galarreta for their help in the experimental and simulation discussion of phase change materials. From my cohort, I would like to thank especially Emanuele Gemo, Zahid and David for their constant effort discussions. Especially thanks to Miquel, Valentin and Hannah who made me feel like home since I met them. Thank you also to the IT technicians and the laboratory officers for their attention and dedicated work. I would like to thank my football team, Exeter United, for their constant support during these years and for making me see a different side of life, especially to Kev Hunter, Hawkar, Sammy and Ali. I would like also to thank Mariona, Alba and Pedro for making me happy playing Pinturillo while I was writting the thesis.

Of course, I have to acknowledge the support of my parents and brother that have always been there, backing me and giving me courage and strength in all ventures during my life.

Abstract

This thesis is concerned with the design, fabrication, testing and development of tunable silicon photonic integrated circuits based on functional materials. This tunability is achieved by integrating liquid crystals, 2D materials and chalcogenide phase-change materials with silicon and silicon nitride integrated circuits. Switching the functional materials between their various states results in dramatic changes in the optical properties, with consequent changes in the optical response of the individual devices. Furthermore, such changes are volatile or non-volatile depending on the materials.

The first part of this thesis is dedicated to the design, fabrication and characterisation of 1D integrated silicon photonic crystal resonators based on liquid crystals, working at telecommunications wavelengths, specifically at wavelengths corresponding to the C and L-band (1530 to 1625 nm). The photonic crystal acts as high quality factor resonator when the liquid crystal injected into specific photonic crystal grooves is tuned using applied voltages around 10 V. Such behaviour can be used for high selectivity wavelength division multiplexers in both bands (C and L-band) for optical communications, high selectivity lasers on chip, or bio-sensing applications. The fabricated devices demonstrated a quality factor of $\sim 10^4$, and a small footprint.

In the second part of this thesis, a complete design and study of tunable silicon-rich nitride micro-ring resonators based on graphene capacitors is presented for application in high performance computing. By gating the graphene capacitor, a change in the refractive index of the graphene cladding occurs resulting in a volatile reconfigurable ring resonator on chip. Silicon-rich nitride platform improves the performance of the devices compared with silicon and stoichiometric silicon nitride, reducing the footprint of the devices, increasing the speed up to 64 GHz while maintaining an extinction ratio of 16.5 dB for an energy consumption per bit of 0.22 pJ. Furthemore, a graphene micro-heater on chip is designed and used as an active material to achieve the phase change transition of a chalcogenide phase change material unit cell deposited on top of an integrated waveguide.

In the third part of the thesis, a comparison between the O and C band optical properties of silicon nitride waveguides with integrated cells of the well-known phase change material, $Ge_2Sb_2Te_5$, is shown. A high contrast between the phase change material states as high as

2.5 dB/μm in the C-band and 6.4 dB/μm in the O-band are reported. High quality factor resonances are shown in both ranges of the spectrum using rib silicon nitride ring resonators and an ON-OFF switch is characterized in the O and C-bands with an ER of 12 and 18 dB respectively. Finally, with the view to provide a comparison of the wavelength-dependent optical switching, a 3-dimensional finite-element method simulation is peformed and a comparison in the optical-to-thermal energy conversion in both ranges of the spectrum is shown. For the different wavelengths, a marginal variation of efficiency is observed for the crystal case, with an efficiency value in the C-band lightly higher than the O-band, yielding a ratio between efficiencies of 0.8. However,for the amorphous case,the O-band efficiency is typically around 4 times higher than the corresponding C-band value,in the whole range of investigated pulse duration.

In the last part of the thesis, a reconfigurable and non-volatile Bragg grating in the telecommunication C-band based on the combination of novel low-loss phase-change materials (especifically $Ge_2Sb_2Se_4Te_1$ and Sb_2S_3) with a silicon nitride (Si_3N_4) platform is proposed and designed. The Bragg grating is formed by arrayed cells of phase-change material, whose crystallisation fraction modifies the Bragg wavelength and extinction ratio. These devices can be used in integrated photonic circuits for optical communications applications in smart filters and Bragg mirrors and can also find use in tunable ring resonators, MZIs or frequency selectors for future laser on chip applications. Moreover, an O-band Mach-Zehnder interferometer (MZI) based on a N-rich silicon nitride platform combined with $Ge_2Sb_2Te_5$ for future optical communication applications is experimentally demonstrated. The device operation relies on controlling the waveguide's losses using a phase change material cell which can be changed from amorphous (low-loss) to crystalline (high-loss). An extinction ratio (ER) as high as 11 dB was obtained between the amorphous (ON) and the crystalline (OFF) states of the MZI optical building block. The insertion loss of the MZI structure per cell unit length was measured to be as high as 0.87 dB/μm in OFF state and as low as 0.064 dB/μm in ON state for TM polarisation.

Table of contents

List of figures

List of tables

Nomenclature

α	Loss coefficient
δ	Mass density
v_g	Phase velocity
v_g	Group velocity
ω	Angular frequency
ρ	Electric charge density
σ	Electric conductivity
c	Speed of light
C_p	Heat capacity
k	Thermal conductivity
k	Wavevector
n_g	Group index
n_{eff}	Effective refractive index
Q	Heat source
Q	Quality factor
T_g	Glass transition temperature
T_m	Melting point
T_{max}	Maximum temperature

ASIC Application-specific integrated circuit

ASPIC Application-specific photonic integrated circuit

c-Si Crystalline Silicon

CMOS Complementary metal-oxide-semiconductor

CVD Chemical vapor deposition

DEMUX DE-multiplexer

DUV Deep ultraviolet

E-O Electro-optic

EBL Electron beam litrography

FP Fabry-Pérot

FPGA Field-programmable gate array

GC Grating coupler

HWGC Hybrid waveguide based on graphene capacitor

IL Insertion loss

LC Liquid crystal

MMI Multimode interference

MUX Multiplexer

MZI Mach-Zehnder Interferometer

NIR Near infrared

PCM Phase change material

PECVD Plasma Enhanced chemical vapor deposition

PhC Photonic crystal

PIC Photonic Integrated Circuit

PVD Physical vapor deposition

RI Refractive index

RIU Refractive index unit

SB Stop band

SEM Scanning electron microscope

Si Silicon

SiN Silicon nitride

SOI Silicon-on-insulator

SRN Si-rich nitride

T-O Thermo-optic

TE Transverse electric

TIR Total internal reflection

TM Transverse magnetic

TMDs Transition metal dichalcogenide

TPA Two-photon absorption

VMPM Volatile multilevel photonic memories

WDM Wavelength division multiplexer

WG Waveguide

Chapter 1

Introduction

1.1 Photonic integrated circuits

Photonic integrated circuits (PICs) overcome some of the major drawbacks that electronics faces today, particularly in terms of the limited transmission speed and high power consumption, by using light to process, transmit and store information [1]. Nowadays, we are on the cusp of revolutionary changes in communications and micro-systems technology due to the marriage of photonics and electronics on a single platform. Many types of devices on chip are emerging, which combine large-scale photonic integration with large-scale electronic integration [2]. Electronic-photonic circuits will be relevant in different areas such as: optical communications [3], high speed data in mobile devices [4], high performance computing [5], and medical applications [6].

The same foundries and processes that were developed to build transistors are being repurposed to build chips that can generate, detect, modulate and manipulate light. We should not expect that we can directly integrate photonic functionalities into CMOS (complementary metal-oxide-semiconductor) or bipolar silicon wafers without making any change in the fabrication processes. CMOS fabrication process were developed to facilitate the highest performance of electronic circuits. Consequently, the processes will not be as efficient in the fabrication of realistic competitive photonic devices. However, during the last 20 years, silicon photonics technology has emerged as a powerful platform to create photonic devices.

Companies like LUMENTUM, Intel, Rockley Photonics, IBM and Hewlett-Packard are considering silicon photonics as the future technology for high-speed data transfer, and some already have products on the market. Furthermore, the silicon photonics community has developed process flows that permit the re-use of CMOS fabrication infrastructure to build complex photonic circuits, where the information can be transferred from electronic to optical domain and back again [7].

The wafers that are commonly used in silicon photonics are "silicon on insulator" (SOI). The typical size is 12" wafer which consists of a 725 μm silicon substrate, 2 μm of silicon dioxide (buried oxide, or BOX) and 220 nm of crystalline silicon. For applications in the visible range or in the mid-infrared, silicon is no longer a useful guiding material due to its strong absorbent properties, however, silicon nitride (Si_3N_4) shows far less absorbance in these ranges of the spectrum while retaining similar properties and material interactions to those seen for silicon in the near infrared [8, 9]. The waveguide structures and photonic circuits are patterned on top of the crystalline silicon or silicon nitride wafer. Consequently, the material properties of silicon and silicon nitride are important for the device design. Silicon and silicon nitride photonic integrated circuits (PIC) are already established as a mature technology and different devices such as modulators [10–16], photodetectors [17], switches [18], and memories [19] have been demonstrated. Si_3N_4 optical properties allow less confinement of the optical mode within the photonic circuit components, improving the interaction with the materials that can be deposited on the top of the passive structures [20]. Due to the bending losses of the Si_3N_4 structures [20], the footprint of the devices will be larger than in silicon, however, Si_3N_4 do not suffer the very large two-photon absorption (TPA) coefficient and can avoid the TPA problem present in silicon [21–23].

1.2 Reconfigurable systems

Programmable integrated photonics is an emerging new paradigm that aims at designing common integrated optical hardware resource configurations, capable of implementing an unconstrained variety of functionalities by suitable programming, following a parallel but

not identical path to that of integrated electronics in the past two decades of the last century. Programmable integrated photonics is raising considerable interest, as it is driven by the surge of a considerable number of new applications in the fields of telecommunications, quantum information processing, sensing, and neurophotonics, calling for flexible, reconfigurable, low-cost, compact, and low-power-consuming devices that can cooperate with integrated electronic devices to overcome the limitation expected by the demise of Moore's Law [24].

Reconfigurability is now commonplace in electronics components, circuits and systems and the FPGA (field-programmable gate array) device being a good example. Freeman's FPGA patent application filled in 1989 highlights the nature of a reconfigurable system [25]. FPGAs were initially conceived with the idea to compete with application specific integrated circuits (ASICs) and after thirty years since their introduction, FPGAs have practically replaced ASICs in most applications [26]. FPGA devices have gained this wide coverage because of the benefits of Moore's law, cost reductions due to non-recurring engineering costs and the trend in fusing practical engineering and design principles. In conclusion, FPGA concepts have shown the potential of reconfigurability to become a disruptive technology in information and communication systems [27]. Reconfigurable systems are sometimes criticised because they require overhead, which may lower performance and add complexity, possibly reducing reliability. However, these systems also present some advantages. A reconfigurable system can be considered as a building block which can be reshaped leading to a reduction in engineering expenses, design rectification or having different functionalities in the same chip. Furthermore, by software programming it is possible to create self-healing and/or cooperative multi-tasking systems.

Programmable integrated photonics aims to provide a complementary approach to that based on application-specific photonic integrated circuits (ASPICs), which has been dominant during the last years. The goal is to approach and seek similar advantages to those FPGAs brought over ASICs in electronics [28], see Table 1.1. Programmable integrated photonics has raised the attention of different research communities for different emerging applications that are demanding flexibility and reconfigurability as well as low-cost, compact and low-power consuming devices. One area in which considerable seminal work has been produced

	FPGA	ASPIC
Time to market	Fast	Slow
NRE	Low	High
Design flow	Simple	Complex
Unit cost	High	Low
Performance	Medium	High
Power consumption	High	Low
Unit size	Medium	Low

Table 1.1 Comparison between FPGAs and ASPICs.

is in quantum information technologies [29, 30] and neuromorphic computing [31]. In the field of telecommunications, different applications can be found in signal processing functionalities, such as arbitrary mode converters [32, 33], fiber wireless interfacing devices [34], broadband switches [35] for computer interconnects [36], or in the field of sensing, the programmable PICs can lead to a generic class of programmable measuring devices [37], which can be integrated as a building block in the future internet of things (IoT). The success in PIC relies on designing suitable basic building blocks able to carry elementary signal processing operations and interconnection hardware architectures that can offer the possibility to independently reconfigure the device.

A range of volatile [38] and non-volatile [39] reconfigurable PICs have already been demonstrated. One of the crucial building blocks is the modulator, which is based on the plasma dispersion effect [40], quantum confined Stark effect [41] or Frantz Keldysh effect [42]. These processes are usually not cost effective as they require tens of fabrication steps and are only available for silicon and germanium based waveguides. Over the last 10 years, a substantial effort has been invested in terms of the simplification of fabrication processes by looking at novel reconfigurable technologies for PICs providing equivalent or better performance compared to group IV based materials. Ideal candidate is graphene enabled modulators or photodetectors, able to compete with the speeds and power consumption requirements of the state of the art modulators. For large scale programmable photonic integrated circuits, in applications such as, neuromorphic computing, or quantum computing, where the speed requirements are lower (in the order of microseconds), liquid crystals as

volatile materials and optical phase change materials as non volatile materials are ideal candidates and can easily be integrated with most passive PIC.

1.3 Objectives of the thesis

The main goal of this thesis is the design, fabrication, testing and development of tunable silicon photonic integrated circuits based on functional materials. This tunability is achieved by integrating: liquid crystals, 2D materials and chalcogenide phase-change materials with silicon and silicon nitride integrated circuits.

In particular, the following research challenges are addressed:

- The development of computational tools and techniques that allow for the proper design and simulation of the performance of reconfigurable silicon and silicon nitride photonic integrated circuits based on functional materials.
- The experimental fabrication of different device designs, paying particular attention to photonic integrated waveguides, Mach-Zehnder inteferometers, ring resonators, Bragg gratings, deposition of graphene or phase change materials and infiltration of liquid crsytals on integrated circuits.
- The development of tunable devices suited to operate in different ranges of the spectrum, comprising the O, C and L-bands (1260-1625 nm) for optical communications and optoelectronic applications.

1.4 Thesis Outline

Chapter 1: In the first chapter, the context of the thesis is given from a broad perspective. The concepts of photonic integrated circuits and reconfigurable systems are introduced to illustrate the demand on reconfiguable photonic integrated circuits and their different applications.

Chapter 2: The concepts and ideas explained in Chapter 2 serve as background to understand the results extracted in the thesis. These are selected topics from individual photonic integrated building blocks and functional materials, from where the developed ideas in the subsequent chapters are built upon. The discussion starts by explaining silicon and silicon nitride individual building blocks, specifically, waveguides, photonic crystals, ring resonators, Mach-Zehnder interferometers and Bragg gratings. Finally, the different functional materials used to make the passive individual building blocks tunable are introduced, starting from liquid crystals and finishing with graphene and phase change materials.

Chapter 3: The third chapter is dedicated to the computational and experimental techniques used in the thesis. The part concerning the computational techniques describes the different computational tools used and the mathematical formulation that corresponds to the different physical situations relevant to the thesis. The part dedicated to the experimental techniques describes all fabrication and characterisation methods used in the development of the conceived devices in the different chapters.

Chapter 4: In the fourth chapter, the first integrated silicon building block is demonstrated and experimentally characterized. Design, fabrication and characterisation of 1D integrated silicon photonic crystal devices based on liquid crystals, working at telecommunications wavelengths is shown, specifically at wavelengths corresponding to the C and L-band (1530 to 1625 nm). The 1D integrated silicon photonic crystal acts as a high quality factor resonator when the liquid crystal (in this case E7) inside some of the 1D photonic crystal grooves is tuned using a bias of around 10 V.

Chapter 5: Different designs using graphene as a reconfigurable material for integrated optical communications applications are discussed in the fifth chapter. Specifically, a graphene capacitor is presented with applications in high performance computing. By gating the graphene capacitor, a tuning in the refractive index of the graphene layer covering the waveguide is produced, giving birth to a volatile reconfigurable ring resonator on chip. Finally, a graphene micro-heater is designed and proposed to act as a heater that enables the switching, between amorphous and crystalline states, of a chalcogenide phase-change material cell deposited on top of a silicon nitride rib waveguide.

Chapter 6: In chapter 6, a comparison between the O and C-band optical properties of the well-known phase change material, $Ge_2Sb_2Te_5$, integrated on a silicon nitride platform is shown. A high contrast between the phase change material states as high as 2.5 dB/μm in the C-band and 6.4 dB/μm in the O-band are reported. High quality factor resonances are shown in both ranges of the spectrum using rib silicon nitride ring resonators and an ON-OFF switch is characterized in the O and C-bands with an ER of 12 and 18 dB respectively.
Chapter 7: In this chapter, an O-band Mach-Zehnder interferometer (MZI) based on a N-rich silicon nitride platform combined with $Ge_2Sb_2Te_5$ for future optical communication applications is experimentally demonstrated. The device operation relies on controlling the waveguide's losses using a phase change material cell which can be changed from amorphous (low-loss) to crystalline (high-loss). Moreover, a reconfigurable and non-volatile Bragg grating in the telecommunication C-band based on the combination of novel low-loss phase-change materials (specifically, $Ge_2Sb_2Se_4Te_1$ and Sb_2S_3) with a silicon nitride (Si_3N_4) platform is designed and proposed.
Chapter 8: In this chapter, the conclusions of the thesis and suggestions for further related work are discussed.

1.5 Journal and conference papers and presentations

1.5.1 Journal papers

- One-Dimensional multi-channel photonic crystal resonators based on silicon-on-insulator with high quality factor, **J Faneca**, TS Perova, V Tolmachev, A Baldycheva Frontiers in Physics 6, 33 7, 2018.

- Silicon Nitride Photonics for the Near-Infrared, TD Bucio, C Lacava, M Clementi, **J Faneca**, I Skandalos, A Baldycheva, ... IEEE Journal of Selected Topics in Quantum Electronics 26 (2), 1-13 3, 2019.

- Tuning silicon-rich nitride microring resonances with graphene capacitors for high-

performance computing applications, **J Faneca**, BT Hogan, IR Diez, FY Gardes, A Baldycheva Optics Express 27 (24), 35129-35140 2, 2019.

- O-band N-rich silicon nitride MZI based on GST, **J Faneca**, TD Bucio, FY Gardes, A Baldycheva Applied Physics Letters 116 (9), 093502, 2020.

- On-chip sub-wavelength Bragg grating design based on novel low loss phase-change materials, **J Faneca**, Liam Trimby, Ioannis Zeimpekis, Matthew Delaney, Daniel William Hewak, Frederic Gardes, David Wright, and Anna Baldycheva, Optics Express, 2020.

- Performance characteristics of phase-change integrated silicon nitride photonic devices in the O and C telecommunications bands, **J Faneca**, SGC Carrillo, Emanuele Gemo, CR de Galarreta, TD Bucio, Frederic Gardes, David Wright, and Anna Baldycheva, Optical Materials Express, 2020.

- Spatial tracking of individual fluid dispersed particles via Raman spectroscopy, BT Hogan, J O'Dowd, **J.Faneca**, A Baranov, A Baldycheva, Scientific reports , 2020

- Tunable optical metasurfaces enabled by chalcogenide phase-change materials: from the visible to the THz, CR de Galarreta, SGC Carrillo, YY Au, E Gemo, L Trimby, J Shields, **J.Faneca**, Anna Baldycheva and David Wright, Journal of Optics, 2020.

1.5.2 Conference papers and presentations

- February 2017: Oversight Board, Physics Building, Exeter, UK (POSTER) Photonic metamaterials for WDM (wavelength division multiplexing) optical communications applications.

- May 2017: ITMO University, Metalab, Doctoral Summer School, Russia (POSTER) Photonic metamaterials for WDM (wavelength division multiplexing) optical communications applications.

- May 2017: Progress in electromagnetism research symposium (PIERS) St Petersburg, Conference paper: Liquid Crystal WDM Filter in Si Photonic Crystal Technology with Individual Channel Fine-tuning Capability, (POSTER).

- June 2017: EOS Optical Technologies - Conferences at the World of Photonics Congress (WPC 2017), Munich, Conference paper: Multichannel Si Photonic Crystal filters with Fine-Tuning Capability of Individual Channels for WDM optical interconnects (ORAL).

- June 2017: EOS Optical Technologies - Conferences at the World of Photonics Congress (WPC 2017), Munich, Conference paper: Novel fluid materials for CMOS photonic WDM systems (POSTER).

- July 2017 Nanofabrication Workshop, GW4, University of Bath, UK: (POSTER) Novel materials and nanofabrication of WDM for optical communications interconnect applications.

- September 2017: RAMS - Recent Appointees in Materials Science, Exeter, UK, Conference paper: 2D materials using silicon micro-ring resonators for CMOS photonic WDM systems (POSTER).

- October 2017: Photonex - Silicon Photonics, Coventry, UK, Conference paper: 2D materials and liquid crystals integrated into silicon nitride platform for WDM optical interconnects applications (POSTER).

- January 2018: SPIE Photonics West, San Francisco, US, Conference paper: 2D materials using silicon micro-ring resonators for CMOS photonic WDM systems (ORAL).

- January 2018: SPIE Photonics West, San Francisco, US, Conference Paper: Add-drop filters based on microring structures with fine-tuning capability for WDM optical interconnects (POSTER).

- April 2018: RMS Photonics and optoelectronics materials, Exeter, UK, Conference paper: 2D materials and liquid crystals integrated into silicon nitride platform for WDM optical interconnects applications (POSTER).
- August 2018: SPIE OPTICS + PHOTONICS, San Diego, US. SPIE president of University of Exeter student Chapter. Poster: EUOPS (Exeter University Optics and Photonics Society) activities.
- October 2018: Photonex - Silicon Photonics, Coventry, UK, Conference poster: Reconfigurable materials for integrated optical communications applications. (1st Poster Prize technical winner award by Professor David Payne).
- December 2018: SNAIA (Smart Nanomaterials) - Paris, France, Conference Presentation Reconfigurable materials for integrated optical communications applications. (1st Prize best student presentation award).
- April 2019: POEM (Photonic and Optoelectronic materials conference) - London, UK, (Invited Talk) Reconfigurable materials for smart photonic integrated circuits (SPIC).
- July 2019: ePIXfab Silicon Photonis Summer school (4th Edition) - Pisa, Italy- Poster.
- July 2019: IONS Exeter - Exeter, UK - (Talk) Reconfigurable Photonic Integrated Circuits (RPIC) based on functional materials for integrated optical communications applications.
- September 2019: Emerging technologies for 5G networks - Thessaloniki, Greece - (Talk) Reconfigurable materials for optical communications applications.
- December 2019: SNAIA (Smart Nanomaterials) - Paris, France, Conference Presentation, (Invited Talk) Functional materials for integrated optical communications applications.
- February 2020: SPIE Photonics West, San Francisco, US, Conference paper: Reconfigurable photonic integrated circuits (RPIC) based on functional materials for integrated optical communication applications.

- February 2020: SPIE Photonics West, San Francisco, US, Conference paper: Reconfigurable Bragg grating design based on novel low-loss phase-change material GSST2241 on SiNx platform (POSTER).

1.5.3 Prizes and awards

- SPIE SCHOLARSHIP PROGRAM: In 2019 SPIE awarded education scholarships to 85 outstanding individuals around the world for their potential long-range contribution to optics, photonics, or other related fields.
- (1st Poster Prize technical winner award by Professor David Payne) October 2018: Photonex - Silicon Photonics, Coventry, UK.
- (1st Prize best student presentation award) December 2018: SNAIA (Smart Nanomaterials) - Paris, France, Conference Presentation Reconfigurable materials for integrated optical communications applications.
- Officer travel grant (SPIE).
- EUIMWP (CA 16220) COST Action GRANT for attending the event of Emerging Technologies for 5G networks.
- Host IONS conference in Exeter (OSA scholarship) (IONS) conference in Exeter in 2019.
- Grant for a PGR led careers development event.

Chapter 2

Background

2.1 Silicon Photonics

2.1.1 Waveguides

One of the most essential building blocks of every PIC is a waveguide (WG). An optical WG is a physical structure that guides electromagnetic waves in the optical spectrum. Exploiting the difference between the refractive index of the WG and the surrounding medium, multiple reflections take place to propagate light from one point of the circuit (A) to another point (B) with low-losses through the WG. Common types of optical WGs include optical fiber and rectangular WGs. Integrated optical WGs are used as components in integrated optical communication circutis and systems as the transmission medium. Optical WGs can be classified according to their geometry (rib, strip or buried WGs [Fig 2.1]), mode structure (single-mode, multi-mode), refractive index distribution (step or gradient index), and material (glass, polymer, semiconductor).

Effective refractive index (n_{eff}) and Group Index (n_g)

In a standard silicon photonic WG, the mode can be characterized by the effective refractive index (n_{eff}), that is related to the propagation constants in the z direction (defined as direction of propagation) as described in Fig 2.2:

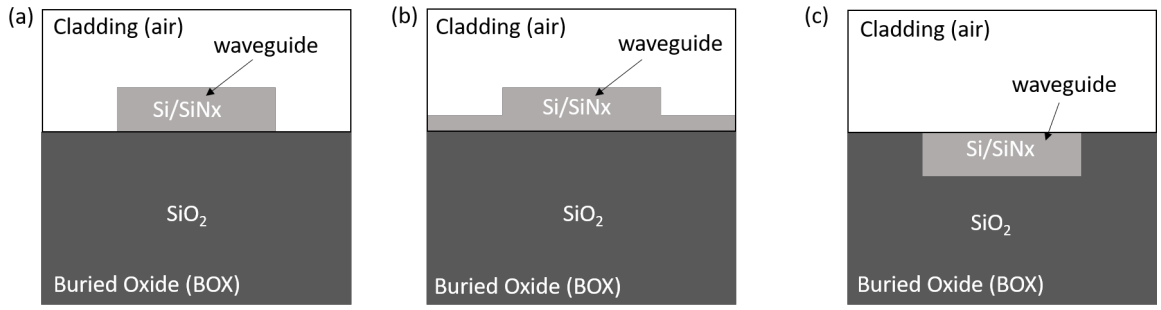

Fig. 2.1 Different WGs geometries cross-sections : (a) ridge or strip WG cross-section (b) rib WG cross-section (c) buried WG cross-section.

$$k_z = n_1 k_0 \sin\theta_1 \tag{2.1}$$

$$k_y = n_1 k_0 \cos\theta_1 \tag{2.2}$$

where k_0 is the propagation constant in free space, n_1 is the propagating medium refractive index, k_z is the propagation constant in the z direction and indicates the rate at which the wave is propagating in the z direction, k_y represents the propagation constant in the y direction of propagation and indicates the rate at which the wave is propagating in the y direction. Normally, the nomenclature of the propagation constant in the direction of propagation k_z adopts the form of β but is perfectly interchangeable with k_z.

A parameter n_{eff} defined as effective refractive index is equivalent to a mode propagating along the WG, without zigzagging back and forth, with refractive index n_{eff}, and the propagation constant along the z direction has the form $k_z = k_0 \cdot n_{eff}$. Once the effective refractive index has been defined, it is important to consider the limiting values of n_{eff}.

The lower bound on β is defined by the critical angles of the WG. For an asymmetrical WG, ($n_2 \neq n_3$ in Fig 2.2) the smaller of the two critical angles is usually defined by the upper cladding layer, as this usually has a lower refractive index than the lower cladding layer. Normally, in the case of silicon or silicon nitride, the lowest possible value of the refractive index of the upper cladding is 1.0, if the upper cladding is air. This means that the total internal reflection is limited by the lower cladding, which will have a larger critical angle

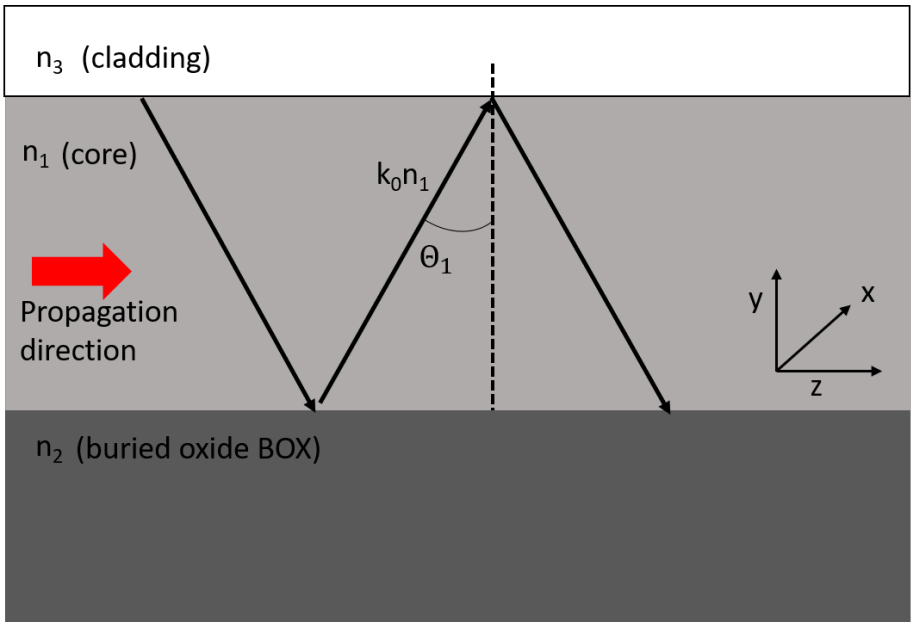

Fig. 2.2 Propagation principle in a planar WG, the relations between the propagation constants in the y, z directions are presented.

that needs to be exceeded for total internal reflection to occur. Hence $\theta_1 \geqslant \theta_l$, where θ_l is the critical angle and the lower bound on β is given by:

$$\beta \geqslant n_1 k_0 \sin(\theta_l) = k_0 n_2 \tag{2.3}$$

The upper bound on β is governed by the maximum value in θ and is 90°. Consequently, the values of n_{eff} will be constrained between n_1 and n_2 [43]:

$$n_1 \geq n_{eff} \geq n_2 \tag{2.4}$$

The wavelength dependence of the WG's n_{eff} and group index (n_g) is important for the simulation of complex devices or systems that operate in different parts of the optical spectrum. n_{eff} is used to describe the phase velocity of the light, v_p, they are related trough the speed of light (c). However, it is the n_g that determines the propagation speed of a pulse, namely group velocity v_g, the group index and the group velocity are also related trough the speed of light (c):

$$v_p(\lambda) = c/n_{eff}, \quad v_g(\lambda) = c/n_g \tag{2.5}$$

The n_g is a crucial parameter in PIC designs since it is the n_g that determines the mode spacing (free-spectral-range) in resonators and interferometers. The n_g can be related to the n_{eff} by [44]

$$n_g(\lambda) = n_{eff}(\lambda) - \lambda \frac{dn_{eff}}{d\lambda} \tag{2.6}$$

Mode propagation

Silicon-on-insulator (SOI) is a platform that offers a very high refractive index contrast and consequently strong light confinement; this allows one to reduce the core of the WG cross section down to micrometer dimensions. The core size for a single mode propagation at the telecommunication range (λ=1.3-1.5 μm) is a few hundred nanometers in width ($\sim$500 nm) for silicon and increases to 1200 nm width for silicon nitride. This light confinement also allows the minimum bending radius to be reduced to the micrometer range and offers the possibility of designing ultra-dense PICs on chip [45].

Two-dimensional rectangular WG modes require two subscripts to identify them. Normally, Cartesian coordinates are used to describe them. In a rectangular WG there exist two families of modes, the TE (transverse-electric) mode and the TM (transverse-magnetic) modes. In common with the skew modes of an optical fiber, these are mostly polarized in the TE or TM directions. Therefore the modes are designated $TE_{p,q}$ or $TM_{p,q}$, where the integers p and q represent the number of consecutive field maxima in the x and y directions respectively. These modes are also referred to as $HE_{p,q}$ and $EH_{p,q}$ modes. Hence the fundamental modes are referred to as $TE_{0,0}$ and $TM_{0,0}$, [Fig 2.3] which is the most common convention.

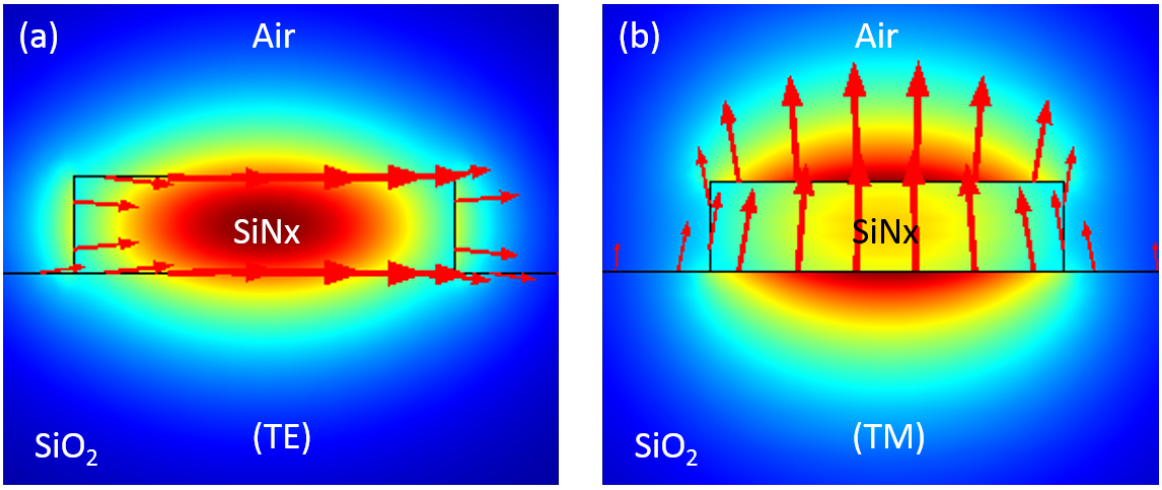

Fig. 2.3 (a) TE mode profile of a silicon nitride WG cross-section, electric field direction is represented by red arrows (b) TM mode profile of a Silicon Nitride WG cross-section, electric field direction is represented by red arrows.

Losses in WGs

In optics, the refractive index n of a material is a dimensionless number that describes how light propagates through that medium. It is defined as $n = c/v_p$, where c is the speed of light and v_p is the phase velocity of light in medium. The refractive index is in general a complex quantity and it can be defined as

$$n' = n_r + jk_i \tag{2.7}$$

where n_r is the real part and k_i the imaginary part of the refractive index. The propagating field through the WG can be expressed as

$$E = E_0 e^{j(kz-wt)} \tag{2.8}$$

where $k = k_0 n'$. Therefore introducing [Eq 2.7] in [Eq 2.8]

$$E = E_0 e^{j(k_0 n' z - wt)} = E_0 e^{jk_0 n_r z} e^{-k_0 k_i z} e^{-jwt} \tag{2.9}$$

The term $e^{-k_0 k_i z}$ is often redesignated as $e^{-\alpha/2}$ where the term α is called the **loss coefficient**.

The factor $1/2$ is included in the definition above because, by convention, α is an intensity loss coefficient and we can write:

$$I = I_0 e^{-\alpha z} \tag{2.10}$$

Losses for SOI and silicon nitride WGs are typically in the range of 0.1-1 dB/cm [46, 47].

Contribution to losses

There are three different sources of loss in optical WGs: scattering, absorption and radiation.

- Scattering: The scattering in an optical WG can be one of two types: volume scattering or interface scattering. The volume scattering is due to the imperfections in the bulk WG material, such as voids, contaminant atoms or crystal defects. Interface scattering is caused by the roughness at the interface between the core and the cladding of the WG. Normally, if the fabrication process has been controlled sufficiently, the volume scattering is negligible. It has been shown that the contribution to volume scattering is related to the number of defects, their size with respect to the wavelength of propagation, and the correlation length along the WG [48]. In bulk media, Rayleigh scattering is the dominant loss mechanism, which exhibits a λ^{-4} dependence. However, for confined waves the wavelength dependence is related to the axial correlation length of the defects. For correlation lengths shorter than, or on the order of, the wavelength, the scattering loss exhibits a λ^{-3} dependence, because the reduction of confinement for longer wavelengths partially counters the λ^{-4} relation. For long correlation lengths compared to the wavelength, radiation losses dominate and a λ^{-1} dependence is observed [49, 50].

- Absorption: The two main potential sources of absorption loss for semiconductor WGs are band edge absorption (or inter-band absorption) and free carrier absorption. Inter-band absorption occurs when photons with energy greater than the bandgap are absorbed to excite electrons from the valence band to the conduction band. Conse-

quently, a wavelength shorter than the absorption edge wavelength of the WG material should be used. Therefore, semiconductor WGs should suffer negligible band edge absorption when operating at a suitable wavelength. Free carrier absorption may be significant in semiconductor WGs. The concentration of free carriers will affect both the real and imaginary parts of the refractive index [51].

- Radiation : The radiation loss from a straight optical WG should ideally be negligible. The radiation loss implies a leakage from the WG into the surrounding media, typically the upper or lower cladding, or for a rib WG, into the planar region adjacent to the guide. If the WG is well designed this loss will not normally be significant, although unwanted perturbations in the WG due to, for example, a slightly damaged fabrication mask may cause scattering of light from one mode to another [52].

2.1.2 Photonic crystals

Modern Silicon fabrication technology has advanced remarkably over the last two decades, demonstrating an unprecedented level of photonic integration [53–58]. Particular attention is paid to different types of photonic devices based on one-dimensional, two-dimensional and three-dimensional photonic crystals with a consequent variation of layers of different refractive indices in these (various) directions [56–58]. Development of integrated compact multi-channel filters in particular, for applications including communication systems [59, 60], multifunctional sensing [61–63] and spectral imaging detection [64] is an active area of research in this field. Vertically etched silicon one-dimensional photonic crystals (1D PhCs) have attracted particular interest, due to their easy fabrication and integration onto a chip with in-plane light propagation [65–67]. Other advantages of these structures are the possibility of tuning their optical properties [68–70], as well as their easy adoption for micro/nano-fluidic devices [71–73].

These advantages have resulted in the development of a variety of opto-electronic devices, including multimode filters for wavelength division multiplexing (WDM) as well as opto-fluidic devices for biochemical and biomedical sensing. The desired characteristics for these

devices are high quality factor (Q), large modulation depth, also known as extinction ratio (E.R), high selectivity, high out-of-band rejection, low power consusmption, low insertion losses and a small footprint, see, for example, Ref. [1]. The use of vertical 1D PhCs for sensing is particularly important for the near- and mid-infrared regions and may be extended in future to the far-infrared and even the THz regions [74]. Another attraction of these structures is that the delivery of chemical or biological substances into the air gaps can be performed via standard "flow-over" (see, for example [75]) and "flow-through" approaches. The latter method is achieved by pumping through the channels as well as by capillary action [76–78].

These demanded filters are fabricated by creating a cavity of extended size in a Fabry-Pérot (FP) resonator, as well as by using cascaded and coupled resonators [79–81]. These cascaded structures consist of separate FP filters connected in series. Changing the optical properties of individual filters does not affect the properties of the neighboring filters [82, 81]. The use of 1D PhC technology to create the FP cavities can remarkably improve the tuning capability of individual channels within these filters and optical switches for WDM optical interconnect applications. PhC technology can also reduce the footprint and provide an easier integration process [83]. Tunable multichannel PhC filters rely on the tuneability of the refractive index n, of several periods within the periodic photonic structure, allowing the formation of coupled resonators, via thermo-tuning, electro-tuning and a photorefractive effect [84–88]. These devices allow fine-tuning of individual channels in the filter system, by, for example, varying the temperature or applying an electric or magnetic field.

One-dimension (1D) photonic crystals have been widely used in silicon photonics due their simple structure and multiple working regimes: diffraction, Bragg reflection, and sub-wavelength regimes. Thanks to recent development of photonic technologies and high-resolution lithography, many 1D photonic crystal-assisted silicon integrated devices have been proposed and demonstrated to further increase integration density and improve device performance [89]. Two-dimensional (2D) photonic crystals have also been used, because their remarkably low group velocity is a promising solution for buffering and time-domain

processing of optical signals. It also offers the possibility for spatial compression of optical energy and the enhancement of linear and nonlinear optical effects [90].

A Photonic Crystal (PhC) is a periodic optical nanostructure that affects the motion of photons in much the same way that ionic lattices affect electrons in solids. In a PhC, the atoms or molecules are replaced by macroscopic media with different dielectric constants or a periodic refractive index. If the dielectric constants in the material are sufficiently different, and if the absorption of light by the material is minimal, the refraction and reflection of light from all the various interfaces can produce many of the same phenomena for photons that the atomic potential produces for electrons. We can design and construct PhCs with photonic bandgaps or stop bands (SBs), preventing light from propagating in certain directions with specified frequencies [91]. Different dimensions of photonic crystals can be fabricated (1D, 2D and 3D), in this section, only 1D and 2D PhCs will be discussed in detail due to the relevance they have to planar PIC.

- 1D Photonic crystals (1D PhCs): The simplest possible PhCs consist of alternating layers of material with different dielectric constants, a multi-layer film [Fig. 2.4]. These kinds of structures can act as mirrors, Bragg gratings, cavities and filters. These systems can be analysed using the transfer matrix method that takes into account the reflections and refractions of each of the interfaces. For better understanding and extrapolation to different structures, we will use the approach of the analysis of the band structures. 1D PhC, like traditional crystals, do not have continuous translational symmetry. Instead, they have discrete translational symmetry, that means they are invariant to translations of any distance which is a multiple of some fixed distance. The translational symmetry in the x direction is still present, but we have discrete translational symmetry in the z direction [Fig. 2.4] . The basic step distance is the lattice constant (a), and the basic step vector is called the primitive lattice vector, which in this case is $\mathbf{a} = a\hat{\mathbf{z}}$. Because of this discrete symmetry, $n(\mathbf{r}) = n(\mathbf{r} \pm \mathbf{a})$. By repeating this translation, we see that $n(\mathbf{r}) = n(\mathbf{r} \pm \mathbf{R})$ for any $\mathbf{R}$ that is an integer multiple of $\mathbf{a}$, that is, $\mathbf{R} = l\mathbf{a}$, where l is an integer. The dielectric unit that we consider to be repeated over the distances is highlighted in [Fig. 2.4] with a red box and is

known as the unit cell. If we apply translation operators, $\hat{T}$, to the eigenfunctions, considered plane waves in the x direction, $e^{jk_x x}$ [92]

$$\hat{T}_{d\hat{\mathbf{x}}} e^{jk_x x} = e^{jk_x(x-d)} = (e^{-jk_x d}) e^{jk_x x} \tag{2.11}$$

$$\hat{T}_{\mathbf{R}} e^{jk_z z} = e^{jk_z(z-la)} = (e^{-jk_z la}) e^{jk_z z} \tag{2.12}$$

where k_x and k_z are the the wavevectors in the x and z direction respectively. The PhC modes can be classified by specifying k_x and k_z. However, not all the values of k_z yield different eigenvalues. Consider two modes, one with a wave vector k_z and the other with wave vector $k_z + 2\pi/a$. Inserting this into [Eq. 2.12] shows that they have the same eigenvalues. In fact, all the modes with wavevectors of the form $k_z + m(2\pi/a)$, where m is an integer, form a degenerate set; they all have the same eigenvalue of $e^{-j(k_z la)}$ for $\hat{T}_{\mathbf{R}}$. Increasing k_z by an integral multiple of $b = 2\pi/a$ leaves the state unchanged. $\mathbf{b} = b\hat{\mathbf{z}}$ is known as the reciprocal lattice vector.

Since any linear combination of these degenerate eigenfunctions is itself an eigenfunction with the same eigenvalue, a linear combination, $\mathbf{H}_{k_x,k_z}(\mathbf{r})$, of the original modes can be taken and written in the form

$$\begin{aligned} \mathbf{H}_{k_x,k_z}(\mathbf{r}) &= e^{jk_x x} \sum_m \mathbf{c}_{k_z,m}(z) e^{j(k_z+mb)z} \\ &= e^{jk_x x} e^{jk_z z} \sum_m \mathbf{c}_{k_z,m}(z) e^{jmbz} \\ &= e^{jk_x x} e^{jk_z z} \cdot \mathbf{u}_{k_z}(y,z) \end{aligned} \tag{2.13}$$

where the c's are expansion coefficients to be determined by explicit solution, and $\mathbf{u}(y,z)$ is (by construction) a periodic function in z: by inspection in [Eq. 2.13] it can be verified that $\mathbf{u}(z+la,y) = \mathbf{u}(z,y)$.

The discrete periodicity in the z direction leads to a z dependence for $\mathbf{H}$ that is simply

the product of a plane wave with a z periodic function. It can be seen as a plane wave modulated by a periodic function due to the periodic lattice

$$\mathbf{H}(\ldots, z, \ldots) \propto e^{jk_z z} \cdot \mathbf{u}_{k_z}(z, ..) \tag{2.14}$$

and this result is known as **Bloch's theorem.**

By applying symmetry arguments we can describe the electromagnetic modes supported by the crystal. The material is periodic in the z direction and homogeneous in the x, and y directions.

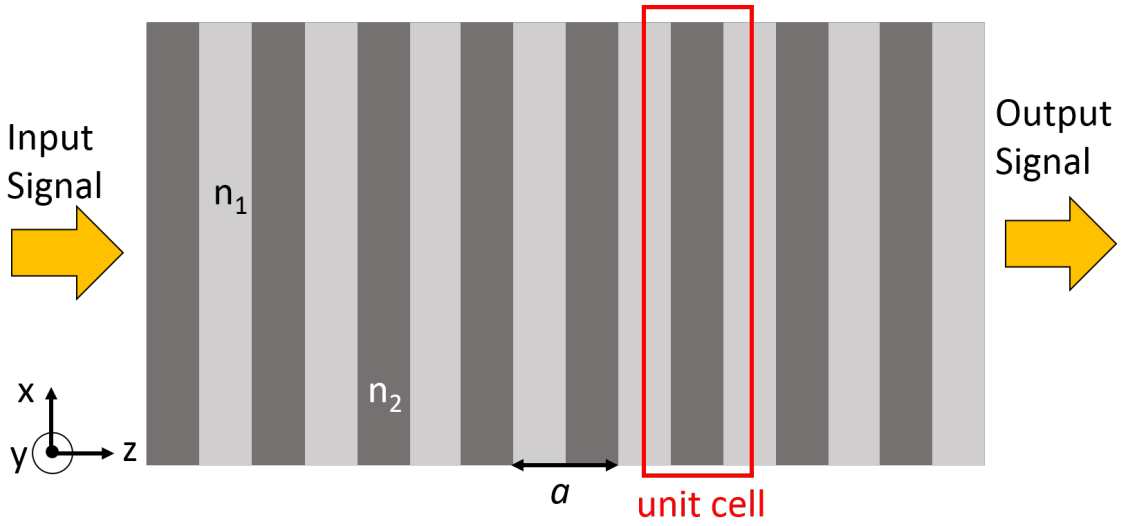

Fig. 2.4 Multilayer film, one-dimensional photonic crystal, the refractive index varies along the z direction, dark and light gray represents different refractive index of the material (n_1 and n_2) with an spatial period a, red box represents the structure unit cell.

We can classify the modes using $k_{||}$, k_z and j, the wave vector in the plane (with ρ the radial coordinate), the wave vector in the z direction, and the band number. The wave vectors specify how the mode transforms under translation operators, and the band number increases with frequency. We can write the modes in the Bloch form

$$\mathbf{H}_{j,k_z,k_{||}}(\mathbf{r}) = e^{ik_{||}\rho} e^{ik_z z} \mathbf{u}_{j,k_z,k_{||}}(z) \tag{2.15}$$

The function $\mathbf{u}(z)$ is periodic with the property $\mathbf{u}(z) = \mathbf{u}(z+R)$ whenever $\mathbf{R}$ is an integer multiple of the spatial period a. Because the crystal has continuous translational symmetry in the x,y plane the wave vector $k_{||}$ can assume any value. But k_z can be restricted to a finite interval, the one-dimensional Brillouin zone, because the crystal has discrete translational symmetry in the z direction. If the primitive lattice vector is $a\hat{\mathbf{z}}$ then the primitive reciprocal lattice vector is $2\pi/a\hat{\mathbf{z}}$ and the Brillouin zone is $-\pi/a < k_z \leq \pi/a$.

Consider the wave that propagates entirely in the z direction, crossing the layers of the PhC at normal incidence. In this case, $k_{||} = 0$ and only the wave vector component k_z is important. In Fig. 2.5, a plot of the angular frequency, $\omega_j(k)$ for two different multilayer films is shown. The left-hand plot [Fig. 2.5 (a)] is for a system in which all of the layers have the same refractive index, so the medium is homogeneous in all directions. The right hand plot [Fig. 2.5 (b)] is a structure in which the layers in the z direction are alternated with different media, creating a photonic bandgap, there is no allowed mode in the crystal that has a frequency within this gap regardless of k [93–97].

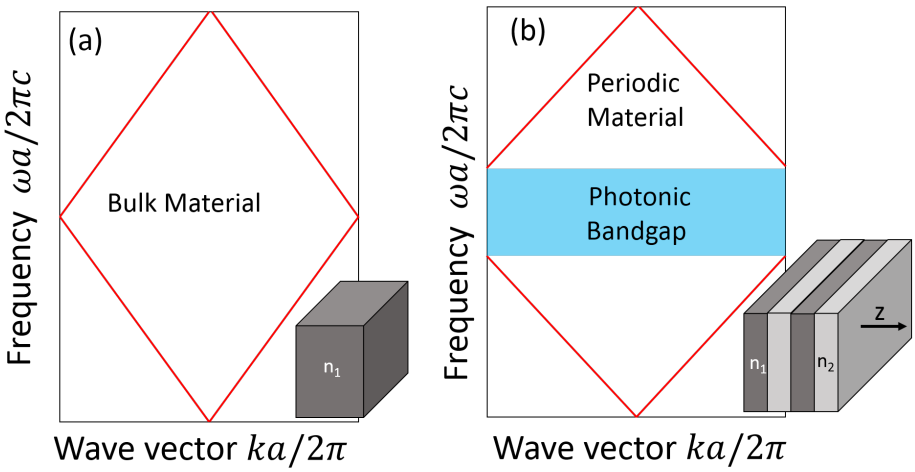

Fig. 2.5 Photonic band structures for on-axis propagation for two different configurations. (a) every layer has the same refractive index and (b) the refractive index of the layers alternate between two different values (n_1 and n_2) resulting in a photonic bandgap.

- 2D PhCs : A two-dimensional PhC is periodic along two of its axes and homogeneous

along the third axis [Fig 2.6]. It is possible to make use of the symmetries of the crystal to characterize the modes. The system is homogeneous in the z direction, the modes must be oscillatory in that direction with no restrictions on the wave vector k_z, furthermore, the system has discrete translational symmetry in the xy plane. We can write the modes in the Bloch form

$$\mathbf{H}_{j,k_z,k_{||}}(\mathbf{r}) = e^{ik_{||}\rho} e^{ik_z z} \mathbf{u}_{j,k_z,k_{||}}(\rho) \tag{2.16}$$

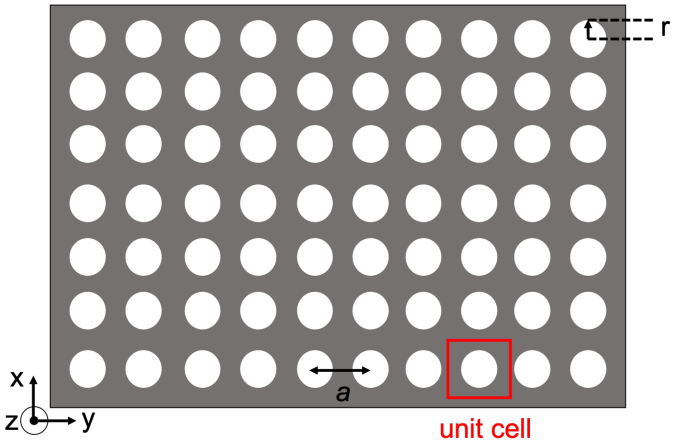

Fig. 2.6 Two dimensional PhC. This material is a square lattice of dielectric air holes, with radius r and dielectric constant $\varepsilon = 1$. The material is homogeneous along the z direction, and periodic along x and y with a lattice constant a. The gray material represents silicon or silicon nitride

where ρ is the projection of r in the xy plane and $\mathbf{u}(\rho)$ is a periodic function, in this case $k_{||}$ is restricted to the Brillouin zone and k_z is unrestricted. The band structures for TE and TM modes can be completely different. It is possible that there are photonic bandgaps for one polarisation but not for the other. By perturbing a single lattice site, we can create a single localized mode or a set of closely spaced modes that have frequencies within the gap. We can use point defects in PhCs to trap light. Using linear defects it is possible to guide light from one point of the photonic structure to another point of the photonic structure [Fig. 2.7 (a)]. Light that propagates in the WG with a frequency within the bandgap of the crystal is confined and can be directed

along the defect [98–100]. In the same way that a linear defect is created in a PhC structure, a cavity defect around a fixed point can be achieved [101]. Ring resonators or cavities are created in a PhC as multiplexers, lasers on chip, sensors or filters in optical communication applications [102] [Fig. 2.7 (b)].

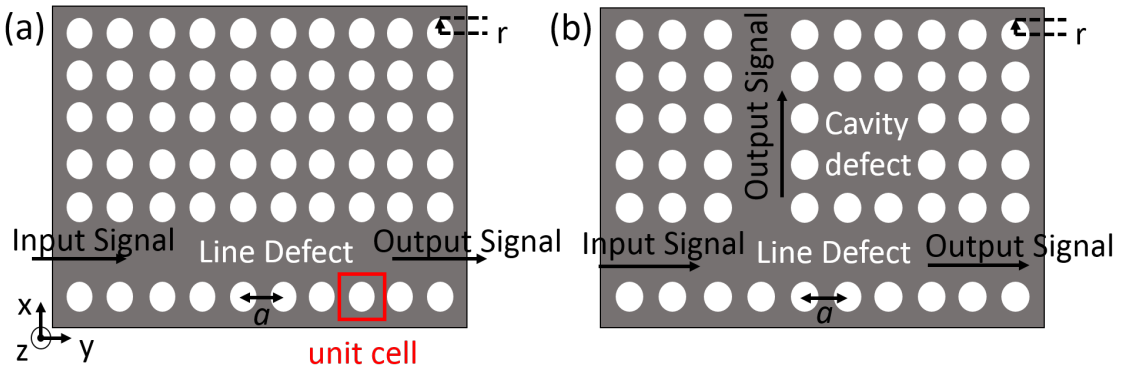

Fig. 2.7 Two-dimensional silicon or silicon nitride photonic crystal. (a) Schematic illustration of line defects in PICs, perturbing one row in the crystal (removing air holes in one of the lines in the PhC) a line defect is created and light with frequency within the bandgap of the crystal is confined in the defect and can be directed along the silicon or silicon nitride substrate waveguide. (b) Schematic illustration of a PhC cavity generated by the introduction of defects in the crystal for multiplexers and filters.

2.1.3 Ring resonators

Among various silicon photonic structures for multi-channel applications, silicon micro-ring resonators feature many advantages such as wavelength agility, high quality factors ($10^5 - 10^6$), high sensitivity and compact footprint. Many silicon photonics research groups worldwide have employed silicon micro-ring resonators as core building blocks to build optical multiplexers and demultiplexers (MUX/DEMUX) [103–106].

The light in a micro-ring resonator is coupled from the WG by the evanescent mode and is partially confined along the cavity sidewall by total internal reflection (TIR). At certain wavelengths, the cavity field phase matches with itself upon each round trip, giving rise to an optical resonance [107]. The resonance phase-matching condition is given as follows

$$n_{eff} L = m\lambda_m \tag{2.17}$$

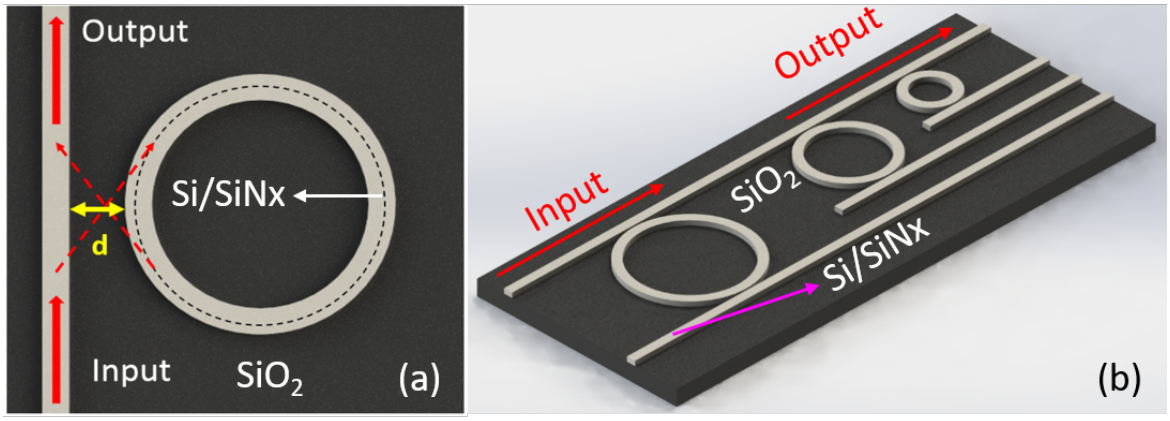

Fig. 2.8 (a) WG coupled to a micro-ring resonator schematic separated by a distance, d (b) Add-drop filters schematic based on ring resonators

where n_{eff} is the effective refractive index of the micro-ring resonator WG optical mode, L is the cavity round-trip length, λ_m is the m_{th} order resonance wavelength in free space, and m is the integer number of wavelengths along an optical round-trip length. In the case of a micro-ring with radius R, L is given by $2\pi R$. The n_{eff} is wavelength dependent in a dispersive medium. Taking into account the material dispersion, the free-spectral range, FSR, in wavelength units between adjacent orders of resonance about λ_m is given as [108]

$$FSR = \lambda_m^2 / n_g L \tag{2.18}$$

where n_g is the group index. The quality factor, Q, is used to characterize the micro-resonator loss of energy and is given by

$$Q = \omega_0 \frac{U}{P_L} \tag{2.19}$$

where ω_0 is the angular resonance frequency. We define the cavity energy loss rate P_L as the drop in cavity stored energy U over time, i.e.

$$P_L = -\frac{dU}{dt} = \frac{\omega_0}{Q} U \tag{2.20}$$

with the stored energy varying over time $U(t)$ expressed as

$$U(t) = U_0 e^{-\omega_0 t/Q} = U_0 e^{-t/\tau} \tag{2.21}$$

where U_0 is the initial cavity energy. We define a cavity lifetime as

$$\tau = \frac{Q}{\omega_0} \tag{2.22}$$

The cavity lifetime is proportional to Q and gives the time taken for the cavity energy to decay to $1/e$ of the initial energy U_0.

In a WG-coupled micro-ring resonator, the WG coupling perturbs the resonator and imposes a slight shift in the resonance wavelength and additional energy loss. The total quality factor, Q, of a WG coupled micro-ring resonator therefore comprises two contributions, the intrinsic cavity quality factor, Q_0, and the coupling quality factor, Q_c. The Q_0 is related with the intrinsic cavity power loss coefficient, α. The Q_c is related with the WG to micro-ring coupling coefficient κ. The relations of Q, Q_0, Q_c, α, and κ are described as follows [109]

$$Q^{-1} = Q_0^{-1} + Q_c^{-1} \tag{2.23}$$

and Q_0, Q_c are defined as

$$Q_0 = \omega_0 \tau_0 = \frac{2\pi c}{\lambda_0} \cdot \frac{n_g}{\alpha c} = \frac{2\pi n_g}{\alpha \lambda_0} \tag{2.24}$$

$$Q_c = \omega_0 \tau_c = \frac{\omega_0 \tau_{rt}}{|\kappa|^2} \tag{2.25}$$

where τ_0 is the intrinsic cavity energy $1/e$ lifetime, τ_c is the extrinsic WG-coupling energy

$1/e$ lifetime, τ_{rt} is the round-trip light propagation time, and λ_0 is the cavity resonance wavelength in free space.

As discussed previously, photonic integrated micro-ring resonators can be used as the key component for wavelength division multiplexer (WDM) systems. WDM is a technology that for many years has been used to multiplex a number of optical carrier signals onto a single optical fiber. This technique enables bidirectional communications over one strand of fiber, as well as multiplication of capacity. High data rates can be transmitted through individual optic fibers (Terabits/s). WDMs have been considered for building optical interconnects and ultra-high data rate networks [110–112, 82].

- Demultiplexer (DEMUX): a demultiplexer is a 1 x j device which splits a signal that contains all the information into different wavelengths through the output ports [Fig 2.9 (a)].

- Multiplexer (MUX): a multiplexer is the inverse of a demultiplexer, in this case we have a j x 1 device which merges the different input signals (1,2,3....j) into a unique output signal [Fig 2.9 (b)].

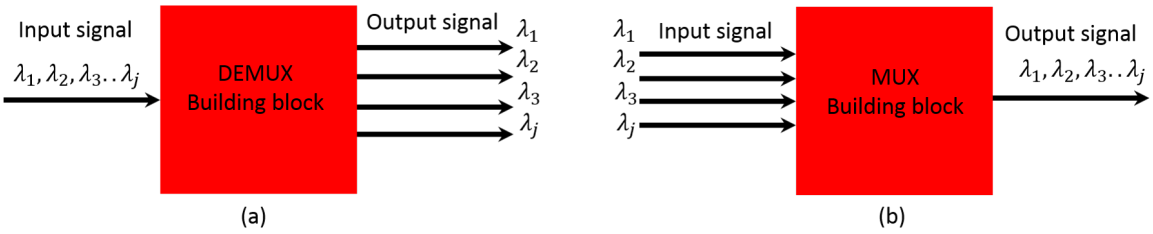

Fig. 2.9 (a) Demultiplexer (DEMUX) building block principle (b) Multiplexer (MUX) building block principle

Wavelength division multiplexing is categorized into two categories, coarse and dense, depending on the number of channels and the channel spacing.

1. Coarse WDM (CWDM) systems use a few channels with widely spaced wavelengths (20 nm or more). An example is a system with two wavelengths, one at 1310 nm and another at 1550 nm

2. Dense WDM (DWDM) systems have a large number of channels (generally more than 8) with closely spaced wavelengths. At a wavelength of 1550 nm in the C band a frequency spacing of 200 GHz corresponds to a wavelength spacing of 1.6 nm. DWDM systems can use channel spacing as small as 50 GHz, or sometimes even 25 GHz corresponding to wavelength spacing of 0.4 nm and 0.2 nm respectively.

2.1.4 Mach-Zehnder Interferometer

The Mach-Zehnder Interferometer (MZI) is a common device in optical circuits, being the basis of several other devices such as modulators, switches and filters [113–115]. A MZI consists of an input wave separated, evenly or not, into two by a splitter (Y-branch) or multi-mode interference coupler (MMI) [Fig 2.10]. The intensities in the two arms of the MZI can be the same or not depending on the splitter and combiner design. We can represent the electric field of the propagation modes in arm 1 and arm 2 of the interferometer as E_1 and E_2 respectively, where

$$E_1 = E_i e^{-jwt - j\beta_1 L_1} e^{-\frac{\alpha_1}{2} L_1} \tag{2.26}$$

$$E_2 = E_i e^{-jwt - j\beta_2 L_2} e^{-\frac{\alpha_2}{2} L_2} \tag{2.27}$$

L_1 and L_2 are the lenght of the arms 1 and 2 of the MZI respectively, β_1 and β_2 are the propagation constant for each of the arms of the MZI and α_1 and α_2 are the absoption coefficient of the MZI arm 1 and 2 respectively. For the moment, we have considered the two fields to have the same amplitude, E_i, but different propagation constant and losses. The two fields propagate along their respective arms of the interferometer and recombine at the output WG. When the first splitter divides the input wave in two, they are both in phase. However, when the fields recombine using a combiner (Y-branch or multimode interference (MMI)) the two fields may no longer be in phase, either due to different optical path lengths in the

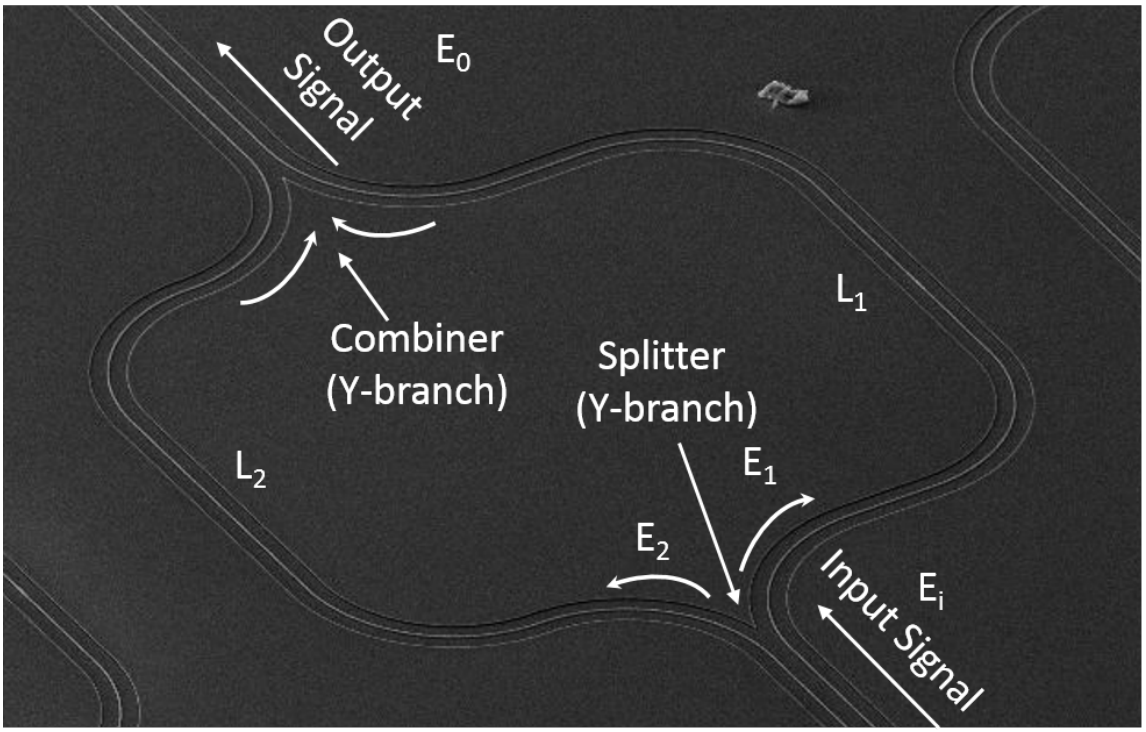

Fig. 2.10 MZI scanning electron microscope (SEM) image for the illustration of the working principle.

arms or due to different propagation constants caused by, for example, depositing a material to partially cover one of the arms. At the end of the two WGs (at the input of the combiner, Y-branch or MMI), the fields are:

$$E_1 = E_1 e^{-j\beta_1 L_1 - \frac{\alpha_1}{2} L_1} = \frac{E_i}{\sqrt{2}} e^{-j\beta_1 L_1 - \frac{\alpha_1}{2} L_1} \tag{2.28}$$

$$E_2 = E_2 e^{-j\beta_2 L_2 - \frac{\alpha_2}{2} L_2} = \frac{E_i}{\sqrt{2}} e^{-j\beta_2 L_2 - \frac{\alpha_2}{2} L_2} \tag{2.29}$$

The output of the second Y-branch (the combiner) is:

$$E_0 = \frac{1}{\sqrt{2}} (E_1 + E_2) = \frac{E_i}{2} \left[e^{-j\beta_1 L_1 - \frac{\alpha_1}{2} L_1} + e^{-j\beta_2 L_2 - \frac{\alpha_2}{2} L_2} \right] \tag{2.30}$$

The FSR of the response of the MZI interference, if the WGs in both arms are identical, can be determined by:

$$FSR = \frac{\lambda^2}{n_g \Delta L} \tag{2.31}$$

where ΔL is the difference in the arms of the MZI. Let's assume that $L_1 > L_2$, then $\Delta L = L_1 - L_2$, λ being the central wavelength and n_g the group index. The resonant condition for a MZI is determined by:

$$m\lambda_m = n_{eff}\Delta L \tag{2.32}$$

where m is the integer number of wavelengths along an optical round trip length and λ_m is the m_{th} order resonance wavelength in free space.

2.1.5 Grating coupler

A grating coupler (GC) is a periodic structure that can diffract light from propagation in the waveguide (in plane) to free space (out of plane) [116–120]. GCs are normally used as inputs and outputs to couple light between an optical fiber and silicon or silicon nitride integrated waveguides. In Fig. 2.11 (a), a cross-section of a fully etched grating coupler is presented. In order to couple light into a waveguide mode, as depicted in figure 2.11 (b), it is necessary for the components of the phase velocities in the direction of propagation (z direction) to be equal, this is called the phase matching condition. We can consider an incident ray upon the surface of the waveguide at an angle θ_a, the ray will propagate in medium n_3 with the propgation constant $k_0 n_3$ in the direction of propagation. Therefore, the z directed propagation constant in medium 3 will be:

$$k_z = k_0 n_3 \sin\theta_a \tag{2.33}$$

and therefore the phase matching condition will be:

$$\beta = k_z = k_0 n_3 \sin\theta_a \tag{2.34}$$

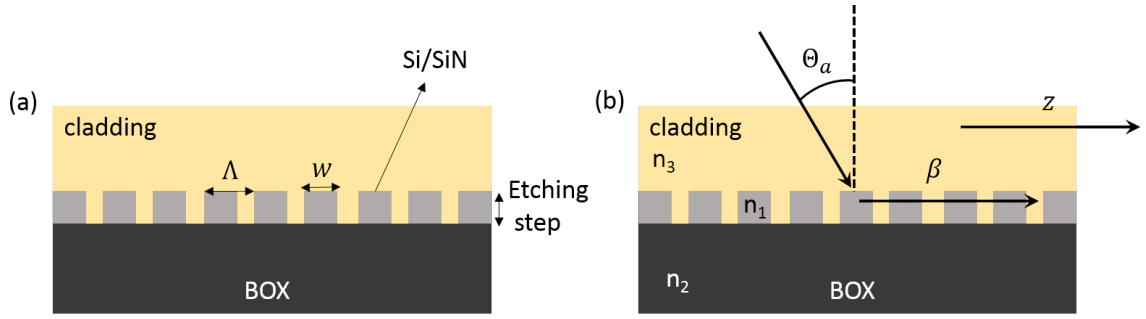

Fig. 2.11 (a) Grating coupler schematic (b) Light incident upon the surface of a waveguide, and the working principle of grating couplers.

where β is the waveguide propagation constant. We know from Eq. 2.4 that $\beta \geqslant k_0 n_3$, and the condition of Eq. 2.34 can never be satisfied, since $\sin\theta_a$ will be less than unity. This is the main reason why a prism or a grating is needed to couple light on to a chip. The periodic nature of the grating causes a periodic modulation of the effective refractive index of the waveguide. For an optical mode with propagation β_m when the grating is not present, the modulation results in a series of possible propagation constants, β_p given by:

$$\beta_p = \beta_m + \frac{2p\pi}{\Lambda} \tag{2.35}$$

where Λ is the period of the grating, w is the slab width (see Fig. 2.11 (a)), and $p = \pm 1, \pm 2, \pm 3$, etc. The modes are equivalent to different diffraction orders and the propagation constants corresponding to positive values of p can not exist in the waveguide because the propagation constant will still be less than $k_0 n_3$. Only negative values of p can result in a phase matching condition. For $p = -1$, the propagation constants becomes:

$$\beta_p = \beta_m - \frac{2\pi}{\Lambda} \tag{2.36}$$

the phase matching condition will occur when:

$$\beta_m - \frac{2\pi}{\Lambda} = k_0 n_3 \sin\theta_a \tag{2.37}$$

In order to have this expression in terms of the effective refractive index, eq. 2.37 becomes:

$$k_0 n_{eff} - \frac{2\pi}{\Lambda} = k_0 n_3 \sin\theta_a \tag{2.38}$$

and substituting k_0 we obtain:

$$\Lambda = \frac{\lambda}{n_{eff} - n_3 \sin\theta_a} \tag{2.39}$$

which is the well known equation for GCs and allow us to determine the waveguide grating period for a desired input angle in air or another material cladding to couple to the mode with propagation constant β_m.

2.2 Functional materials

2.2.1 Liquid crystals

A liquid crystal is a state of matter which is liquid-like and crystalline at the same time. Crystalline mesophases possess some typical properties of a liquid, such as fluidity, formation and coalescence of droplets and the inability to support shear. These mesophases also have certain crystalline properties, such as anisotropy of optical, electrical, and magnetic properties, as well as a periodic arrangement of molecules in one or more spatial directions. Depending on the arrangement of the molecules in a mesophase, liquid crystals are subdivided into nematics, smectics and cholesterics [121] [Fig. 2.12].

- **Nematic liquid crystal**: In a nematic mesophase, molecules possess a long-range orientational order with molecular long axes aligned along a preferred direction. The preferred direction may vary throughout the medium and is called a director. The orientation of the director is represented by a unit vector, **d(r)**. In a nematic, the molecules

are able to rotate around their long axes, and there is no preferential arrangement of their ends [Fig. 2.12 (a)].

- **Smectic liquid crystal**: The important feature of a smectic mesophase, which distinguishes it from a nematic or a cholesteric one, is its stratification. The molecules are arranged in layers and exhibit some correlations in their positions in addition to the orientational ordering. The layers can slide freely over one another. Depending on the molecular order in layers, a number of different types of smectics have been observed. In a smectic, molecules are aligned perpendicular to the layers,without long-range crystalline ordering within the layers [Fig. 2.12 (b)].

- **Cholesteric liquid crystal**: In a cholesteric mesophase the average molecular orientation twists through the medium with a certain periodicity, p. The cholesteric mesophase is similar to the nematic: it has a long-range orientational order, but no long-range positional order of the centers of mass of molecules. It differs from the nematic mesophase in that the director varies throughout the medium in a regular way even in an unstrained state. The director distribution is precisely what would be obtained by twisting a nematic aligned along the y axis about the x axis. In any plane perpendicular to the twist axis, the long axes of the molecules align along a single preferred direction in this plane, but in a series of parallel planes this direction rotates uniformly [Fig. 2.12 (c)].

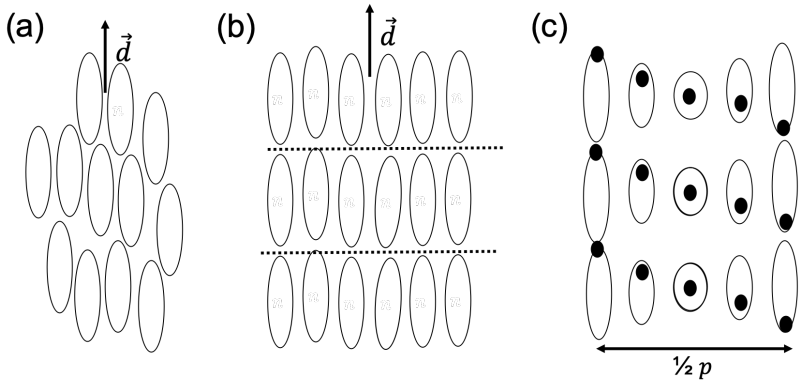

Fig. 2.12 (a) Nematic liquid crystal (b) Smectic liquid crystal (c) Cholesteric liquid crystal.

The liquid crystals used to make electro-optic devices are usually of sufficiently high resistivity that they can be treated as ideal dielectric materials [122]. Because of the elongated shape of the constituent molecules, and their ordered orientation, liquid crystals have anisotropic dielectric properties with uniaxial symmetry. The electric permittivity is $\varepsilon_{||}$ for electric fields pointing in the direction of the molecules and $\varepsilon_{\perp}$ in the perpendicular direction.

A uniaxial crystal is an optical element that has a single optic axis. In other words, a uniaxial crystal has one crystal axis different from other two crystallographic axes. In this case, the indexes are usually denoted $n_1 = n_2 = n_o$ and $n_3 = n_e$, which are known as ordinary and extraordinary indexes, respectively. The crystal is said to be positive uniaxial if $n_e > n_o$, and negative uniaxial if $n_e < n_o$. Liquid crystals for which $\varepsilon_{||} > \varepsilon_{\perp}$ (positive uniaxial) are usually selected for electro-optic applications [123, 124]. When a steady electric field is applied, electric dipoles are induced and the resultant electric forces exert torques on the molecules. The molecules rotate in a direction such that the free electrostatic energy, $-1/2 \cdot \mathbf{E} \cdot \mathbf{D} = -1/2 \left[\varepsilon_{\perp} E_1^2 + \varepsilon_{\perp} E_2^2 + \varepsilon_{||} E_3^2\right]$, is minimized. The electric field components are in the directions of the principal axes. Due to the positive uniaxial condition, for a given direction of the electric field, minimum energy is achieved when the molecules are aligned with the field, so $E_1 = E_2 = 0$ and $\mathbf{E} = (0,0,E)$, and the energy is then $-1/2 \cdot \varepsilon_{||} E^2$. If an electric field is generated by applying a voltage across transparent conductive electrodes coated on the inside of glass plates, the resultant electric forces tend to tilt the molecules toward alignment with the field, but the elastic forces at the surfaces of the glass plates resist this motion. The equilibrium tilt angle θ for most molecules is a monotonically increasing function of voltage (V) and can be described as

$$\theta = \begin{cases} 0, & V < V_c \\ \pi/2 - 2 \cdot \tanh\left[e^{-\frac{V-V_c}{V_0}}\right], & V > V_c \end{cases} \tag{2.40}$$

where V is the applied voltage, V_c a critical voltage at which the tiliting process begins, and V_0 a liquid crsytal material dependence constant. When $V - V_c = V_0$, $\theta \approx 50°$. As $V - V_c$ increases beyond V_0, θ approaches 90°. When the electric field is removed, the orientation of the molecules near the glass plates is reasserted and all of the molecules tilt back to their

original orientations, in planes parallel to the plates. The liquid crystal refractive index angle dependence can be described by

$$n_c(\theta) = \frac{n_o n_e}{\sqrt{n_o^2 \sin^2(\theta) + n_e^2 \cos^2(\theta)}} \tag{2.41}$$

In a sense, the liquid-crystal material may be viewed as a liquid with memory. Different reconfigurable photonic integrated circuits can be designed and fabricated exploiting the tunability of the liquid crystal refractive index.

2.2.2 2D materials

Normally, when we are talking about the term 2D materials, we are talking about a crystalline material which consists of a single or a few layers of atoms, with a thickness varying from one atomic layer to multi-layer [125]. Owing to their atomic layer thickness, strong light-matter interaction, high non-linearity, broadband optical response, fast tunability, controllable optoelectronic properties, and high compatibility with other photonic structures, 2D materials, including graphene, transition metal dichalcogenides and black phosphorus, have been attracting increasing attention for photonic integrated applications. By tuning the density of carriers in 2D materials by electric field effect or optically, their physical properties (e.g Fermi level or nonlinear absorption) can be tuned. The refractive index of 2D materials can be instantly changed, making them versatile for different reconfigurable PIC applications in optical communications.

Graphene

Graphene is a single layer of a graphite crystal. It consists of a single atomic layer of pure covalently bonded carbon atoms arranged in a two-dimensional (2D) hexagonal lattice structure. Each carbon atom has six electrons surrounding its nucleus, two in the inner shell and four in the outer electron shell. Three out of these four electrons are the electrons of nearest-neighbor atoms and creates the strong chemical bonds that makes graphene one of the strongest materials, whereas the other electron in the outer electron shell of each

carbon atom is delocalized in the whole graphene layer [126]. The energy band structure of the delocalized electron determines graphene's conductivity. While in non-conducting or semiconducting materials the full valence band and the empty conduction band are separated by an energy gap, there is no gap between the conduction and valence bands in pure graphene. Thus, pure graphene can be regarded as a zero-gap semiconductor. Similarly, while in metals the valence band is partially filled, in pure graphene the Fermi level lies at the point where the conduction and valence bands meet (the Dirac point) [127].

The duality between semiconductor and metallic behaviour can be controlled by tuning the position of the Fermi level from the Dirac point, either by chemical additions, or, more easily, by using the electric field effect, applying a constant voltage (gating the graphene) between a graphene and a metallic layer or a graphene capacitor, separated by a very thin insulator. The resulting electric field will modify the quantity of conduction carriers and consequently graphene's electrical conductivity. For a given polarity of the voltage, that is, for a given direction of the DC electric field, the conduction band fills up, which means that electrons are added to the system. For the other polarity, the number of electrons in the valence band is reduced, which means that holes are added to the system [Fig. 2.13].

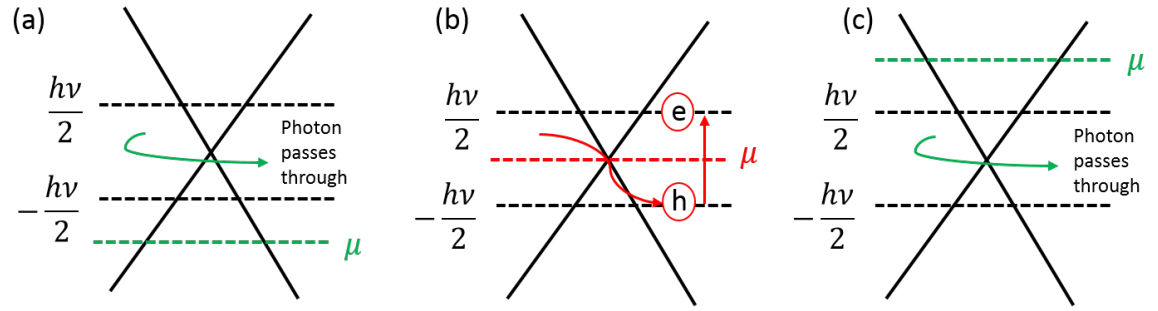

Fig. 2.13 Schematic of a graphene band diagram gated when (a) The Fermi level (μ) is below the valence band and no absorption occurs because both the valence and the conduction bands are empty. (b) Absorption takes place when the Fermi level is between the valence and conduction band generating electron-hole pairs and (c) Fermi level is above the conduction band and no absorption occurs due to the full valence and conduction bands.

The special behavior of graphene is due to both its two-dimensional (2D) structure, which confines electrons in one atomic layer, and to its low density of states (DOS) near the Dirac point, which causes the Fermi energy (E_F) to shift significantly varying the carrier density

[128]. For example, a Fermi level up to 0.9 eV has been experimentally demonstrated using the electrostatic field gating technique [129]. The tunable band-gap of graphene offers great opportunities and flexibility for infrared and visible light manipulation on chip.

Transition Metal Dichalcogenides (TMDs)

2D TMDs are atomically thin semiconductors of the type MX_2 , where **M** is a transition metal atom and **X** is a chalcogen atom. Typically, TMDs have bandgaps ranging from 1 to 2.5 eV, corresponding to near-infrared and visible frequencies. The bandgap of bulk TMD material down to a thickness of two monolayers is indirect, so the emission efficiency is lower compared to monolayer materials. The emission efficiency is about 10^4 greater for a TMD monolayer than for bulk materials [130]. The bandgaps of TMD monolayers are in the visible range (between 400 nm and 700 nm). Owing to their direct bandgap, TMD monolayers are promising materials for optoelectronics applications as emitters on chip. Two of the most studied and promising TMD materials are MoS_2 and WS_2, [131] which maintain some of the outstanding properties of graphene [Fig. 2.14].

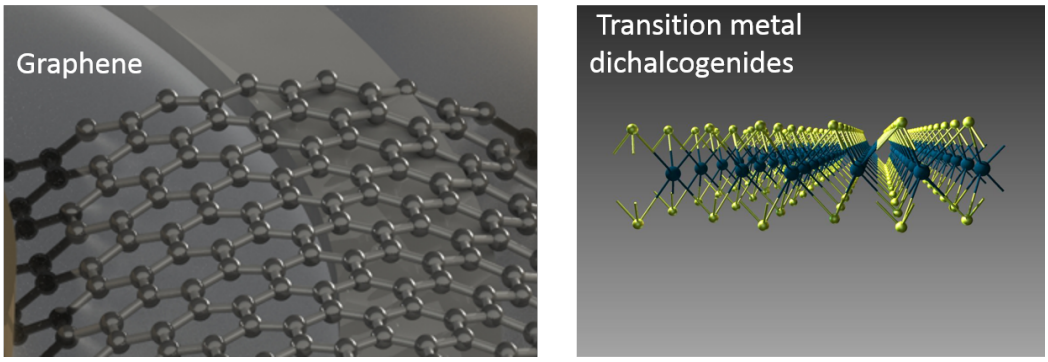

Fig. 2.14 Intrinsic single-layer graphene is a zero-bandgap semi-metallic material while its Fermi level (μ) can be tuned up to 1 eV under external electric field, covering the range from THz to visible wavelength. The transition metal dichalcogenides have layer number-dependent bandgaps ranging from 1.0 to 2.5 eV [125].

2.2.3 Phase change materials

Phase change materials (PCMs) are characterized by the difference between properties, along with the fact they can be switched quickly and repeatedly between phases, and that both

phases are stable at room temperature for long periods, i.e. whether they are amorphous or crystalline [132]. This combination of properties is attractive for different opto-electronic applications. Phase change material based technology initially found applications in optical disks (CDs, DVDs) where the fast write time for changing the state, relatively high potential data density and ability to be rewritable were significant advantages. Typically, the thermal excitation (necessary to change phase) is achieved using a laser pulse, but can also be provided electrically (Joule heating) or by any other method by which heat can be transferred to the sample [133, 134]. The phase change can be either a liquid-solid change or a solid-solid change where the molecular structure is reconfigured from an amorphous state to an ordered crystalline state and is a reversible process [Fig 2.15]. In rewriteable optical data storage employing phase change materials a short pulse of a focused, high intensity laser beam locally heats the phase change material above its melting temperature. Rapidly cooling the phase change alloy (at rates typically around several degrees per nanosecond) quenches the liquid-like state into a disordered, amorphous phase [135]. This amorphous state has different optical properties, leading to a different reflectivity, than the surrounding crystalline state. Hence, detecting regions with amorphous structure is straightforward and can be achieved by employing a laser beam of low intensity. To erase the stored information, a laser pulse with intermediate power is utilized. The laser locally heats the phase change film above the crystallization temperature. At elevated temperatures above the glass transition temperature the atoms become increasingly mobile and can revert to the energetically favourable crystalline state, erasing the recorded information [136].

In electronic memory applications of phase change materials, a short and relatively high current pulse is used to locally melt the crystalline material. The resulting amorphous state has a high resistance which exceeds the resistance of the crystalline state by several orders of magnitude $(10^2 - 10^3)$ [137]. An intermediate power pulse is used to heat the material above its crystallization temperature to switch it back to the crystalline, low resistance state, while a low power pulse is used to determine the resistance of the phase change material.

Different phase change materials have been developed where the temperature required to change the phase as desired can span a large range of possible values [138] . On changing

the phase of the material, the refractive index for the material is altered, and the tunability of the refractive index gives rise to potential applications in reconfigurable PICs to provide the much needed non-volatile reconfigurability in integrated photonic components [134]. The crucial feature of integrated PCMs compared with conventional thermo-optic based programmable circuits is that energy is only consumed during the actual switching process (due to non-volatility of PCMs). Different technological applications of PCM-based photonic devices such as switches [139, 140], wavelength division multiplexers [141], directional couplers [142], memories [143, 144, 141, 145] and neuron and synapse mimics [146, 147] have been already demonstrated, all operating in the C-band range of the spectrum.

The combination of the Si_3N_4 or Si platform and phase-change materials enables a variety of fast, non-volatile, and re-configurable devices for a range of on-chip applications [148–150].

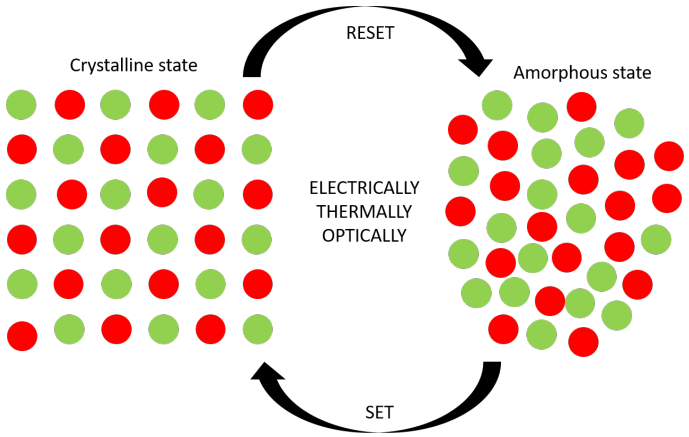

Fig. 2.15 Phase change material working principle. The PCM can be switched between states, optically, thermally or electrically, when switch occurs from amorphous to crystalline (SET) or when switch occurs from crystalline to amorphous (RESET).

Chapter 3

Methods

3.1 Device Design

In this section, we will describe the design and optimisation of the passive and active devices demonstrated in this thesis. All the designs and studies were performed using two different simulation tools: COMSOL Multiphysics® software to perform the numerical modelling and MATLAB for data processing and analytical solutions. Each of these programs provide a variety of specialised solvers that can be used to calculate the modes within a device and their propagation in different stages of the design phase. The layouts of all the devices were created with an open access tool called "Nazca design" using python functions generated by the author of the thesis with the goal of building his own library for photonic integrated circuits. This section contains an overview of these tools, along with a brief description of how they were used to design the devices detailed in the following chapters.

3.1.1 Mode Analysis

The MODE Solutions in COMSOL Multiphysics® is a design environment based on an eigenmode solver which determines the solution to Maxwell's equations for arbitrary waveguide geometries. It allows us to calculate the profile and physical properties of the modes supported by a waveguide at particular wavelengths as shown in [Fig. 3.1]. This method provides understanding of how the light propagates within the simulated structures. Hence, it is particularly useful for designing photonic integrated devices with a uniform geometry and a large propagation length such as waveguides, ring resonators or MZIs. From the simulations, we obtain the effective refractive index associated to the propagated mode, $n_{eff} = n^r_{eff} + jk_{eff}$.

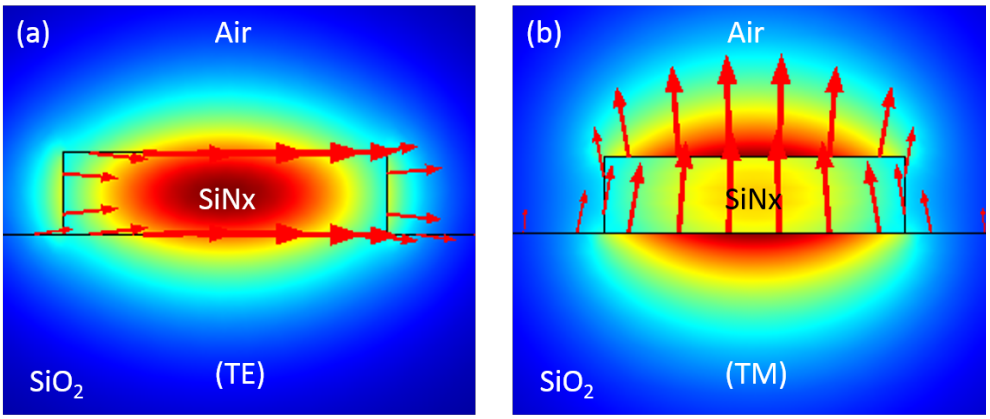

Fig. 3.1 (a) TE mode profile of a Silicon Nitride waveguide cross-section where the electric field direction is represented by red arrows (b)TM mode profile of a Silicon Nitride waveguide cross-section where the electric field direction is represented by red arrows.

3.1.2 1D Photonic crystal

In this sub-section, a description of how to model 1D PhCs will be presented and explained in detail. First, a complete study regarding the passive 1D PhC structures with an analytical calculation of the reflection and transmission coeffcients is presented, followed by the introduction of reconfigurable materials in the passive structures to make tuneable 1D PhC structures based on smart materials, paving the way to future smart photonic integrated circuits for optical communications applications.

Passive structures

For modelling and designing 1D photonic integrated crystals a 2 x 2 transfer matrix method (TMM) can be used. The TMM is so general that it can be applied to treat the transmission and reflection properties of a general multilayer structure.

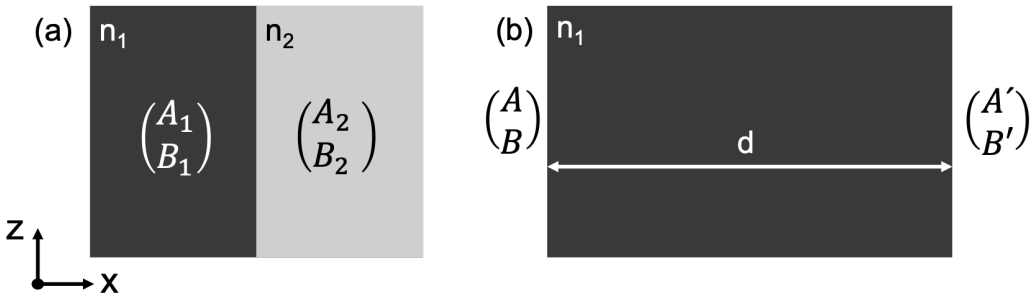

Fig. 3.2 (a) 1D PhC interface structure between two different mediums (b) Light travelling distance, d, along the homogeneous part of the 1D photonic structure.

To introduce the TMM, a general case of plane wave propagation on two sides of a dielectric interface is considered [Fig. 3.2 (a)]. The electric field can be written

$$E = \begin{cases} \left(A_1 e^{-jk_{1x}x} + B_1 e^{+jk_{1x}x}\right) e^{-j\beta_z} & \text{medium 1} \\ \left(A_2 e^{-jk_{2x}x} + B_2 e^{+jk_{2x}x}\right) e^{-j\beta_z} & \text{medium 2} \end{cases} \tag{3.1}$$

where A_1 and A_2 are the amplitudes of the right-travelling wave (along $+x$ direction), B_1 and B_2 are the amplitudes of the left-travelling wave (along $-x$ direction), β is the z component of the wavevector and k_{1x} and k_{2x} are the x components of the wavevector. Note that β is the same in both media as the structure is homogeneous in the z direction. These components of the wavectors are related by the following equations

$$\begin{aligned} k_{1x}^2 + \beta^2 &= (n_1 \omega/c)^2 \\ k_{2x}^2 + \beta^2 &= (n_2 \omega/c)^2 \end{aligned} \tag{3.2}$$

Based on the definition of the transmission and reflection coefficients associated with the interface, the amplitudes are related by the following equations

$$\begin{aligned} B_1 &= A_1 r_{12} + B_2 t_{21} \\ A_2 &= A_1 t_{12} + B_2 r_{21} \end{aligned} \tag{3.3}$$

where r_{12}, r_{21}, t_{12}, and t_{21} are the Fresnel reflection and transmission coefficients. Solving A_1 and B_1 in terms of A_2 and B_2, we obtain

$$\begin{aligned} A_1 &= \frac{1}{t_{12}} A_2 - \frac{r_{21}}{t_{12}} B_2 \\ B_1 &= \frac{r_{12}}{t_{12}} A_2 + \left(t_{21} - \frac{r_{12} r_{21}}{t_{12}}\right) B_2 \end{aligned} \tag{3.4}$$

and taking into account that the Fresnel coefficients satisfy the following relationships

$$\begin{aligned} t_{12} t_{21} - r_{12} r_{21} &= 1 \\ r_{21} &= -r_{12}, \end{aligned} \tag{3.5}$$

the previous equation can be rewritten as

$$A_1 = \frac{1}{t_{12}} A_2 + \frac{r_{12}}{t_{12}} B_2$$
$$B_1 = \frac{r_{12}}{t_{12}} A_2 + \frac{1}{t_{12}} B_2 \tag{3.6}$$

or equivalently, in a matrix form

$$\begin{bmatrix} A_1 \\ B_1 \end{bmatrix} = \frac{1}{t_{12}} \begin{bmatrix} 1 & r_{12} \\ r_{12} & 1 \end{bmatrix} \begin{bmatrix} A_2 \\ B_2 \end{bmatrix} \equiv T_{12} \begin{bmatrix} A_2 \\ B_2 \end{bmatrix} \tag{3.7}$$

where T_{12} is defined as the transition matrix between layers 1 and 2. The transition matrix relates the field column vector on two sides of a dielectric interface.

We now need a matrix for propagation from one end of a homogeneous layer to the other end of the layer. Referring to [Fig. 3.2 (b)], let us consider propagation of plane waves in a homogeneous medium with thickness d and refractive index n_1. Using the column vector for the field representation, we obtain

$$\begin{bmatrix} A \\ B \end{bmatrix} = \begin{bmatrix} e^{j\phi} & 0 \\ 0 & e^{-j\phi} \end{bmatrix} \begin{bmatrix} A' \\ B' \end{bmatrix} \equiv P \begin{bmatrix} A' \\ B' \end{bmatrix} \tag{3.8}$$

where A and B are the field amplitudes on the left end of the medium, whereas A' and B' are the field amplitudes on the right end of the medium. The phase shift is given by

$$\phi = 2\pi n d/\lambda - j\alpha/2 \tag{3.9}$$

and the diagonal matrix P is defined as the propagation matrix, where n is the refractive index and α is the loss coefficient, both defined in Chapter 2. For lossless media, the propagation matrix is unitary. The transition matrix T and the propagation matrix P can now be employed to treat a general multilayer structure [Fig. 3.3 (a)].

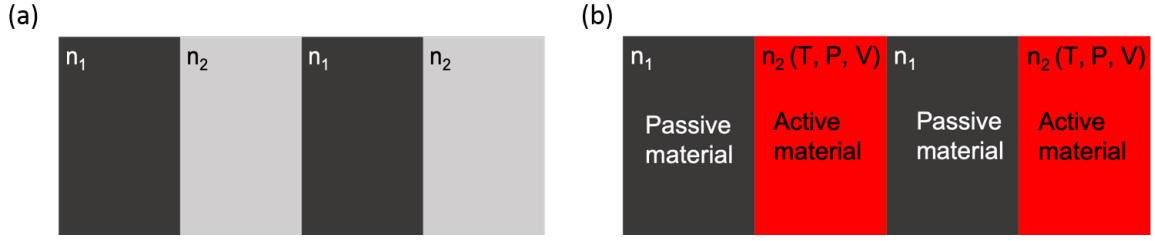

Fig. 3.3 (a) 1D Photonic Crystal multilayer structure. (b) 1D Photonic crystal multilayer structure based on funtional materials for tunable device design.

By multiplying the propagation and transition matrices a 2x2 matrix M can be obtained. For the particular case of 4 stack layers ($N = 4$), the matrix can be described by

$$M = T_{01}P_1T_{12}P_2T_{21}P_1T_{12}P_2 \tag{3.10}$$

The propagation matrix is polarisation independent, whereas the transition matrix depends on the sate of polarisation . Finally, the transmission and reflection coefficients, t and r respectively are given by

$$\begin{aligned} t &= \frac{1}{M_{11}}, \\ r &= \frac{M_{21}}{M_{11}}, \end{aligned} \tag{3.11}$$

For calculating the transmittance, T and reflectance, R of a layered structure, the following expressions should be taken into account

$$tt^{'*} + rr^* = 1, \quad tr^{'*} + rt^* = 0 \tag{3.12}$$

These are known as the Stokes relationships and it can also be shown that for a lossless layered structure,

$$R + T = 1 \tag{3.13}$$

Active structures

To introduce the active materials in the design, the refractive index, n, in the propagation, P, and transition, T, matrices should be modified. P and T are temperature (T), voltage (V) or optical power (P) dependent due to the change in the refractive index of the functional materials. Consequently, an active tunability appears in the response of the matrix multiplication M and in the optical response [Fig. 3.3 (b)].

The phase shift will be given by

$$\phi = 2\pi n(T,P,V)d/\lambda - j\alpha(T,P,V)/2 \tag{3.14}$$

and the r_{12} or t_{12} coefficients will have a temperature, power or voltage dependence. Another option to make tuneable devices based on 1D photonic crystal is to reduce or increase the homogenous distance d. Using some stress it will be possible to change the dimensions of

the 1D photonic crystal and make reconfigurable devices based on the applied force and not based on a reconfigurable material.

3.1.3 Ring resonators

In this sub-section, a description of how to model integrated ring resonators is given. First, a complete study regarding the passive ring resonator structures with the analytical calculation of the coupling coefficient is presented, followed by the introduction of functional materials in the passive structures to make tunable ring resonators based on smart materials, paving the way to future smart nanosystems.

Passive structure

One of the most crucial parameters for the design of a ring resonator is the coupling coefficient between the waveguide and the ring structure. The waveguide centers are separated by a distance $2s$ [Fig. 3.4 (a)]. From Ref. [151], the instantaneous coupling strength is evaluated by the overlap integral

$$\kappa[s(z)] = \frac{\varepsilon_0 \omega}{4} \int_{-\infty}^{\infty} (n_1^2 - n_0^2) e_1(x) e_2^*(x) dx \tag{3.15}$$

where $e_1(x)$ and $e_2(x)$ are the power normalized modal fields in individual waveguides 1 and 2, ε_0 is the permittivity of free space, and ω is the angular frequency. The net coupled amplitude is proportional to the integral of $\kappa[s(z)]$ over the interaction region, weighted by the phase mismatch of the waveguide modes

$$\kappa = \int_{-\infty}^{\infty} \kappa[s(z)] e^{-j\Delta\beta z} dz \tag{3.16}$$

The phase mismatch is $\Delta\beta = \beta_1 - \beta_2$, where β_i is the propagation constant of waveguide i. The coupling coefficient, $\kappa(s)$, depends exponentially on waveguide separation [152], s, and is only non-negligible in the region of smallest separation. We treat the curvature (γ) as parabolic, thus we have

$$\begin{aligned} s &= s_0 + \gamma z^2 \\ \gamma &= 1/2R \\ R &= \frac{R_1 R_2}{R_2 + R_1} \end{aligned} \tag{3.17}$$

where R is the effective radius of curvature and $2s_0$ is the smallest separation between the

waveguide centre to centre [Fig. 3.4 (a)] and z is the direction of propagation. In the particular case of the coupling between a straight waveguide and a ring resonator $R_1 \to \infty$ and $R = R_2$ [Fig. 3.4 (b)]. An analytical general solution can be described accurately by [152]

$$\begin{aligned}\kappa = \frac{\omega\varepsilon_0 \cos(k_{x_2} w_2)}{2\sqrt{P_1 P_2}\left(k_{x_1}^2 + \alpha_2^2\right)}(n_1^2 - n_0^2) \\ \cdot\sqrt{\frac{\pi R}{\alpha_2}} e^{\alpha_2(w_2 - 2s_0)} \\ \cdot[\alpha_2 \cos(k_{x1} w_1)\sinh(\alpha_2 w_1) \\ + k_{x1}\sin(k_{x1} w_1)\cosh(\alpha_2 w_1)]\end{aligned} \tag{3.18}$$

where ω is the angular frequency, w_i is half of the waveguide width, with refractive index, n_i, in a surrounding cladding of index n_0. The waveguide centers are separated by the distance $2s$. Both waveguides are assumed to be rings with radius R_1 and R_2, measured to the waveguide centers. P_i is the mode power, α_i is the decay constant in the cladding, and k_{xi} is the transverse propagation constant in the core, all for waveguide i, thus, we have

$$\begin{aligned} P_i &= \frac{\beta_i}{2\omega\mu_0}\left(\omega_i + \frac{1}{\alpha_i}\right) \\ \alpha_i &= \sqrt{\beta_i^2 - n_0^2 k^2} \\ k_{xi} &= \sqrt{n_i^2 k^2 - \beta_i^2}\end{aligned} \tag{3.19}$$

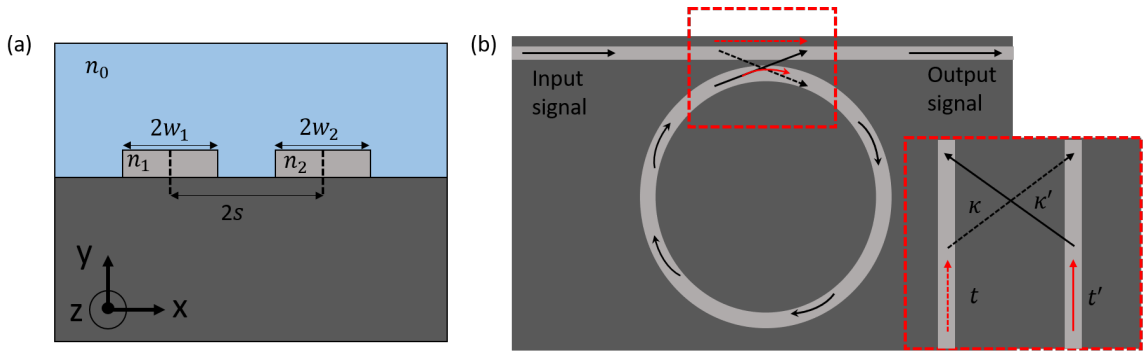

Fig. 3.4 (a) Schematic cross-section of the coupling region between ring to ring waveguide or ring to straight waveguide. (b) Schematic top view of the coupling between a straight waveguide and a ring resonator.

The proposed ring resonators design model is based on the Transfer Matrix Method

(TMM) [153, 107] and all the coding was implemented in MATLAB. For the passive modelling the crucial matrix in the TMM is the ring resonator matrix, P

$$P = \begin{pmatrix} 0 & e^{(j\beta-\alpha/2)L_1} \\ e^{(j\beta-\alpha/2)L_2} & 0 \end{pmatrix} \tag{3.20}$$

where the elements of the matrix without any active material deposited on top of the ring structure are related to the wavevector and the attenuation coefficients of the passive structure that we extract from the MODE Analysis, $\beta = 2\pi n_{eff}/\lambda$ and $\alpha = \frac{k_{eff}\cdot 4\pi\cdot 10}{\lambda_0 \cdot \ln 10}$, where L_1 and L_2 are the length of the first and the second half of the ring resonator respectively [Fig. 3.5 (a)]. To completely describe the optical response of an integrated ring resonator structure, the global matrix, M, should be defined. This matrix comprises two terms, firstly, the coupling coefficient matrix (C), and secondly, the propagation matrix (P). The coupling coefficient matrix (C) is described by

$$C = \begin{pmatrix} -t/\kappa' & 1/\kappa' \\ \frac{\kappa\kappa' - tt'}{\kappa'} & t'/\kappa' \end{pmatrix} \tag{3.21}$$

where t and κ are the transmission and coupling coefficients from the waveguide to the ring resonator and t' and κ' the transmission and coupling coefficients from the ring resonator to the waveguide [Fig. 3.4 (b)]. Finally, to obtain the response of the whole system, the transmittance, T, through the bus waveguide from the coefficients of the global matrix $M = C \cdot P$ should be extracted as

$$T = \left(-\frac{M_{11}}{M_{12}} \right)^2 \tag{3.22}$$

Active structures

By adding active material on top of the ring resonator [Fig. 3.5 (b)], a change in the propagation constant of the ring resonator mode is induced. In this configuration [Fig. 3.5 (b)], the optical mode will have two different effective refractive indices along the ring path depending on if an active material is deposited on top or not, as indicated previously, (n_{eff}) or ($n_{eff}^{\tilde{a}}$). These two values are calculated using the MODE analysis previously described. The propagation constant and the attenuation coefficient were calculated using COMSOL Multiphysics® for the bare and hybrid structure, the hybrid structure being that which corresponds to the region with the active material. Taking this into account, the new matrix for the ring resonator including the hybrid structure (P_a) should have two contributions: one corresponding to the bare ring and another corresponding to the hybrid structure

$$P_a = \begin{pmatrix} 0 & e^{(j\beta-\alpha/2)(L_1-L_a)}e^{(j\beta_a-\alpha_a/2)L_a} \\ e^{(j\beta-\alpha/2)L_2} & 0 \end{pmatrix} \tag{3.23}$$

where β_a, α_a and L_a correspond to the propagation constant, the attenuation coefficient and the length of the hybrid structure, respectively, and β_0 and α_0 to the propagation constant and attenuation coefficient of a bare ring resonator structure (without the active material). β_a, α_a and L_a are voltage (V), power (P) and/or temperature dependent (T). Consequently, applying a voltage, a power pulse, or increasing the temperature, will change the propagation constant or the attenuation of the active region due to the active material

$$\begin{aligned} \beta_a &= 2\pi n_{eff}^{\tilde{a}}(P,T,V)/\lambda \\ \alpha_a &= \frac{k_{eff}(P,T,V)\cdot 4\pi\cdot 10}{\lambda_0 \cdot \ln 10} \end{aligned} \tag{3.24}$$

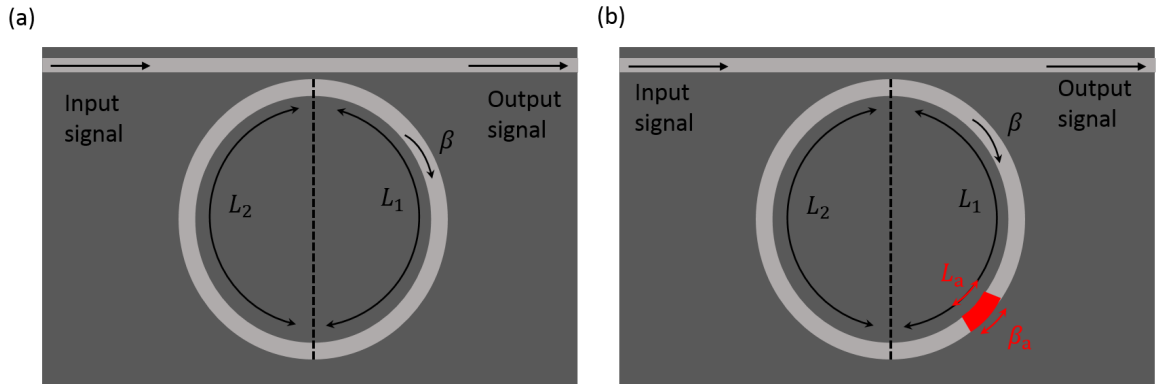

Fig. 3.5 (a) Passive ring resonator filter schematic with a propagation constant along the ring equal to β (b) Hybrid ring resonator. Active material deposited on top of a ring resonator structure in order to actively tune the optical response, L_a is the length of the active region in which the propagation constant is equal to β_a.

3.1.4 Mach–Zehnder interferometer

In this sub-section, a description of how to model a Mach-Zehnder inteferometer (MZI) will be explained. First, a complete study regarding the passive MZI structures considering different lengths in the MZI or different waveguides dimensions will be presented, followed by the introduction of reconfigurable materials in the passive structures to make tuneable MZI based on functional materials.

Passive structures

According with [Eq. 2.30] the intensity at the output of a MZI is

$$I_0 = \frac{I_i}{4}\left[e^{-j\beta_1 L_1 - \frac{\alpha_1}{2}L_1} + e^{-j\beta_2 L_2 - \frac{\alpha_2}{2}L_2}\right]^2 \tag{3.25}$$

where $\beta_1 = 2\pi n_{eff_1} L_1$ and $\beta_2 = 2\pi n_{eff_2} L_2$, are the propagation constants of arms 1 and 2 of the MZI, where n_{eff_1} and n_{eff_2} are the real parts of the effective refractive index n^r_{eff} of arm 1 and 2. α_1 and α_2 are related with the imaginary part of the effective refractive index calculated in the Mode Analysis and are the attenuation of each of the arms. $L_1$and L_2 are the MZI arm lengths [Fig. 3.6 (a)].

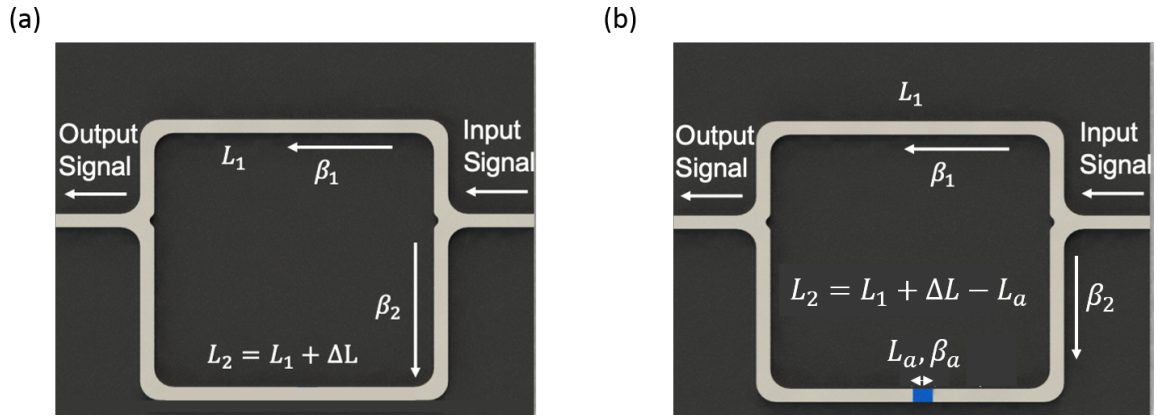

Fig. 3.6 (a) Passive MZI schematic, β_1, β_2, L_1, and L_2 are the propagation constants and the lengths along the MZI arms 1, and 2 respectively (b) Active MZI schematic, L_a is the length of the active region in which the propagation constant is equal to β_a.

Active structures

For the modelling of the active reconfigurable MZIs, an active material is deposited on one of the arms of the MZI structure. It can be deposited on both arms, but for simplicity in the model, we will consider just one arm covered partially by an active material. Following the previous notation, β_1 and β_2 retain their definitions, but in the arm where we have deposited the active material (arm 2) the propagation constant is different in the region with the active material compared to the region without (as in the ring resonator). The optical mode travelling through arm 2 will encounter two different effective refractive indeces, and consequently two different propagation constants along the waveguide path depending on if an active material is deposited on top (β_a) or not (β_2) as indicated in [Fig. 3.6 (b)]. These two values are calculated using the MODE analysis previously described.

The propagation constant and the attenuation coefficient are calculated using COMSOL

Multiphysics® for the bare and hybrid structure. The hybrid structure corresponds to the region with the active material. Taking this into account, the new analytical formula is described by:

$$I_0 = \frac{I_i}{4}\left[e^{-j\beta_1 L_1 - \frac{\alpha_1}{2}L_1} + e^{-j\beta_2(L_2-L_a)-\frac{\alpha_2}{2}(L_2-L_a)}e^{-j\beta_a L_a - \frac{\alpha_a}{2}L_a}\right]^2 \tag{3.26}$$

3.1.5 Grating coupler

In this sub-section, a description of how to analytically design a grating coupler (GC) will be presented. Based on the Bragg condition described in Chapter 2, the desired grating coupler can be designed. Firstly, a calculation of the two effective refractive indices for the two different grating elements (cells) of the grating should be evaluated, see Fig. 3.7. In the particular case of having a rib or ridge waveguide, the grating coupler will have one grating element with one thickness ($t_1 \neq 0$) [Fig. 3.7 (a)] and a second grating element with a different thickness ($t_2 \neq 0$) [Fig. 3.7 (b)] in the case of a rib design or t_2= 0 nm in the case of a ridge waveguide. Each grating element is associated to an effective refractive index, which depends on the thickness. $n_{eff_1}(t_1)$ and $n_{eff_2}(t_2)$ represent the effective refractive indices for each grating element respectively.

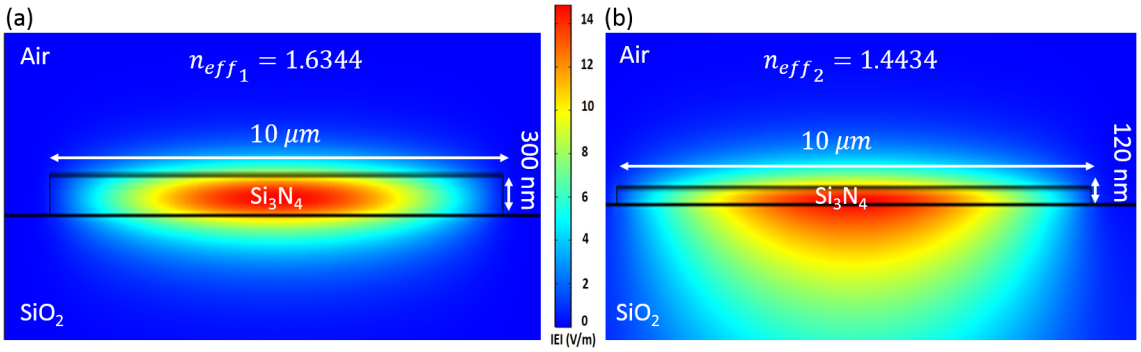

Fig. 3.7 Eigenmode simulation of fundamental TE optical mode propagating with (a) 300 nm thick silicon nitride, and (b) 120 nm thick silicon nitride, using air as cladding material and 10 μm width waveguide.

Normally, it can be assumed an infinite width for the GCs, this assumption holds because the width of the GCs are normally 10 μm, which is much larger than the central wavelength. This width is selected in order to convert the mode coming from the optic fiber to the integrated waveguide mode. The effective refractive index of the total grating (n_{eff}) can be evaluated using the effective index of the first grating element (n_{eff_1}) and the effective index of the second grating element (n_{eff_2}) (calculated using COMSOL Multiphysics®)

$$n_{eff} = FF \cdot n_{eff_1} + (1 - FF) \cdot n_{eff_2} \tag{3.27}$$

where FF is the fill-factor. In this example, the effective refractive indeces are, $n_{eff_1} = 1.6344$ and $n_{eff_2} = 1.4434$ at the wavelenght, $\lambda_0 = 1550$ nm for a silicon nitride rib waveguide. Selecting $FF = 0.5$, the weighted-average effective index of the grating region is $n_{eff} = 1.5389$. Using Eq. 2.39, air as cladding material and an incident angle of $\theta_{air} = 14^o$ are selected, and the period (Λ) of the grating can be calculated. The period of the grating for these specific conditions is $\Lambda = 1195$ nm. In Ref. [154] it was found that the analytic calculations yield a design that is very close to the optimal for an uniform grating coupler optimized by Finite-difference time-domain method.

3.1.6 Mask Design

The layout of all the devices that were fabricated in this thesis were generated using Nazca design. Nazca design is an open-access program created for designing the layout of photonic integrated circuits. It was selected amongst other tools because it has a powerful user programming interface that allows the creation of Python scripts to automate the layout generation. Along with the fact that it is open-access, this allows us to combine the layout and the modelling in the same source in the form of a future Process Design Kit (PDK). A library of Python functions designed to draw the different devices (ring resonators, MZIs, grating couplers, Bragg gratings, WDM, 1D and 2D photonic crystals) was created and then used to efficiently produce layouts with a range of parameter variations. An example can be seen in [Fig. 3.8] where a U- shaped waveguide and a ring resonator add-drop filter on SiNx platform is designed for future fabrication and characterization in the C-band range of the spectrum.

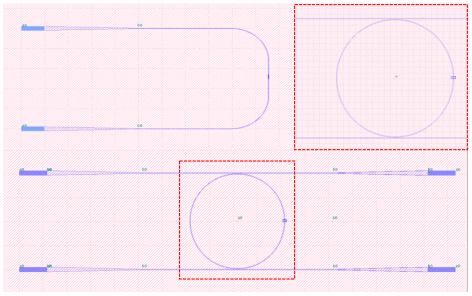

Fig. 3.8 U-waveguide and add-drop filter layout using Nazca design for future fabrication.

3.2 Fabrication

The majority of the devices discussed in this thesis consist of a waveguide structure with a Si or SiN core embedded in a SiO_2 or air cladding. The devices were fabricated at the University of Exeter, Tyndall and the Southampton Nanofabrication Centre following the process flow depicted in [Fig. 3.9]. The wafers used for the fabrication were 6-inch bulk silicon wafers, as the majority of the tools have a configuration set to work with these wafer dimensions. First, a SiO_2 bottom cladding was grown on bulk silicon substrates. Then, the SiN device layer was deposited using an optimised NH_3-free PECVD recipe [155]. Once the SiN was grown, the desired structures were patterned using deep ultraviolet (DUV) lithography using a wavelength of 248 nm or electron beam lithography (EBL), and inductive coupled plasma etching (ICP) or reactive-ion etching (RIE) was carried out. Finally, the devices were may covered with a top PECVD SiO_2 cladding [156]. This flow is by no means a comprehensive description of the steps followed during the fabrication stage of all the devices, but it includes the general aspects that will be discussed in this chapter . The following chapters will present more specific details for the fabrication of each device.

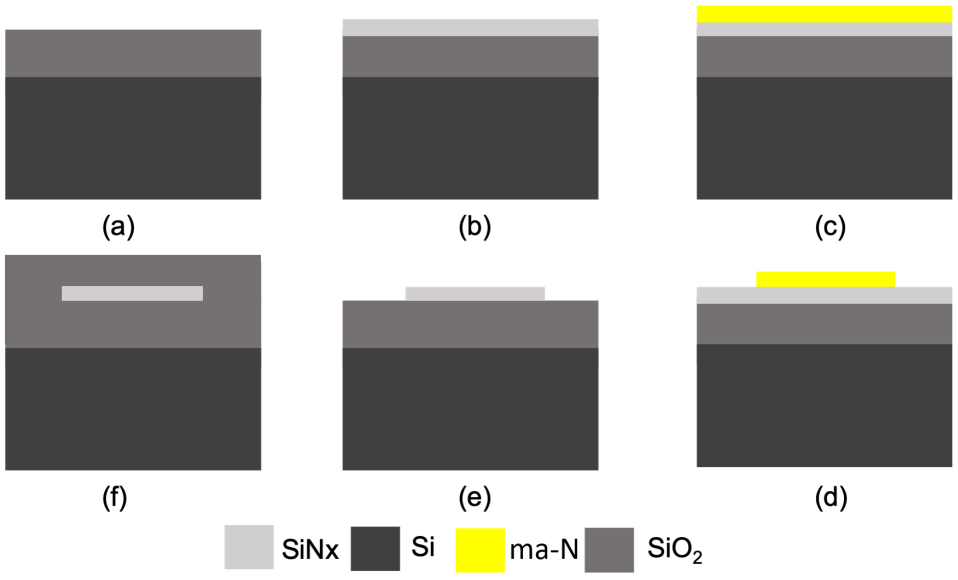

Fig. 3.9 Cross-sectional view of the process flow for the fabrication of Si or SiN waveguides: (a) a 2–3μm thick layer of SiO_2 is deposited on a bulk silicon substrate, (b) a SiN layer is deposited on top using PECVD, (c) a layer of ma-N 2403, Polymethyl methacrylate (PMMA) or ZEP520A resist is spin coated onto the substrate and patterned, (d) e-beam or DUV lithography (e) the pattern is transferred to the SiN layer using ICP dry etching or RIE, and (f) top PECVD SiO_2 cladding deposition (optional step).

3.2.1 Passive Devices

Material deposition

Plasma Enhanced Chemical Vapor Deposition (PECVD) is a process by which thin films of various materials can be deposited on substrates at lower temperature than that of standard Chemical Vapor Deposition (CVD). In PECVD processes, deposition is achieved by introducing reactant gases between parallel electrodes (a grounded electrode and an RF-energized electrode). The capacitive coupling between the electrodes excites the reactant gases into a plasma, which induces a chemical reaction and results in the reaction product being deposited on the substrate. The substrate, which is placed on the grounded electrode, is typically heated to 250°C to 350°C, depending on the specific film requirements. In comparison, CVD requires 600°C to 800°C. The lower deposition temperatures are critical in many applications where CVD temperatures could damage the devices being fabricated.

As shown in the first step of [Fig. 3.9], bulk silicon wafers were initially prepared by adding a SiO_2 layer with a thickness greater than 2 μm. This layer was deposited with the *Oxford Plasma Technology 100 PECVD* system using a temperature of 350 °C, pressure of 1000 mTorr, and radio frequency (RF) power of 20 W. The standard recipe comprises a gas mixture of 4.24 standard cubic centimeters per minute (sccm) of SiH_4, 350 sccm of N_2O and 80 sccm of N_2 that yields a refractive index of 1.452 when measured at a wavelength of 1550 nm, with a thickness non-uniformity smaller than 2%. Once the SiO_2 has been deposited as undercladding, the SiN layers were deposited on the wafers using the *Oxford Plasma Technology 100 PECVD* system as illustrated in [Fig. 3.9 (b)]. The deposition temperature of all of these was fixed at 350ºC to ensure the compatibility of the deposition process with multilayer integration. In addition, the pressure of the chamber was set to 950 mTorr and the RF power to 60 W in order to achieve the lowest thickness non-uniformity possible without compromising the deposition rate of the layers. Finally, the SiH_4 and N_2 flows were tailored to obtain either N-rich, Si-rich or stoichiometric layers with low propagation losses. In all cases, the deposition time was adjusted to obtain the desired SiN thickness according to the deposition rate of the selected recipe [156].

Electron Beam Lithography

Electron beam lithography (EBL) is a process that allows us to write patterns onto the surface of a substrate by moving a tightly focused beam of electrons to expose an electron-sensitive organic film, known as resist. The electron beam changes the chemical structure of the resist as the surface is scanned in the desired pattern, so that unwanted areas can be selectively dissolved with a suitable solvent. This technique allows us to write high resolution patterns

with nanometre scale features that are difficult to achieve using other lithography methods. However, the high resolution of such small features come at the price of longer processing times [157].

After the deposition process, EBL was used to define the layout of different designed structures. According to the third step depicted in [Fig. 3.9], a negative-tone e-beam resist layer, ma-N 2403, was spun onto the wafers to pattern the desired structures. ma-N 2403 is a high resolution negative resist capable of producing features as small as 40 nm. It exhibits good thermal stability of the resist patterns, high wet and dry etch resistance and is easy to remove. This lithography step is exposed using TI PRIME adhesion promoter spun at 4000 rpm for 30 seconds and baked at 120°C for 120 seconds, and ma-N 2403 negative tone resist spun at 3500 rpm for 30 seconds and baked at 90°C for 120 seconds. The development was carried out using MF 319 developer for 30 seconds. In the case of a positive tone photoresist (PMMA), in which you create windows, the PMMA 950K A4 resist is spun at 4000 rpm for 60 seconds to have a resist film thickness of 200 nm. The development was carried out in a IPA: MIBK:MEK (15:5:1) mixture for 35 seconds. Finally, the substrates were rinsed in IPA for PMMA or in deionized water for ma-N 2403 and dried with N_2 afterwards for both, positive and negative tone pohotoresists before the next processing step. The system used in the fabrication of the devices in this thesis is a 30 kV to 100 kV *Nanobeam NB4 electron beam*. The nanobeam can deliver currents as small as $\sim$1 nA that, along with the voltages used in the fabrication (80 kV), which are ideal to get extremely high resolution patterns [158].

Thermal evaporator

Thermal evaporation is a common method of physical vapor deposition (PVD). It is one of the simplest forms of PVD and typically uses a resistive heat source to evaporate a solid material in a vacuum environment to form a thin film. The material is heated in a high vacuum chamber until vapor pressure is produced. The evaporated material, or vapor stream, traverses the vacuum chamber with thermal energy and coats the substrate. Thermal evaporation represents one of the oldest thin film deposition techniques. High vacuum is critical for resistive evaporation processes for two reasons; first, when gas is evacuated from a chamber, vapor molecules inside it can travel longer distances before they collide with a gas molecule. Collisions with gas molecules are undesirable during evaporation because they change the material vapor's direction of travel, adversely affecting the coverage of the substrate. When the gas pressure is below 10^{-5} Torr, the average distance of travel of a vapor molecule before colliding with a gas molecule (also called the mean free path) is greater than 1 meter, which is typically larger than the chamber dimensions. This means

that the molecules would travel in a straight line from the source to the substrate, making resistive evaporation highly directional. Secondly, high vacuum is also integral for film purity. Background gases in the chamber can lead to contamination of the growing film [159]. In this thesis HHV Auto306 thermal evaporator has been used to deposit chromium (∼5 nm) and gold (∼50 nm) as electrical contacts or markers. A schematic of the HHV Auto306 thermal evaporator is presented in Fig. 3.10.

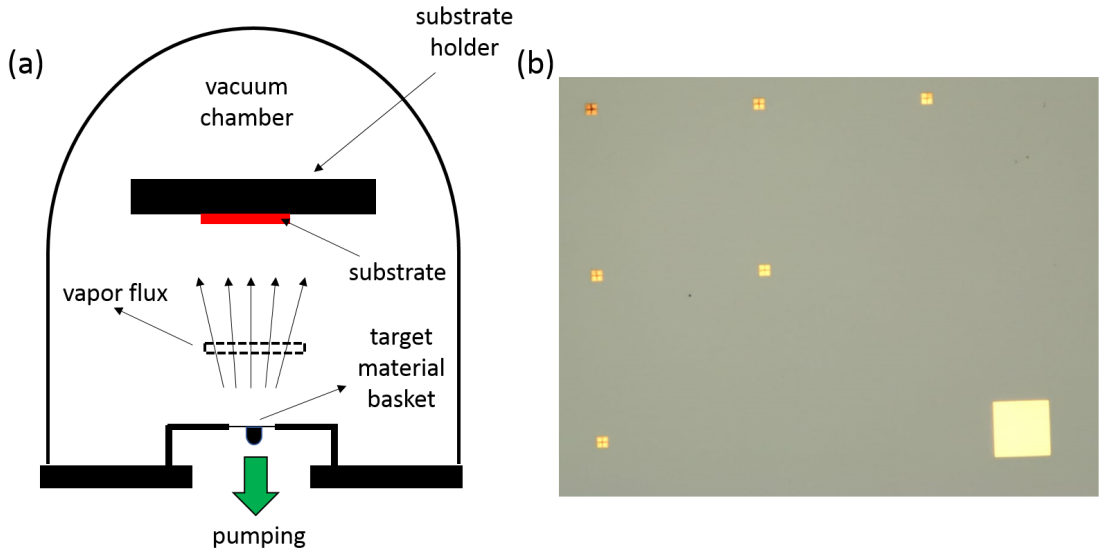

Fig. 3.10 (a) Schematic of the thermal evaporation technique used to deposit chromium or gold on the devices fabricated in this thesis. (b) Optical microscope image of the fabricated markers using the thermal evaporation technique.

Etching

Etching refers to the controlled removal of material from the silicon wafer surface via a chemically reactive or physical process, there are typically two etching techniques, dry etching or wet etching, both techniques have advantages and disadvantages, but for reproducing features of sub-micron dimensions dry etching dominates. Low loss silicon and silicon nitride waveguides have been produced by both wet [160] and dry [161] etching, but the requirement for flexible process capability, high tolerances and reproducible production, dry etching is regarded as the most suitable solution. Two different etching techniques have been used in the thesis, reactive-ion etching (RIE) and inductively coupled plasma etching (ICP).

- **Reactive ion etching (RIE)** is a directional etching process which uses ion bombardment to reduce material volume. This etch process is commonly used in micro

fabrication processes; the process uses a chemically reactive plasma in a vacuum chamber to aggressively etch in a vertical direction. Horizontal etching is purposefully minimized in order to leave clean, sharp corners. Plasma is produced in the system by applying a strong RF (radio frequency) electromagnetic field to the electrode, generally at 13.56 MHz. Other frequencies are available, but 13.56 MHz provides the best results for this etch process. In plasma etching systems, the substrate is placed in a vacuum chamber on the cathode of the plasma generator and gases are introduced to produce the reaction [Fig. 3.11 (a)]. The RF is applied, creating reactive plasma by oscillating the electric field and ionizing the gas molecules by stripping them of electrons. Ions in the plasma will bombard the cathode similar to sputtering. This action creates an additional source of energy that can accelerate the etch rate parallel to the ion trajectories. Because ions are directed at normal incidence to the cathode, this has the effect of accelerating the etch rate normal to the substrate. The electrons are electrically accelerated up and down in the vacuum chamber in cycles, striking the upper wall of the chamber and the wafer platter. The chamber is made of aluminum and grounded so they exit the system continuously during the plasma process [162]. Different recepies have been used in order to etch silicon and silicon nitride substrates [Fig. 3.11 (b)]. The standard recipe comprises a gas mixture of 15 standard cubic centimeters per minute (sccm) of SF_6, 15 sccm of Argon with a pressure of 45 mT and a power of 50 W.

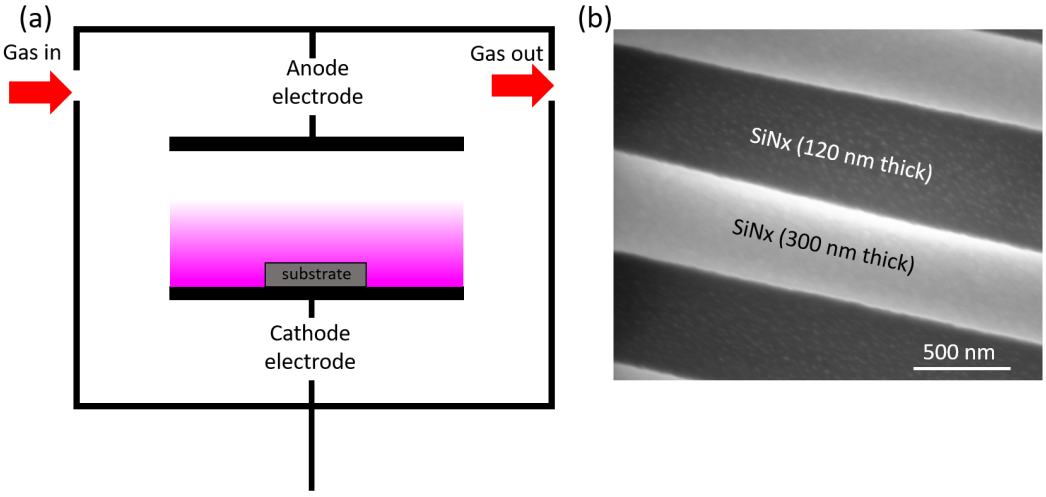

Fig. 3.11 (a) Schematic of the RIE etching use in the thesis. (b) SEM image of a silicon nitride grating coupler designed for a wavelength of 1550 nm after the RIE etching.

The etching process was monitored constantly by measuring the thickness of the material layer in the profilometer. Similarly, the thickness of the resist was measured to ensure that there was enough remaining material in order to avoid surface damage of the underlying material. Once the process was finished, the remaining ma-N 2403 resist was removed using acetone and oxygen plasma afterwards. The etching rate of the silicon nitride layers ranged between 28–35 nm/min according to their composition. In order to etch graphene mono-layers or bi-layers a mixture of argon and oxygen in a 2:1 ratio is utilized [163].

- **Inductively coupled plasma (ICP) etching** is a dry etching technique that chemically removes the material deposited on a substrate with a high-density reactive plasma [164]. This plasma is driven by an electromagnetic field created by a RF generator oscillating typically at 13.56 MHz. Additional physical etching occurs due to the flow of high-energy ions that attack the wafer surface. ICP etching provides high etching rates with low surface damage [Fig. 3.12]. Moreover, the RF bias applied to the ICP system enables obtaining anisotropic etch profiles with high verticality [165]. Once the layout was defined through EBL lithography, the patterns were transferred to the SiN layers using the *Oxford Instruments ICP 380* system as portrayed in the fourth step of [Fig. 3.9]. The ICP chamber was first conditioned for 20 minutes using a plain silicon wafer with resist on top.

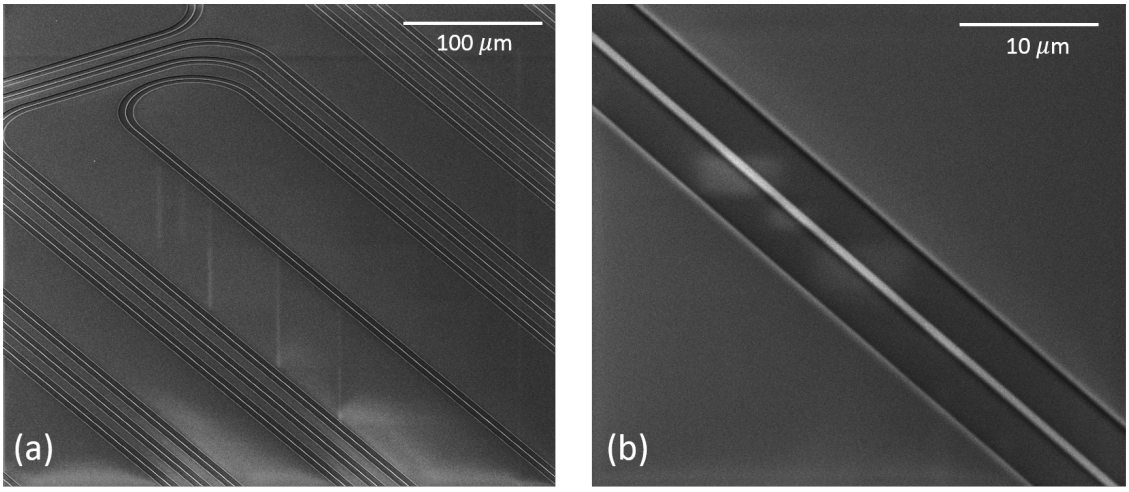

Fig. 3.12 (a) SEM image of ICP etched silicon nitride waveguides. (b) SEM zoom image of a 600 nm thick and 700 nm width silicon nitride waveguide designed at 13310 nm wavelength using ICP etching technique.

Subsequently, the wafers were etched at 15 ºC with an ICP power of 1400 W, RF power of 50 W, and chamber pressure of 14 mTorr using SF_6 (65 sccm) and CHF_3 (35

sccm) chemistry. The etching rate of the layers ranged between 5–7 nm/s according to their composition. The etching time depended on their thickness. The etching process was monitored constantly by measuring the thickness of the SiN layer in a 1 x 1 mm metrology box using an ellipsometer. Similarly, the thickness of the resist was measured to ensure that there was enough remaining material in order to avoid surface damage of the underlying material. Once the process was finished, the remaining ZEP520A resist was removed using a *Tepla 300* O_2 plasma asher.

3.2.2 Active Devices

Liquid crystal infiltration

Several methods have been used in order to infiltrate liquid crystals on silicon or silicon nitride integrated components, in the devices fabricated in this thesis the infiltration of liquid crystals was carried out using micro-needles [Fig. 3.13 (a)]. Micro-needles are dipped in the liquid crystal to coat the tip. The micro-needle tip is then touched to the surface of the infiltration site. The hydrophilic nature of the infiltration site causes the liquid crystal to spread [Fig. 3.13 (b)], being deposited from the needle to the chip. Capillarity action then causes the liquid crystal to become preferentially dispersed in microfluidic channels specially prepared on the chip, see Fig 3.13.

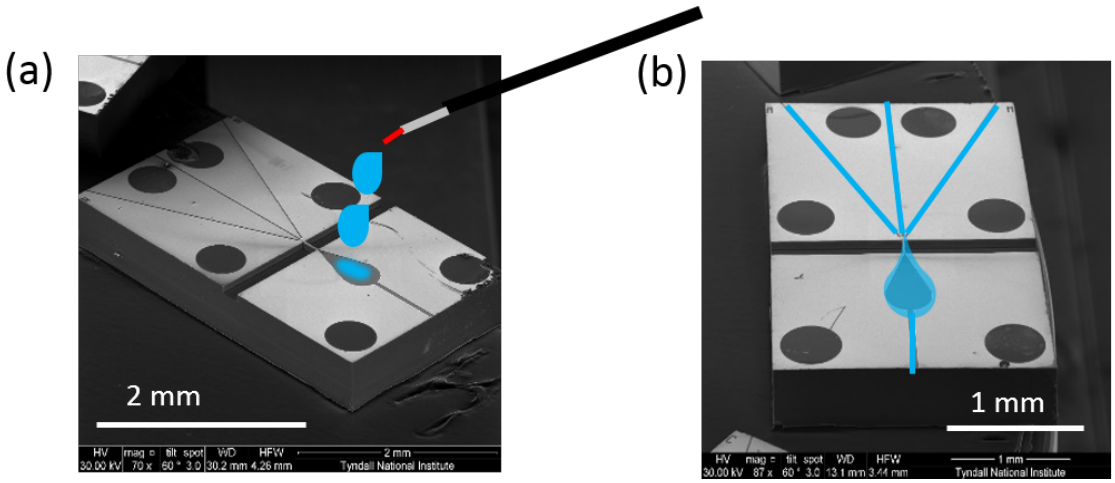

Fig. 3.13 (a) Schematic of the liquid crystal infiltration process using micro-needles. (b) The hydrophilic nature of the infiltration site causes the liquid crystal to spread.

Deposition of 2D materials

Several methods have been developed by which 2D materials can be produced, each with their own advantages and disadvantages. Firstly, a mechanical cleavage method can be used (the so-called 'sticky-tape' method) where layers are separated by attaching one layer to a sticky surface and mechanically peeling it away from the bulk [166]. This method produces very pure materials with few induced defects and can also give relatively large areas of material coverage, tens of microns square typically. However, this method has poor scalability and production of large quantities of 2D material is extremely time intensive. Alternatively, a vapour deposition method can be used. In this case, a 2D material is grown directly on a substrate from vaporized precursor molecules at very high temperatures [167–170]. This method can produce large areas of 2D material and can be scaled to produce large quantities. However, there are numerous sources for the introduction of defects in the material including substrate induced defects and impurities in the vapours used, amongst others. Adoption of 2D materials in novel device applications is often limited by challenges surrounding the scalability, cost of production processes, or limited quality of materials produced. In this work, three different deposition methods have been explored:

- **Liquid exfoliation deposition**: In liquid phase exfoliation, a bulk material is dispersed in a solvent and then the individual constituent layers are broken apart [171–174]. In the standard liquid phase exfoliation process which is illustrated in [Fig. 3.14], the bulk material layers are broken apart using ultrasonic agitation [Fig. 3.14 (c)]. High frequency sound waves are transmitted through the solution [175–178] to induce the formation of bubbles and cavities between layers which break the layers apart as they expand. However, they also cause additional intralayer strains in the material which cause cleavage of the particles, reducing the size of the particles obtained after exfoliation. The use of intercalating surfactants to weaken the interlayer forces before exfoliation can greatly increase the yield of the exfoliation [171, 173], but the subsequent removal of the surfactant is liable to negatively impact the quality of the exfoliated product. Methods other than ultrasonic agitation have been developed for liquid phase exfoliation, including strong acid induced oxidation reactions causing cleavage [179], and freezing of water intercalated layered structures where expansion of the water causes interlayer cleavage [180]. Following on from the exfoliation, particles of specific sizes can be isolated through high speed centrifugation of the dispersion [181, 182] [Fig. 3.14 (d)], solvent induced selective sedimentation, or by pH-assisted selective sedimentation [183] amongst others. Fractionation [Fig. 3.14 (e)] then allows selection of a suitable range of particle sizes depending on the application, with homogeneous distributions of particle sizes obtainable [Fig. 3.14 (f)].

A significant advantage of using liquid phase exfoliation is the possibility of obtaining liquid crystal phase dispersions through the careful selection of size and concentration of the dispersed particles. Liquid crystal phase dispersions facilitate the deposition of films with greater uniformity [184]. In this work, graphene was produced from graphite by exfoliation in water, using sodium cholate as a surfactant. Dispersions were ultrasonicated for around 5 hours, and centrifuged for 5 mins at 2000 rpm to separate out any unexfoliated particles from the solution. An aliquot containing all the non-sedimented particles was then transferred and used for further processes. A similar method was used for the exfoliation of transition metal dichalcogenides. In these cases, isopropanol was used as the solvent and no surfactant was required. Ultrasonication processes and ultracentrifugation where carried out for the same lengths of time and speeds. The resultant dispersion of exfoliated 2D materials was then filtered through polytetrafluoroethylene (PTFE) membranes to produce thin films on the membrane. These films can then be transferred to other substrates as required.

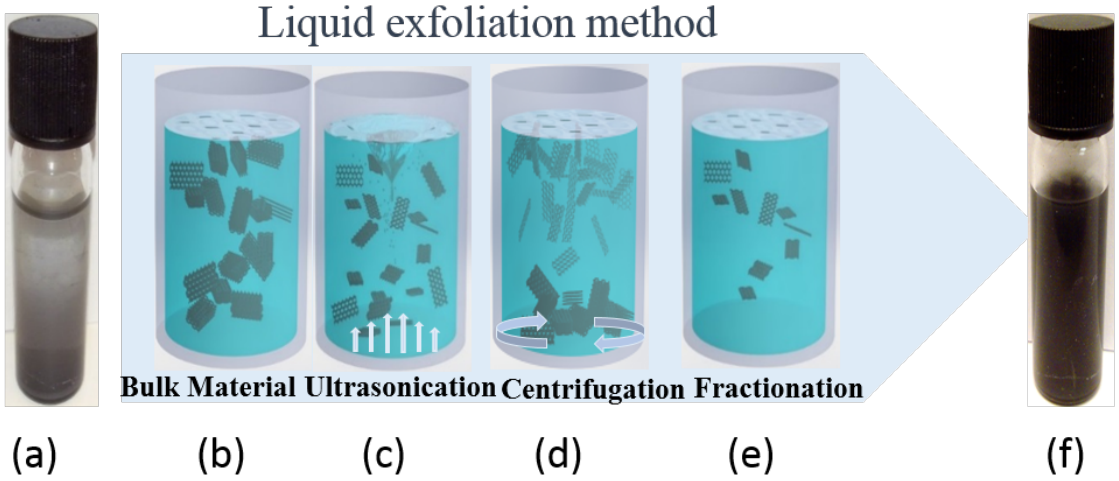

Fig. 3.14 (a) A dispersion of bulk material (b) Schematic of the liquid phase exfoliation of bulk layered materials to low- or two-dimensional particles. (c) Ultrasonication is used to exfoliate down to smaller flake sizes. (d) Centrifugation then aggregates the largest particles, with the smallest remaining suspended in the solution (e) Fractionation allows the selection of aliquots containing (f) the resultant homogeneous distributions of similarly sized particles.

- **CVD (Chemical vapour deposition) graphene deposition.** Graphene was grown by CVD on copper foils, as described in ref. [185] and then transferred onto a silicon nitride sample following the procedure described in ref. [186]. Graphene patterning was carried out using EBL and PMMA or ma-N resist, while etching was performed using conventional O_2 plasmas [187], see Fig. 3.15.

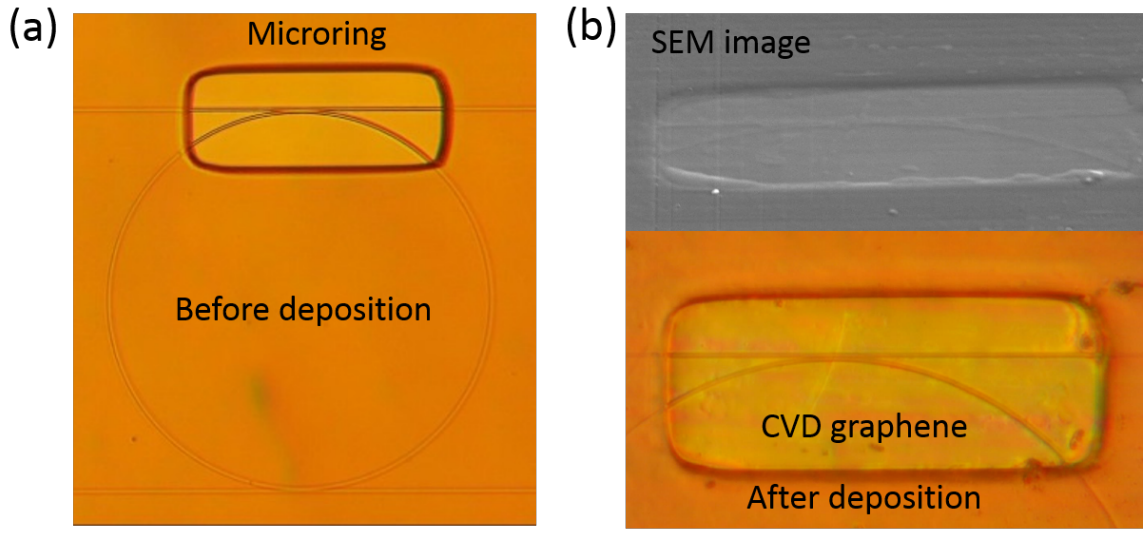

Fig. 3.15 (a) Silicon nitride micro-ring resonator optical microscope image before CVD deposition. (b) SEM and optical microscope image of a silicon nitride micro-ring resonator after CVD graphene deposition.

- **Back-end CMOS fabrication process** is used for the large-scale integration of 2D materials on SOI (Silicon-on-insulator) platform. This method is used to integrate 2D material thin films on Si_3N_4 or silicon photonic wafers. In the first step, EBL followed by inductively coupled plasma reactive ion etching (RIE) was used to fabricate waveguide and ring devices from a 150 nm-thick Si_3N_4 layer, supported on a SiO_2 bottom cladding layer of 2 μm [Fig. 3.16 (a)]. Above the Si_3N_4 photonic layer, a 1 μm thick photoresist was produced via spin-coating. This was followed by pattering using a laser writing method with a precision of 0.6 μm and wet etching of defined structures and trenches within the photoresist layer, down to the photonic layer [Fig. 3.16 (b-c)]. With the photoresist removed from the required areas, CVD or liquid exfoliated 2D materials were transferred onto the top of the wafer [Fig 3.16 (d)]. After removal of the photoresist mask, final individual devices with specific, micron-size structures of 2D materials- as desired and designed were achieved [Fig. 3.16 (e-f)].

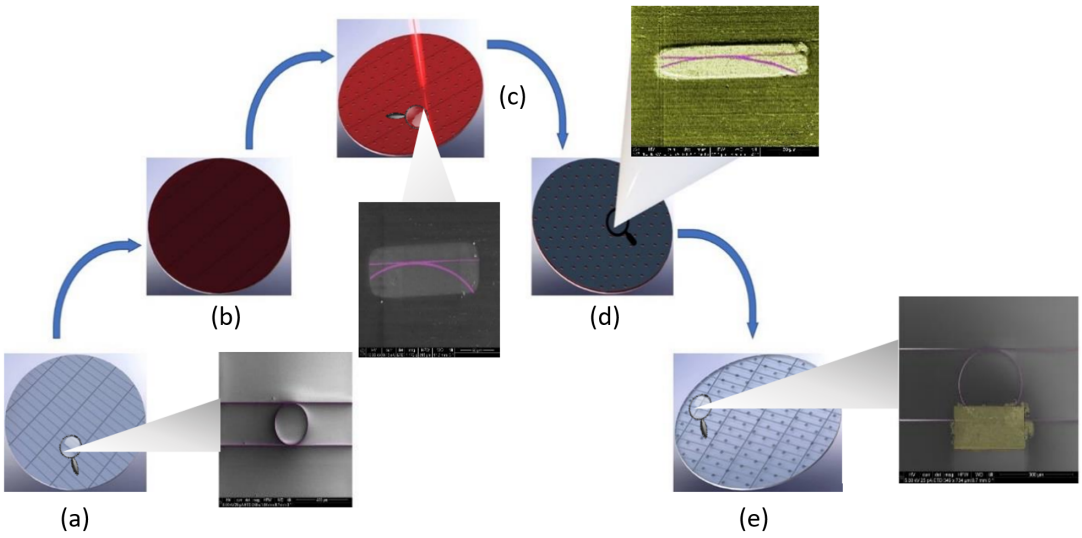

Fig. 3.16 Back-end CMOS fabrication process flow. (a) SOI wafer with photonic microchips. (b) Photoresist deposition on the photonics wafer. (c) Development of micro-trenches and other structures within the photoresist layer, down to the photonic waveguide layer. (d) Wafer scale transfer of 2D material thin film. (e) SOI photonic wafer with integrated 2D materials into the photonic circuits after photoresist removal.

Phase change material deposition

Sputtering deposition is classified under the methods known as physical vapour deposition (PVD). A target of the material that is desired to be deposited is bombarded with energetic ions of inert gases (e.g. argon) and the forceful collision of these energetic ions with the target ejects target atoms that are then deposited on the substrate. Usually, the plasma is formed by a noble gas, such as argon or argon mixed with other gases for 'reactive' sputtering (e.g. N_2 for deposition of nitrides, O_2 for deposition of oxides), under the action of an appropriate electric potential where the target is the cathode and the substrate and the wall chamber are the anode [Fig. 3.17 (a)]. There are different modalities of this technique. For instance, in the *DC magnetron sputtering* deposition technique the use of magnetrons to confine the plasma directly above the target leads to higher deposition rates. Furthermore, *DC magnetron sputtering* is not a suitable method to deposit electrical insulating materials such as most oxides. However, the use of RF generators allows the generation of an alternating current in the insulating target (the target acts similarly to a capacitive load in the RF circuit), allowing the plasma to spark and vaporise material from the target. This technique is known as *RF magnetron sputtering* deposition. There are a number of parameters involved in the sputtering

process, such as the pressure of the inert gas used to form the plasma, the electrical power used for the deposition, or the temperature of the substrate. All these parameters will have an impact on the morphology of the layer in terms of roughness, compactness, stresses, average grain size [188], or even purity [189], which in turn will impact physical properties such as electrical and thermal conductivity or refractive index.

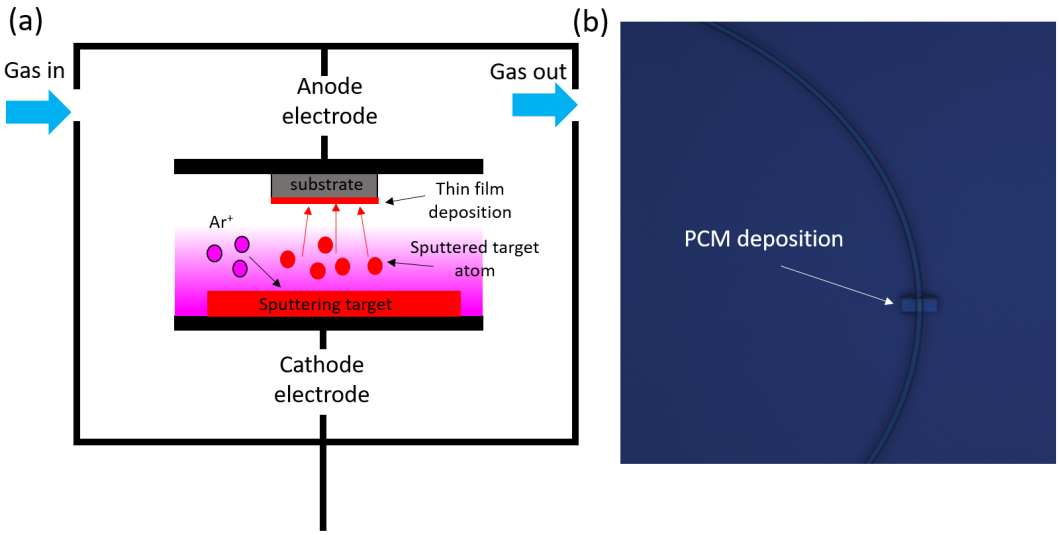

Fig. 3.17 (a) Schematic representation of the operation of a standard DC sputtering system. In this case the argon ions in the plasma are accelerated towards the target and, as a result of the impact, atoms are torn out of the target and end up being deposited on the substrate and on the wall of the chamber. (b) Optical microscope image of a phase change material thin film cell deposited on a silicon nitride micro-ring resonator.

The thin films in the different devices developed in this thesis were deposited in three different machines at the University of Exeter:

- **Nordiko 2000**: This machine can be considered an industrial machine due to the size of the target materials (four spaces for targets of six inches in diameter, ideal for wafer-scale manufacture and optical disc memories deposition and the quality of the base pressure achieved ($\sim 10^{-8}$ Torr). The machine comes with a rotary pump as the primary pump and a cryo-pump as the secondary pump. As well as this, it also has RF and DC capabilities, and therefore it is possible to deposit dielectrics as well as conductive materials.

- **Custom-built sputtering machine**: This machine is a purpose built sputtering machine with three spaces for targets of two inches in diameter. It has several advantages

such as very good reliability and the fact that it is easy to repair. This machine has a rotary pump as a primary vacuum pump and a turbomolecular pump as a secondary pump. The usual base pressures achieved in this machine are not as good as in the Nordiko 2000, however they are good enough to have good quality films in the materials deposited in it ($\sim 10^{-6}$ Torr). The machine only comes with DC capabilities.

- **Moorfield nanoPVD model T10A**: The machine has three spaces for targets of two inches in diameter. In this system a scroll pump is the primary pump and a turbomolecular pump is the secondary pump. The base pressure achieved with this pump setup is on the order of 10^{-7} Torr. The machine comes with DC as well as RF capabilities.

3.3 Characterization

The material and optical properties of the SiN and Si layers fabricated in this project and the reconfigurable materials used to make the devices actively tunable were systematically evaluated using different characterisation techniques including ellipsometry and scanning electron microscopy (SEM). This section provides an overview of these characterisation techniques along with a description of the experimental set-up used to characterise the fabricated devices in the near-infrared (NIR) wavelength region.

3.3.1 Scanning electron microscopy

SEM is a type of imaging technique based on a focused beam of electrons that scans the surface of a sample to produce an image. The electrons of the beam interact with the surface of the studied sample producing signals that provide information regarding the composition and topography of the scanned surface. Scanning electron microscopy was predominantly used in order to certify that the dimensions of the patterned structures fabricated by EBL were indeed correspondent to the ones in the design models in order to calibrate the parameters of the EBL lithography tool. The sample exposure in the devices measured in this thesis was usually done at a range of 30 to 10 kV and 0.13 nA. The maximum resolution that can be achieved with the scanning electron microscope used in this thesis is between 1 and 2 nm. A scanning electron microscope model *xT Nova Nanolab 600* was used to take the images of the fabricated devices in this thesis. [Fig. 3.18] shows examples of SEM images obtained for some of the fabricated SiN devices.

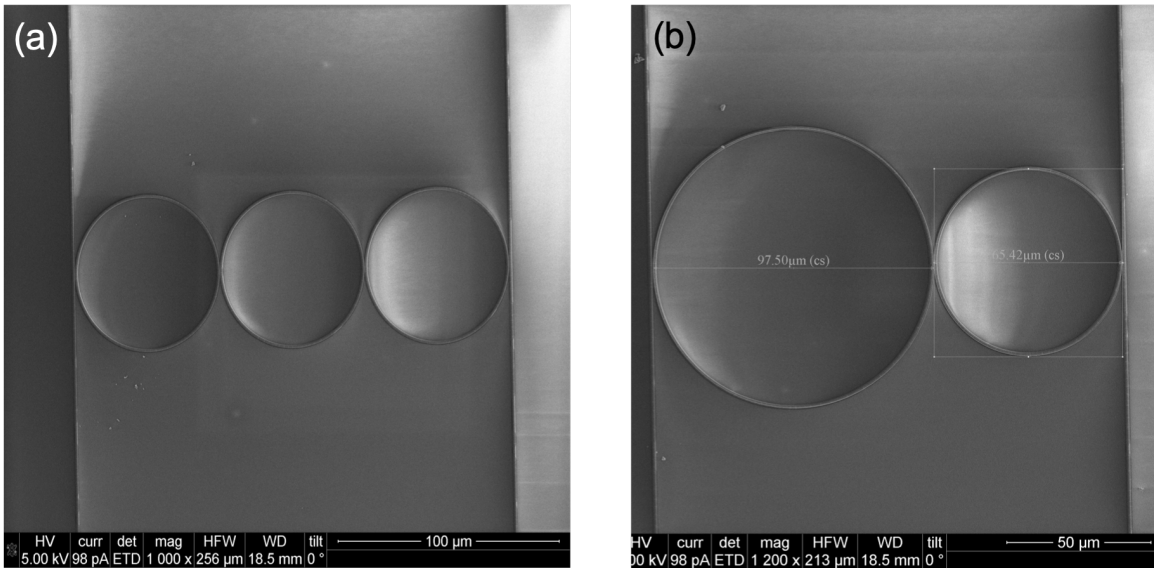

Fig. 3.18 (a) SEM image of three ring resonators in series after the fabrication process. (b) SEM image of two ring resonators in series with different radii after fabrication.

3.3.2 Spectral Response

The spectral response of the different fabricated devices was characterised in the NIR with two different tunable laser sources. An Agilent 8163B Lightwave Multimeter for the response at λ = 1550 nm and a similar Agilent 8164B Lightwave Measurement System for the response at λ = 1310 nm. The output of these lasers was connected to a polarisation maintaining fiber, this fiber was then coupled to a single mode fiber (SMF) that passed through a polarisation controller. This allowed polarisation control of the output of the laser to minimise the ripples in the spectral response of the devices due to polarisation beating. The SMF is fixed to a metal tunable-angle support which is placed on top of a micro-manipulator to control the position and the angle of the optic fiber which couples light into the chip. Then, the laser light was coupled to the devices through grating couplers by maximizing the measured transmission. The light at the output of the chip was gathered by another SMF connected to a polarisation controlled fiber leading to a power meter that measures the transmission spectrum of the studied device in the range of wavelengths emitted by the lasers. As can be seen in [Fig. 3.19 (a)], we placed a Panasonic GP-KR222 camera above the measured chips to facilitate the alignment of the fibers with the grating couplers. Furthermore, the chips are placed on top a of a Peltier thermoelectric cooler driven by an *ILX Lightwave LDT 5810Ba* temperature controller. This was used to set the desired temperature before any measurement was taken during different experiments and at the same time allows us to create a vacuum to

fix the chip position. Electrical probes were added in the set-up for the measurement of the active devices in the NIR range of the spectrum [Fig. 3.19 (b)].

The transmission spectrum of different devices was recorded using the Keysight Photonic Application Suite to sweep the wavelength emitted by the laser in the range of interest. In all cases, a reference spectrum was captured in order to normalise the data of the subsequent devices by eliminating the losses coming from the grating couplers. Once the normalisation data was obtained, the transmission spectra of different devices was captured and saved for further processing and data analysis.

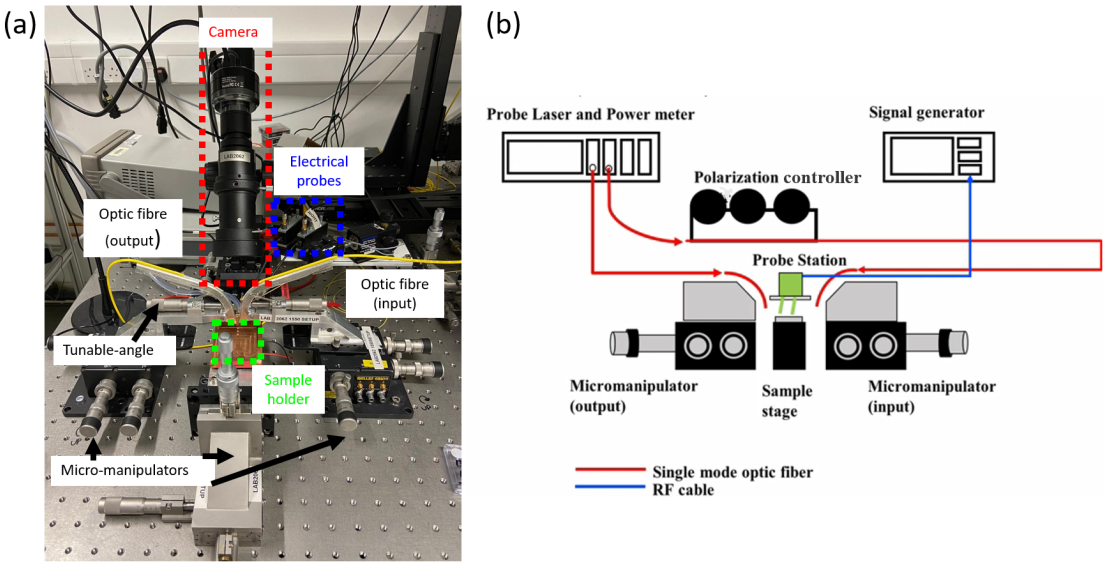

Fig. 3.19 (a) Optical characterization set-up. Laser source, polarizer, optic fibers, signal generator, electrical probes, micro-manipulators, tunable angle holders. (b) Schematic of the spectrum measurements set-up.

Chapter 4

1D silicon photonic crystal based on liquid crystals

4.1 Overview

In this chapter, a novel design for multichannel integrated filters based on silicon-on-insulator (SOI) photonic crystal concepts and optofluidics technology is proposed. By infiltrating specific periods of a 1D PhC with a reconfigurable liquid filler, an efficiently coupled Fabry-Pérot micro-resonator [Fig. 4.1] can be realized in which the wide stop band (SB) is used for frequency channel separation. Using a coupled triple-cavity 1D PhC filter operated using the third SBs, a refractive index control within individual cavities using a reconfigurable fluid have been demonstrated, enabling independent fine tuning of each channel in the system by an applied voltage. By applying a voltage to one of the cavities, a triplet resonance is achieved with a significant increase in the Q factor for one of the resonance peaks.

The development of integrated compact multi-channel optical filters is a rapidly developing area. Coupled microresonators are used in waveguide structures [190] and ring resonators [191], which can be tuned by injecting carriers, leading to a change in refractive index typically less than 10^{-4}, resulting in a relatively small tunable range. By using liquid crystals with a larger range of Δn , up to 0.4, tuning of the resonance modes has been significantly extended, for example, in a cascade resonator [82]. In Cos et al. [192] the design of an optical equalizer, or tunable filter, is proposed, with the possibility of changing the shape of the interference bands by changing n within different periods of the 1D PhC structure.

The optical properties of a system of two coupled Fabry-Pérot microresonators were investigated theoretically in Kaliteevski et al. [193], where the interaction of localized photon states is considered, leading to a splitting of the optical modes of the system. In

that study, the coupling parameter, the reflection, R, of the common mirror, is identified, characterizing the interaction force between the modes. A decrease in R led to an increase in the splitting of the peaks in the spectrum. By using coupled FP resonators and exploiting the possibility of individual tuning of n in each resonator, a 1D PhC structure with two defects and various options to control the position of the doublet of resonance modes was investigated in Tolmachev et al. [194].

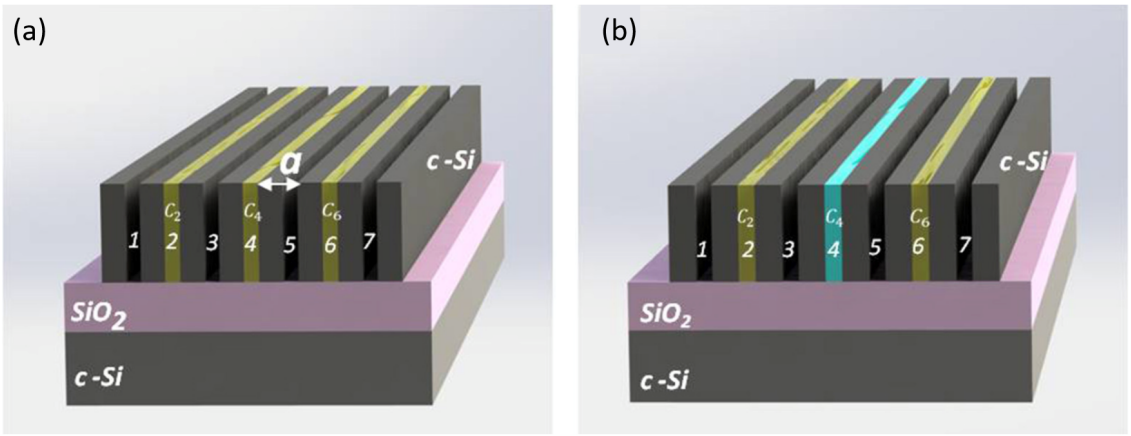

Fig. 4.1 (a) Schematic diagram of 1D PhC based on a Si-air structure with three central air channels (c_2, c_4, and c_6) infiltrated with a nematic liquid crystal (LC) of tunable refractive index, n_c. (b) Schematic diagram of 1D PhC in which the refractive index of the central cavity n_{c4} is changed without changing n_c in the edge cavities, giving a new sequence of n_c. The notation (a) stands for the lattice constant of the 1D PhC and is equal to a sum of the thicknesses of crystalline Si (c-Si) rib, d_{Si}, and the air (or LC) channel, d_{air}.

4.2 Design

In this section, the optical properties of 1D PhCs based on a Si-air structure with three central air channels infiltrated with a LC of tunable refractive index, n_c, is described. These structures form three coupled FP resonators with triple-defect modes within the photonic SBs. The optical properties of these structures were estimated using the TMM, see 3 for details. The introduction of three cavities, infiltrated with a filler of tunable n_c, to a 1D PhC, leads to the formation of triple conjugated FP resoantors, [Fig. 4.1 (a)]. The transfer matrix for three coupled resonators (M_{3CR}) can be written as

$$M_{3CR} = H(LH)^{mB_r} L_{c2} \left[(HL)^{mo} H\right] L_{c4} \left[(HL)^{mo} H\right] L_{c6} \left[(HL)(HL)^{mB_r} H\right] \tag{4.1}$$

where H stands for the matrix of the high-refractive index component and L stands for the matrix of the low-refractive index component, c_2, c_4 and c_6 refer to the resonator cavities (2, 4, and 6), mB_r, the number of periods for the Bragg mirror and mo the number of periods for the internal mirror. The refractive index of the air is taken as $n_{air} = 1$, while the data for the dispersion of Si, $n_{Si}(\nu)$, is taken from Salzber and Villa [195]. For the calculations, various combinations of n_c in the FP-resonator cavities, with parallel or cross-tuning in the range 1.5–1.7 were used. From the large range of possible n_c available, four specific cases which may be of practical interest for different applications were selected. The calculations were performed for the following geometrical parameters of a 1D PhC: $d_{Si} = 0.718\mu m$ and $d_{air} = 2.5\mu m$ (i.e., $a = 3.218\mu m$) and $mBr = mo = 1$.

4.2.1 Parallel tuning of triplet FP Resonator

In the initial state, when the filler in all three cavities of the resonator has $n_c = 1.585$ [Fig. 4.2 (a)], a triplet of defect modes appears in the spectrum of the 1st SB, see Fig. 4.2 (c)-bottom. The distance between the peak positions in this triplet is $\Delta\nu \approx 40\ cm^{-1}$, the linewidth, i.e, the full width at half- maximum, FWHM, for the edge and central peaks is 2.5 and 5.5 cm^{-1} respectively, and the Q factors for each peak are 420 and 190, respectively. When n_c in all three cavities is decreased from 1.585 to 1.515 [Fig. 4.2 (b)], the triplet as a whole experiences a blue shift by $\Delta\nu$ =30 cm^{-1} [Fig. 4.2 (c)-top spectrum], or in relative units by $\Delta\nu/\Delta n_c$ =429 cm^{-1}/RIU, where RIU stands for refractive index unit. Taking into account the linewidth of the peaks and the distance between them, equal to $\Delta\nu \approx 40\ cm^{-1}$, as well as the possibility of changing the values of n_c to a high degree of accuracy, it is possible to obtain other triplets occupying different positions in the spectrum. Thus, it is possible to achieve tuning of 4 triplets, with 12 resonant peaks in total, covering the range $\Delta\nu_{total}$ =116 cm^{-1} [Fig. 4.2 (d)].

The tuning effect can be increased by using higher order SBs. To obtain non-overlapping peaks, it is possible to use an almost full range of n_c variation in the range 1.5–1.7, [Fig. 4.3 (a)]. Calculations show that in the 3rd SB the linewidth of the peaks remains the same as in the 1st SB, with 2.5 cm^{-1} for the edge peaks and 4.5 cm^{-1} for the central peak. The distance between the two nearest peaks is 40 cm^{-1} and the tuning range increased 5-fold from 30 to 167 cm^{-1}, [Fig. 4.3 (b)]. The relative tuning is $\Delta\nu/\Delta n_c$ =835 cm^{-1}/RIU, a

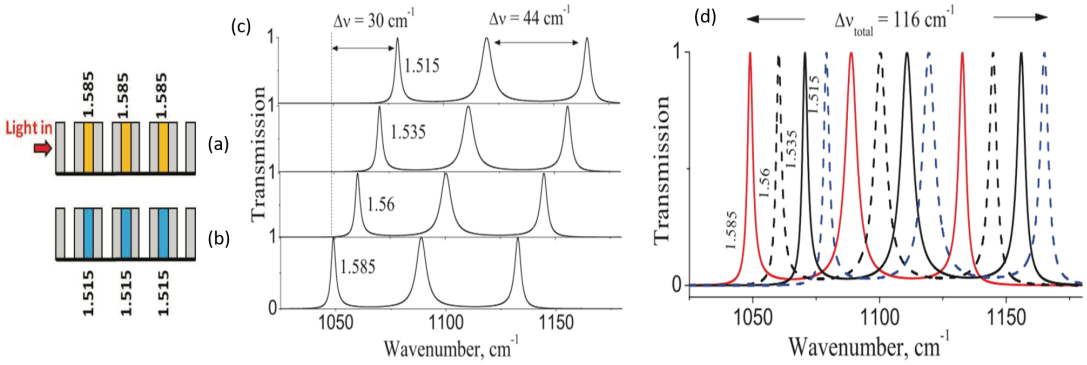

Fig. 4.2 Schematic diagram of three coupled resonators with tuning of n_c of the filler from (a) 1.585 to (b) 1.515; (c) parallel tuning of the triplet mode with $\Delta\nu$ =30 cm^{-1} for the 1st SB, (d) the full range of 12 resonance peaks with $\Delta\nu_{total}$ =116 cm^{-1}. The numbers beside the peaks are the refractive indices, n_c, of the filler liquid in the resonator cavities.

2-fold increase. We note that 12 resonant peaks were obtained using only four possible values of n_c in the range 1.5–1.7, including the lowest and the highest n_c values. However, to obtain the maximum number of non-overlapping peaks, further fine tuning of the n_c values within this range is required. The spectrum in [Fig. 4.3 (b) (bottom-spectrum)] shows only one triplet for $n_c = 1.585$, whereas in all other spectra in this Figure, two triplets are shown for the larger and smaller values of n_c to save space. [Fig. 4.3 (c)] shows the positions of all 27 peaks in the range $\Delta\nu_{total} = 420\ cm^{-1}$, exhibiting good resolution between the peaks. As in the case of double resonators [193, 196] the central position of the resonance peaks in the 3rd SB, with a linewidth of $\omega_{3^{rd}SB} \approx 600\ cm^{-1}$, made it possible to use over 2/3 of the SB to create a wide range of tunable resonances within it. In contrast, for the 1st SB, only 15% of the width of the band, $\omega_{1SB} \approx 770\ cm^{-1}$, can be used in this manner.

4.2.2 Tuning of the edge peaks in the triplet

Other options for triplet tuning are available. The initial state of the resonators is described by the following sequence of n_c: 1.515–1.515–1.515, [Fig. 4.4 (a)]. The calculated transmission spectrum, T, for the 1st SB is shown in [Fig. 4.4 (d)]. The n_c of the central cavity is changed to 1.585 without changing n_c in the edge cavities, giving a new sequence of n_c: 1.515–1.585–1.515 [Fig. 4.4 (b)] with the corresponding spectrum shown in [Fig. 4.4 (e)]. Finally, by changing n_c in the central cavity to 1.7, [Fig. 4.4 (c)], we obtain the spectrum shown in [Fig. 4.4 (f)]. The result of this tuning is a red shift of two edge defect modes at $\Delta\nu$ =45 cm^{-1}. In relative units, the shift is small, i.e, $\Delta\nu/\Delta n_c = 225\ cm^{-1}/RIU$, and the central

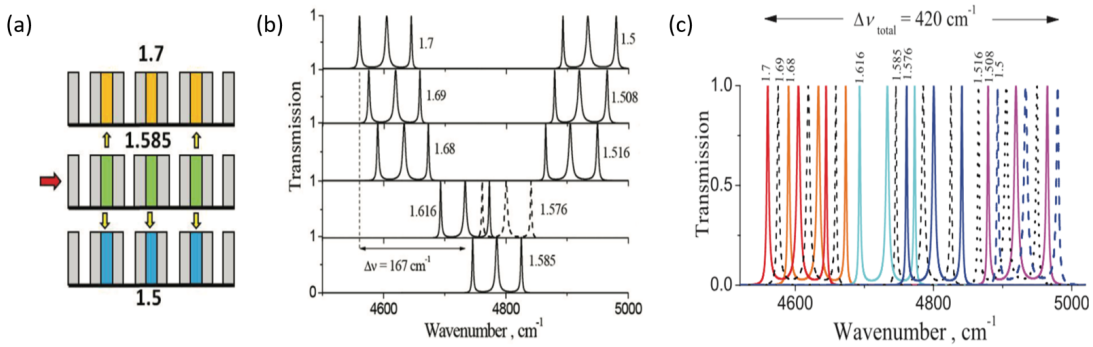

Fig. 4.3 (a) Schematic diagram illustrating n_c tuning in resonator cavities, (b) nine triple peaks in the spectra of the 3rd SB with parallel tuning of the n_c filler from 1.5 to 1.7, (c) the full range of 27 resonance peaks with $\Delta\nu_{total}$ =420 cm^{-1}. Numbers beside the peaks correspond to the values of n_c for the fillers in all three cavities of the resonators.

mode within the triplets remains stationary. This is more clearly manifested in the 3rd SB shown in [Fig. 4.4 (g–i)]. Indeed, splitting of the triplet into a double peak (doublet) and a single peak (mono-peak) occurred, and, as seen in [Fig. 4.4 (i)], both peaks in the doublet merge to form a single broadened peak, while the monopeak is narrowed greatly. Formation of the doublet structure is explained by the interaction between two resonators with identical resonant frequencies. These are the two extreme cavities, with n_c = 1.515, connected through a central resonator. Its resonant frequency, with a change of n_{c2} to 1.585 and then to 1.7, differs from the frequency of the resonators forming a doublet. For the initial state, the central resonator was in resonance with the edge cavities and its intrinsic frequency begins to increase as n_c increases. This, in turn, reduces the interaction between the resonances in the edge cavities, due to the appearance of a reflector at their intrinsic frequency, ultimately greatly weakening their interaction, resulting in minimal peak splitting in the doublet [Fig. 4.4 (i)]. From [Fig. 4.4 (g–i)], the total shift as a result of the tuning is $\Delta\nu$ =270 cm^{-1}, which is significant if expressed in relative units, with $\Delta\nu/\Delta n_c$ =1,350 cm^{-1}/RIU. In addition, the quality factor, $Q = \nu_{res}/\Delta\nu$, where ν_{res} is the resonance peak position and $\Delta\nu$ is the linewidth, is significantly increased from 1,400 to 21,200 for the left peaks in [Fig. 4.4 (g,i)] respectively.

Let us now consider the following tuning option utilizing the 3rd SB: n_c in the edge cavities unchanged and equal to 1.6, while the n_c of the central cavity (n_{c2}) changes to a larger or smaller value from n_c, that is, $n_{c2} = \pm\Delta n$, where $\Delta n = 0.035$. A schematic of the n_c changes is shown in [Fig. 4.5 (a–c)]. Figure 4.5 (d) shows the original triplet, obtained in the 3rd SB with splitting of the peaks by $\Delta\nu$ =40 cm^{-1} for the original state with n_c = 1.6 in all 3 cavities of the resonator. Furthermore, by increasing or decreasing n_c by Δn = 0.006, 0.017,

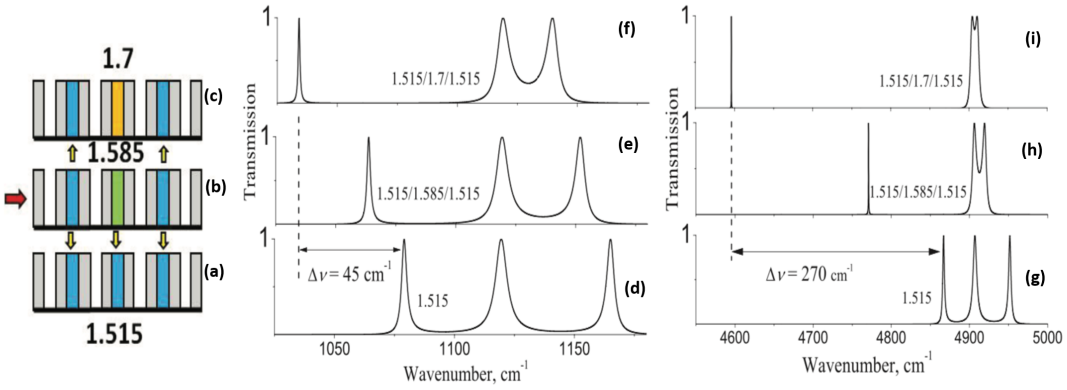

Fig. 4.4 (a-c) Schematic diagram illustrating tuning of n_c in one of the three cavities of the resonator. Triplet peaks with tuning of the n_c filler from 1.5 to 1.7 in the central cavity with splitting of the triplet into doublet and mono-peaks in the spectra of the 1st SB (d-f) and 3rd SB (g-i). The numbers correspond to the value of n_c of the filler in the resonator cavities.

and 0.035, different triplets were obtained, as presented in [Fig. 4.5 (e–g)]. As a result, the position of the central peak on the graphs remains unchanged while peak splitting is observed. With increased n_{c2} the edge peaks are red shifted, while with decreasing n_{c2} the peaks are blue shifted. In addition, the nature of the peak splitting of the triplet changes. For example, increasing n_c to 1.635, the left peak splits more strongly ($\Delta\nu = 79\ cm^{-1}$), while the right peak approaches the central peak ($\Delta\nu$ =20 cm^{-1}). This situation is analogous to the effect shown in Figures 4.4 (g–i), where splitting of the triplet into a doublet and a mono-peak was observed. This was explained by a weakening of the interaction of the coupled resonators caused by different n_c values within the cavities. Thus, by selecting a more appropriate combination of n_c values, [Fig. 4.5 (a–c)], it is possible to obtain well-separated transmission peaks in the interval $\Delta\nu_{total}$ =157 cm^{-1} as shown in [Fig. 4.5 (h)]. So, it is possible to tune 7 different peak pairs with one common unchanged transmission channel, that is, 15 channels in total. Summarizing the results from the data shown in Figures 4.4 (g–i), 4.5 (d–h), we conclude that changes in the triplet with increasing Δn between the cavities are more pronounced in the 3rd SB when compared with the 1st SB, allowing edge tuning to provide a larger range of transmission channels.

4.2.3 Tuning of the central peak in the triplet

Another option for triplet tuning was investigated where changing n_c simultaneously in all 3 cavities. The variation of n_c was carried out according to the schematic shown in Figures 4.6 (a–c). For the initial state n_c in the cavities (1.6/1.6/1.6), the triplet in the 1st SB is shown in

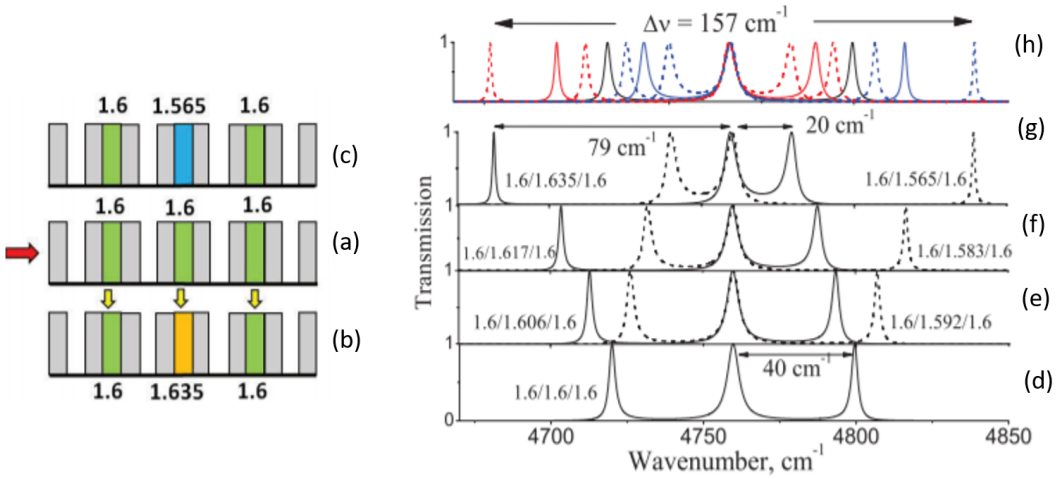

Fig. 4.5 (a–c) Tuning of the n_c filler in the central cavity only: (d–g) 7 triplets in the 3rd SB, realized with different n_{C2} (shown by numbers at the peaks) with a fixed central peak and tuned lateral (edge) resonances, (h) summing peaks for all states of n_c.

Figure 4.6 (d). A decrease of n_{c4} to 1.57 was made in the central cavity of the resonator, with a simultaneous increase of n_{c2} and n_{c6} to 1.625. This state (1.625 /1.57 / 1.625) is depicted in Figure 4.6 (b). Since n_c in the resonators now changes in opposite directions, we refer to this situation as cross-tuning. The original triplet calculated is shown in Figure 4.6 (d) with another triplet obtained using an intermediate value of n_c. Also included are triplets obtained by reverse tuning of n_c in the resonators, as shown in the schematic in Figure 4.6 (c). From Figure 4.6 (d), the positions of the side peaks remain practically the same for the 5 triplets obtained, while the central peak experiences a red shift as the n_{c2} of the central cavity decreases. This is the opposite case to the tuning effect for a single peak in a classical FP resonator. In a single peak in a classical FP resonator, a decrease in the optical thickness of the cavity results in the resonance peak experiencing a blue shift. Examining this effect for the 3rd SB in Figures 4.6 (e–h), it is apparent that as the cross-sectional change in n_c increases, resonance effects split the triplet into a doublet and a mono-peak, as observed earlier, see Figure 4.4. Indeed, the central peak of the triplet in this case experiences a red shift. Thus, for the 3rd SB, performing cross-tuning of n_c in the cavities enables control of the doublet structure, shifting it to the red. The edge cavities with the same refractive index are responsible for the appearance of the doublet structure. n_c in this case increases, leading to a red shift of the doublet, and the central peak responsible for its creation. This red shift is apparent in Figures 4.6 (e–h). It should be noted that because of strong splitting due to cross tuning of n_c in the cavities in the 3rd SB, the side peaks in the triplet cannot be fixed, as was possible in the 1st SB. Attempts to realize a similar resonator, i.e., fixed edge

channels—tuning of the central channel, for the well-divided peaks in the 3rd SB failed, even when changing the values of n_c by small amounts.

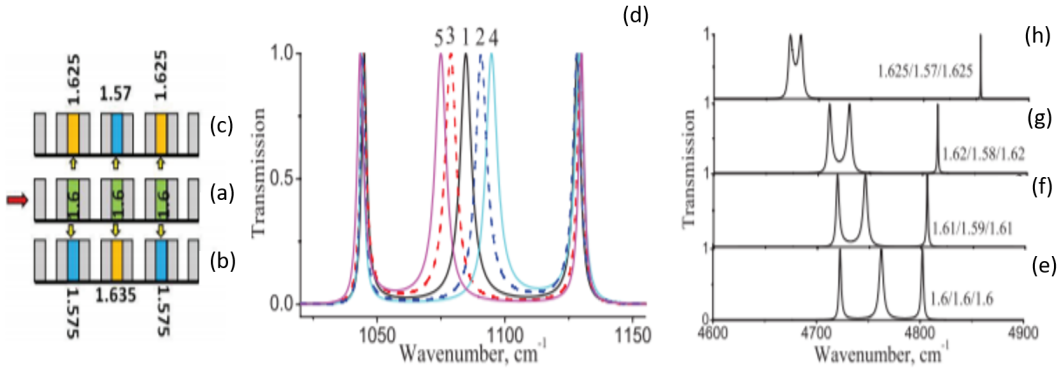

Fig. 4.6 (a–c) Schematic diagram illustrating cross-tuning of the n_c filler, (d) 5 triplets in the 1st SB with fixed edge peaks and a tunable central peak, (e–h) the original triplet and 3 triplets in the 3rd SB, demonstrating the split into a doublet and a mono-peak. Numbers at the peaks are the values of n_c for the fillers in the cavities of the resonators. In panel (d) the numbers beside the curves correspond to the following set of n_c: 1 – 1.6/1.6/1.6; 2 – 1.585/1.62/1.585; 3 – 1.615/1.58/1.615; 4 – 1.575/1.63/1.575; 5 – 1.625/1.57/1.625.

4.2.4 Tuning with suppression of the edge peaks

Another type of cross-tuning of the n_c state in resonators is considered here, where the changes in n_c occur in the edge cavities, while n_c in the central cavity is kept constant. The initial state of n_c in the cavities is shown in Fig. 4.7 (a) (1.6 / 1.6 / 1.6), and the corresponding triplet in the 1st SB is shown in Fig. 4.7 (d). Furthermore, the value of n_{c4} in the central cavity remains unchanged (1.6), while in the leftmost cavity of the resonator an increase of n_{c4} to 1.66 is made, with a simultaneous decrease of n_{c4} in the rightmost cavity to 1.57, resulting in a state of 1.66 / 1.6 / 1.57, as depicted in Fig. 4.7 (b). The resulting triplet is shown in Fig. 4.7 (e), showing a decrease in the amplitude of the side peaks of the triplet together with their splitting. Further adjustment of n_c in the edge cavities to the state 1.7 / 1.6 / 1.53 [Fig. 4.7 (c)] results in the triplet being converted to the spectrum shown in Fig. 4.7 (f). From this Figure, the lateral peaks are almost completely suppressed and their splitting has been further increased. It is important to note that these tunings of n_c hardly affect the amplitude and shape of the central peak. Similar effects occur in the 3rd SB [Figs. 4.7]. Almost complete suppression of the edge peaks in this triplet is observed with a difference in n_c of only $\pm$ 0.03. The edge peaks were split more significantly and their amplitude is minimised. In addition, the central peak becomes narrower [Fig. 4.7 (j)]. The decrease in

amplitude observed is a clear sign of the degradation of resonance effects in the cavities. Since n_c in the extreme cavities became significantly different in both the 1st and the 3rd SBs with maximum tuning, the resonance effect between these oscillators also decreased sharply

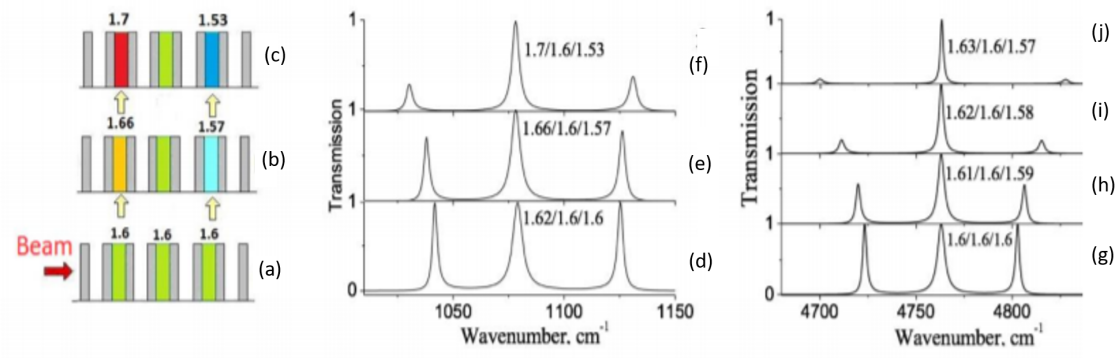

Fig. 4.7 (a-c) Cross-tuning n_c of the filler. Static central peak within triplet and suppression of the amplitude of the edge peaks to minimum transmission in the 1st SB (d-f), and eliminating them in the 3rd SB (g-j). Numbers at peaks correspond to the value of n_c for the filler in the cavities of the resonators.

4.3 Fabrication

Prototypes of integrated triple-cavity PhC filters were designed and fabricated on a Silicon-On-Insulator (SOI) platform. The triple-channel resonator device was fabricated on a <100> p-type SOI wafer with a silicon device layer thickness of 4.5 μm and a 1 μm thick buried oxide layer. Electron-Beam Lithography followed by plasma etching was used to fabricate the nano-scale structures with a lattice constant of 1600 nm and a Si wall thickness of 1040 nm [Fig. 4.8].

These design parameters for the 1D PhC structures were selected in order to create triple resonances in the telecommunication wavelength range after infiltration of the 2nd, 4th, and 6th grooves with a nematic liquid crystal filler E7, [Fig.4.9 (a)]. This liquid crystal was chosen mainly because of its high birefringence, $n_e - n_o = 0.21$, where n_e and n_o correspond to the extraordinary and ordinary refractive indices respectively, as well as a wide nematic temperature range (from $10^{\circ}C$ to 59 $^{\circ}C$). Electrical isolation of the 2nd, 4th, and 6th grooves of the 1D PhC was achieved by dry-etching the micro-channels across the chip. One cone-shape cavity is designed for the easy infiltration of these grooves with LC E7, [Fig. 4.9 (a-d)]. A 500 nm layer of aluminum was deposited by sputtering for the contact pads. Optical

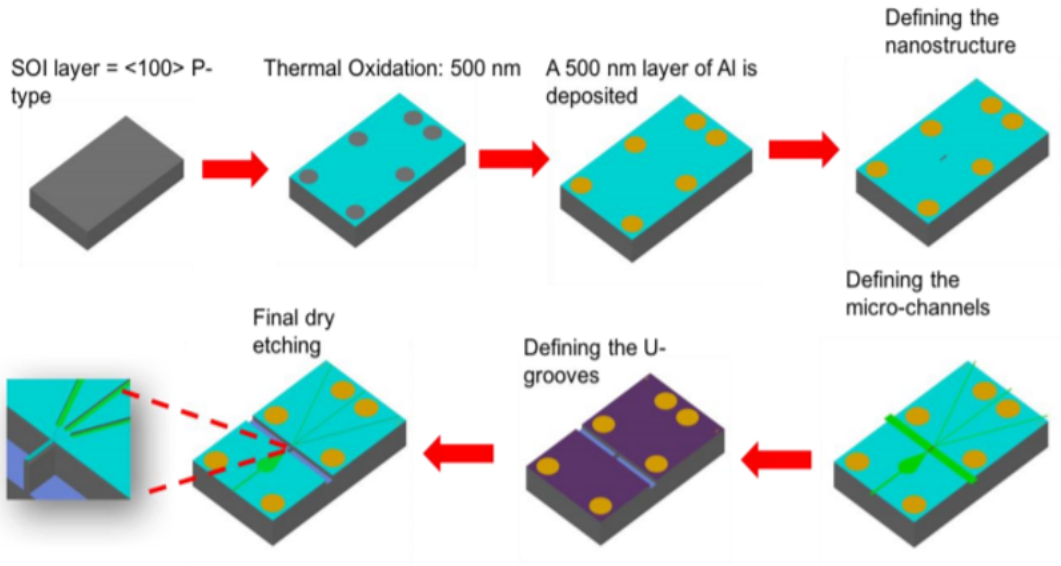

Fig. 4.8 Sequence and layout of Si-Air 1D PhC fabrication.

lithography followed by a wet etch process was used to define the contact pads, as shown in Fig.4.10 (a). Finally, U-grooves with a depth of 60 μm were etched from both sides of the nano-structure for easier integration of the optical fibers and direct coupling to the device [Fig.4.10 (b,c)].

4.4 Characterization

By applying a voltage to the aluminum contact pads, different orientations of the LC molecules were obtained in the individual grooves, allowing manipulation of the refractive index in the 2nd, 4th, and 6th grooves [Fig 4.10 (a-d)]. In Figure 4.11, the electro-optical effect obtained for three channels is demonstrated with crossed-polarized optical microscopy. The black stripes are silicon electrodes, orange lines are air grooves and light stripes are grooves filled with a LC, [Fig. 4.11]. A rectangular pulse train is applied to the three channels, alternating between 0 and 10 V, with a pulse duration of τ_p = 1 ms and a frequency of f_p = 100 Hz. The applied voltage causes the Fredericks transition [197] to occur in the LC in the grooves, as demonstrated by the change in color of the groove stripes.

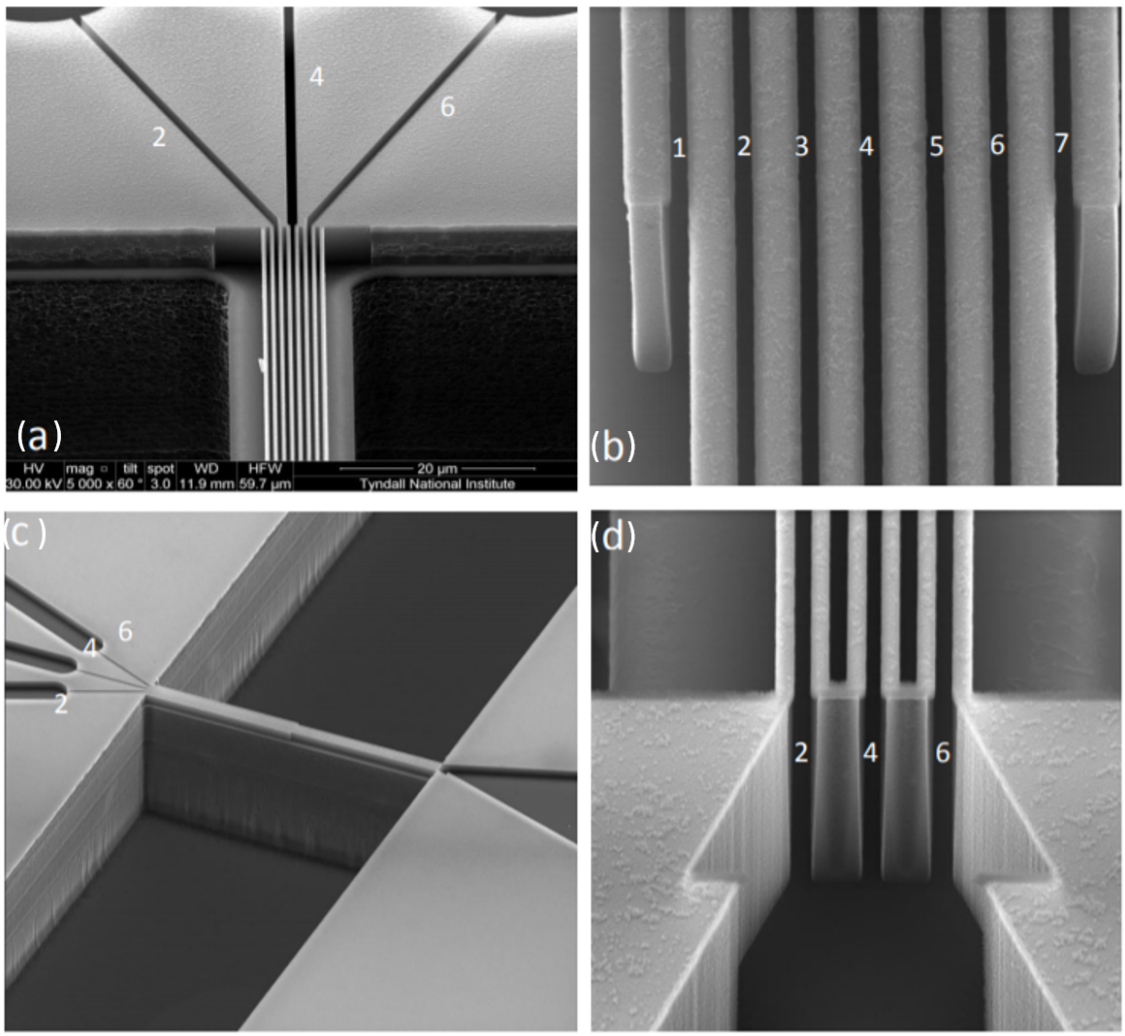

Fig. 4.9 (a) SEM image of the fabricated SOI-based defect-free PhC structure with connected three microfluidic channels to 2nd, 4th and 6th grooves; (b) A closer view on the defect-free 1D PhC with 7 air-grooves. (c) The total view on PhC structure sitting on the pedestal surrounded by the U-grooves with input and output microfluidic channels connected to the 2nd, 4th and 6th grooves. (d) A closer view on the liquid reservoir connected to the 2nd, 4th and 6th channels on the other side of the structure.

A demonstration of the appearance of the full set of resonance peaks within the 1st and 3rd SBs under applied voltage was not possible in this work due to limitations in the wavenumber range available for measurements in our fiber-coupling set-up. However, a shift of the resonance peak position by the applied electric field of different strength (and, therefore, by fine-tuning of n_c) was demonstrated earlier [198]. The experimental verifications of these calculations were provided using Fourier-transform infrared microspectroscopy (FTIR). On-chip in-situ transmission testing of the device with an electric field applied to the micro-

fluidic cavities was performed in the geometry demonstrated in Fig. 4.10 (c). Light from the Yeniast Tunics T100S tunable laser source in the range 1,540– 1,630 nm was coupled into the chip on the left-hand side. The transmitted signal was collected from the right-hand side, using standard optical fibers. Output power was measured using an optical spectrum analyser (OSA), Yenista Optics FP002417 OSA, see Fig. 4.12.

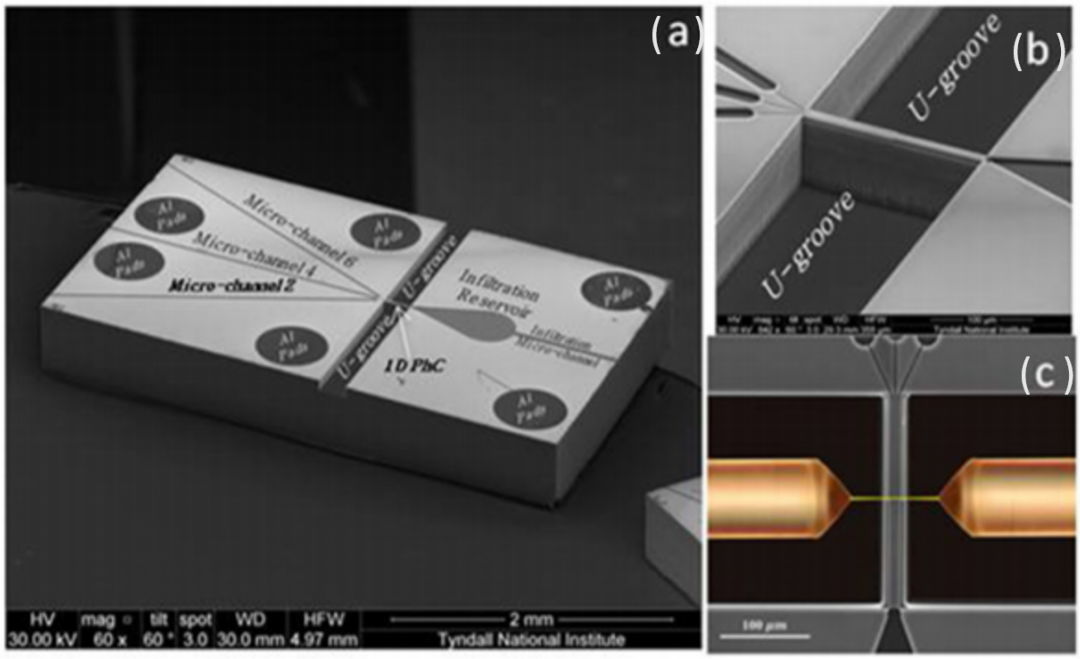

Fig. 4.10 SEM images of the fabricated (a) SOI-based chip with integrated triple-coupled defect photonic crystal filter with connected microfluidic channels to the 2nd, 4th, and 6th periods (clearly indicated beside the output channels) and metal contact pads (circles), and (b) closer view of the defect-free 1D PhC with three-channels connected to the 2nd, 4th, and 6th grooves for infiltration purposes. (c) Schematic representation of light coupling with optical fibers integrated on-chip using U-grooves from both sides of the PhC structure.

In Fig. 4.12, the fitted n_c value corresponds to a homeotropic alignment of rod-like LC molecules perpendicular to the Si walls, expected to occur with an applied electric field across the 1D PhC groove channels. This experimental result demonstrates for the first time, electrically controllable, ultrahigh sensitivity of a single resonance device based on the triple cavity Fabry-Pérot system. The LC filler in the 2nd and 6th cavities can be replaced by any other liquid filler analyte or gas with arbitrary refractive index, while the electrically tunable 4th central cavity can be used as a highly-sensitive reference liquid. The nematic LC E7 can demonstrate a relatively high-quality factor and sensitivity for high-order stop-bands in particular [199]. It should be pointed out however, that for SOI electro-optical devices, that

required a fast tuning of the refractive index of liquid crystal, the LC E7 is not very suitable, since its operation time is in the range of milliseconds. However, the other nematic LCs like, for example, 5CB and CCN-47 not only characterized by their high birefringence but also demonstrate an impressive electro-optical switching time in the range of 30–50 nanoseconds, as recently was demonstrated under specific experimental conditions in Geis et al. [200] and Borshch et al. [201]. In addition to that, it was shown during the last decade that some new type of liquid crystal molecules (for example, banana-shaped or bent-core LCs) can demonstrate also fast switching time at microseconds/nanoseconds level [202, 203].

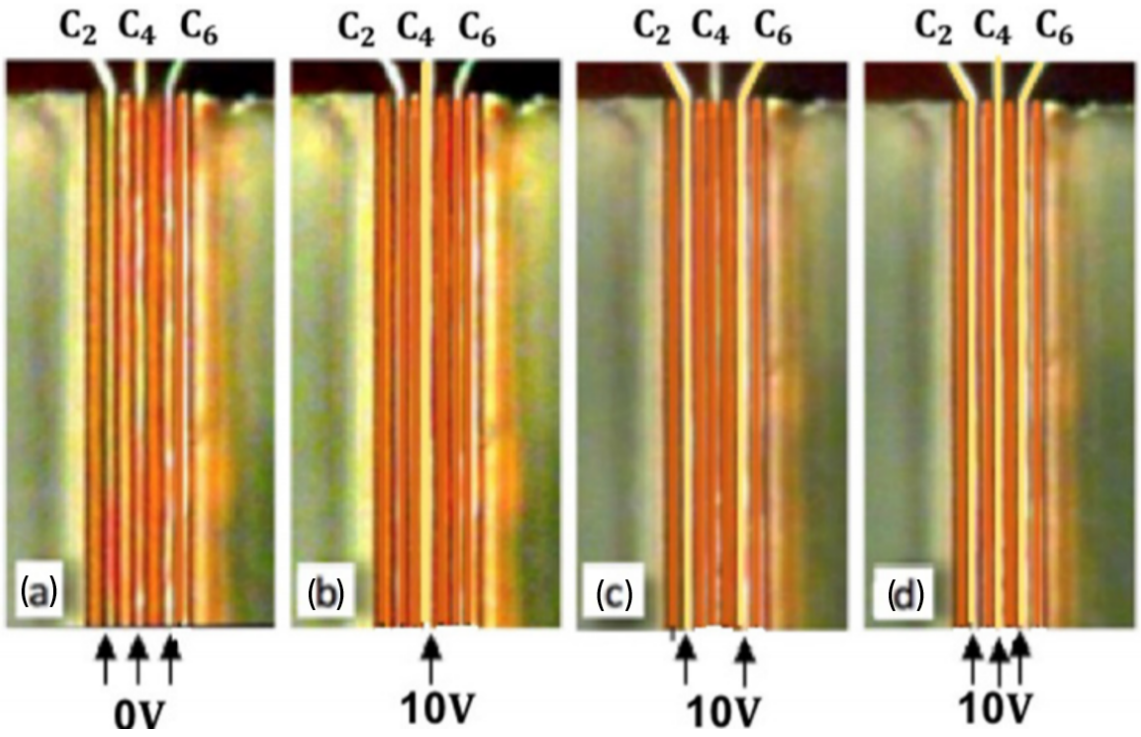

Fig. 4.11 Polarized Optical Microscope images showing a top view of the channels: (a) no applied electric field (0 V), (b) under applied electric field of 10 V to the 4th central channel, (c) under applied electric field of 10 V to the 2nd and the 6th channels and (d) under applied electric field of 10V to all three channels. Note: Applied voltage indicated by numbers (0 and 10) in Volts.

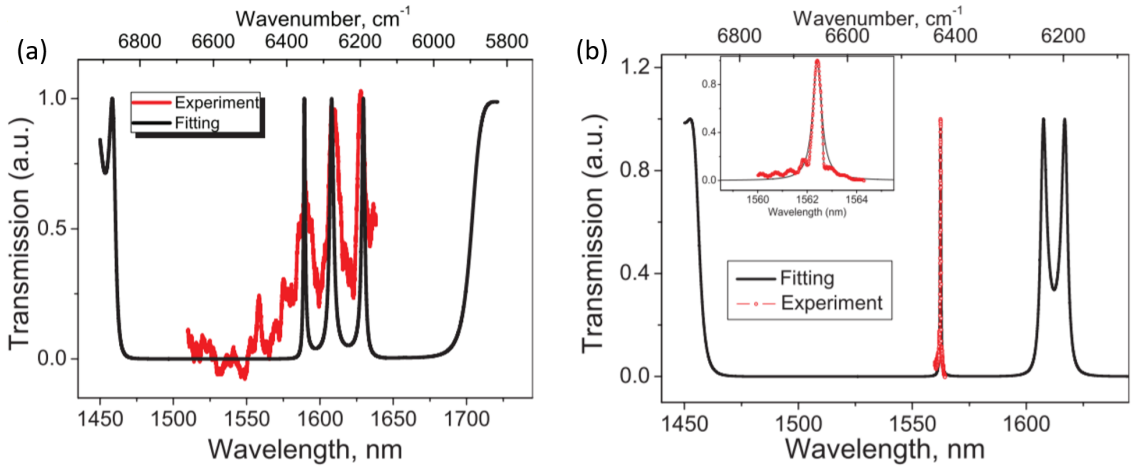

Fig. 4.12 Both figures are for the same device with different voltage applied to the central channel, simulated (black) and experimental (red) transmission spectra of (a) triple resonance system with refractive index of LC filler of n_c =1.68 in 2nd, 4th, and 6th grooves with 0 V applied in the central cavity and (b) single resonance system realized by application of 10 V to the 4th groove and reduction of refractive index to n_c = 1.458. A magnified view of the single resonance peak can be found in the inset figure. B.

4.5 Summary

A Fabry-Pérot (FP) resonator based on a Si-air one-dimensional photonic crystal (1D PhC) with coupled triple-cavity modes (or defects) has been demonstrated. These defects are obtained by filling selected air channels in the 1D PhC with an actively reconfigurable fluid. Simulations of the optical properties of these FP resonators were performed in the wide infrared spectral range. It is shown that by changing the refractive index, n_c, of the fluid simultaneously in all three channels, a set of narrow triple resonance peaks can be obtained within wide stop-bands of different order in the infrared range. In addition, at certain values of n_c, splitting of the triple resonance peaks into a doublet and a single peak with a significantly larger quality factor, Q, occurs. Prototype devices based on Silicon-On-Insulator platform were fabricated and characterized by electro-optical and spectroscopic measurements. The electro-optical measurements demonstrate the possibility of refractive index manipulation of the filler in the FP channels individually or simultaneously. Spectroscopic measurements performed in the range 1540–1630 nm using fiber-coupling confirm the presence of triple resonance peaks in the 3rd stop-band in the absence of an electric field applied to the FP channels. At an applied voltage of 10 V to the middle channel, an increase of Q to 3720 in the single peak is registered respect to the triplet where a quality factor of Q =923 was measured for 0 V.

Chapter 5

Graphene enabled tunable PIC

Graphene is attracting significant interest from the photonics community due to its unique combination of thermal, electronic, and optical characteristics [204]. The linear dispersion found around the Dirac points in graphene's band structure leads to the universal optical conductance of the interband transition [205, 206]. Single-layer graphene demonstrates broad conductive transparency - it absorbs only 2.3% of normally incident light within the infrared-to-visible spectral range. The density of states of carriers near the Dirac points is low, and as a consequence, graphene's Fermi energy can be tuned significantly with relatively low electrical energy required [128]. This Fermi level tuning changes the refractive index (RI) of the graphene. Thus combining graphene with integrated silicon waveguides opens great possibilities for the design of tunable components in PICs. In this chapter, two different graphene applications on-chip are explored. First, a Silicon-rich nitride modulator based on a graphene capacitor is designed and studied. Then, a graphene micro-heater is designed and explored on top of an stoichiometric rib silicon nitride waveguide to switch thermally a phase change material thin film in order to tune the waveguide transmission depending on the state of the phase change material.

5.1 Si-rich nitride graphene based optical modulator

Currently, the library of developed and tested individual photonics components for integration into PIC systems is extensive. However, one of the main challenges inherent to standard photonics components is the high cost of the SOI material platform, and associated high-cost of production, due to the complex multi-stage fabrication processes involved [207]. Implementation of reconfigurable materials is the most promising solution, since the complexity of designs for actively tunable devices can be simplified. Beyond the well-established reconfigurable materials, such as phase change materials (PCMs) [39], liquid crystals [208] and p-n

junctions technology [209–211], new technologies are emerging, such as: hyperbolic metamaterials based optical modulators [212], and nano-opto-mechanical effects in integrated waveguides [213]. Graphene and graphene-related materials [214] are truly outstanding candidates for application in reconfigurable PICs, with the potential to facilitate endless opportunities for construction of reconfigurable integrated photonic components such as modulators [14, 215–217], switchers [10], and photodetectors [218]. Herein, a graphene capacitor as the key component for future optical routing systems, modulators or volatile multilevel photonic memories (VMPM) is proposed. Volatile memories find their main applications in general-purpose random-access memories, and in data security systems for the protection of sensitive information [219]. To date, integrated photonic volatile memories have been demonstrated as solutions for optical logic processing [220, 221], ensuring data security [222], quantum computing [64], and deep learning. A graphene-enabled VMPM concept based on a multiplexed design of SRN micro-ring resonators structures on chip that allows optical routing and fast data processing is described, Fig. 5.1. The proposed SRN platform allows high density memory integration through multilevel stacking of SRN layers achieved via the low temperature fabrication process recently developed by Bucio *et al.* [223]. In this section, the concept and designs of electrically-driven graphene capacitor structures integrated with SRN photonic waveguides and microring structures are introduced. This is followed by a systematic study of the operational performance depending on the geometrical parameters of the designs. Then, the concept and designs of triple microring systems and assess the operational characteristics in the context of VMPM applications are introduced.

5.1.1 Design and modelling of a reconfigurable graphene capacitor based on electric field effect in SRN micro-ring resonators.

Graphene capacitor optical modelling

The considered device (shown in Fig. 5.1) consists of a SRN waveguide structure partially covered by a graphene capacitor structure. The graphene capacitor consists of a thin layer of (Si_3N_4) insulating material sandwiched between two layers of graphene electrodes [187] (shown in Fig. 5.2 (a)). To accurately assess the operation of electrically-tunable hybrid waveguides based on graphene capacitors (HWGCs) within the optical communications wavelength range, the optical properties of graphene must first be defined. One of the most important functional characteristics of graphene is its gate-variable optical conductivity [224]. Graphene's conductivity can be tuned by the application of a voltage to a graphene capacitor structure. Applying the voltage changes the carrier density of graphene and, consequently, the Fermi level. The dependence of graphene's optical conductivity on inter- and intra-band

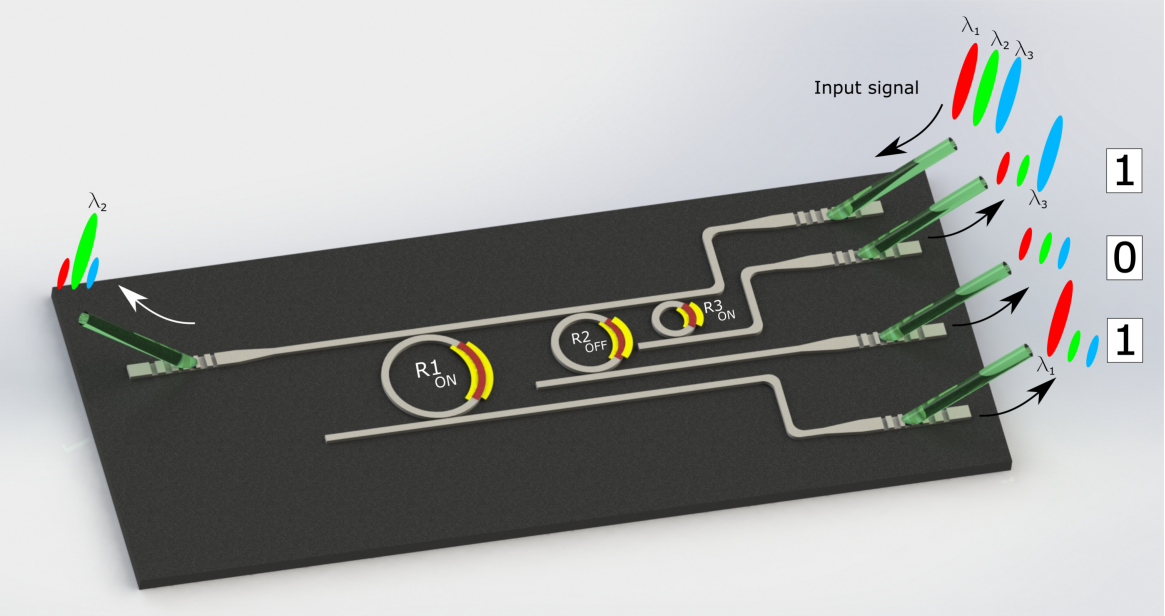

Fig. 5.1 Schematic of the integrated parallel volatile photonic memory based on a multiplexed system of hybrid graphene capacitor-SRN microring circuits. The photonic circuit consist of three microrings of radii R_1, R_2, R_3 with integrated graphene capacitor sections (graphene- red; electrical contacts- yellow). The schematic depicts coding for the binary number "101" where transmission of different wavelengths is tuned by switching the graphene capacitors 'ON' or 'OFF' on different rings.

transitions has previously been analytically derived at 0 K and at 300 K [225]. The complex optical conductivity $\sigma(\omega,\mu,\Gamma,T)$ depends on the temperature, T, the angular frequency, ω, the Fermi level, μ, and the charge particle scattering rate, $\Gamma = \tau^{-1}$, where τ is the relaxation time, and can be described as [226] :

$$\sigma_t(\omega,\mu,\Gamma,T) = \sigma_{intra} + \sigma_{inter}^{'} + \sigma_{inter}^{''} \tag{5.1}$$

The intraband conductivity σ_{intra} follows Drude's model:

$$\sigma_{intra} = \frac{4\sigma_0\mu}{\pi(\hbar\tau_1^{-1} - j\hbar\omega)}, \tag{5.2}$$

where $\sigma_0 = \pi e^2/2h$ is the universal optical conductance and τ_1^{-1} is the relaxation rate associated with intraband transitions.

The interband contribution can be described as:

$$\sigma_{inter}^{'} = \sigma_0\left(1 + \frac{1}{\pi}tan^{-1}\left(\frac{\hbar\omega - 2\mu}{\hbar\tau_2^{-1}}\right) - \frac{1}{\pi}tan^{-1}\left(\frac{\hbar\omega + 2\mu}{\hbar\tau_2^{-1}}\right)\right) \tag{5.3}$$

and

$$\sigma''_{inter} = -\frac{\sigma_0}{2\pi} ln\left(\frac{(2\mu+\hbar\omega)^2+\hbar^2\tau_2^{-2}}{(2\mu-\hbar\omega)^2+\hbar^2\tau_2^{-2}}\right), \tag{5.4}$$

where τ_2^{-1} is the relaxation rate associated with inter-band transitions. The complex dielectric function, $\varepsilon(\mu)$, can be obtained from the complex optical conductivity through the relationship:

$$\varepsilon(\mu) = 1 + \frac{j\sigma(\mu)}{\omega\varepsilon_0\delta}, \tag{5.5}$$

where δ is the graphene thickness layer, and ε_0 is the vacuum permittivity. The Fermi level is directly linked to the surface charge density, n_s, by the following relation:

$$\mu = \frac{h\nu_F}{2\pi}\sqrt{\pi|n_s|}, \tag{5.6}$$

where $h \simeq 6.62 \cdot 10^{-34} m^2 \cdot kg \cdot s^{-1}$ is Planck's constant and $\nu_F \simeq 9.5 \cdot 10^7 cm \cdot s^{-1}$ is the Fermi velocity. Graphene's charge surface density, and consequently the Fermi level, can be actively tuned by application of voltage to the capacitor structure. The applied voltage, V, required to adjust the Fermi level to a value μ can be described as:

$$|V| = \frac{en_s}{C} + 2\frac{\mu}{e}, \tag{5.7}$$

$$|V| = \frac{e}{\pi(h\nu_F)^2} \cdot \frac{\mu^2}{C} + 2\frac{|\mu|}{e}, \tag{5.8}$$

where e is the charge on an electron, and $C = \frac{\varepsilon_0\varepsilon_{ins}}{t_{ins}}$ is the capacitance per unit area, determined by insulating layer's relative permittivity, ε_{ins}, and thickness, t_{ins}.

The complex dielectric function, or consequently the refractive index, $n^2(\mu) = \varepsilon(\mu)$, determines the mode supported by the SRN waveguide structure. To facilitate interaction between a propagating mode in the waveguide and the graphene capacitor on top, the Fermi level should be tuned to a position between the valence and conduction bands. The main principle of operation for the device is the same as that for graphene optical modulators [227]; energy is transferred from photons in the propagating mode to the electrons in the graphene electrodes (photons are "absorbed"). If the Fermi level is situated above the conduction band or below the valence band, no photon absorption occurs, as either the bands are both filled (and there is nowhere for electrons to go when gaining energy) or both empty (and there no electrons to gain energy) respectively [218].

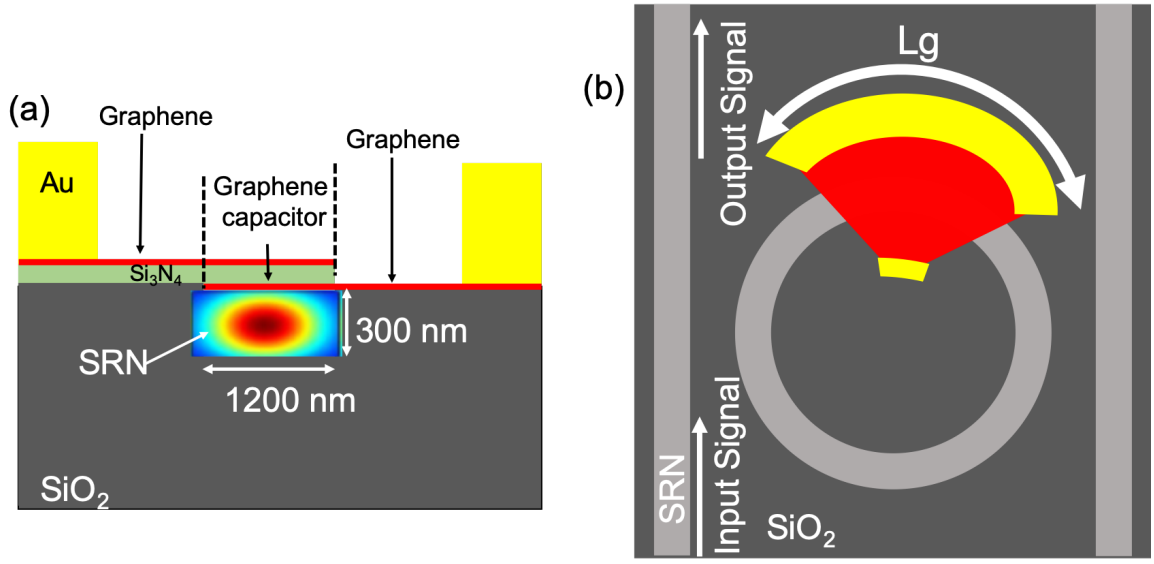

Fig. 5.2 (a) Schematic cross-section of the HWGC structure - a SRN ridge waveguide with a graphene-(Si_3N_4) capacitor on top. (b) Top view of an embedded micro-ring resonator partially covered by a graphene capacitor incorporating golden contacts for the application of a voltage to the device.

Mode Analysis

The device characteristics were simulated for a wavelength of 1550 nm and a SRN (n = 2.54) ridge waveguide cross-sectional area of 1200 x 300 nm was selected to give a single-mode integrated waveguide. By using the commercial software COMSOL Multiphysics®, the graphene capacitor structure on top of a ridge waveguide was then analysed. The profile of the propagating mode within the SRN waveguide and how this mode is affected by the graphene capacitor at different voltages was determined. This change has been quantified in terms of change of the effective refractive index $n_{eff} = n^c_{eff} + jk^c_{eff}$ experienced by the mode. A graphene capacitor consisting of a $t_{ins} = 10$ nm of Si_3N_4, ($\varepsilon_{ins} = 4$) acting as insulator between two graphene layers is considered. To achieve electro-absorption operation in the graphene capacitor, the Fermi level (μ) should reach the breakdown value of 0.5 eV (see Fig. 5.3). Through Eq. 5.6 a graphene charge density $n_s = 2 \cdot 10^{13} cm^2$ is needed in order to shift the Fermi level to μ = 0.5 eV. This corresponds to an electric field across the capacitor insulator of:

$$E_{0.5eV} = \frac{qn_s}{\varepsilon_{ins}\varepsilon_0} \approx \frac{3.6 \cdot 10^7}{\varepsilon_{ins}} \left[\frac{V}{cm}\right] \tag{5.9}$$

where ε_{ins} is the relative dielectric constant of the insulator. Eq. 5.9 determines which insulators allow device operation without reaching the dielectric breakdown limit. For example, silicon dioxide (SiO_2, ε_{ins} = 2.9 [228]), requires $E_{0.5eV} = 9.3 \cdot 10^6 \text{V cm}^{-1}$ which is close to the breakdown fields of thermal SiO_2 thin films (on the order of 10^7Vcm^{-1} [228]). Similarly, alumina (Al_2O_3 with ε_{ins} = 9 [229]) requires $E_{0.5eV} = 4 \cdot 10^6$ Vcm^{-1} , which is again very close to the reported breakdown fields of Al_2O_3 [229]. However, silicon nitride (Si_3N_4, ε_{ins} = 4 [230]) represents a suitable alternative with $E_{0.5eV} = 5 \cdot 10^6$ V cm^{-1} to be compared to a breakdown field on the order of 10^7V cm^{-1} [231].

From the mode profiles, the real and imaginary part of the mode's n_{eff}, i.e. $n^c_{eff}(\mu)$ and $k^c_{eff}(\mu)$ respectively, were calculated, for a range of Fermi levels between 0 and 0.55 eV. $k^c_{eff}(\mu)$ is equivalent to the loss coefficient $\alpha_c[dB/\mu m] = 4.34(4\pi k^c_{eff})/\lambda$. The attention on the TE mode is selected because light with this polarization interacts with the in-plane dielectric permittivity of graphene sheets, as the E-field is parallel to the graphene plane.

Fig. 5.3 (a) shows the effect on the mode's n_{eff} as the Fermi level is varied. The maximum value for the voltage is limited by the breakdown electrical field strength of the silicon nitride insulator between the two graphene layers which has a value of 11 MV cm^{-1} [231], i.e. 11 V for the thickness of 10 nm as used here. Three different regimes can be defined in terms of the loss coefficient, α_c. In Region I: for $\mu < 0.4$ eV graphene exhibits a high loss state. In Region II: for values around $\mu \sim 0.4$ eV the transition from high to low loss occurs. In Region III: for $\mu > 0.4$ eV, graphene exhibits a low loss state and acts as a quasi-transparent material. Eq. 5.8 allows to directly exchange the Fermi level values for voltage values, and thus, plot the mode's n_{eff} in terms of the voltage applied to the graphene capacitor as in Fig. 5.3 (b). In terms of the voltage: Region I: 0-4 V, OFF state, high loss (electro-refractive modulator); Region II: 4-9 V, transition state, (electro-absorption modulator); Region III V>9V, ON state, low loss (electro-refractive modulator).

Ring resonator

Among various silicon photonic device structures for multichannel applications, silicon microring resonators possess many advantages such as wavelength agility, high quality factors ($10^5 - 10^6$), high sensitivity and compact footprint. Silicon micro-ring resonators have been employed as core building blocks for optical multiplexers and demultiplexers [104–106]. The light in a micro-ring resonator is coupled from the waveguide by the evanescent field of the mode and is partially confined along the cavity sidewall by total internal reflection (TIR). The cavity field phase matches with itself upon each round trip for specific wavelengths, giving rise to an optical resonance. The resonance phase-matching condition is given as follows:

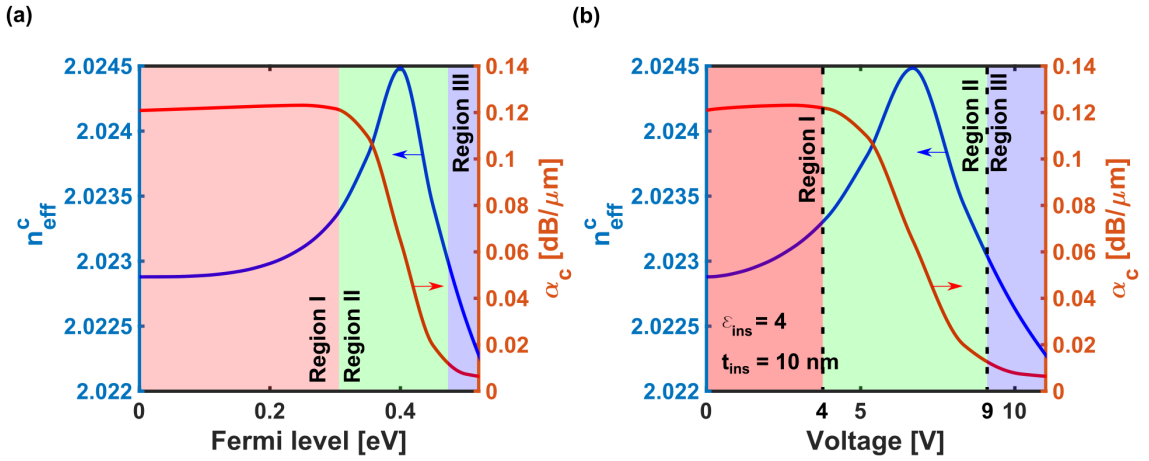

Fig. 5.3 The effective refractive index of the mode propagating in the hybrid structure made of a graphene capacitor on top of a 1.2 x 0.3 μm SRN (n=2.54) ridge waveguide, plotted against (a) the graphene's Fermi level and (b) the voltage applied to the capacitor. The graphene capacitor is made of a layer of 10 nm of (Si_3N_4) acting as the insulator between two graphene sheets. The real part of the n_{eff}, n_{eff}^c, is represented by the blue line (left y-axis) and the imaginary part (k_{eff}^c), expressed in terms of the loss coefficient, is represented by the red line (right y-axis).

$$n_{eff}L = m\lambda_m \tag{5.10}$$

where n_{eff} is the effective refractive index of the micro-ring resonator waveguide, L is the cavity round-trip length, λ_m is the m_{th} order resonance wavelength in free space, and m is the integer number of wavelengths along an optical round-trip length. In the case of a micro-ring with radius R, L is given by $2\pi R$. By positioning the graphene capacitor on top of the ring resonator, as shown in Fig. 5.2 (b), the n_{eff} of the microring can then be modified by applying a voltage across the graphene capacitor (see Fig. 5.3 (b)). The change in n_{eff} allows the reconfigurability of the ring resonator resonances [232]. A Transfer Matrix Method (TMM) [153] was used to model the performance of reconfigurable micro-ring resonators with a gap between the waveguide and the rings of 300 nm.

5.1.2 Graphene modulator performance

Passive tuning

In addition to the active tuning already discussed, a passive tuneability of the devices is inherent in the fabrication process. By choosing the length of the graphene capacitor

structure (L_g), the effective refractive index of the ring can be further tuned. The choice of this parameter is crucial because it cannot be modified after fabrication, contrary to the actively tunable voltage mechanism. By increasing the length of the capacitor, the degree of interaction between the mode and the capacitor structure increases. This causes a shift in the resonance of the ring resonator structures as shown in Fig. 5.4 (a). In terms of the spectral response, increasing the length of the graphene capacitor gives rise to a red shift of the ring resonator resonance. In Fig. 5.4 (b) the resonance shift produced by the different capacitor lengths with the corresponding extinction ratio achieved for given dimensions of the capacitor is shown. For example, a 6.4 nm shift can be achieved using a graphene capacitor that covers 25% of the ring resonator. Different voltages V_{ON} and V_{OFF} are used to tune the extinction ratio (ER) of each of the graphene capacitor lengths individually. Fig. 5.4 (b) also shows how the difference in the extinction ratio between the ON and OFF states decreases when the length of the capacitor increases for the same ring resonator radius ($R = 65\mu$m).

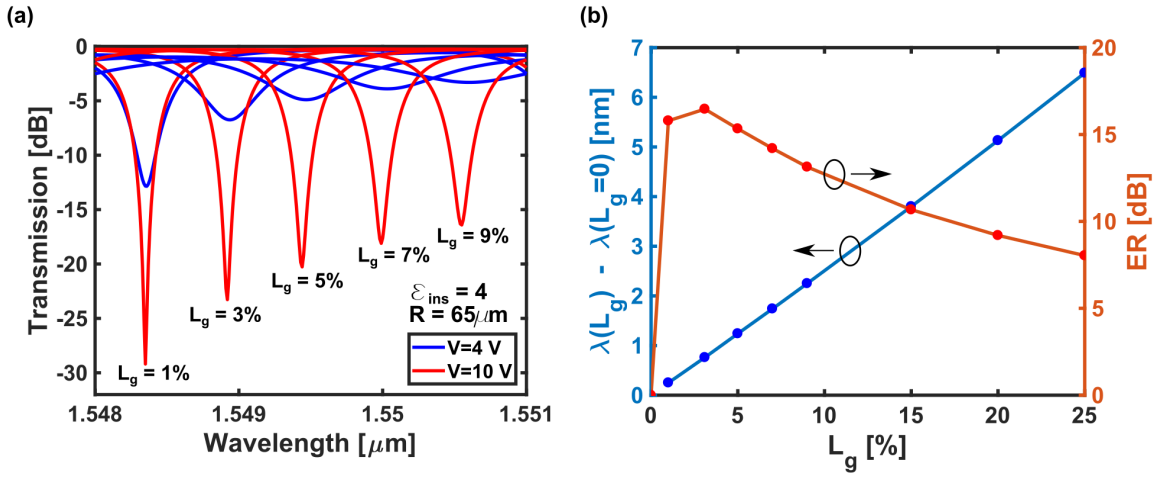

Fig. 5.4 (a) Resonant wavelength as a function of the length of graphene capacitor for a fixed ring resonator radius ($R = 65\mu$m). (b) Resonant wavelength shift produced by the graphene capacitor for different lengths (blue) and extinction ratio difference achieved for different graphene capacitor length (red).

Graphene enabled high performance computing

Exploiting the electro-absorption effect of the graphene capacitor modulator (Region II: 4V - 9V) to tune the imaginary part of the n_{eff} of graphene paves the way for photonic volatile multi-level memory and optical routing. The proposed device is based on SRN micro-ring resonators placed as add-drop filters with a single input waveguide and N output waveguides, with N being, the number of micro-ring resonators. An example with $N = 3$

is depicted in Fig.5.1. The operation of the device is based on controlling the transmission for each of the channels by tuning the voltage of the individual HWGC structures. A device consisting of three ring resonators with ring radii of R_1=70 μm, R_2= 65 μm and R_3=60 μm is considered. Different resonant frequencies ($\lambda_1 = 1.55497$ μm λ_2 =1.55475 μm and $\lambda_3 = 1.55451$ μm) are resonantly coupled to each ring respectively. The voltage-dependent transmission measured through the input waveguide is plotted in Fig. 5.5 (a) for the three ring resonators. A state of high transmission through the input waveguide corresponds to a low transmission from the output waveguide (OFF state). The OFF state can be defined as a 0-bit. A state of low transmission through the input waveguide corresponds to a high transmission from the output waveguide (ON state). The ON state can be defined as an 1-bit. Therefore, a 0 or 1 in the output bus waveguide of each channel will be measured depending on the voltage applied to the corresponding HWGC. Three ring resonators are used with two possible states each; hence 2^3 possible configurations can be achieved. The 2^3 possible codifications are shown in Fig. 5.5 (b). The number of combinations can be increased by increasing the number of ring resonators. This presents a trade-off between the number of combinations and the footprint of the device. SOI waveguides can increase the number of rings in a smaller footprint (higher density) of the proposed device, but the interaction between the mode and the graphene capacitor will be smaller due to the strong confinement of the modes. SRN can allow a greater interaction with the graphene capacitor than silicon and at the same time can confines the mode more strongly than (Si_3N_4). Using SRN, the distance (d_s), as shown in Fig. 5.6, can be reduced compared with Si_3N_4 allowing faster devices and smaller footprint while maintaining the same ER.

Electrical simulations

In order to calculate the speed of the device and the time response, an equivalent RC circuit as shown in Fig. 5.6 (a) is defined. The time response of the RC circuit can be calculated using $V(t) = V_0 e^{-t/\tau}$ where $\tau = RC$ [Fig. 5.6 (b)] and the speed of the device can be calculated using the response bandwidth, which is determined by:

$$Bdw = \frac{1}{2\pi[2(R_c + R_s)] \cdot C} \tag{5.11}$$

where R_c and R_s are the contact and sheet resistances of graphene respectively, and C is the capacitance of the device. The contact resistance of graphene emerges from the Fermi level mismatch between the graphene and the metallic electrodes. This parameter depends on the quality of the graphene and the metal selected for the electrode [233]. Experimental results have previously shown values of the contact resistivity (ρ_c) in the range of 100 to 1000

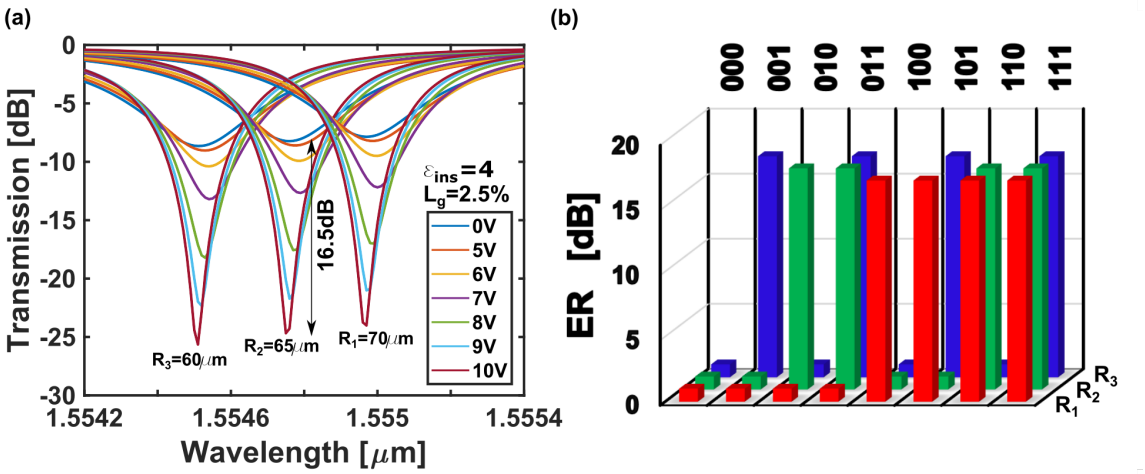

Fig. 5.5 (a) Transmission at the input waveguide for three different ring resonators with radii R_1=70 μm, R_2=65 μm and R_3=60 μm and different voltages applied individually to each of the rings. (b) Binary coding combinations obtained by individually tuning each ring resonator graphene capacitor. The extinction ratio difference (ER) between the ON and OFF states at the output waveguides for each of the individual ring resonators (R_1, R_2 and R_3) allows one to code 2^3 combinations.

$\Omega\mu m$ [234, 235]. The total contact resistance of graphene is calculated as $R_c = \rho_c/L_g$. The graphene's sheet resistance, is usually defined by the resistance per square, R_{SQ}. The values of R_{SQ} for graphene are typically between 100 and 500 Ω/sq [236–238], in all calculations, a conservative value of 500 Ω/sq is considered. To obtain the total sheet resistance of graphene, the contribution of all the squares constituting the device should be taken into account. The total sheet resistance can be expressed as $R_s = R_{SQ} \cdot \frac{d_s}{L_g}$. The width of the graphene capacitor is selected to be d_c=1.2 μm entirely covering the waveguide as shown in Fig. 5.6. Using a (Si_3N_4) waveguide, the distance between the gold contacts is selected to be 1 μm to ensure that the metal does not contribute to the losses. A bandwidth response of 12.5 GHz has been calculated in this case. Using SRN as the waveguide material instead of Si_3N_4, the contacts can be closer to the waveguide (400 nm) without affecting the mode propagation (see Fig. 5.7 (a)), reducing by 600 nm the distance between the graphene capacitor and the golden contact compared with Si_3N_4. Consequently, R_s is reduced and the calculated device bandwidth increases to 15.6 GHz. For the best case scenario of contact resistance ($\rho_C = 100\ \Omega\ \mu m$) maintaining a conservative value in the sheet resistance ($R_{SQ} = 500\Omega/sq$), the bandwidth will increase up to 31.2 GHz and 62.41 GHz for Si_3N_4 and SRN respectively (see Fig. 5.7 (b)). Examining Eq. 5.11 one can observe that when the capacitance and resistances are multiplied, the length of the device L_g is cancelled out; therefore, the length of the device has no impact on the response bandwidth and only influences the insertion losses (IL). The IL

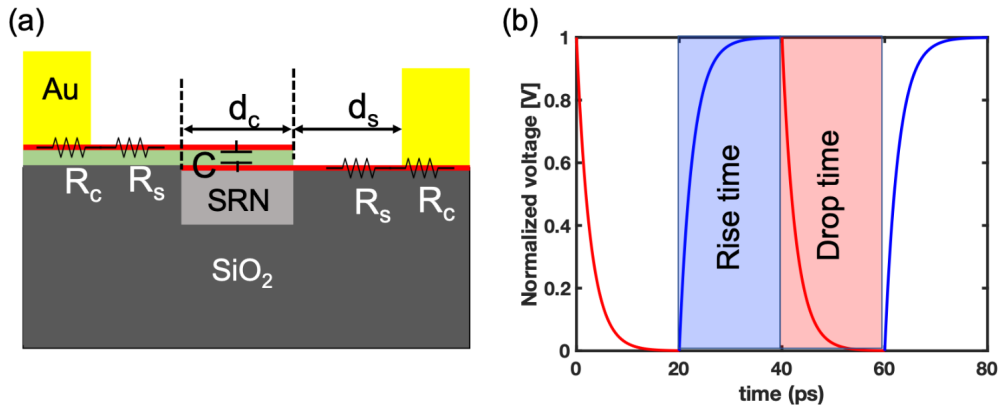

Fig. 5.6 (a) HWGC cross-section showing the defined equivalent circuit of the graphene capacitor and contacts where R_c, R_s are the contact and the sheet resistance respectively and C is the capacitance. d_c is the graphene capacitor width and d_s is the distance between the contacts and the waveguide. (b) Time response of the HWGC.

per unit length of our graphene capacitor devices are 0.13 dB/μm and 0.01 dB/μm for the OFF and ON states respectively (shown in Fig. 5.3).

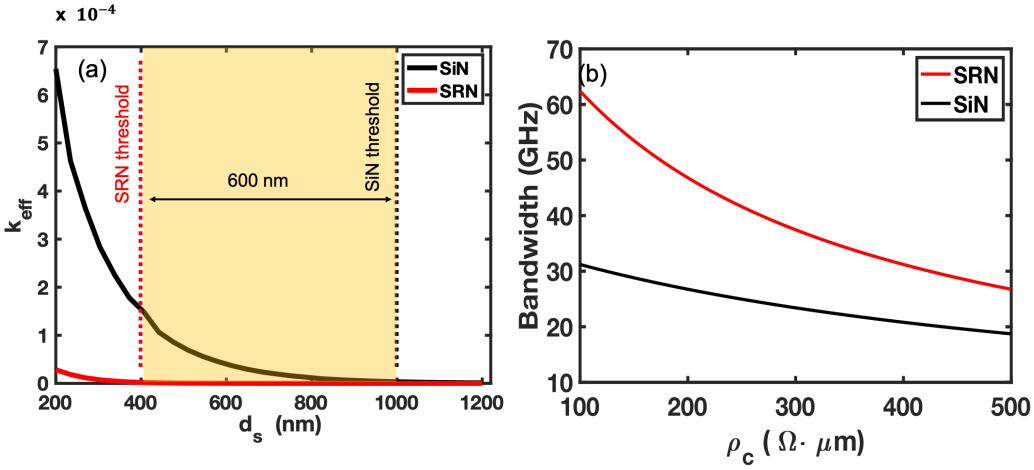

Fig. 5.7 (a) Parametric sweep study of the k_{eff} in the mode against the distance between the contact and the graphene capacitor (d_s) for values between 200-1200 nm for Si_3N_4 (black line) and for Silicon Rich Nitride (SRN) (red line) (b) Parametric sweep study of the contact resistance for Si_3N_4 platform (black line) and for SRN (red line). The ridge waveguide dimensions are 1200 nm width and 300 nm thick.

Energy consumption

The average energy consumption of the devices, expressed as energy per bit, is given by the formula:

$$E_b = \frac{1}{4}CV^2 = \frac{1}{4}\frac{\varepsilon_0\varepsilon_{ins}}{t_{ins}}L_g \cdot d_c \cdot [V_{ON} - V_{OFF}]^2 \tag{5.12}$$

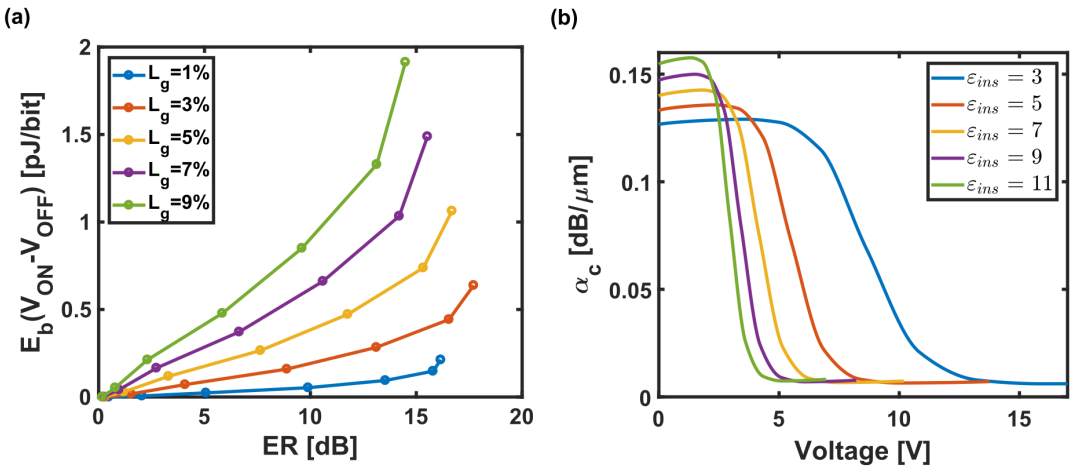

Fig. 5.8 (a) Plot of the energy per bit against the Extinction Ratio (ER) between the ON and OFF state achieved for different lengths of the graphene capacitor. For each curve, each circle marker corresponds to a different value of V_{ON} used for the ON-state, at 1 V intervals; with the first marker representing 5 V and the last one 11 V. In all cases, the values used for the OFF-state is $V_{OFF} = 4$ V. (b) The loss coefficient α_c of the guided mode along the HWGC structure against the operating voltage. Several curves are plotted for different values of the dielectric constant of the insulator between the plates of the capacitor, ε_{ins}.

In the proposed device, the graphene capacitor lengths for each ring resonator are $L_{g1} = 10.9956\ \mu$m, $L_{g2} = 10.2102\ \mu$m and $L_{g3} = 9.4248\ \mu$m. The energy consumptions per bit (E_b) for each ring resonator (R_1, R_2 and R_3) respectively are $E_{b1} = 0.2921$ pJ/bit, $E_{b2} = 0.2712$ pJ/bit and $E_{b3} = 0.2503$ pJ/bit, respectively. The energy per bit can be reduced by either: reducing the thickness of the insulator (but that will increase the capacitance and reduce the speed of the device); or increasing the permittivity of the graphene capacitor insulator, as indicated in Fig. 5.8 (b). By increasing the permittivity the difference between the ON and OFF voltages is reduced. From Eq. 5.12 it can be seen that the voltage dependence is quadratic whereas the permittivity dependence is linear, giving the overall effect that E_b will be reduced. The relation between the energy consumption per bit of the device and the extinction ratio achieved for different graphene capacitor lengths is shown in Fig. 5.8 (a). The behaviour of the threshold voltage for different insulator permittivities is shown in Fig. 5.8

(b). Increasing the insulator permittivity, the threshold voltage is reduced and paves the way to lower power consumption devices for future reconfigurable photonic integrated circuits in optical communications applications. The devices' IL due to the graphene capacitor are around 1.3 dB in the OFF-state and 0.1 dB in the ON-state.

5.2 Optical GST memory based on graphene micro-heaters

Reconfigurability of different photonic integrated circuits (PICs) is attracting more attention due to the growing demand on photonic-electronic integrated systems [148]. Neuromorphic computing [147], microwave photonics [239, 240] , and quantum computing [241, 242] are using silicon photonic building blocks as the key component to achieve high density, scalable, and different photonic functionalities in the same chip. Different materials are emerging as possible switching materials on chip (as discussed in the introduction). Most of these technologies are volatile with switching mechanism being thermo-optic (T-O) or electro-optic (E-O), while the change in the refractive index between states is relatively small ($\Delta n \sim 0.21$). Using non-volatile chalcogenide phase change materials, the refractive index difference can be achieved as high as $\Delta n \sim 2$. PCMs are currently being used inside photonic integrated circuits in order to manipulate light and create non-volatile optical switches and memories [243]. However, PCMs based photonic integrated circuits required optical amplifiers off chip in order to switch the phase of the material on chip optically. Previously, reversible phase transitions of PCMs on PICs have been demonstrated by free space optical heating, on-chip optical heating, or electrical threshold switching. Free-space optical heating [244, 245] by far-field focused laser pulses is not viable for large-scale integration due to the slow, diffraction-limited, inaccurate alignment process [148]. On-chip optical heating [243, 39, 246, 247], assisted by evanescent coupling of near-field optical pulses from waveguides to PCMs, can support fully integrated all-optical operations but has difficulty in switching large-area PCMs and complex light routing, leading to limited switching contrast and system complexity. Both optical heating approaches also suffer from the low extinction coefficient or weak photo-thermal effect of the amorphous state in the re-crystallization process [248, 249]. Whereas classical electrical threshold switching [144] allows large-scale integration, the limited phase transition volume due to the crystallization filamentation [250] and nonuniform heating is not suitable for photonic applications. Recently, electrical switching with external heaters [251–253] has shown promising results in PCM-integrated photonics. However, in these demonstrations, a large insertion loss is incurred due to the use of indium tin oxide

(ITO) heaters [251, 252] or uniformly doped silicon heaters [253]. In order to overcome these drawbacks and make this technology scalable, an integrated rib silicon waveguide with phase change material based on thermally switching has been recently demonstrated in silicon-on-insulator (SOI) platform using in-situ silicon PIN heaters [254] with near-zero additional loss (~ 0.02 dB/μm).

Si_3N_4, SiO_2 and a variety of passive integrated circuits platforms can not be doped using phosphorous or boron and they require a different approach for switching the PCM state in order to make the non-volatile integrated photonics technology scalable in these passive platforms. One possible solution is the use of graphene micro-heaters to control the temperature of the phase change material, allowing the switching between amorphous and crystalline state repetitively, and consequently, control the optical properties of the thin film phase change material cell. Graphene's large thermal conductivity [255] and optical transparency [256] overcome the drawbacks presented by conventional metallic microheaters, which presents losses of hundreds of dB/mm when they are positioned in the vicinity of photonic integrated components [257]. In this section, a complete graphene micro-heater design, deposited on top of a rib silicon nitride waveguide is shown. Different electrical pulses are applied across the CVD graphene layer to be able to control the PCM cell temperature [Fig. 5.9].

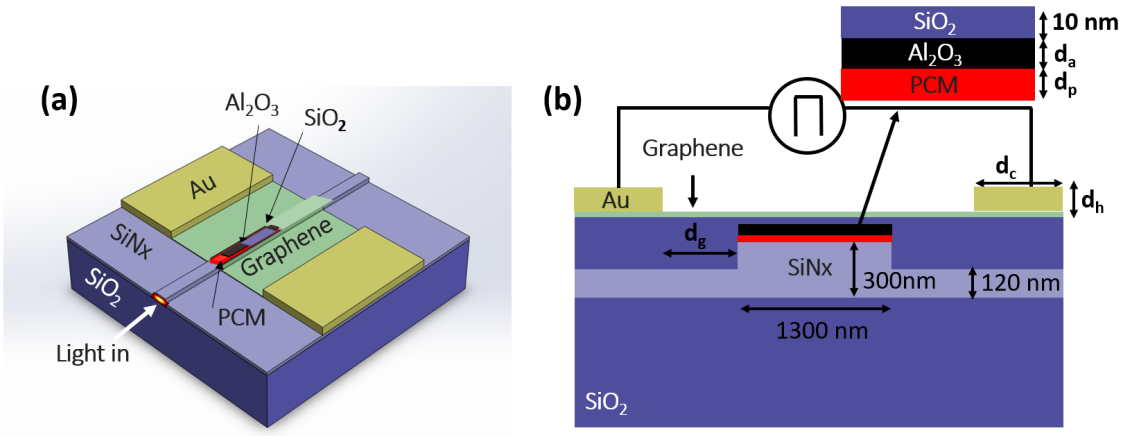

Fig. 5.9 (a) Integrated graphene micro-heater schematic. (b) Cross-sectional view of the graphene micro-heater deposited on top of a rib silicon nitride waveguide with width and thickness of 1300 and 300 nm respectively, the rib thickness is set to 120 nm. Under the graphene micro-heater, a thin layer of aluminum oxide (Al_2O_3) and a thin layer of PCM, all capped by 10 nm of SiO_2 to avoid oxidation are placed.

5.2.1 Design and modelling

A coupled electro-thermal 2D finite element method model using COMSOL Multiphysics® to simulate the thermal response of the graphene micro-heater has been used. The multiphysics coupling is a Joule heating effect, where the flow of electrical current through a conductive material leads to heat generation which lead to a rise in temperature. The simulation comprises an elecric current module, which is based on Poisson's and current continuity equations to predict the electric potential, current density, and carrier density distributions

$$\nabla \cdot \mathbf{J} = \frac{\partial \rho}{\partial t}, \quad \mathbf{J} = \sigma \mathbf{E} + \frac{\partial \mathbf{D}}{\partial t} \tag{5.13}$$

where $\mathbf{J}$ is the current density expressed as the sum of the conduction and displacement current density, ρ is the electric charge density, σ represents the electric conductivity, $\mathbf{E}$ is the electric field vector, and $\mathbf{D}$ is the electric displacement. In this case, the only boundary conditions used are the values of the voltage in the outer boundaries of the model. A heat transfer module is also utilized and is based on the heat transfer equation:

$$\delta C_p \frac{\partial T}{\partial t} = \nabla(k \nabla T) + Q \tag{5.14}$$

where C_p is the heat capacity, k, the thermal conductivity, δ, is the mass density, and Q is the heat source. The design consists of a silicon nitride $(n = 2.01)$ rib waveguide, 300 nm thick and 1300 nm wide. The rib thickness is set to 120 nm. A thin film of PCM and a thin film Al_2O_3 layer (deposited on top of the PCM) capped with 10 nm silicon dioxide layer to avoid oxidation [Fig. 5.9 (a)] are placed above the waveguide. Finally, a CVD graphene layer is placed on top of the silicon oxide acting as micro-heater.

In order to optimize the micro-heater design, a parametric sweep of the geometry structure has been evaluated. The geometrical parameters are: the distance between the gold contacts and the silicon nitride rib waveguide core (d_g), the contacts thickness (d_h) and the contacts width (d_c) [Fig. 5.9 (b)]. All the electrical and thermal properties of the different materials used in the simulation are presented in table 5.1.

5.2.2 Performance study

Different electrical pulses are applied through the top single layer graphene in order to control the temperature in the phase change material cell. An example as concept illustration is shown in Fig. 5.10 (a), where a peak pulse of 10 V with 10 μs pulse width (right axis, solid red line), and the temperature reached in the centre of the PCM cell (left axis, solid blue

Property	Graphene	SiO_2	Si_3N_4	a-GST	c-GST	Al_2O_3
C_p (J $kg^{-1}K^{-1}$)	2082	703	673	213	199	900 [258]
k ($Wm^{-1}K^{-1}$)	3000	1.38	10	0.19 [259]	0.5 [259]	30 [260]
σ (Sm^{-1})	$1.79{\cdot}10^5$	$1.1{\cdot}10^{-14}$	$2{\cdot}10^{-12}$	-	-	-
n	*	1.444	2.01	3.94 + j 0.045	6.11 + j 0.83	1.5886
δ (kgm^{-3})	2267 [261]	2203	3000	5870	6270	3100

Table 5.1 Thermal and electrical properties of the different materials used in the simulations. (*) Graphene optical properties are taken from eq. 5.5 described previously.

line) are presented. In Fig. 5.10 (b), a temperature dependence with the peak pulse in time is shown.

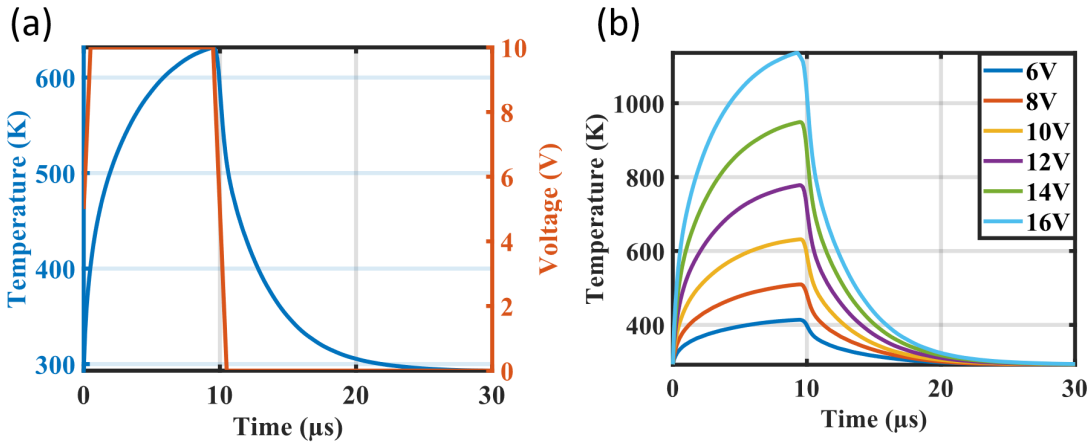

Fig. 5.10 (a) Temperature in the centre of the PCM cell for an electrical pulse of 10 V peak and 10 μs width (b) Temperature in the centre of the PCM cell for different values of the electrical pulse power.

Micro-heater contacts optimization

First, a complete study in how the graphene micro-heater geometry affects the temperature of the phase change material cell when a 10 V peak pulse is applied trough the graphene layer is presented [Fig. 5.11]. Different values of the contact geometry, specifically, d_g and d_h, have been evaluated to obtain the difference in the temperature in the centre of the PCM cell. The minimum value for the separation between the contacts and the silicon nitride rib waveguide core (d_g) is fixed to 1 μm in order to not generate high losses in the mode due to metal proximity, as explained in the previous section. In Fig. 5.11 (a), different distances between the contacts and the rib waveguide core are explored, the distances, d_g, are ranging between 1 μm and 4 μm. In Fig. 5.11 (b), different contact thickness are explored. The thickness values range

from 30 nm up to 100 nm. Both figures indicate that the maximum temperature reached in the centre of the phase change material cell has not a linear dependence with the distance, d_g, or thickness, d_h. A stronger temperature dependence with the distance between the contacts compared with the thickness is demonstrated. The maximum temperature (T_{max}) dependence shows a quadratic behaviour for both cases in the explored range as can be seen in Figs. 5.12 (a-b). From the fitted curves, an analytic expression for the maximum temperature (T_{max}) reached in the centre of the PCM cell (in the studied range) for the contact geometry dependence can be obtained

$$T_{max} = 25.16 d_g^2 - 202.7 d_g + 802.4 \tag{5.15}$$

$$T_{max} = 1.6 \cdot 10^{-3} d_h^2 - 0.3534 d_h + 659.8 \tag{5.16}$$

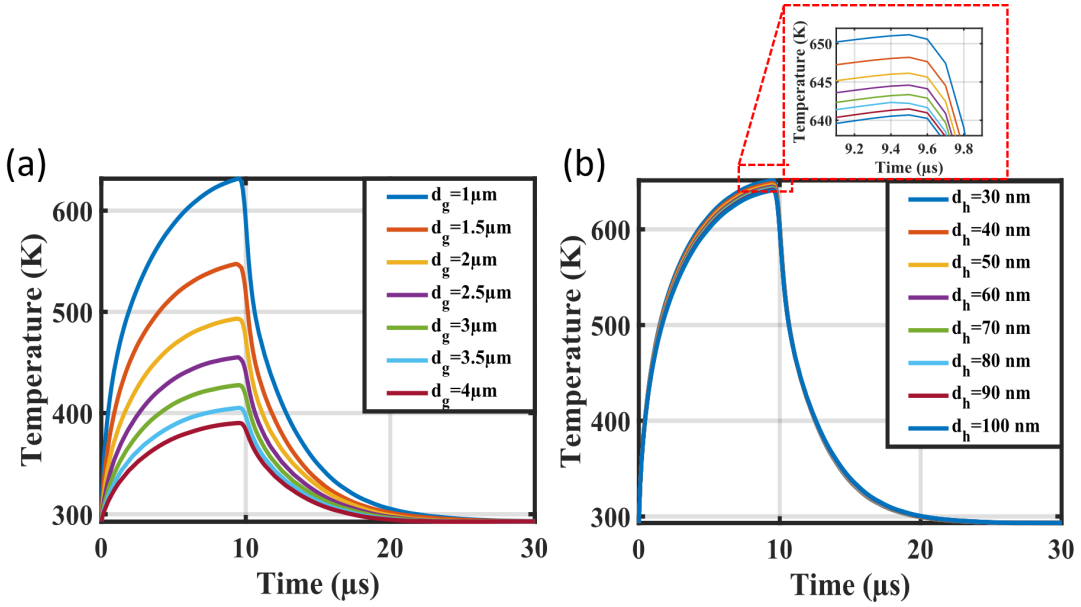

Fig. 5.11 Time temperature dependence in the central part of the PCM cell for different golden contacts geometrical parameters is shown, (a) for different distances between the core waveguide and the contact (d_g) and (b) for different golden contact thickness values (d_h).

The contact parameters are selected to be d_g = 1 μm and d_h = 30 nm to get the maximum temperature in the phase change material cell using the lower voltage peak pulse possible to reduce the energy consumption of the device.

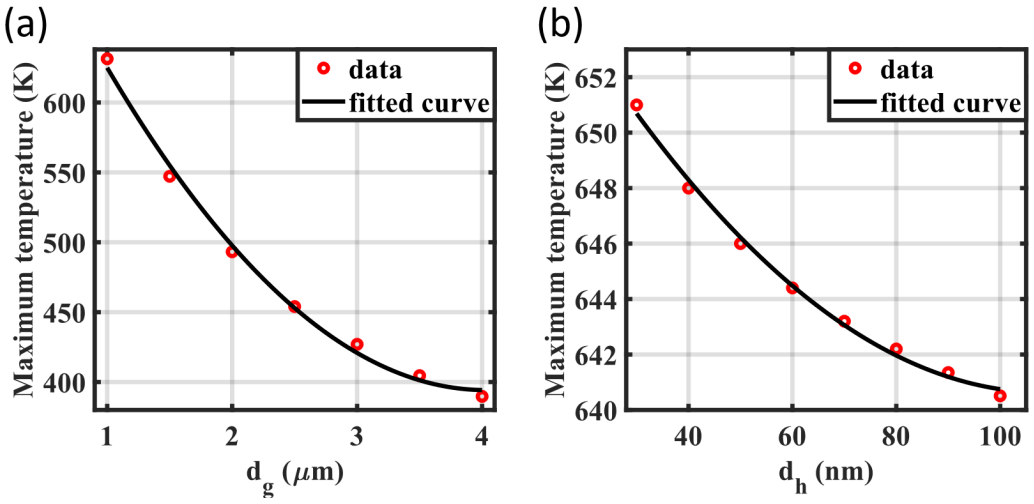

Fig. 5.12 Maximum temperature reached in the PCM cell for (a) different contact distances (d_g) and (b) different contact thickness (d_h).

Optical memory

In order to select the pulse peak and the pulse width to crystallize (Set process) the PCM, the electrical pulse should be long enough and with enough power to ensure that the GST was heated above its glass transition temperature (T_g) but below the melting point (T_m). The nucleation of small crystallites and subsequent growth can, therefore, proceed, leading to an elevated refractive index (n) and extinction coefficient (k) of the GST and a reduced optical transmission of the device after the pulse. The programming speed in a phase change cell relies on the kinetics of crystallization in the pulsed regime. As demonstrated in Ref. [262], the crystallization temperature that needs to be reached in the PCM cell for having a faster crystallization process is around 670 K. In the structure presented here, the voltage utilized is 13V peak and 5 μs pulse width with 100 ns falling time [Fig. 5.13].

For the re-amorphization (Reset process), a single pulse with a short falling edge and smaller pulse width should be utilized to melt the GST and then rapidly quench it below T_g, forming the disordered glass state with low optical absorption and increased optical transmission of the device after the pulse. This glass transition from molten state is a rather complicated process that has yet to be completely understood [263]. The overall switching period is then determined by the pulse width as well as the dead time due to the thermal relaxation. A pulse width of 50 ns with 2 ns falling time and 35 V pulse peak is applied in order to achieve re-amorphisation with a cooling rate of 5 K ns^{-1}, which is in the order of cooling rates needed to melt-quench GST into its amorphous phase [Fig. 5.14].

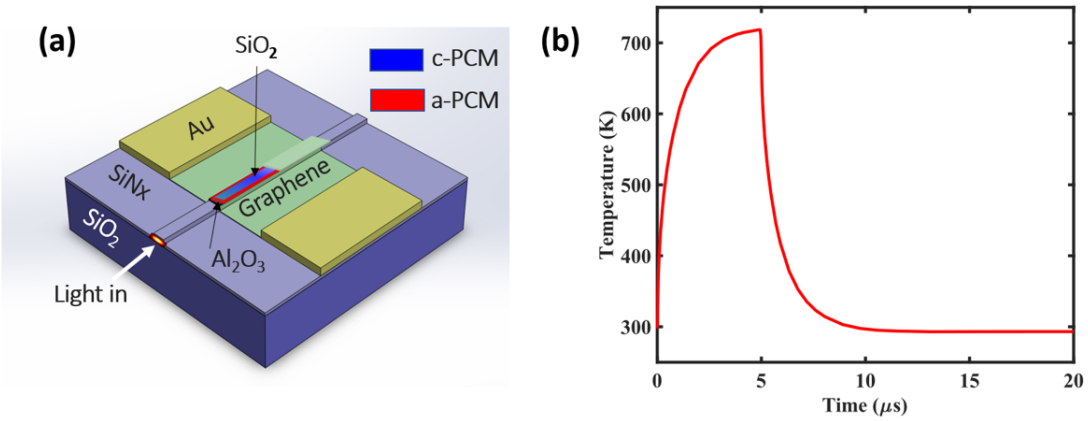

Fig. 5.13 (a) Set process schematic. (b) Temperature reached in the centre of the PCM cell for an electrical pulse of 5 μs pulse width and 13 V pulse peak.

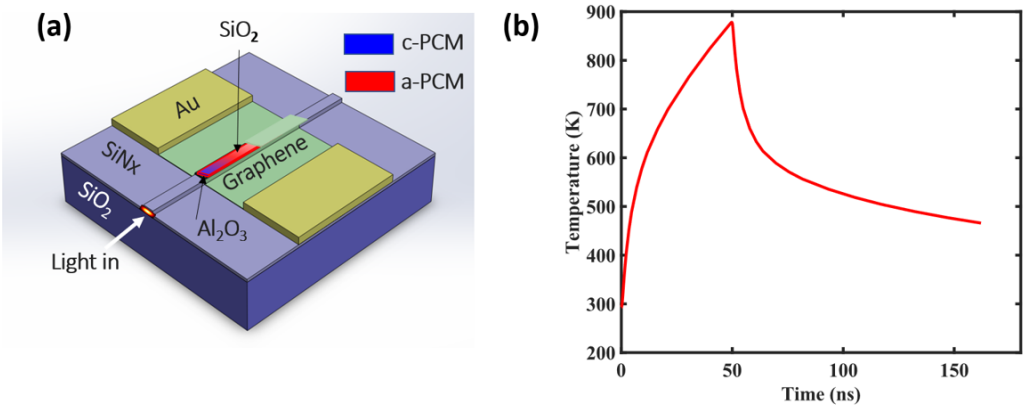

Fig. 5.14 (a) Reset process schematic. (b) Temperature reached in the centre of the PCM cell for an electrical pulse of 50 ns pulse width and 35 V pulse peak.

Energy consumption

In order to estimate the power consumption of the device, the approach followed in Refs. [264, 265] are taken. The power consumption due to the heat is

$$P_h = V^2/R_{total} \tag{5.17}$$

in this case

$$R_{total} = R_{graphene} + 2 \cdot R_{contact} = \frac{R_s L_g}{w_a} + \frac{2R_c}{w_c} \tag{5.18}$$

where the total power consumption is

$$P_h = \frac{V^2}{\frac{R_s L_g}{w_a} + \frac{2R_c}{w_c}} \tag{5.19}$$

and finally, the energy consumption is

$$E = P_h \cdot \Delta t \tag{5.20}$$

where Δt is the pulse width and the energy consumption is evaluated to be 2 μJ and 0.13 μJ for the crystallization and amorphisation process respectively.

5.3 Summary

The potential of a graphene capacitor structure on SRN micro-ring resonators for multitasking and HPC have been shown. The electro-absorption effect can be used to develop multilevel volatile memories for communications applications, optical routing and binary coding. By tuning the capacitor length, a shift in the resonant wavelength is produced giving rise to a broadband multilevel photonic volatile memory. An increase in the device speed has been shown to be achieved by using a silicon rich nitride (SRN) waveguide in place of Si_3N_4, due to the increased confinement of the propagating mode allowing a smaller device footprint.The possibility to double the speed of the devices from 31.2 GHz up to 62.41 GHz in this way has been demonstrated. A study of the relation between the device energy consumption, extinction ratio and capacitor length has been shown. Finally, it has been demonstrated that increasing the permittivity of the insulator layer in the capacitor structure, the energy consumption per bit can be reduced.

Furthermore, a graphene heater has been employed on top of a rib silicon nitride waveguide in oder to create an optical memory using electrical pulses to set or reset the phase change material cell to control the transmission. The energy consumption of the optical memory is 2 μJ and 0.13 μJ for the crystallization and amorphisation process respectively.

Chapter 6

Phase-change integrated silicon nitride photonic devices in the O and C telecommunications bands

6.1 Overview

Different technological applications of PCM-based devices such as switches [139], wavelength division multiplexers [141], directional couplers [142], memories [143, 144, 141, 145] and neuron and synapse mimics [146, 147] have been already demonstrated, all operating in the C-band range of the spectrum and using $Ge_2Sb_2Te_5$ phase-change cells. Recently, an O-band nitrogen rich silicon nitride Mach–Zehnder interferometer has been demonstrated in Ref. [140]. The contrast between the phase-change optical material properties (n and k) is used as the key component for phase-change photonic device operation and the values used for the films in this paper are as in Fig. 6.1, obtained by ellipsometric measurements.

Photonic integrated circuit applications are mainly conducted in the wavelength region where optical fibers have low transmission loss. This low-loss wavelength region ranges from 1260 nm to 1625 nm, and is divided into five wavelength bands referred to as the O-, E-, S-, C- and L-bands. The O-band, ranging from 1260 nm to 1360 nm, stands for the original band. It was "originally" considered as the primary wavelength band used for optical communication in the mid 1970s because silica glass has a zero-material dispersion wavelength in the O-band, and thus it was expected that signal distortion, arising from fiber chromatic dispersion, would be minimized. Even though optical fiber manufacturing technology has improved and nearly achieved the elimination of water molecules, moving the lowest attenuation to the C-band, the O-band is still in extensive use for optical communication, mainly because

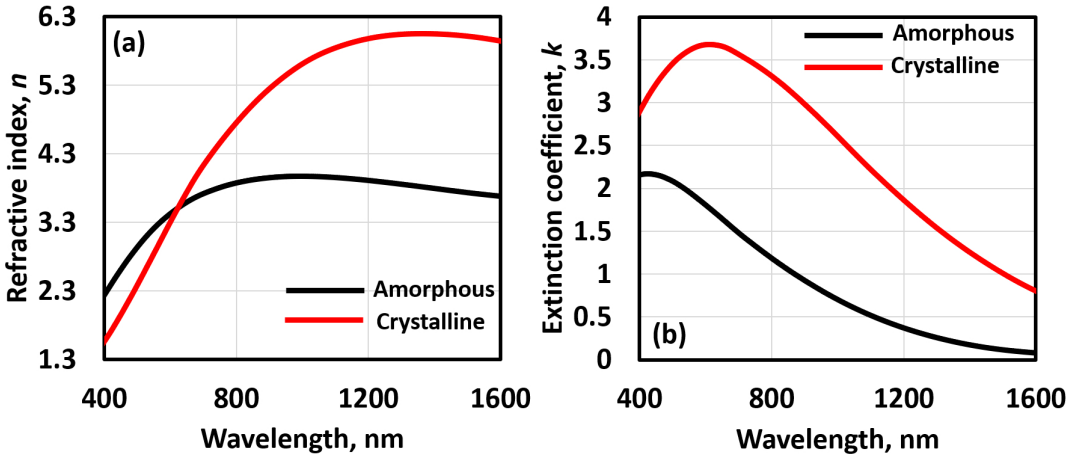

Fig. 6.1 (a) Refractive index, n, and (b) extinction coefficient, k, ellipsometry measurements in amorphous (solid black lines) and crystalline (solid red lines) state for $Ge_2Sb_2Te_5$ (GST).

optical communication systems that do not require dispersion-compensation schemes offer advantages in both the initial investment (lower transceiver price) and operation cost (lower power consumption), both key requirements for a data center where high-speed Ethernet is heavily used.

The C-band (conventional band: 1530-1565 nm) is commonly used in many metro, long-haul, ultra-long-haul optical transmission systems combined with wavelength-division multiplexing (WDM) and erbium-doped fiber amplifier (EDFA) technologies. The C-band is favored for long-distance transmission because the attenuation of modern optical fiber has its minimum in the C-band, as discussed previously. The current lowest loss of optical fiber is 0.14 dB/km at 1560 nm, reported in 2018 [266, 267].

In this chapter, an experimental evaluation and comparison of the optical properties in the O and C bands of silicon nitride rib waveguides with integrated $Ge_2Sb_2Te_5$ phase-change cells is reported, with a view to possible future applications in both ranges of the spectrum. Furthermore, ring resonators with $Ge_2Sb_2Te_5$ (GST) deposited on top of the ring structure and used to turn ON or OFF the resonance are reported in both bands, demonstrating the building blocks for potential future application in opto-electronic oscillators (OEO) [268], frequency combs [269], multifunctional reconfigurable photonic integrated circuits (PICs) [270], or arbitrary radiofrequency waveform generators (AWG) [271].

6.2 Design

6.2.1 O-band

In the O-band, the optical platform consists of a Si_3N_4 $(n = 2.01)$ rib photonic waveguide. The rib width and inner height are designated as W = 900 nm and H= 300 nm respectively, and the outer region of the rib has a thickness of $H - h$ = 120 nm, see Figs. 6.2 (a-b). This waveguide geometry enables mode propagation in the O-band (both TM and TE) with losses (<1 dB/cm). TE polarization was selected in this work due to the grating couplers' fabrication optimization and the stronger mode interaction with the PCM cell compared with the TM mode.

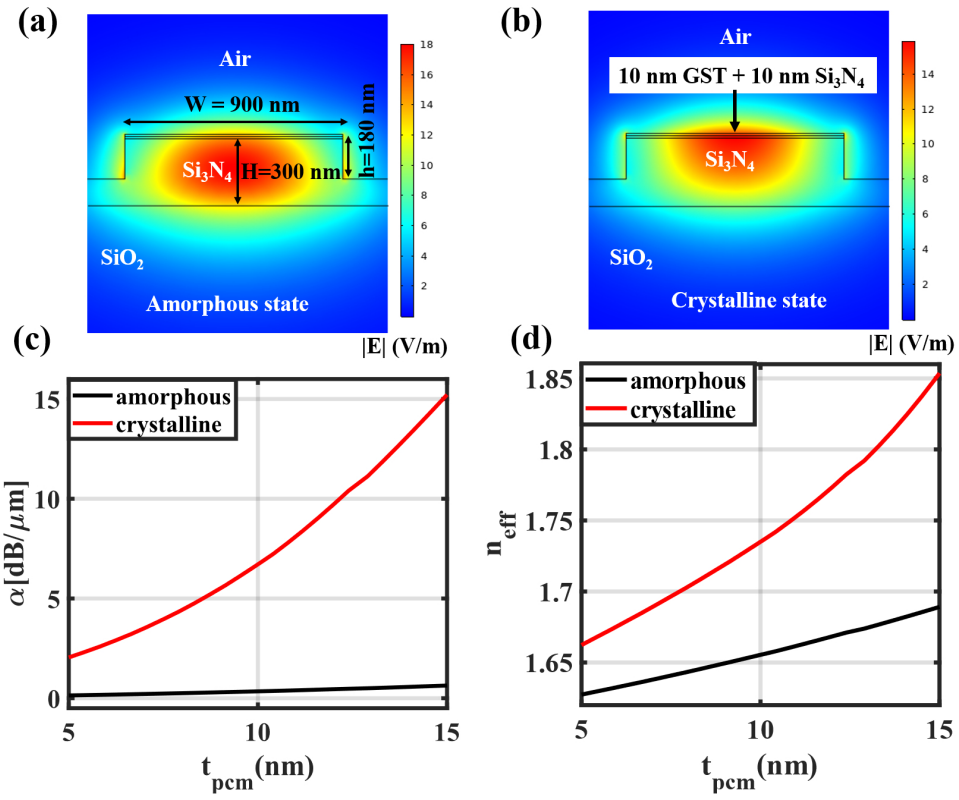

Fig. 6.2 Eigenmode simulation of the fundamental TE optical mode of a rib silicon nitride waveguide at 1310 nm wavelength, with a GST thin layer cell on top in the (a) amorphous state (b) crystalline state; (c) mode attenuation and (d) effective refractive index both as a function of PCM layer thickness.

A phase-change material cell was deposited on top of the rib waveguide in order to make

the passive building block tunable. The tunability consists of controlling the losses of the waveguide by switching the PCM layer between its amorphous and crystalline states. The thickness of the cells was selected to be 20 nm, comprising a 10 nm PCM ($Ge_2Sb_2Te_5$) layer, capped with 10 nm of Si_3N_4 to prevent oxidation. In order to achieve a good contrast (distinguishable difference in attenuation between the amorphous and crystalline states of the phase change material cell) while at the same time maintaining a good signal-to-noise ratio in the output optical signal of the waveguide, a 10 nm thick PCM layer was selected for the devices which, as can be seen in 6.2 (c-d), provides a good trade-off between contrast and output signal level. COMSOL Multiphysics® was used to calculate the effective refractive indices and the cell absorption in both states of the PCM (amorphous and crystalline), see Figs. 6.2 (a-b). The attenuation constant (α) and the effective refractive index (n_{eff}) of the structure strongly depend on the thickness of the PCM layer (t_{pcm}) as shown in Figs. 6.2 (c-d); a thickness of 10 nm was selected as it provides a good balance between attenuation and total transmission in the device between states. The optical constants used in the simulations at 1310 nm can be found in Fig. 6.1.

6.2.2 C-band

In the C-band, the optical platform consists of a Si_3N_4 ($n = 2.01$) rib photonic waveguide. The rib width and inner height are designated as W = 1300 nm and H= 300 nm respectively, and the outer region of the rib has a thickness of $H - h$ = 120 nm, see Figs. 6.3 (a-b).

This waveguide geometry enables mode propagation in the C-band (both TM and TE) with losses (<1 dB/cm). The phase-change cell deposited on top of the waveguide is identical to that described above for the O-band, and COMSOL Multiphysics® was again used to calculate the effective refractive indices and the cell absorption in both states of the PCM (amorphous and crystalline). As in the O-band, the absorption (attenuation) and the phase shift (effective index) induced by the phase change material strongly depend on the thickness of the PCM layer (t_{pcm}), as shown in Figs. 6.3 (c-d). The optical constants used in the simulations at 1550 nm can be found in Fig. 6.1.

6.3 Fabrication

The various devices were fabricated using electron beam lithography (EBL), using three exposure steps, on silicon nitride-on-insulator substrates. The layer stack consists of 300 nm of Si_3N_4 over 2 μm of SiO_2, deposited on a silicon carrier wafer.

In a first lithography step, windows for gold alignment markers were opened using the

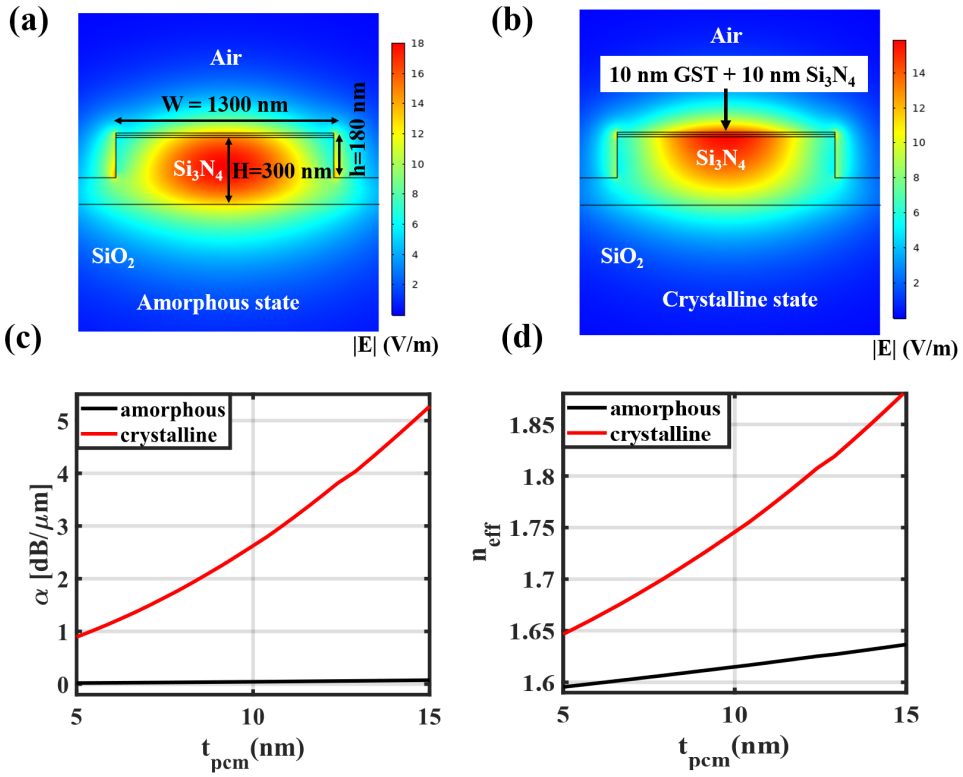

Fig. 6.3 Eigenmode simulation of the fundamental TE optical mode of a rib silicon nitride waveguide at 1550 nm wavelength, with a GST thin layer cell on top in the (a) amorphous state (b) crystalline state; (c) mode attenuation and (d) effective refractive index both as a function of PCM layer thickness.

PMMA 950K A4 resist spun at 4000 rpm for 60 seconds, yielding a resist film thickness of 200 nm. The development was carried out in an IPA: MIBK: MEK (15:5:1) mixture for 35 seconds. After depositing 5 nm of chromium and 50 nm of gold using a thermal evaporator (HHV Auto306), a lift-off in acetone was carried out and alignment marks for the next lithography steps were thus patterned. In a second lithography step, the waveguides and ring resonators were exposed using a TI PRIME adhesion promoter spun at 4000 rpm for 30 seconds and baked at 120°C for 120 seconds, and ma-N 2403 negative tone resist spun at 3500 rpm for 60 seconds and baked at 90°C for 120 seconds. The lift-off in this case was carried out using MF 319 developer for 35 seconds, followed by reactive ion etching (RIE) using a recipe which comprises a gas mixture of 15 standard cubic centimeters per minute (sccm) of SF_6 and 15 sccm of Argon with a pressure of 45 mTorr, and a power of 50 W, to

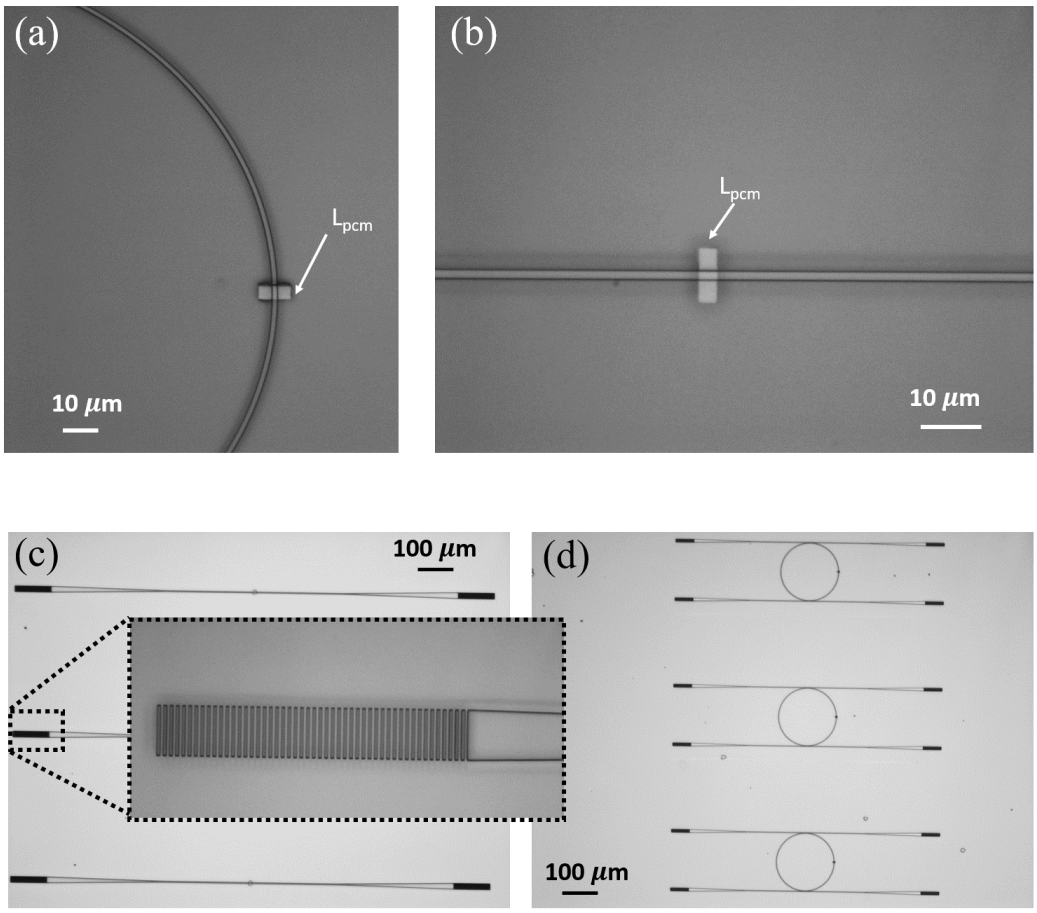

Fig. 6.4 Optical microscope images of the fabricated structures. (a) Rib micro-ring resonator waveguide at 1550 nm with the deposited phase change material GST. (b) Rib waveguide with a deposited GST cell with length L_{pcm} = 4 μm. (c) Rib waveguides with different lengths of the phase change material and a TE grating coupler inset image. (d) Add-drop filters with the phase change material deposited in the right-hand side of the ring resonator.

pattern the photonic integrated waveguides and ring resonators on Si_3N_4. The remaining resist was removed in an acetone bath at 80 °C for 10 minutes, followed by 10 minutes of sonication in the warm acetone at 80 kHz. A third and last lithography step consisted of opening the windows for the PCM deposition using the same technique as used for the markers. Finally, the GST cells capped by 10 nm of Si_3N_4 were then integrated on top of the waveguides and rings using physical vapor deposition (PVD) techniques (magnetron sputtering). Examples of as-fabricated devices are shown in Fig. 6.4.

6.4 Characterization

6.4.1 O-band

A set of rib waveguides and ring resonators with width and inner height values of W = 900 nm and H = 300 nm respectively, and the outer region of the rib waveguide with a thickness of 120 nm were fabricated in the O-band. The radii of the ring resonators were selected to be 1arge enough in order to avoid bending losses and obtain high quality factor resonances ($Q \sim 10^5$) without the phase change material cell. All structures were connected to an input and an output grating coupler which consists of a 10 μm width and 50 μm length with a period of 984 nm tapered down to a single-mode waveguide of 900 nm width. The angle between the optical fibers delivering light to the couplers and the couplers themselves was selected to be 14° to the normal, to ensure maximum coupling at the wavelength of interest (1310 nm). The spectral response of the rib waveguide integrated structures for different PCM cell lengths, ranging from 1 μm up to 25 μm, and for both amorphous and crystalline states of the PCM layer, was evaluated using an Agilent 8164B tunable laser source with a tunable wavelength of 1260 to 1360 nm. The polarization of the light was controlled to ensure that only TE modes could propagate through the devices. The measurements of the different rib waveguides for different cell lengths were normalized, extracting the losses due to the grating couplers. The phase change was induced thermally by placing the chip on a hot plate at 230 ºC for 15 min. The experimental losses of the waveguide at 1310 nm using GST as the deposited PCM were found to be as high as 6.66 dB/μm in the crystalline state and as low as 0.228 dB/μm in the amorphous state [Fig. 6.5 (a)]. These results matched quite closely the simulated values, which at 1310 are 6.71 dB/μm and 0.34 dB/μm in the crystalline and amorphous states respectively [Fig. 6.2 (c)]. The loss coefficient of the TE mode for both states of the phase change material was also evaluated experimentally over a range of the spectrum between 1260 and 1360 nm, with losses in the crystalline state showing a slight increase with wavelength, whereas losses in the amorphous state being almost flat, as shown in Fig. 6.5 (b).

A set of 5 rib ring resonator waveguides, each with their own integrated PCM cell, were also coupled to straight waveguides in order to measure their non-volatile tunable resonance properties in the O-band. The rib ring resonators were designed to have radii of 100 μm in order to avoid bending losses. The gap between the ring resonator and the straight waveguide was set to be around 250 nm. A GST cell of 5 μm length and width of 8 μm completely covering the waveguide width was deposited on top of the ring resonator structure [Fig. 6.4 (a)]. First, the bare structure (without phase change material) was characterized and normalized. The optical response can be seen (black dashed lines) in Fig. 6.6 (a), and quality

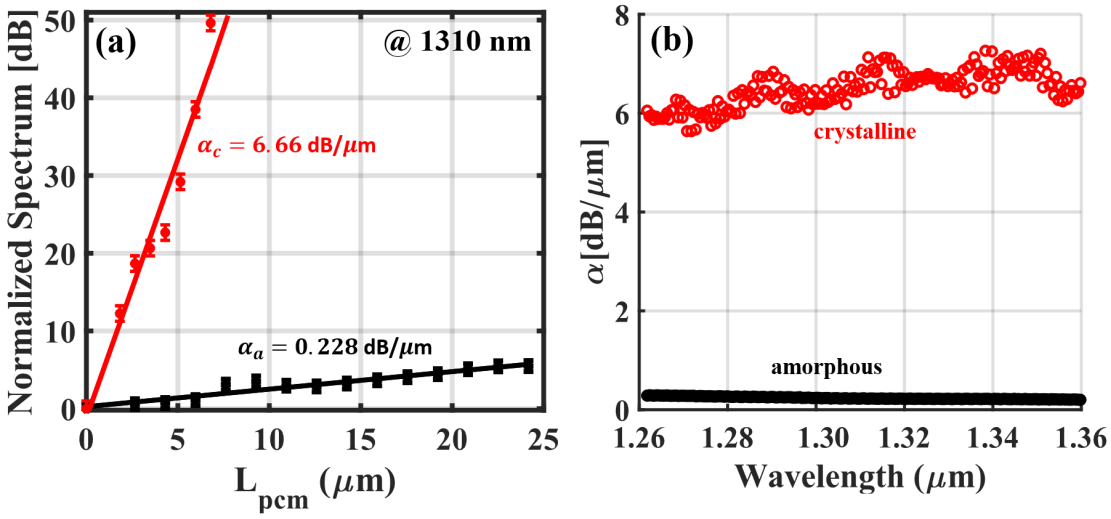

Fig. 6.5 (a) Measured losses in the waveguide for different PCM cell lengths in both states, amorphous (black line) and crystalline (red line) at 1310 nm. (b) Measured loss coefficient for different wavelengths in both cell states, amorphous (black dots) and crystalline (red dots).

factors as large as $Q = 21,840$ were measured with a free-spectral range (FSR) of 1.4 nm. Using the resonance equation of a ring resonator, $m\lambda_m = 2\pi n_{eff} R$, the experimental effective refractive index can be extracted, where λ_m is the resonance wavelength, R is the radius of the ring resonator, m is the number of integer number of wavelengths inside the cavity and n_{eff} is the effective refractive index. In our case, R = 100 μm, m = 757, and λ_m =1.31045 μm, hence, the measured effective refractive index has a value of n_{eff} = 1.5948, which agrees with the simulated extracted effective refractive index n_{eff} = 1.5953.

In Fig. 6.6 (a), the optical responses of the ring resonator structure for both states of the phase change material, amorphous (solid black line) and crystalline (solid red line) are also presented. In Fig. 6.6 (b), a zoomed image of the resonance around 1310 nm is presented. It can be seen that once the phase change material is switched to the crystalline state, the resonance condition is effectively cancelled (i.e. much more attenuated), due to the high extinction coefficient in the crystalline state, and the device to be in an "OFF state" can be considered. However, when the phase change material is in the amorphous state, the ring resonator essentially maintains the original resonances, but shifted in wavelength, and this can be considered as the "ON state". The free spectral range (FSR) in the amorphous and crystalline states of the PCM is maintained and is equal to 1.4 nm for both states. The quality factor is reduced for both states of the PCM as compared with the bare structure. For the

amorphous state, the quality factor is however still relatively large, being $Q = 6590$, due to the low level of losses introduced by the amorphous phase. In the crystalline state, however, the quality factor goes down to $Q = 1450$. The wavelength shift of the resonance peaks compared with the bare structure resonances are $\Delta\lambda_a = 0.46$ nm and $\Delta\lambda_c = 0.63$ nm for amorphous and crystalline states respectively. The extinction ratio (ER) of the resonances in the amorphous state is as high as 12 dB and in the crystalline state it goes down to 3 dB. In Fig. 6.6 (b) an optical switch is shown at 1.3095 nm where a difference in transmission between ON-OFF state of 10 dB is produced.

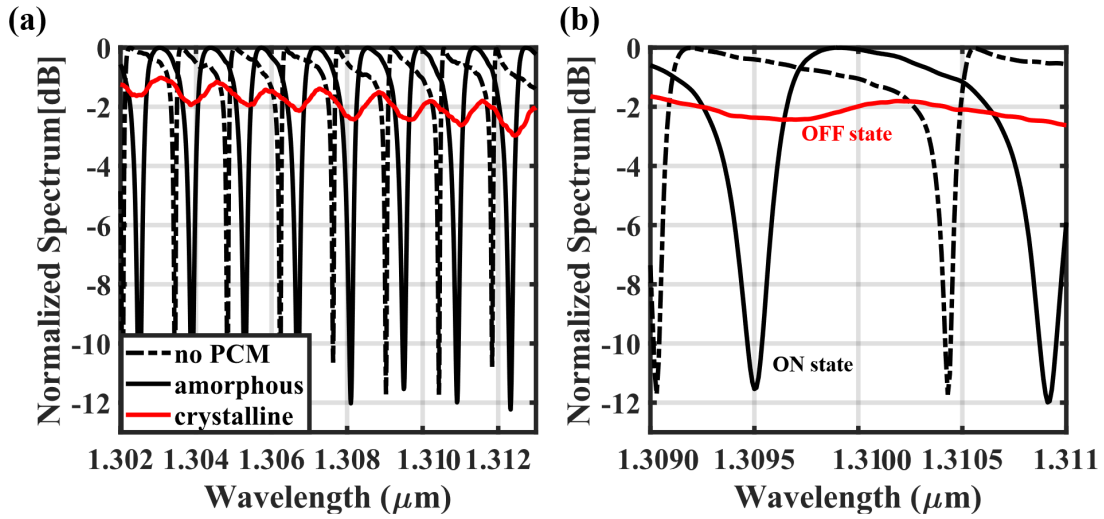

Fig. 6.6 (a) Normalized spectrum of a rib ring silicon nitride resonator waveguide with radius, R= 100 μm, for the bare structure, without the PCM (dashed black lines) and with a phase change material cell length, $L_{pcm} = 5$ μm and 8 μm width deposited on top of the ring structure for both, the amorphous state of the PCM (solid black lines) and the crystalline state of the PCM (solid red line). (b) Zoom in image of the resonances in both states of the phase change material showing the device principle, ON-OFF operation.

In order to experimentally evaluate the effective refractive index of the PCM ring resonator structures, in amorphous and crystalline states of the phase change material cell, the following formula should be considered [149]:

$$\Delta n_{eff}^{(a-c)} = \frac{\lambda}{FSR} \cdot \frac{\Delta\lambda_{(a-c)}}{L_{pcm}} \tag{6.1}$$

where $\Delta n_{eff}^{(a-c)}$ is the variation produced in the effective refractive index when the PCM cell is introduced compared to the bare structure (no PCM), the superscripts a and c refer to

the amorphous and crystalline states respectively, FSR is the free spectral range, L_{pcm} is the phase change material cell length, and $\Delta\lambda_{(a-c)}$ is the shift in the resonance peaks of the amorphous and crystalline states respect to the resonances produced by the bare ring resonator waveguide as introduced previously. The variation in the effective refractive index due to the deposition of the phase change material is $\Delta n^a_{eff} = 0.0861$ and $\Delta n^c_{eff} = 0.1179$ for the amorphous and crystalline states respectively. Finally, the experimental effective refractive index of the PCM ring resonator structures can be evaluated, yielding to values of $n^a_{eff} = 1.68$ and $n^c_{eff} = 1.71$ for the amorphous and crystalline states respectively. These values are close to the simulated results for the the effective refractive index, which were $n^a_{eff} = 1.66$ and $n^c_{eff} = 1.73$ [Fig. 6.2 (d)] for the amorphous and crystalline states respectively, assuming a PCM layer thickness of 10 nm.

6.4.2 C-band

For operation in the C-band, a set of rib waveguides and ring resonators with width and inner height values of $W = 1300$ nm and $H = 300$ nm respectively, and the outer region of the rib waveguide with a thickness of 120 nm were fabricated. Similar input/output couplers were used as described above, but in this case the grating period was 1195 nm and the couplers were tapered down in width to a single-mode waveguide of 1300 nm. As before, the spectral response of the rib waveguides was measured for PCM cell lengths from 1 μm to 25 μm, for both amorphous and crystalline states of the phase change material. The experimental losses of the PCM waveguide at 1550 nm using GST as the deposited PCM were found to be as high as 2.86 dB/μm in the crystalline state, and as low as 0.039 dB/μm in the amorphous state [Fig. 6.7 (a)]. These are again close to the simulated values for the losses at 1550 nm, which were 2.625 dB/μm and 0.044 dB/μm in the crystalline and amorphous states respectively [Fig. 6.3 (c)]. These values are consistent with the recently published values in Ref. [272], and other previous work [273]. The experimental loss coefficient of the TE mode for both states of the phase change material over a range of the spectrum between 1520 to 1610 nm is shown in Fig. 6.7 (b), from where it can be seen that losses are essentially flat over this wavelength range.

The resonance properties of a set of 5 rib ring resonator waveguides designed for operation in the C-band were also experimentally evaluated, using the same procedures as described above for the O-band case. Here, a gap between the ring resonator and the waveguide was set to be around 300 nm, and a GST cell of 4 μm length and width of 8 μm completely covering the waveguide width was deposited on top of the ring resonator structure [Fig. 6.4 (d)]. Results are shown in Fig. 6.8. Without any PCM layer, quality factors as large as $Q = 1.4 \cdot 10^4$ were measured, with a FSR of 2.02 nm. Using the resonance equation of a ring

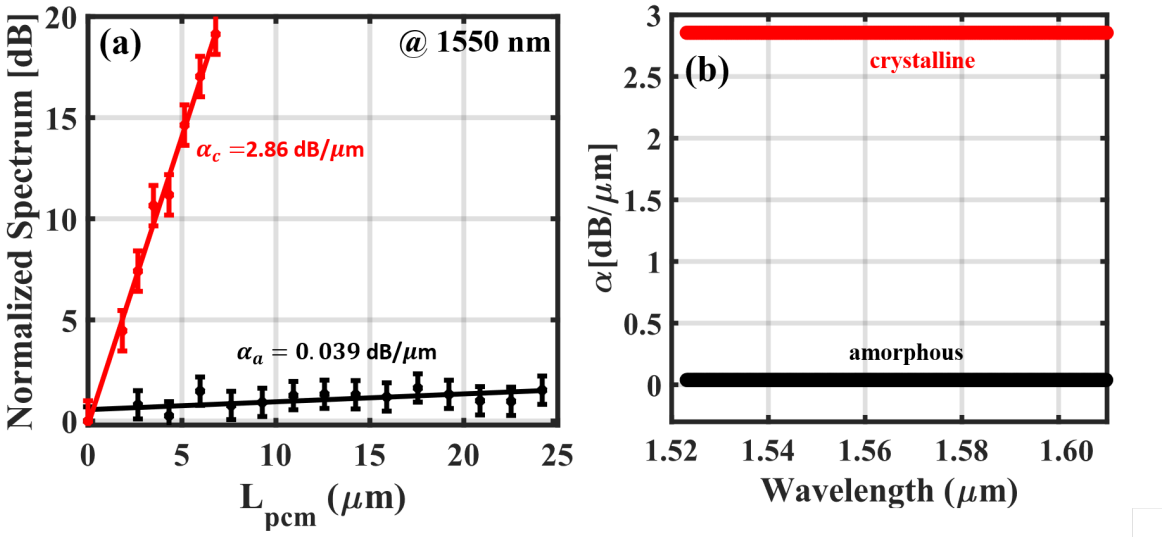

Fig. 6.7 (a) Measured losses in the waveguide for different PCM cell lengths in both states, amorphous (black line) and crystalline (red line) at 1550 nm. (b) Measured loss coefficient for different wavelengths in both cell states, amorphous (black dots) and crystalline (red dots).

resonator described previously ($m\lambda_m = 2\pi n_{eff} R$), in this case with R = 100 μm, m = 636, and λ_m=1.5493), the measured effective refractive index was found to be , n_{eff} = 1.5682, which agrees well with the simulated extracted effective refractive index n_{eff} = 1.5688.

As in the case for O-band operation, once the PCM layer in the resonator structure is switched to the crystalline state, the resonance condition is effectively cancelled, but with the PCM layer in the the amorphous state the ring resonator essentially maintains the original resonances, but slightly wavelength shifted (see Fig. 6.8 (a) and zoomed version in Fig. 6.8 (b)). The FSR in the amorphous and crystalline states of the PCM is maintained, and is equal to 2.02 nm for both states. The quality factor (Q) is again reduced for both states of the PCM as compared with the bare structure, being Q = 3869 for the amorphous state and Q = 1938 for the crystalline state. The distance between peaks compared with the bare structure resonances are $\Delta\lambda_a$= 0.2 nm and $\Delta\lambda_c$= 1 nm for amorphous and crystalline states respectively. The extinction ratio (ER) of the resonances in amorphous state are as high as 24 dB and in the crystalline state it goes down to 2 dB. In Fig. 6.8 (b) an optical switch is shown at 1.5495 nm where a difference in transmission between ON-OFF state of 18 dB is produced. The variation in the effective refractive index due to the deposition of the phase change material is Δn^a_{eff} = 0.0328 and Δn^c_{eff} = 0.1638 for the amorphous and crystalline states respectively. Finally, the experimental effective refractive index of the PCM ring resonator structures

can be evaluated, yielding to values of n^a_{eff} = 1.60 and n^c_{eff} = 1.74 for the amorphous and crystalline states respectively, again very close to the simulated values of n^a_{eff} = 1.62 and n^c_{eff} = 1.75 [Fig. 6.3 (d)].

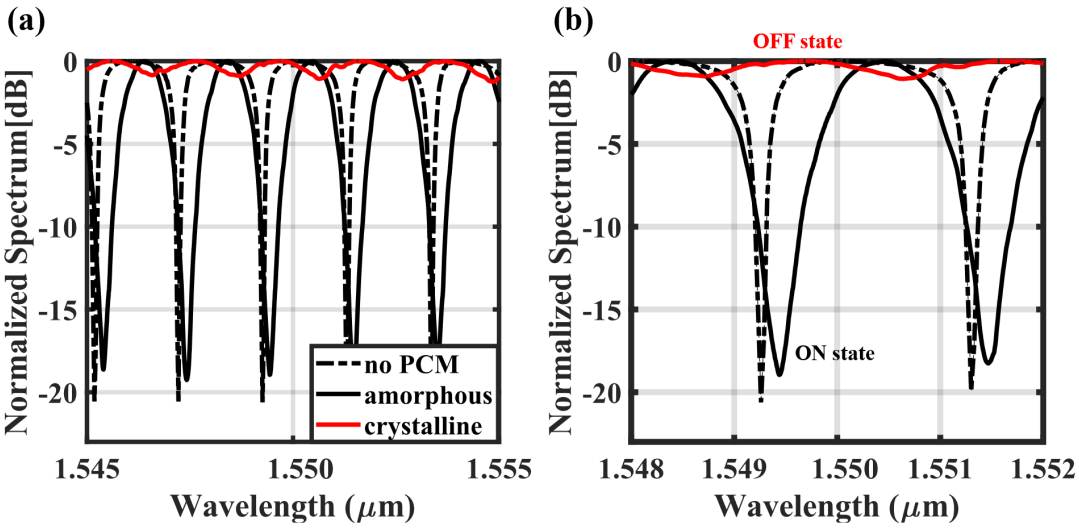

Fig. 6.8 (a) Normalized spectrum of a rib ring silicon nitride resonator waveguide with radius, R= 100 μm, for the bare structure, without the PCM (dashed black lines) and with a phase change material cell length, L_{pcm} = 4 μm and 8 μm width deposited on top of the ring structure for both, the amorphous state of the PCM (solid black lines) and the crystalline state of the PCM (solid red line). (b) Zoom in image of the resonances in both states of the phase change material showing the device principle, ON-OFF operation.

6.4.3 Comparison between O and C-bands

A complete performance comparison between the devices fabricated in the O and C-bands is presented in Table 6.1. In the O-band, the absorption is much higher than in the C-band for both states of the PCM, which implies that lower power energies will be required to switch the phase change material optically using laser pulses on-chip. However, the contrast in the effective refractive index is higher in the C-band. Consequently, operating in the O-band, a complete set of low power consumption devices can be expected, nonvolatile photonic integrated circuits exploiting the large absorption contrast (between crystalline and amorphous states) in this spectral range. However, the readout signal amplitude (and hence the signal-to-noise-ratio) will also be reduced for a given readout signal power, as compared to the C-band. A large contrast between states can also make re-writability more difficult,

Device performance	@1310 (Experimental)	@1310 (Simulated)	@1550 (Experimental)	@1550 (Simulated)
α_a	6.66 dB/μm	6.71 dB/μm	2.86 dB/μm	2.63 dB/μm
α_c	0.228 dB/μm	0.34 dB/μm	0.039 dB/μm	0.044 dB/μm
FSR	1.4 nm	1.7 nm	2 nm	2.4 nm
Q_a	6590	$6.4 \cdot 10^3$	3869	$3.7 \cdot 10^3$
Q_c	1450	$1.3 \cdot 10^3$	1938	$1.85 \cdot 10^3$
Q_{bare}	$2.2 \cdot 10^4$	$2 \cdot 10^4$	$1.4 \cdot 10^4$	$1 \cdot 10^4$
n_{eff}	1.5948	1.5953	1.5687	1.569
n^a_{eff}	1.68	1.66	1.60	1.62
n^c_{eff}	1.71	1.73	1.74	1.75
$\Delta\lambda_a$	0.46 nm	0.42 nm	0.2 nm	0.31 nm
$\Delta\lambda_c$	0.63 nm	0.85 nm	1 nm	1.1 nm
ER	12 dB	14 dB	18 dB	20 dB

Table 6.1 The device performance comparison between the O-band (1310 nm), C-band (1550 nm) and theoretical simulated results is presented.

as explained in Ref.[143], though this difficulty is alleviated somewhat by the use of the so-called double-step pulse for re-writing (see Ref. [274]). If the desired characteristic is a tuning in the optical phase without having large absorption, the C-band is no doubt a better selection than O-band, and of course many devices operating in the C-band and exploiting absorption contrast have already been demonstrated [245, 275–277]. Thus, it is clear that operating in the O- and C-bands comes with various advantages and disadvantages, and that different building blocks for future emerging applications can be fabricated in both ranges of the spectrum.

With the view to provide a comparison of the wavelength-dependent optical switching performance, a 3-dimensional FEM simulation of the O-band and C-band straight waveguide device with the PCM cell deposited on top was performed, to observe the temperature profile arising from the delivery of a 15 mW, 20 ns rectangular pulse through the waveguide (as used for successful experimental switching at 1550 nm in Ref. [143]). Details of the modelling methodology may be found in Ref. [145]. The thermo-optical effect is also a fundamental contribution to the time-dependent evolution of the PCM temperature profile, and so this effect is included in our model using data provided by Stegmaier et al [278]. The simulation results are shown in Fig. 6.9, where it can be seen that when the PCM layer is in the crystalline phase the 15 mW, 20 ns switching pulse raises the peak temperature in the PCM layer above the melting temperature of GST (approximately 900 K) in both the O- and C-bands (Fig. 6.9 (a)). When the PCM layer is amorphous, the same switching pulse

raises the peak temperature to over 600 K in the O-band (a temperature conducive to rapid crystallization [279]), but in the C-band only a marginal increase in temperature, insufficient for crystallization, is observed. Turning to the average temperature in the PCM layer, as shown in Fig. 6.9 (b).

In the O-band the melting temperature (for a crystalline PCM layer) is reached after only 9 ns, whereas in the C-band the average temperature never reaches melting, again revealing a superior efficiency in the optical-to-thermal energy conversion in the former case.

As for the simulated recrystallization process (i.e. pulse delivery to the amorphous unit cell), in the C-band our simulation barely reports any temperature increase. Instead, in the O-band a peak temperature of 600 K was calculated, and an average temperature of 450 K. Once more, the numerical results show how the higher optical loss in the O-band is responsible for a much more efficient temperature increase.

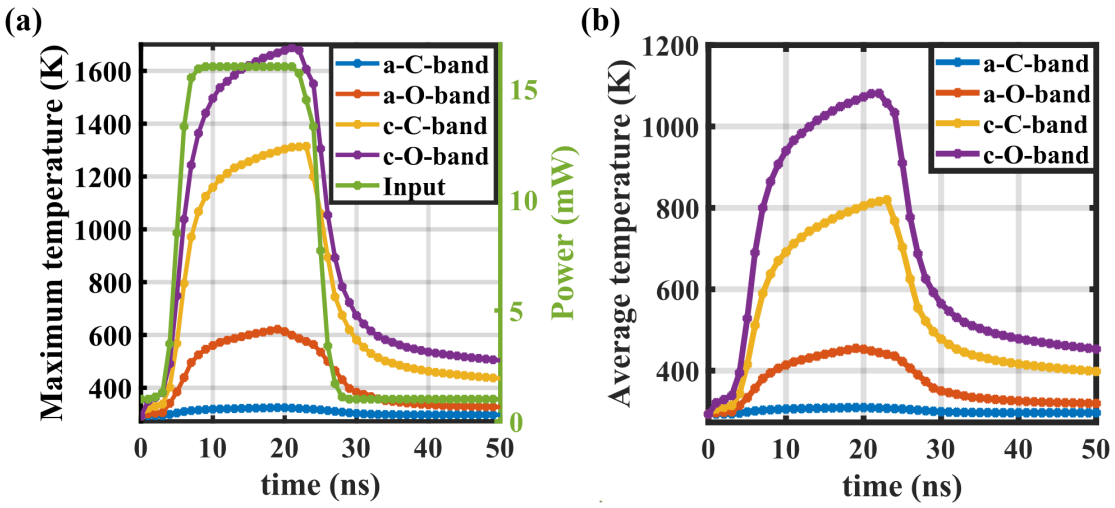

Fig. 6.9 (a) Maximum temperature and (b) average temperature reached in the PCM unit cell for four different states: amorphous state in the C-band (a-C-band) in blue, crystalline state in the C-band (c-C-band) in yellow, amorphous state in the O-band (a-O-band) in red and crystalline state in the O-band (c-O-band) in purple. Also, the input pulse is represented in the right axes of figure (a) in green.

Following the approach proposed in Zheng et al. [280], the energy efficiency η is reported, calculated as:

$$\eta = \frac{E_{GST}}{E_{pulse}} = \frac{\int \rho C_P (T - T_0) dV}{P_0 \Delta t}, \tag{6.2}$$

where ρ is the material density, C_p is the specific heat, T_0 is the initial ambient temperature

(293 K), and the integral domain is over the entire GST film. A parametric sweep for several pulse widths (up to 10 ns) using a fixed pulse power of 15 mW and another parametric sweep for powers (from 1 to 25 mW) using a fixed pulse width of 1 ns was performed, to cover a wide range of the reported experimental switching pulse parameters values in Ref. [143]. Fig. 6.10 (a) shows the value of η for different input powers for both ranges of the spectrum, 1550 nm and 1310 nm and for the amorphous and crystalline state of the PCM. Here it is possible to observe how the crystal phase efficiency values are consistently higher than the amorphous case, regardless of the input power. This is due to the great difference in optical loss, which is also proportional to the generated heat.

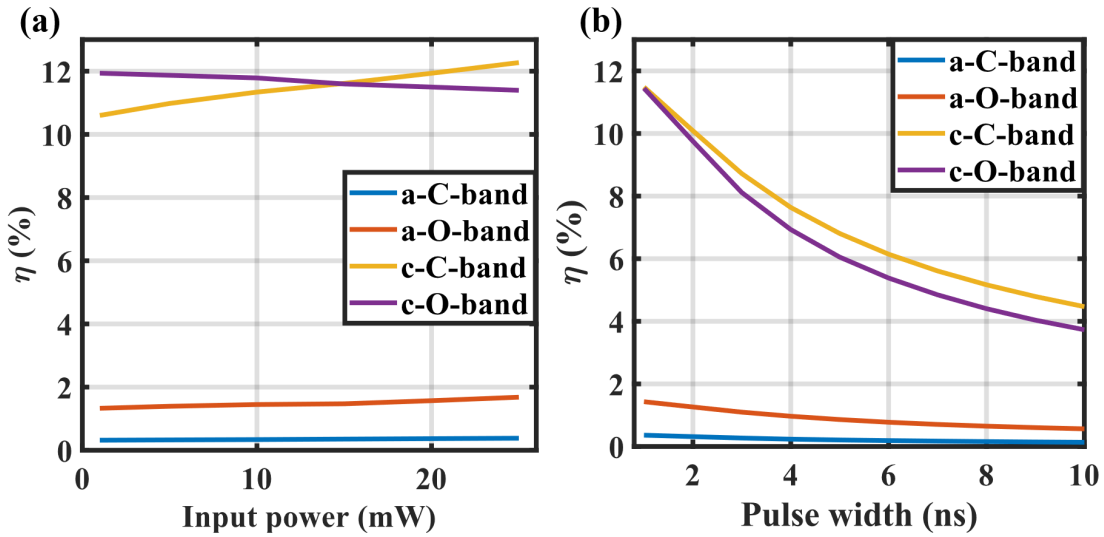

Fig. 6.10 Efficiency of the PCM cell heating for (a) different input powers for a fixed pulse width of 1 ns and (b) different pulse widths for a fixed input power of 15 mW: amorphous state in the C-band (a-C-band) in blue, crystalline state in the C-band (c-C-band) in yellow, amorphous state in the O-band (a-O-band) in red and crystalline state in the O-band (c-O-band) in purple.

For the crystal phase, with increasing power it is possible to observe a decrease in efficiency for the O-band, and an increase in efficiency for the C-Band; nevertheless, the efficiency values remains roughly within the same range, from 11% to 12%. For the amorphous case, once more a consistently higher value of the efficiency for the O-band, confirming how a higher suitability for the switching mechanism is found within the O-band device.

With respect to the different wavelengths, a variation of η is marginal for the crystal case, with an efficiency value in the C-band slightly higher than the O-band, yielding to

a ratio between efficiencies (η_{1310}/η_{1550}) of 0.8. A much more significant divergence is found for the amorphous case, with the O-band calculated efficiency consistently found 4 times higher than the corresponding C-band value, in the whole range of investigated pulse duration. These values hints to the increased suitability for switching purposes of the O-band device, which would see a considerably lower energy requirement for recrystallization.

6.5 Summary

The evaluation and comparison of the optical properties in the O and C bands of silicon nitride rib waveguides with integrated $Ge_2Sb_2Te_5$ phase-change cells is reported. In straight rib waveguides, a high transmission contrast is observed in both bands when the $Ge_2Sb_2Te_5$ cell is switched between states, being up to 2.5 dB/μm in the C-band and 6.4 dB/μm in the O-band. In the case of silicon nitride ring resonator waveguides, high quality factor resonances ($Q \sim 10^5$) are found in both bands, leading to the provision of an ON-OFF switch characterized by an extinction ratio of 12 and 18 dB in O and C bands respectively. Finally, with the view to provide a comparison of the wavelength-dependent optical switching of the phase-change cell, a 3-dimensional finite-element method simulation is performed and a comparison of the optical-to-thermal energy conversion in both bands given.

Chapter 7

PIC components based on PCMs

7.1 Bragg grating design based on novel low loss phase-change materials

Most technologically useful PCMs are binary, ternary or quaternary chalcogenide alloys. These materials have been exploited for a variety of tunable photonic applications ranging from filters [281] to metamaterials [282–284]. Different periodic photonic structures have been demonstrated using the well-known PCM, GST-225 [285]. Recently, a contra-directional coupler switching enabled by a Si-GST grating has been demonstrated in Ref. [286] and a Bragg grating in photosensitive $Ge_{23}Sb_7S_{70}$ chalcogenide micro-ring resonators via a novel cavity-enhanced photo inscription process, in which injection of light at the targeted C-band resonance frequency induces a spatially varying refractive index change, has been demonstrated in Ref. [287]. Sb_2S_3 and $Ge_2Sb_2Se_4Te_1$ (GSST) are recently developed PCMs [288, 289], they were selected for this work due to their particularly low losses in the C-band, whilst still maintaining a reasonably high contrast (between phases) in refractive index. The optical properties of the PCMs (Sb_2S_3 and GSST) in amorphous and crystalline states have been measured using ellipsometry. The samples were deposited using magnetron sputtering at Ar pressure of $5 \cdot 10^{-3}$ mbar and power of 15 W. All samples were deposited on a silicon substrate and the thickness of the deposited PCMs was 50 nm. The experimental ellipsometry measurements from 300 nm up to 1700 nm in wavelength are presented in Fig. 7.1.

Among various silicon photonic device structures for filter applications, Bragg Gratings (BGs) are one of the most efficient and commonly used technologies in integrated photonics. BGs are structures with a periodic modulation of the effective refractive index in the direction of propagation of the mode. This modulation in the refractive index can be achieved by

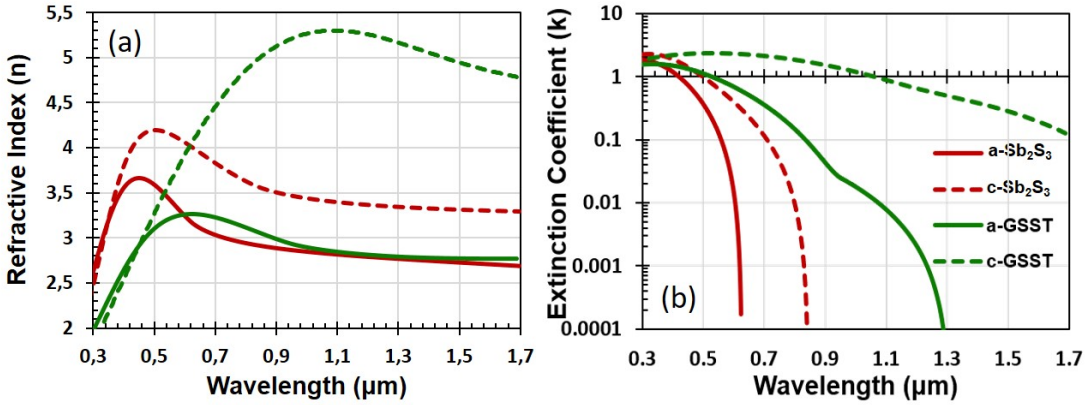

Fig. 7.1 (a) Refractive index, n, and (b) extinction coefficient, k, ellipsometry measurements in amorphous (solid lines) and crystalline (dashed lines) state for Sb_2S_3 (red) and GSST (green).

intercalating two different materials or by generating defects in the structure. In this work, a reconfigurable BG for generating non-volatile reconfigurable smart filters on-chip is proposed. BG structures can also be used in the design of photonic FPGA (field programmable gate arrays) or as components to provide synaptic weight in neuromorphic systems (brain-like computers) [290–292]. Different reconfigurable BGs filters have been demonstrated and proposed using the well known p-n junctions on silicon [293] or more recently, using graphene [294]. These approaches are volatile, and their maximum shift is only in the order of 1 nm. The phase-change BG presented here is non-volatile, and achieves a significantly greater shift of ~ 7 nm using the low-loss Sb_2S_3, and ~ 15 nm using the higher-loss GSST.

7.1.1 Bragg grating design

Mode analysis

The optical platform consists of a Si_3N_4 ($n = 2.01$) ridge photonic waveguide with cross-section dimension of 1200 nm width and 300 nm thickness. This waveguide geometry enables mode propagation in the C-band (both TM and TE) with negligible losses. The BG is produced by periodically spaced cells of phase-change material along the length of the waveguide, as shown in Fig. 7.2. These cells are 20 nm thick, comprising 10 nm of PCM, capped with 10 nm of SiO_2 to prevent oxidation. Cell length (L_{PCM}), period (Λ) and consequently fill-factor (FF), defined as the ratio between the length of the PCM unit

cell and the period (L_{PCM}/Λ), can be efficiently engineered in order to control the device performance.

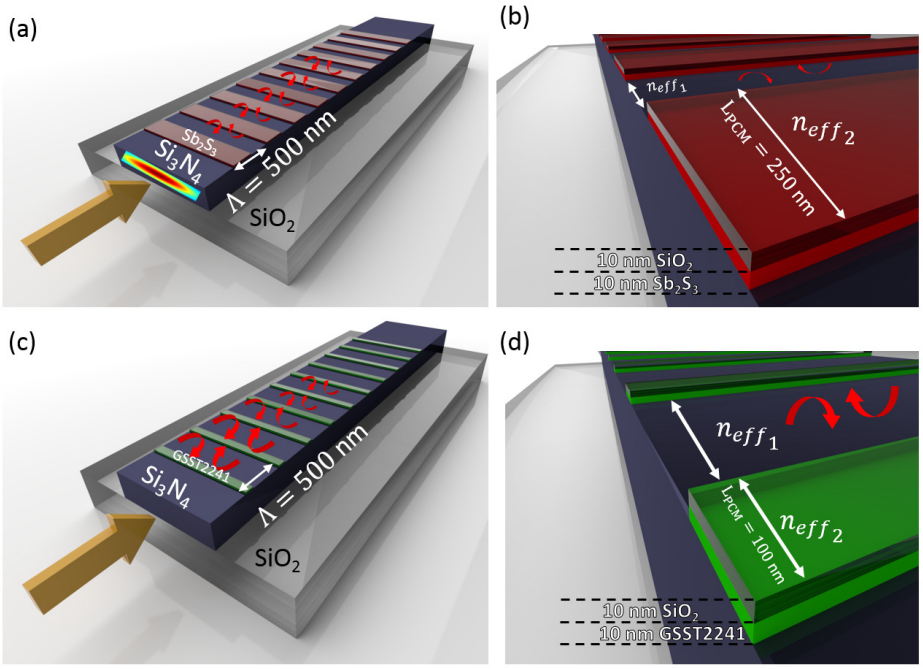

Fig. 7.2 Schematic of two phase-change reconfigurable BGs, both with a period of $\Lambda = 500$ nm , and with a period number N=10. The cells consist of 10 nm of PCM, capped with 10 nm of SiO_2, (a) uses Sb_2S_3 as the PCM, with a fill-factor FF=0.5 (c) uses GSST2241 as the PCM, with a fill-factor FF=0.2. Internal reflections are illustrated in both figures using red arrows. (b-d) Mismatch in the effective refractive index between the bare waveguide region and the hybrid waveguide region is illustrated and the cell length (L_{PCM}) for each phase-change material is indicated.

Finite element simulations (COMSOL Multiphysics®) were used to calculate the effective refractive indices of the bare and hybrid waveguide with cell structure. These effective refractive indices were then used in the transfer matrix method (TMM) to calculate the BG properties (discussed later). The material properties are summarised in Table 1. For this study only TE mode will be considered. The effective contrast (between PCM phases) in the waveguide's effective refractive index is determined by the specific PCM alloy used. For Sb_2S_3 this contrast is $\Delta n_{eff}^{Sb_2S_3} = 1.4 \cdot 10^{-2}$. GSST provides a significantly greater contrast of $\Delta n_{eff}^{GSST} = 7.4 \cdot 10^{-2}$, however, unlike Sb_2S_3, GSST crystalline phase is lossy and contributes to insertion losses depending on the total combined cell length ($\alpha = 0.53$ dB/μm). Different

thickness of phase-change material have been considered to see the effect in the absorption and in the propagation constant, see Fig. 7.3.

Material	n	k	$n_{eff} - jk_{eff}$ (TE)
Si_3N_4 (bare structure)	2.01	$k < 10^{-7}$	1.5348
Sb_2S_3, amorphous (hybrid structure)	2.72	$k < 10^{-5}$	1.5614
Sb_2S_3, crystalline (hybrid structure)	3.31	$k < 10^{-5}$	1.5749
GSST, amorphous (hybrid structure)	2.71	$1.2{\cdot}10^{-4}$	1.5612
GSST, crystalline (hybrid structure)	4.91	0.28	1.635-j0.015
SiO_2	1.44	$k < 10^{-7}$	—

Table 7.1 Material optical properties (n and k) used in the finite element simulations, and the resulting effective refractive index values (all at 1.55 μm) used in the transfer matrix method calculations.

Transfer Matrix Method (TMM)

Since a BG can be considered to be a multi-layer structure, a 2 x 2 TMM [295, 296] can be applied to simulate its reflection and transmission properties. The transfer matrix is defined as:

$$\begin{pmatrix} A_1 \\ B_1 \end{pmatrix} = \begin{pmatrix} T_{11} & T_{12} \\ T_{21} & T_{22} \end{pmatrix} \begin{pmatrix} A_2 \\ B_2 \end{pmatrix} \tag{7.1}$$

where subscript 1 is the incoming electric field amplitude to a grating element (cell), and subscript 2 refers to the amplitude of the electric field exiting the grating element. The transfer matrix for a homogeneous section of the waveguide grating is determined by:

$$T_w = \begin{pmatrix} e^{j\beta L} & 0 \\ 0 & e^{-j\beta L} \end{pmatrix} \tag{7.2}$$

where $\beta = (2\pi n_{eff})/\lambda - j\alpha/2$ is the complex propagation constant for the bare waveguide, including the losses of the waveguide, and L is the length of the BG element considered. When the light jumps from one grating element to the next, there is a mismatch between the effective refractive index which implies internal reflections see [Figs. 7.2 (a-c)]. For example, for going from medium 1 to medium 2, this internal reflection can be described by the following matrix:

$$T_{12} = \begin{pmatrix} 1/t & r/t \\ r/t & 1/t \end{pmatrix} \tag{7.3}$$

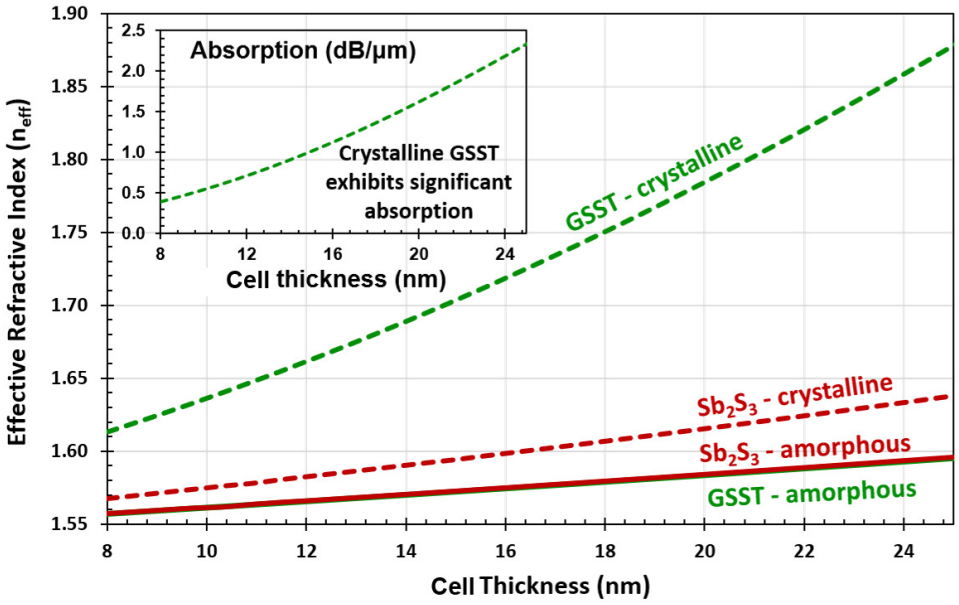

Fig. 7.3 Effective refractive index and cell absorption for different PCM thickness ranging from 8 nm up to 25 nm for both materials, Sb_2S_3 (red) and GSST (green) for amorphous (solid lines) and crystalline (dashed lines) states respectively.

where r and t are the reflection and transmission coefficients respectively, and here are found based on the Fresnel equations. For constructing one grating step, a cascaded construction of each transfer matrix is done by multiplication. Finally, elevating the following equation to N, with N being the number of periods comprising the grating, the complete response of the grating can be evaluated.

To describe the phase-change BG, the following notation is considered, β^a_{PCM} refers to the propagation constant when the phase-change material is fully amorphous, and β^c_{PCM} to the propagation constant in the fully crystalline phase. The phase-change BG can then be described as follows:

$$T_T = \left[T_w T_{21} T^{a-c}_{PCM} T_{12}\right]^N \tag{7.4}$$

where N is the number of periods (Λ) of the grating. The length of the BG is defined as $L_{BG} = N\Lambda$, the fill factor (FF) is defined as L_{PCM}/Λ and T^{a-c}_{PCM} is defined as the transfer matrix for an homogeneous section through the phase change material cell, using the propagation constant β^a_{PCM} or β^a_{PCM} in Eq. 7.2 respectively. The Bragg wavelength, at 1.55 μm, determines the periodicity, which affects the fill-factor, and in turn this affects the effective refractive index.

The centre wavelength of the grating is known as the Bragg wavelength and is described by [297]:

$$\lambda_{BG} = 2n_{eff}\Lambda \tag{7.5}$$

where n_{eff} is the average effective index. n_{eff} = (1-FF)n_{eff_1}+FF (n_{eff_2}), in which, n_{eff_1} corresponds to the effective refractive index of the bare waveguide (without PCM cell), n^{w}_{eff}, while n_{eff_2} is the effective refractive index of the hybrid structures, as shown in Figs. 7.2 (b-d). Consequently, $n_{eff_1} = n^{w}_{eff} = 1.5348$ and $n_{eff_2} = n^{a-c}_{eff}$

$$\Lambda = \frac{\lambda_{BG}}{2 \cdot \left[(1-FF)n^{w}_{eff} + FF(n^{a-c}_{eff})\right]} \tag{7.6}$$

7.1.2 Performance

Two phase-change BGs were designed to operate at 1.55 μm with two different period numbers of N = 100 and N = 200 for each type of PCM. Both designs were studied for the amorphous and crystalline state of the PCM. All BGs used a periodicity Λ= 500 nm, with a PCM thickness of 10 nm, SiO_2 cap thickness of 10 nm and both with 1200 nm width, completely covering the waveguide width. The BGs employing Sb_2S_3 used a FF = 0.5, and the GSST based BGs used a FF = 0.2 (different fill factors were selected due to the difference in the loss between the two phase change materials). Figure 7.4 shows the calculated performance (normalized transmission) of these four different BG combinations.

Table 2 summaries the performance of each BG. In general, the number of periods (N) determines the bandwidth and the extinction ratio (ER) of the filter. Increasing the number of periods causes the ER and reflected power to increase and the bandwidth to reduce. Therefore, to improve selectivity and reflected power, the number of periods can be increased. However, this results in a trade-off between device performance (number of periods) and the total length of the BG (L_{BG}). Internal reflection losses (IRL), scattering losses (SL) and absorptive losses in the cells (PL), all contribute to the insertion losses (IL=PL + IRL + SL). The Sb_2S_3 SLs produced by a unique PCM unit cell have been evaluated yielding to values of $1.6 \cdot 10^{-2}$ dB and $7.3 \cdot 10^{-3}$ dB in the crystalline and amorphous state respectively. In the case of the GSST phase change material, the SLs due to one unit cell have values of $1.5 \cdot 10^{-2}$ dB and $1.6 \cdot 10^{-3}$ dB in the crystalline and amorphous state respectively. Thanks to the near-zero losses of Sb_2S_3 in both phases, the BGs incorporating this PCM have negligible losses due to absorption within the cells (PL) and the only significant contribution is due to the scattering losses. The effective refractive indices for both phases (see Table 1) are also similar enough to that of the bare waveguide to produce near zero IRL. This results in signal strength being

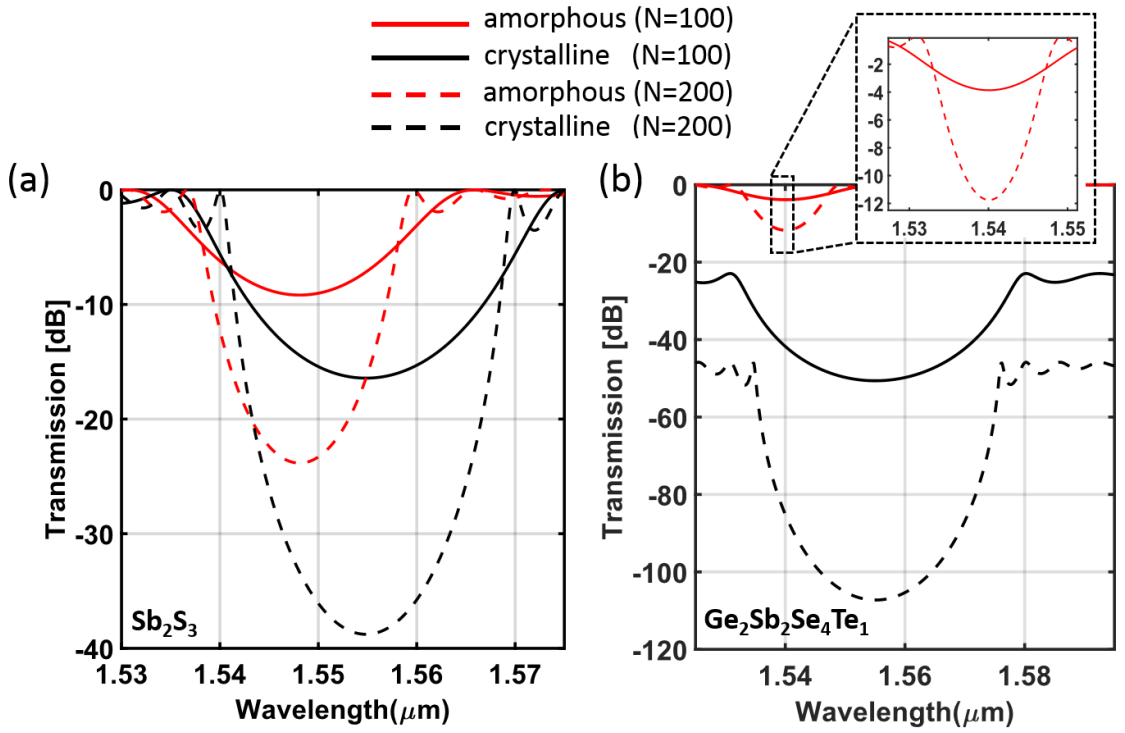

Fig. 7.4 Normalized transmission spectra comparing BG filters using the two studied PCMs, each evaluated with two different number of periods ($N = 100$ yielding $L_{BG} = 49.8761$ μm, and $N = 200$ yielding $L_{BG} = 99.75$ μm). Red curves are amorphous state, black curves are crystalline state. Solid curves are for $N = 100$, and dashed curves for $N = 200$. (a) uses Sb_2S_3 as the PCM. (b) uses GSST2241 as the PCM.

maintained outside of the stop band, whilst providing high extinction ratios (for both the N=100 and N=200 cases). The contrast in refractive index between PCM phases results in the crystalline phase red-shifting the Bragg wavelength by 7 nm.

The BGs incorporating GSST behave very similarly to Sb_2S_3 in their amorphous phases thanks to near-zero losses and similar effective refractive index of the waveguide and cell. Due to the relatively large contrast in the refractive index of GSST, the Bragg wavelength can be shifted by 15 nm. However, once the GSST is crystallised the BG exhibits significant insertion loss due to absorption in the cells of 0.53 dB/μm, internal reflections from the effective index mis-match (see Table 1) and scattering losses. This causes the GSST BGs to behave more like an amplitude switch; in which the amorphous phase attenuates at just 1.55 μm, while the crystalline phase attenuates all wavelengths. The number of periods has negligible effect on amorphous losses, but significantly affects crystalline losses. Therefore,

if employing this filter as an amplitude switch, increasing the period number greatly enhances the all-wavelength ER.

	GSST (N=100)	GSST (N=200)	Sb_2S_3 (N=100)	Sb_2S_3 (N=200)
IL (amorphous)	0.2 dB	0.32 dB	0.73 dB	1.46 dB
IL (crystalline)	23 dB	$\sim$ 50 dB	1.61 dB	3.22 dB
PL (amorphous)	$< 10^{-5}$	$< 10^{-5}$	$< 10^{-5}$	$< 10^{-5}$
PL (crystalline)	0.53 dB/μm	0.53 dB/μm	$< 10^{-6}$	$< 10^{-5}$
ER (amorphous)	4 dB	11 dB	9.2 dB	24 dB
ER (Crystalline)	20 dB	53 dB	16.3 dB	39 dB
Red-shift	$\sim$15 nm	$\sim$15 nm	$\sim$7 nm	$\sim$7 nm

Table 7.2 Bragg grating performance comparison between the two studied phase-change materials. GSST2241 and Sb_2S_3 for different number of periods (N) and different phase-change materials state (amorphous or crystalline)

Fractional crystallization

So far only fully amorphous and fully crystalline PCM phases have been considered. Here the fact that intermediate crystalline phases are also accessible and stable is exploited. These intermediate phases form when insufficient time is available to complete crystallization. Properties of PCM intermediate phases (which crystallise as just described) can be evaluated. In this subsection, the approach taken in Ref. [298] is followed:

$$\varepsilon(f,\varepsilon_a,\varepsilon_c) = \frac{1}{4}\left[2\varepsilon_p - \varepsilon_p^* + \sqrt{(2\varepsilon_p - \varepsilon_p^*)^2 + 8\varepsilon_c\varepsilon_a}\right] \tag{7.7}$$

where f is the fraction of crystallization, ε_a and ε_c are the permittivity of the fully amorphous and crystalline phases, $\varepsilon_p = (1-f)\varepsilon_a + f\varepsilon_c$ and $\varepsilon_p^* = (1-f)\varepsilon_c + f\varepsilon_a$. In order to control the BGs intermediate states, the dependence of the phase change material permittivity with the crystallization fraction (f) is needed.

By controlling the fraction of crystallization, intermediate BG filter states can be achieved, resulting in truly tuneable (rather than switchable) BG filters. In Fig.7.5 BG performance for a range of PCM crystalline fractions has been plotted. Increasing the crystallization of the phase-change material cell results in an increase of both filter bandwidth and extinction ratio. Reliably and repeatably accessing intermediate crystallization states is not straight forward, but has been previously demonstrated [299, 300].

This tuneabale functionality results in a fine control over the bandwidth, and these tuneable BGs could be a key component in smart filters, reconfigurable mirrors, or frequency selectors. A complete study of all the relevant parameters that comprises a Bragg grating

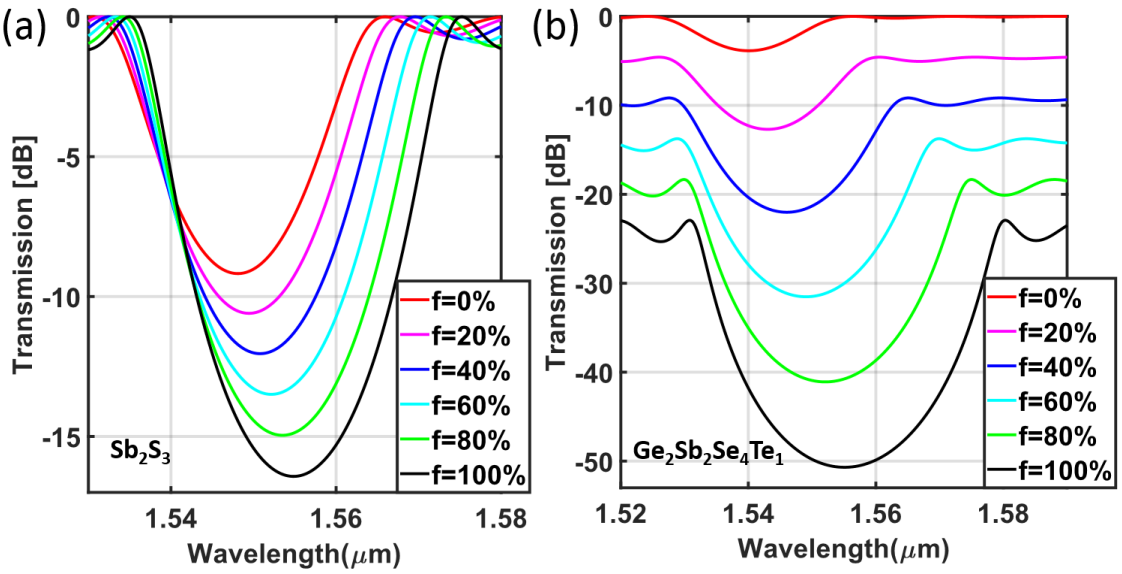

Fig. 7.5 Transmission spectrum of two reconfigurable BG filters for 6 different levels of phase-change material crystallization. Both filters have a period of Λ=500 nm, and $N = 100$ for a BG length of L_{BG}= 50 μm. (a) uses Sb_2S_3 with a fill factor $FF = 0.5$. (b) uses GSST2241 and a fill-factor $FF = 0.2$

.

(central wavelength, extinction ratio, bandwidth and insertion losses) has been made for both phase-change materials and different crystallization fractions and can be found in Fig. 7.6.

The phase change process can be thermally, optically or electrically driven. The modulation speed depends on the switching mechanism and device geometry. Optical switching in integrated photonic devices reaches “ns” modulation ($\sim$ MHz) [301], but faster modulation rates have been demonstrated in the sub-ns regime ($\sim$GHz) [302] by electrical switching, using carbon nanotube electrodes [303]. Using micro-heaters, switching times conventionally lays in the order of "μs", leading to lower modulation rates ($\sim$ kHz) [252, 254]. Crystallization is achieved by heating the material above the glass transition temperature and holding it there long enough for sufficient crystal nucleation and/or growth to occur. Returning to the amorphous state is more challenging, and requires the PCM to be molten and then very rapidly quenched [290]. Not having equal crystallization levels between different PCM cells would of course affect the performance of the grating, for example by changing the peak position and bandwidth. However, the methods described previously for switching the PCM cells should be able to provide a good degree of uniformity of crystallization levels.

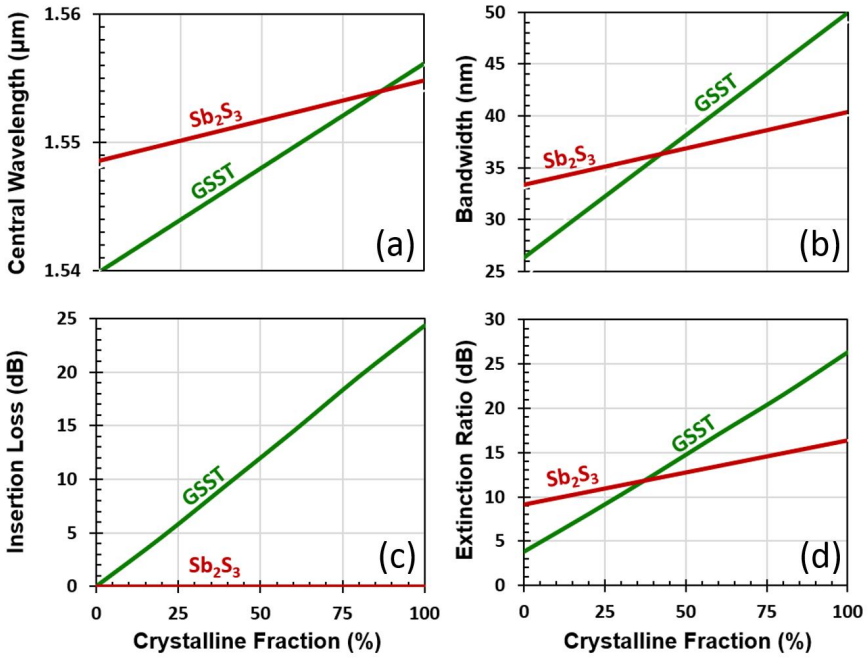

Fig. 7.6 Performance comparison between the two used phase-change materials: Sb_2S_3 with a fill factor $FF = 0.5$ and GSST2241 with a fill-factor $FF = 0.2$ for different crystallization states. (a) Central wavelength shift (b) bandwidth (c) insertion loss and (d) extinction ratio.

Tuneable band-pass filtering

The BGs described previously can be used as a building block to produce a non-volatile tuneable band-pass filter. These filters are capable of dynamically controlling which wavelengths are transmitted along the waveguide. This is achieved by arranging multiple different BG filters in series, with the ability to independently tune each BG, as shown in Fig 7.7 (a).

The BG represented in Fig. 7.7 (a) uses a period of N=100 and a fill-factor of 0.5. Because performance of the BG filters can be controlled just by modifying their period and fill-factor, the specific PCM alloy and its thicknesses can be common across all BG filters. This means all the required filters can be simultaneously fabricated onto the waveguide in a single lithography step. The example device, whose performance is shown in Fig. 7.7 (b), consists of three BG filters in series, with periods of Λ_1=485 nm (L_{BG1}= 48.5 μm), Λ_2= 500 nm (L_{BG2}= 50 μm), and Λ_3=515 nm (L_{BG3}= 51.5 μm). This results in three Bragg wavelengths positioned around λ_{BG1}=1.5 μm, λ_{BG2}= 1.55 μm, and λ_{BG3}=1.6 μm respectively. Each of the central wavelengths can be tuned by 7 nm by changing the state of the Sb_2S_3 from amorphous to crystalline; this means the width of the pass-bands can be

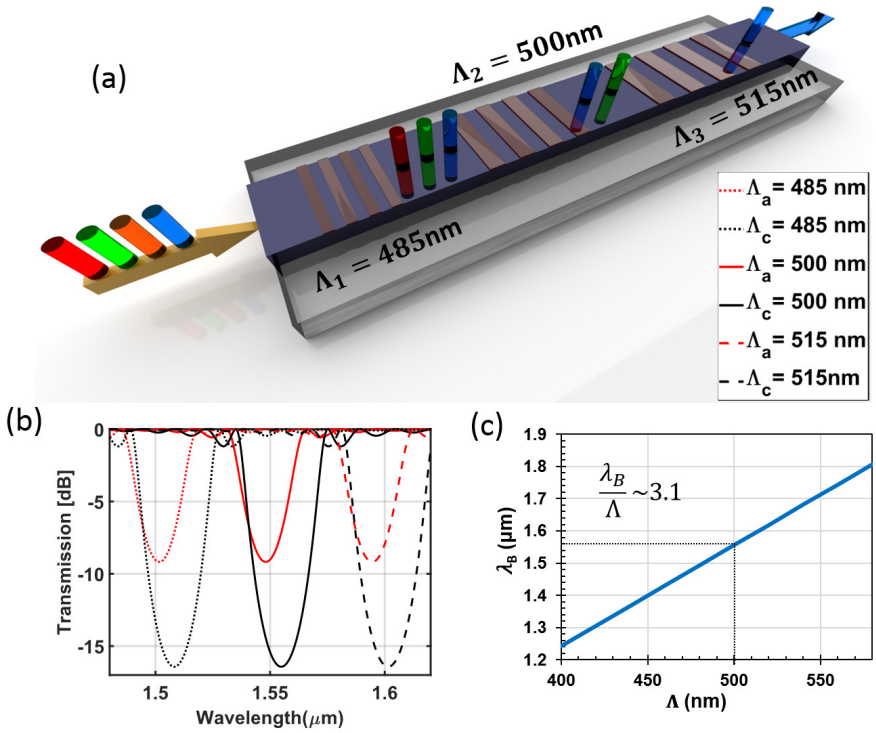

Fig. 7.7 Multilevel tuneable filters consisting of an array of 3 BGs placed in series. Each grating has a different periodicity (Λ_1, Λ_2, Λ_3). (a) Schematic of the filter, showing just 4 periods per grating (actual device consists of N=100 with fill-factor of 0.5). (b) Transmission spectrum for different BG periodicity for different phase-change material state. amorphous (red line) and crystalline (black line): The length of the three different BGs are L_{BG_1}=48.5 μm, L_{BG_2}=50 μm and L_{BG_3}= 51.5 μm respectively and (c) Bragg wavelength for different periods of the grating.

controlled. The extinction ratio for all the gratings in the amorphous state has a value of $\sim$ 9.2 dB and can be increased up to $\sim$16.3 dB when crystallization occurs. A dependence between the Bragg wavelength (λ_b) and the period (Λ) of the grating is shown in Fig. 7.7 (c), the ratio between the period and the wavelength is 3.1. This configuration of filters results in an in-plane on-chip metamaterial that can be used as part of micro-ring resonators or Mach-Zehnder interferometers for future non-volatile frequency selectors.

7.1.3 Combined frequency and amplitude tuning

Incorporating Sb_2S_3 cells on a silicon nitride waveguide, spectral tuneability controlled by the phase of the material (crystalline fraction) has been demonstrated. Furthermore, a BG

structure using GSST, which can provide amplitude tuneability (ON/OFF switching) has been shown. Building a BG primarily from Sb_2S_3 cells, and including a single 'defect' cell of GSST see [Fig. 7.8 (a)] produces two useful effects. Firstly, the defect introduced within the BG (due to the difference between the two effective refractive indices n_{eff} between PCMs) creates an ultra-high quality factor transmission peak. Secondly, while GSST is near-lossless when amorphous, its crystallization fraction controls the amplitude of the new peak via optical absorption, as shown in Figs. 7.8 (b-c).

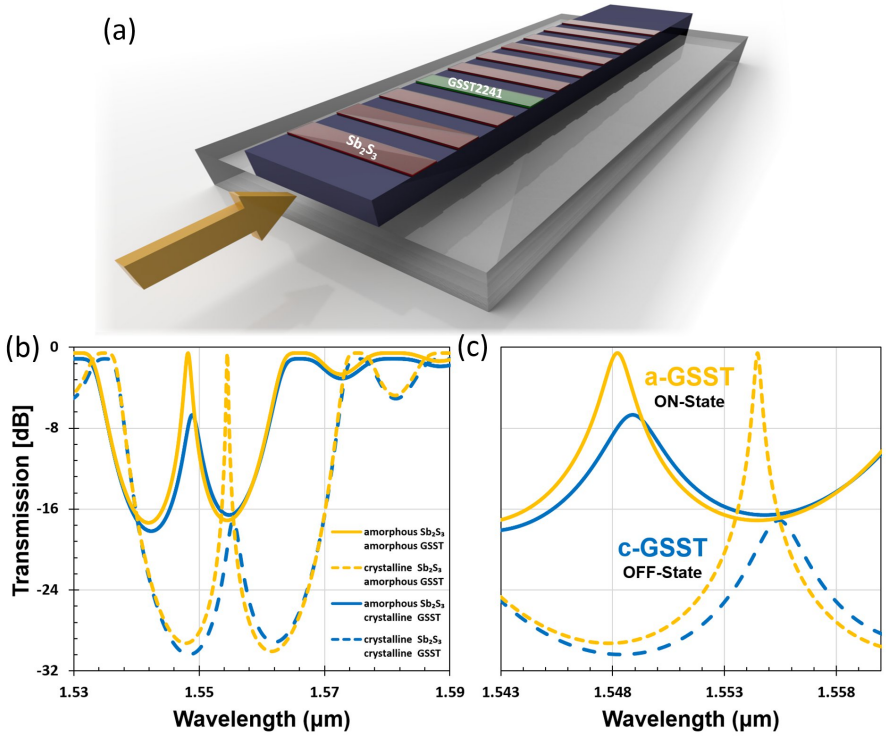

Fig. 7.8 (a) Schematic of a re-configurable, ultra-high quality factor filter based on phase-change materials. A defect in the Sb_2S_3 BG is created by replacing a Sb_2S_3 cell with a GSST cell. This generates an ultra-high quality factor peak in the Bragg resonance. Absorption within the defect (and therefore amplitude of high quality factor peak) can be controlled via the crystallization fraction of the GSST. (b) Transmission response of the proposed device for both phases of both phase-change materials (c) Zoom in of the peak resonance produced by the defect cell.

Due to the low total volume of GSST, the absorption (even when fully crystallised) in the defect cell is typically negligible (PL= 0.53 dB$/\mu m \cdot 0.25\mu m = 0.13$ dB), however, it is greatly enhanced at the high quality factor peak's resonance wavelength. This amplification is due to the Fabry-Pérot like cavity resonance present in this section of the waveguide

due to the two Bragg grating reflectors. In the proposed device, the number of periods (N) for the BG is 200 in total, 100 placed on the left hand side of the defect and 100 on the right hand side of the defect. A fill-factor ($FF = 0.5$) and a period of 500 nm have been selected, obtaining a total length for the device of L_{device} = 100 μm. The GSST cell is also 250 nm long, and is placed between the two BG reflectors. The resulting device produces a transmission peak which can be tuned from 1548 nm to 1555 nm ($\Delta\lambda$ = 7 nm) depending on the Sb_2S_3 crystallization fraction. For amorphous Sb_2S_3, the quality factor is $Q = 609$, with an extinction ratio of ER = 17 dB. When crystallised the quality factor raises up to $Q = 1,028$, and the extinction ratio increases up to ER = 30 dB. The normalized transmission of this peak is near 100 percent when the GSST is amorphous, and can be tuned down to -7 dB for a-Sb_2S_3, and -16 dB for c-Sb_2S_3 for crystalline GSST. Furthermore, this BG filter configuration is also appropriate as a building block to produce band-pass filters like those discussed in the previous section.

7.2 O-band N-rich Silicon Nitride MZI based on GST

The combination of SiNx photonic integrated waveguides and PCMs can lead to fast (ns) non volatile reconfigurable technologies for optical communications applications [304, 150]. The silicon nitride platform refractive index can be tuned modifying the deposition conditions yielding to different silicon nitride platforms, comprising, N-rich silicon nitride ($n = 1.92$), Si-rich silicon nitride ($n = 2.54$), or stoichiometric silicon nitride ($n = 2.01$) [46]. Different silicon and SiNx building blocks have been explored in the C-band using PCMs as the reconfigurable material [305, 145]. In this section, an O-band N-Rich Silicon Nitride Mach-Zehnder Interferometer (MZI) based on the commonly used $Ge_2Sb_2Te_5$ (GST) phase change material is presented, providing a non-volatile material for applications in the O-band for optical communications [Fig. 7.9].

7.2.1 Design

The optical platform consists of a 700 nm wide N-rich silicon nitride strip waveguide formed by etching a 600 nm thick SiNx layer [223]. This design allows both single TE and TM mode propagation with low losses in the O-band (<1dB/cm). The propagation losses measured with this geometry account for both the material absorption losses and the scattering losses produced due to the sidewall roughness of the waveguides. The asymmetric MZI structure is built with two multi-mode interferometers (MMI) that split the input signal into two arms of different length and then combine them into an output signal. A thin layer (15 nm)

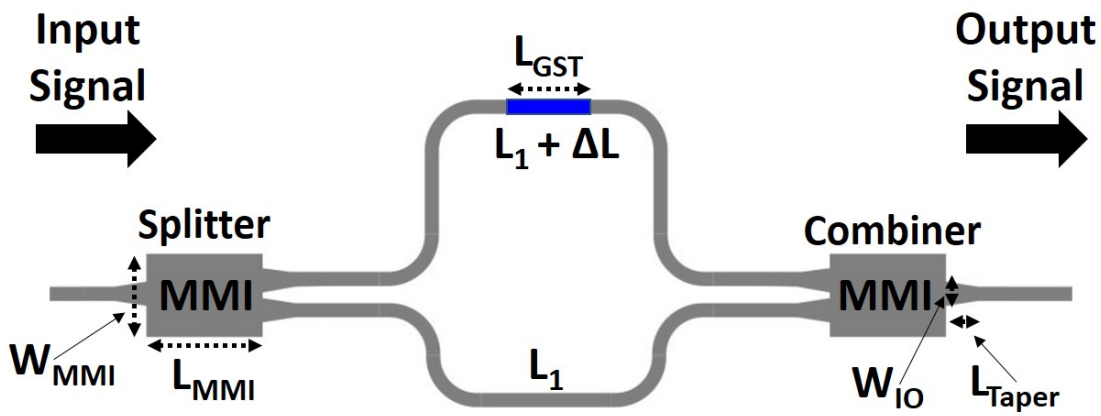

Fig. 7.9 Schematic of the MZI with a GST cell of the length L_{GST}= 5, 10 and 15 μm deposited on the longer arm (top arm) of the length L_1 + ΔL , where L_1 = 614 μm and ΔL = 20, 40 and 60 μm. MMI structure with width W_{MMI} = 15 μm and length L_{MMI}= 168 μm are used as splitters/combiners. The width of the single mode waveguide (700 nm) is tapered to W_{IO} = 6 μm with tapers of length L_{taper} = 100 μm to increase the fidelity of the MMIs.

of phase-change material (PCM) is deposited on top of the longer arm of the asymmetric MZI with cells of different length (5, 10 and 15 μm), with a 10 nm thick protective SiO_2 encapsulation layer. By using an asymmetric MZI design, the engineering of the device performance in two ways: by tuning the length difference between the arms (ΔL) and the geometry of the deposited GST cell is enabled.

A PCM cell thickness of 15 nm was selected as it provides a good balance between attenuation and total transmission in the device between states [Fig. 7.10]. In this work, the phase-change alloy GST is used, due to the well-established fabrication methodology and most importantly, due to thorough characterisation of optical properties in both phases, which determine the partial attenuation of the guided modes, along with the characteristic non-volatile tunability and switching times within the nanosecond scale [306, 307]. This reconfigurable material provides a suitable platform for stable optical modulation exploiting Mach-Zehnder interferometers in the O-band, as demonstrated in this work. In order to estimate the waveguide transmissivity, losses, and the interferometer performances in terms of modulation and frequency selectivity, we numerically analysed the mode profile of each interferometer branch via COMSOL Multiphysics. TM polarization was selected due to the grating couplers fabrication optimization and the stronger mode overlap compared with the TE mode. The straight waveguide without GST layer demonstrated lossless propagation with real effective refractive index value for TM mode of $n_{eff} = 1.6518$. For the hybrid waveguide with the PCM cell, which represents the longer arm of the assymetrical MZI, the

phase of the GST layer and its effect on the different refractive index of the thin layer [Fig. 7.10 (a-b)] was studied for both amorphous and crystalline states.

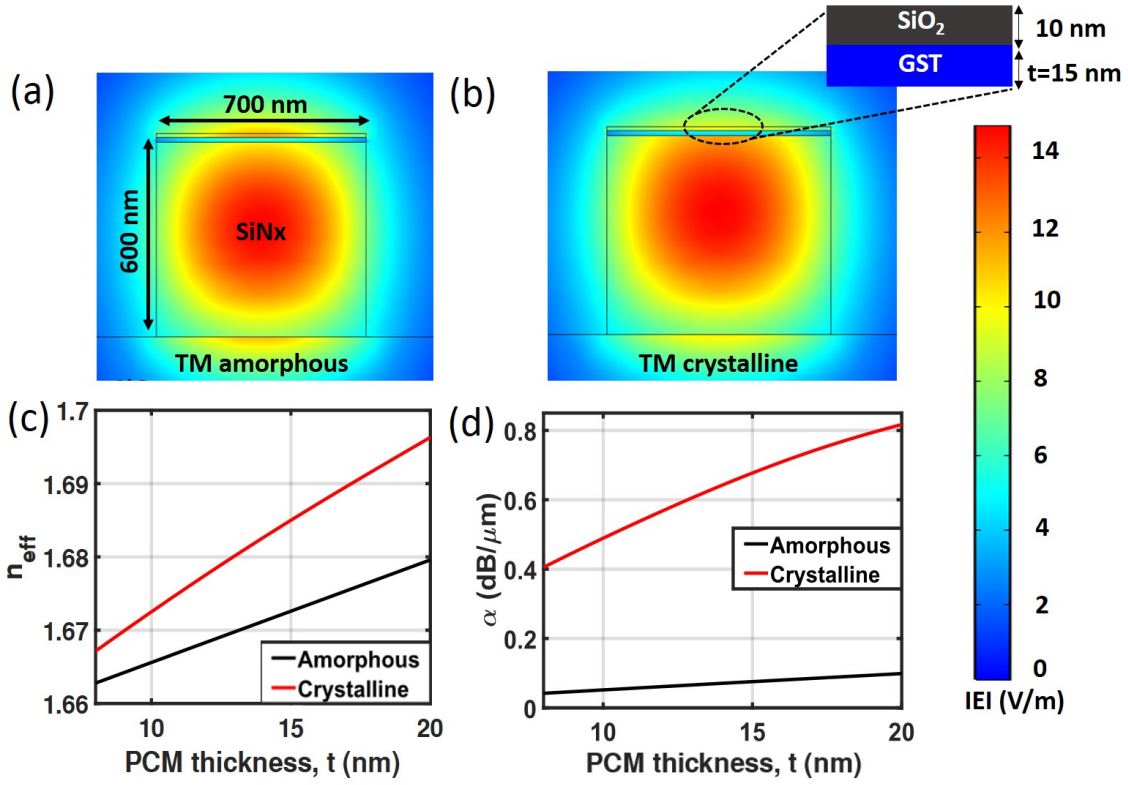

Fig. 7.10 Eigenmode simulation of fundamental TM optical mode propagating with GST layer on top in the (a) amorphous state, using PMMA as cladding and (b) crystalline, using SiO_2 as cladding; (c) effective refractive index and (d) mode attenuation both as a function of cell thickness.

For each case, n_{eff} was obtained. The real part of the effective refractive index (n^r_{eff}) is related with the propagation constant and the imaginary part (n^i_{eff}) is related with the absorption due to the phase state of the phase change material (amorphous or crystalline). The optical constants used in the simulations at 1310 nm are $n_{SiNx} = 1.92$, $n^a_{GST} = 3.96856 + j0.23$, $n^c_{GST} = 6.15 + j1.57$, $n_{SiO_2} = 1.4468$ and $n_{PMMA} = 1.4823$. This resulted in values for the TM mode effective refractive index of $n^a_{eff} = 1.67 + j1.8 \cdot 10^{-3}$ and $n^c_{eff} = 1.68 + j0.016$ for the amorphous and crystalline states respectively [Fig. 7.10 (a-b)]. The interface loss due to the reflection between the bare (no GST) and the hybrid (GST) structure in the longer arm of the MZI waveguide is 0.11 dB for the crystalline state and is 0.03 dB for the amorphous state. Consequently, the difference in the interface losses due to reflection between the amorphous and crystalline states is as low as 0.08 dB per interface [Fig. 7.11].

The theoretical values we have used for the simulations of the crystalline and amorphous state have been compared with measured ellipsometry and are consistent with published values in Ref. [308, 309]. The absorption and the phase shift of the phase change material strongly depend on the thickness of the PCM as shown in [Fig. 7.10 (c-d)] for the amorphous and crystalline states.

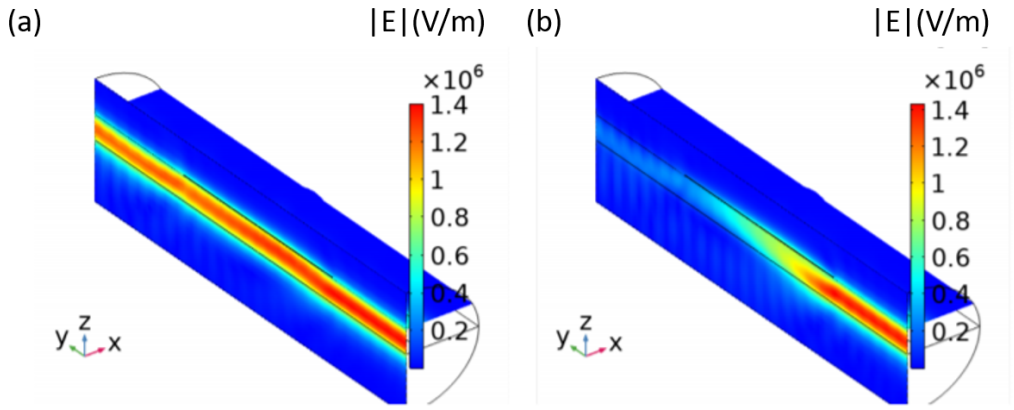

Fig. 7.11 3D simulation of fundamental TM optical mode propagating trough the silicon nitride waveguide with GST layer on top in the (a) amorphous state, using PMMA as cladding and (b) crystalline, using SiO_2 as cladding.

7.2.2 Fabrication

The assymetric MZIs were fabricated on a 600 nm thick nitrogen rich SiN_x layer with a refractive index of 1.92 at a wavelength of 1310 nm. This layer was deposited on a 8"(200 mm) Si wafer with a 2 μm thick thermally grown SiO_2 layer using a NH3-free plasma enhanced chemical vapour deposition (PECVD) process detailed in Ref [310] and Ref. [223]. The device layout was defined on the wafer using deep ultraviolet (DUV) lithography using a wavelength of 248 nm. The written design was then transferred to the SiNx layer using standard inductively coupled plasma (ICP) etching with an etch depth of 600 nm and a SF_6:CHF_3 chemistry. The GST cells capped by 10 nm of amorphous SiO_2 were then integrated on top of the MZIs using physical vapour deposition (PVD) of GST thin film through a lithography mask [Fig. 7.12].

The Mach-Zehnder interferometer, was fabricated with a difference between the arm length (ΔL) of 40, 60 and 80 μm. Three different GST cells with thickness of 15 nm, lengths of 5, 10 and 15 μm, and 700 nm width were deposited on top of the longer arm of the MZIs, capped by a second layer of 10 nm amorphous SiO_2 to prevent oxidation. When the fabrica-

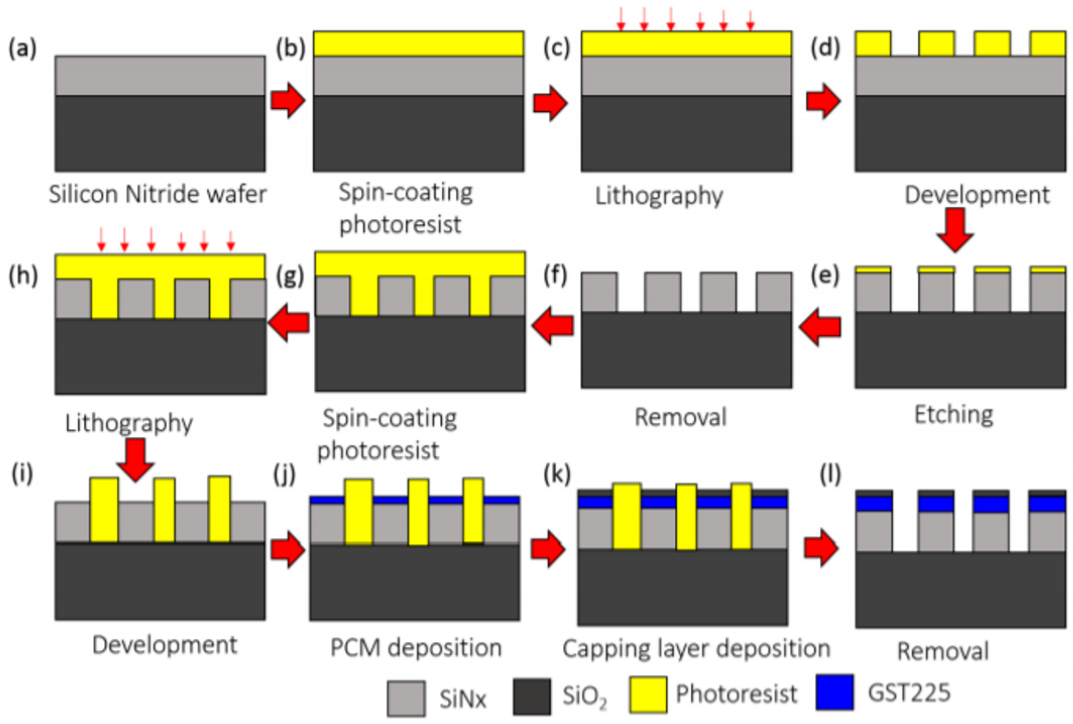

Fig. 7.12 Fabrication process flow: (a) Bare Nitrogen Rich Silicon wafer. (b) Negative photoresist spin-coating (c) MZI structures patterning by DUV lithography. (d) Negative photoresist development. (e) ICP etching. (f) Photoresist removal. (g) Positive photoresist spin-coating (h) Cells patterning by DUV. (i) Positive photoresist development. (j) Phase change material deposition. (k) Capping layer deposition. (l) Photoresist removal.

tion was completed, the devices were spin coated with Polymethyl methacrylate (PMMA) to enhance performance (optimize insertion loss of the grating couplers). PMMA was selected due to its similar optical properties to SiO_2 at 1310 nm, and room temperature process, avoiding thermal crystallization of the GST. Once the amorphous state was characterized, PMMA was removed and we induced the crystallization of the phase change material during the silicon oxide PCVD deposition process when temperatures as high as 350 ºC are reached [311] changing the PCM to its crystalline state. The phase transition is thermally driven (in this case the CVD chamber acted as an oven), GST forms a metastable distorted rocksalt phase [312], in which Te atoms occupy one sublattice, while Ge, Sb, and vacancies occupy the second one in a random fashion. With sufficient thermal energy crystallites will form within the amorphous matrix (nucleation), and grow [313]. SEM and optical microscopy images were taken for the different asymmetric MZI structures with the GST cell deposited on the longer arm [Fig. 7.13].

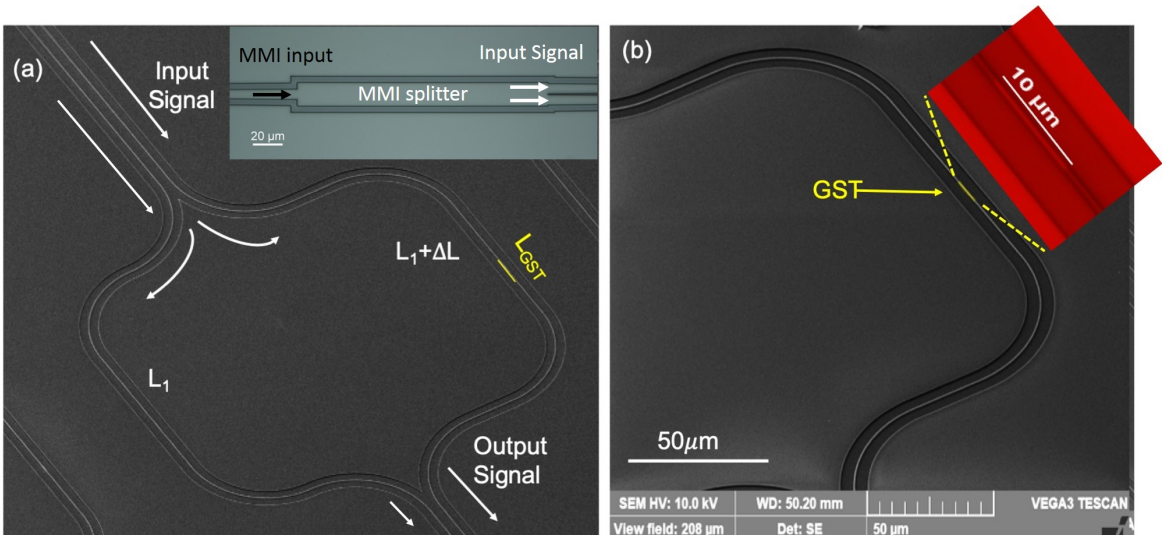

Fig. 7.13 (a) SEM image of an asymmetric MZI based on SiNx and phase change material (GST), SEM image of the MMI splitter as an inset. (b) Zoom in image verifying the position of the phase change material cell (yellow) deposited on the longer arm of the MZI.

7.2.3 Characterization

Using the constructive interference equation of a MZI, the experimental effective refractive index of the waveguide can be determined as:

$$m \cdot \lambda_m = n_{eff} \Delta L \tag{7.8}$$

where λ_m is the interfering wavelength, m is the filter order, n_{eff} is the effective refractive index of the bare 700 x 600 nm ridge waveguide TE mode coated with PMMA on top, and ΔL is the difference between the length of the two arms of the MZI. A bare MZI with ΔL= 20 μm and filter order of $m = 25$ was fabricated. Using the spectral response of the fabricated MZI [Fig. 7.14], the TM effective refractive index of the 700 x 600 nm ridge waveguide structure was obtained, yielding to a value of $n_{eff} = 1.63$. A free spectral range (FSR) of 46 nm and ER of 22.73 dB were measured.

The spectral responses of the MZIs for different cell lengths for both amorphous and crystalline states of the phase change material were characterised using an Agilent 8164B tuneable laser source with a tuneable wavelength of 1260 to 1320 nm [Fig 7.15]. The polarisation of the light was controlled to ensure that only TM modes could propagate through the devices. All MZIs structures were connected to input and output grating couplers consisting of a 10 μm width and 40 μm length with a period of 950 nm tapered down to a single-mode waveguide of 700 nm. The angle of the optical fibers was selected to be 14° to ensure maximum coupling at the wavelength of interest (1310 nm).

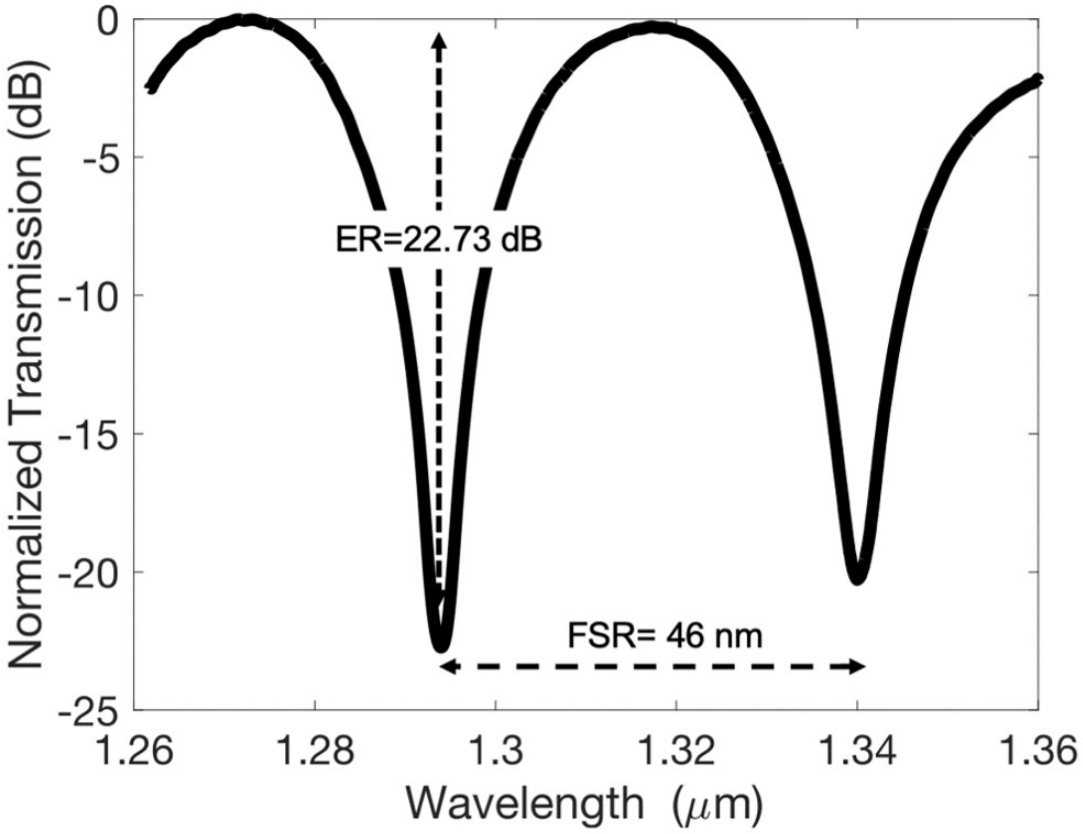

Fig. 7.14 Bare MZI interferometer spectrum for a difference between the arms of ΔL= 20 μm

By switching the state of the GST cell, an optical switch is demonstrated in the O-band. The normalized transmission was calculated by removing the grating couplers contribution to optical insertion losses. Consequently, the measured optical losses are intrinsic to the MZI device. Values for the MZI device losses (DLs) of 0.14 $\pm$ 0.02, 0.42 $\pm$ 0.03 and 0.98 $\pm$ 0.04 dB were measured in the amorphous state of the phase change material for 5, 10 and 15 μm cell, respectively. For the crystalline state, MZI optical insertion loss values were measured as high as 3.9 $\pm$ 0.8 dB, 7.1 $\pm$ 1.7 dB and 13.4$\pm$ 1.6 dB, for the different cell lenghts (5, 10 and 15 μm). The experimental losses measured in these devices are 0.064 dB/μm (ON-state) and 0.87 dB/μm (OFF-state) [Fig 7.16] which matches with the theoretical MZI optical losses for the amorphous and crystalline states of the cell calculated in Fig. 7.10 (d) which are 0.075 dB/μm and 0.68 dB/μm respectively. The discrepancy between experimental and theoretical results are due to the thickness of the GST cell and fabrication defects that affect the effective refractive index calculation [314]. The difference in the insertion loss between the amorphous and crystalline states is the key component for

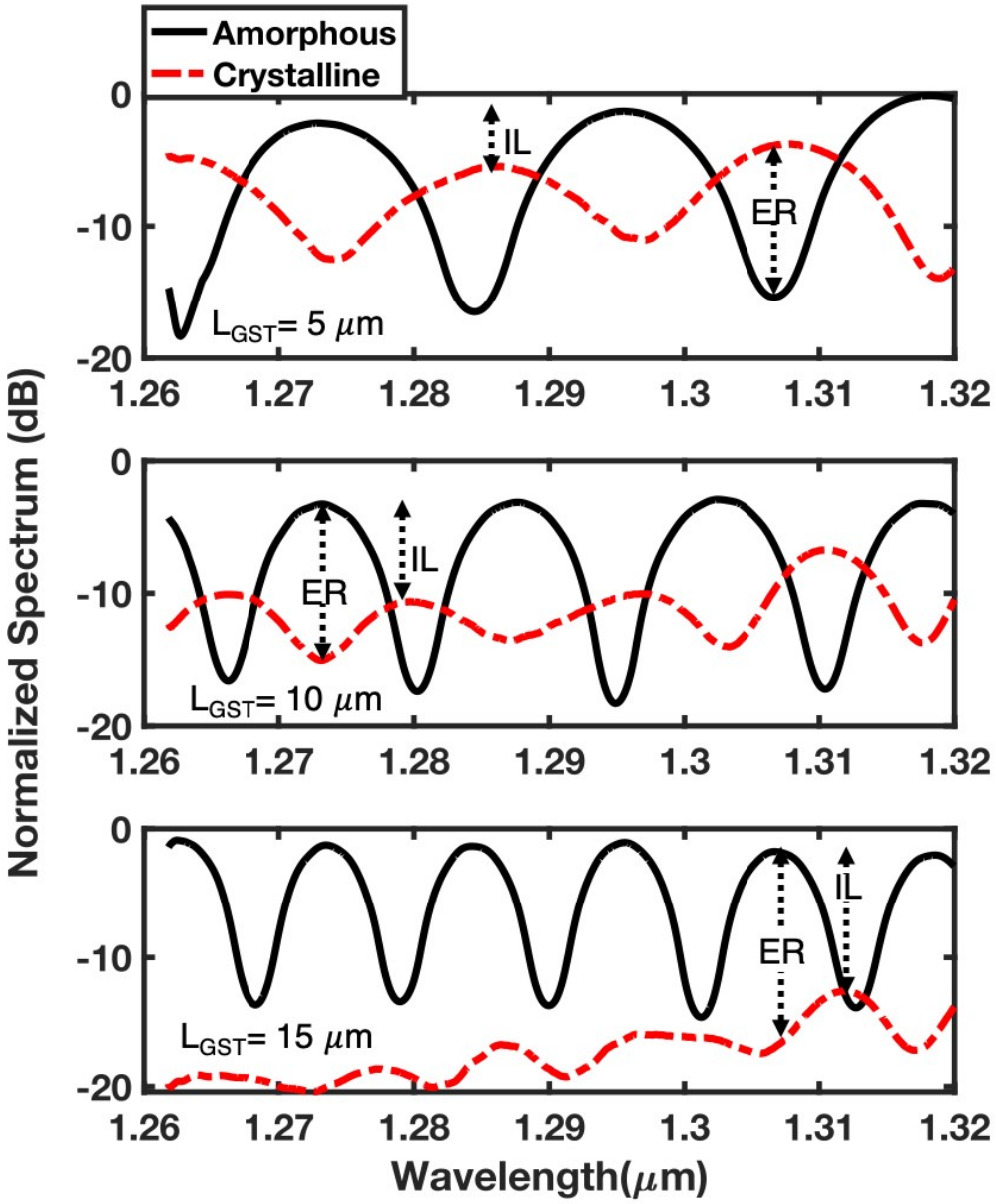

Fig. 7.15 Experimental normalized transmission from top to bottom of a MZI with ΔL= 40 μm and L_{GST}= 5 μm in the amorphous state (black) and in the crystalline state (red) [Top Figure]. Experimental normalized transmission for a MZI with ΔL= 60 μm and L_{GST}= 10 μm in the amorphous state (black) and in the crystalline state (red) [Mid Figure]. Experimental normalized transmission for a MZI with ΔL= 80 μm and L_{GST}= 15 μm in the amorphous state (black) and in the crystalline state (red) [Bottom Figure].

future non-volatile reconfigurable switches in the O-band. An extinction ratio (ER) as high as 11.5 dB in transmission was measured for a L_{GST}= 5 μm at 1307 nm and ΔL= 40 μm with 4 dB insertion loss (IL). IL was calculated using the difference between the DL of the

two different material states. Increasing the length of the cell to L_{GST}= 10 μm and ΔL= 60 μm results in an ER of 12.3 dB at 1273 nm with an insertion loss of 7 dB. Finally, for a cell of L_{GST}= 15 μm and ΔL= 80 μm, a 13 dB extinction ratio was measured at 1310 nm, with an insertion loss of 12 dB [Fig. 7.16]. An extinction ratio (ER) difference between the amorphous and crystalline states for the different cells lengths greater than 11 dB has been demonstrated. The optical switch due to the change of the phase change material state (amorphous or crystalline) allows to distinguish between different transmission levels.

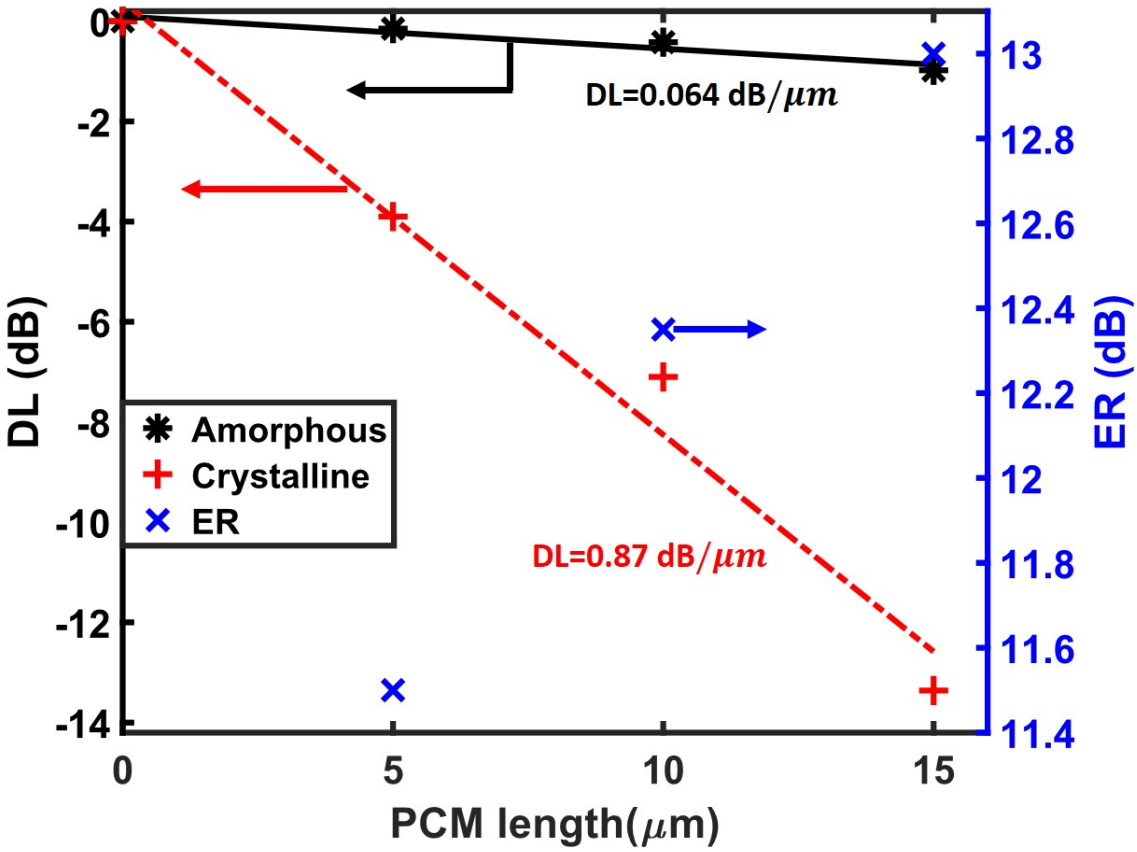

Fig. 7.16 Device Losses (DLs) of the MZI device for the amorphous state (black markers) and crystalline state (red markers) with a linear fitting for the amorphous state (black line) and for the crystalline state (red line) for different GST cell lengths (left axis), Extinction ratio (ER) of the MZI for the different length of the cell (right axis)

Different technologies such as: liquid crystals [315], graphene [316, 317], p-n junctions [38], and micro-heaters [318] have been used as basic components to create silicon or silicon nitride based MZI switches. Other platforms such as $LiNbO_3$ [319, 320] or electro-absorption [321, 322] based switches have been demonstrated and they present an alternative to the CMOS compatible silicon photonic platform. All these technologies are volatile with

switching mechanism being thermo-optic (T-O) or electro-optic (E-O), while the change in the refractive index between states is relatively small (Δn$\sim$0.21). Using non-volatile phase change materials, specifically GST, the refractive index difference can be achieved as high as Δn $\sim$2, however, the losses of the device in the crystalline state are also increased in comparison to the other technologies. An overview table which compares different MZI switches technologies is presented in Table. 7.3.

	IL (dB)	ER (dB)	Switching time	Power (W)	Footprint (mm^2)	Technology
MZI - GST*	7-12	11-13	ns[a]	0.1[a]	0.4	Non-volatile
T-O MZI [323, 318, 324, 325]	4-22	15-35	30-250 μs	0.07-1.9	0.12-2.62	Volatile
E-O MZI [326–329]	6-17	10-30	ps	0.05-1.2	0.04-0.05	Volatile

Table 7.3 Comparison between this work * and the state-of-the-art of MZI based switches. Estimated value [a].

7.3 Summary

A reconfigurable and non-volatile Bragg grating in the telecommunication C-band based on the combination of novel low-loss phase-change materials (specifically $Ge_2Sb_2Se_4Te_1$ and Sb_2S_3) with a silicon nitride platform has been proposed. The Bragg grating is formed by arrayed cells of phase-change material, whose crystallization fraction modifies the Bragg wavelength and extinction ratio. These devices could be used in integrated photonic circuits for optical communications applications in smart filters and Bragg mirrors and could also find use in tuneable ring resonators, Mach–Zehnder interferometers or frequency selectors for future laser on chip applications. In the case of $Ge_2Sb_2Se_4Te_1$, crystallization produces a Bragg resonance shift up to $\sim$ 15 nm, accompanied with a large amplitude modulation (insertion loss of 22 dB). Using Sb_2S_3, low losses are presented in both states of the phase change material, obtaining a $\sim$ 7 nm red-shift in the Bragg wavelength. The gratings are evaluated for two period numbers, 100 and 200 periods. The number of periods determines the bandwidth and extinction ratio of the filters. Increasing the number of periods increases the extinction ratio and reflected power, also narrowing the bandwidth. This results in a trade-off between device size and performance. Furthermore, both phase-change materials in a single Bragg grating to provide both frequency and amplitude modulation are combined. A defect is introduced in the Sb_2S_3 Bragg grating, producing a high quality factor resonance ($Q \sim 10^4$) which can be shifted by 7 nm via crystallization. A GSST cell is then placed in the defect which can modulate the transmission amplitude from low loss to below -16 dB.

Finally, an O-band Mach-Zehnder interferometer (MZI) based on a N-rich silicon nitride platform combined with $Ge_2Sb_2Te_5$ for future optical communication applications in the O-band has been experimentally demonstrated. The device operation relies on controlling the waveguide's losses using a phase change material cell which can be changed from amorphous (low-loss) to crystalline (high-loss). An extinction ratio (ER) as high as 11 dB was obtained between the amorphous (ON) and the crystalline (OFF) states of the MZI optical building block. The insertion loss of the MZI structure per cell unit length was measured to be as high as 0.87 dB/μm in OFF state and as low as 0.064 dB/μm in ON state for TM polarisation.

Chapter 8

Conclusion and Further Work

8.1 Conclusion

This thesis has presented a detailed study of ways in which different active materials can be combined with silicon and silicon nitride photonic integrated building blocks in order to deliver dynamic reconfigurability, and hence additional/new functionality. A particular focus of the work was on integration of liquid crystals, graphene and phase change materials in the amplitude modulators, phase modulators, Fabry-Pérot resonators and photonic memories. An emphasis of the thesis was on the design and development of practicable structures and devices, i.e. ones that (i) can be readily fabricated using CMOS-compatible techniques, (ii) can be used in real-world applications ranging from the O-band to the L-band and (iii) are amenable to in-situ switching using different active methods.

A FP resonator based on a Si-air 1D PhC with coupled triple-cavity modes (or defects) has been demonstrated in Chapter 4. These defects are obtained by filling selected air channels in the 1D PhC with an actively reconfigurable fluid (LC). Simulations of the optical properties of these FP resonators were performed in the wide infrared spectral range. It was shown that by changing the refractive index of the fluid simultaneously in all three channels, a set of narrow triple resonance peaks can be obtained within wide stop-bands of different order in the infrared range. In addition, at certain values of refractive index, splitting of the triple resonance peaks into a doublet and a single peak with a significantly larger quality factor occurs. Combining liquid crystals with 1D photonic crystals can bring different functionalities in silicon integrated circuits like filters for laser on chip applications.

In chapter 5, the potential of a graphene capacitor structure on SRN micro-ring resonators for multitasking and HPC have been shown. The electro-absorption effect can be used to develop multilevel volatile memories for communications applications, optical routing and binary coding. By tuning the capacitor length, a shift in the resonant wavelength is produced

giving rise to a broadband multilevel photonic volatile memory. An increase in the device speed has been shown to be achieved by using a silicon rich nitride waveguide in place of Si_3N_4, due to the increased confinement of the propagating mode allowing a smaller device footprint.The possibility to double the speed of the devices from 31.2 GHz up to 62.41 GHz in this way has been demonstrated. A study of the relation between the device energy consumption, extinction ratio and capacitor length has been shown. Finally, it has been demonstrated that increasing the permittivity of the insulator layer in the capacitor structure, the energy consumption per bit can be reduced. Furthermore, a graphene heater has been employed on top of a rib silicon nitride waveguide in oder to create an optical memory using electrical pulses to set or reset the phase change material cell to control the transmission. The energy consumption of the optical memory is 2 μJ and 0.13 μJ for the crystallization and amorphisation process respectively.

The evaluation and comparison of the optical properties in the O and C bands of silicon nitride rib waveguides with integrated $Ge_2Sb_2Te_5$ phase-change cells is reported. In straight rib waveguides, a high transmission contrast was observed in both bands when the $Ge_2Sb_2Te_5$ cell is switched between states, being up to 2.5 dB/μm in the C-band and 6.4 dB/μm in the O-band. In the case of silicon nitride ring resonator waveguides, high quality factor resonances ($Q \sim 10^5$) are found in both bands, leading to the provision of an ON-OFF switch characterized by an extinction ratio of 12 and 18 dB in O and C bands respectively. Finally, with the view to provide a comparison of the wavelength-dependent optical switching of the phase-change cell, a 3-dimensional finite-element method simulation was performed and a comparison of the optical-to-thermal energy conversion in both bands given in Chapter 6, where for the different wavelengths, a marginal variation of efficiency is observed for the crystal case, with an efficiency value in the C-band lightly higher than the O-band, yielding a ratio between efficiencies of 0.8. However,for the amorphous case,the O-band efficiency is typically around 4 times higher than the corresponding C-band value,in the whole range of investigated pulse duration.

Finally, in chapter 7, a reconfigurable and non-volatile Bragg grating in the telecommunication C-band based on the combination of novel low-loss phase-change materials (specifically $Ge_2Sb_2Se_4Te_1$ and Sb_2S_3) with a silicon nitride platform has been proposed. The Bragg grating is formed by arrayed cells of phase-change material, whose crystallisation fraction modifies the Bragg wavelength and extinction ratio. These devices could be used in integrated photonic circuits for optical communications applications in smart filters and Bragg mirrors and could also find use in tuneable ring resonators, Mach–Zehnder interferometers or frequency selectors for future laser on chip applications. In the case of $Ge_2Sb_2Se_4Te_1$, crystallisation produces a Bragg resonance shift up to $\sim$ 15 nm, accompanied

with a large amplitude modulation (insertion loss of 22 dB). Using Sb_2S_3, low losses are presented in both states of the phase change material, obtaining a $\sim$ 7 nm red-shift in the Bragg wavelength. The gratings are evaluated for two period numbers, 100 and 200 periods. The number of periods determines the bandwidth and extinction ratio of the filters. Increasing the number of periods increases the extinction ratio and reflected power, also narrowing the bandwidth. This results in a trade-off between device size and performance. Furthermore, both phase-change materials are combined in a single Bragg grating to provide both frequency and amplitude modulation. A defect is introduced in the Sb_2S_3 Bragg grating, producing a high quality factor resonance ($Q \sim 10^4$) which can be shifted by 7 nm via crystallisation. A GSST cell is then placed in the defect which can modulate the transmission amplitude from low loss to below -16 dB. Finally, an O-band Mach-Zehnder interferometer (MZI) based on a N-rich silicon nitride platform combined with $Ge_2Sb_2Te_5$ for future optical communication applications in the O-band has been experimentally demonstrated. The device operation relies on controlling the waveguide's losses using a phase change material cell which can be changed from amorphous (low-loss) to crystalline (high-loss). An extinction ratio (ER) as high as 11 dB was obtained between the amorphous (ON) and the crystalline (OFF) states of the MZI optical building block. The insertion loss of the MZI structure per cell unit length was measured to be as high as 0.87 dB/μm in OFF state and as low as 0.064 dB/μm in ON state for TM polarisation.

In conclusion, different active materials such as, liquid crystals, graphene and phase change materials can be combined with different integrated building blocks platforms such as silicon or silicon nitride in order to obtain the desired functionality for the specific required application. Different switching mechanisms can be carried out in the different technologies, electrical, optical or thermal switching, giving a set of devices with volatile and non-volatile behaviour for future reconfigurable integrated photonics.

8.2 Further work

It is interesting to highlight different rewarding routes for further technological development of the concepts put forward in this thesis. One of them is related to the improvement of the performance and robustness of the reconfigurable passive photonic integrated platforms. A second one is related to the use of the proposed devices that work in the near infrared or in the visible part of the electromagnetic spectrum for photonic integrated holography. Finally, this work can be used for future individual building blocks in neuromorphic computing and quantum computing. As it has been pointed out, the performance in terms of switchability

and energy efficiency is expected to be improved by thermally switching the phase change materials on chip.

Preliminary modelling results have been obtained for directional couplers, 2D PhC, and Bragg gratings using novel low-loss phase change materials. Having an experimental demonstration of the correct operation of this structure is something that would have a high value due to its novelty and its potentially superior performance (e.g. in terms of switching speeds and energies) in reconfigurable photonic integrated circuits. As well as this, a detailed study of alternative (to GSST, GLS and GeTe) phase-change materials, 2D materials, and liquid crystals is an area that could potentially be of great benefit for the configurable integrated photonics community, paying particular attention to not only the optical properties (n and k) of the different materials, but also to the electrically-driven in-situ switching capabilities and switching energy. Another aspect of interest to be further explored is the multilevel operation of the designed devices and the improvement of the performance upon switching. Having a multilevel operation implies that the designed devices would be potentially able to carry out more complex tasks.

The main goal of using different technologies is to create all the different components needed in a reconfigurable integrated chip, for example, using 2D materials to create a laser on chip which will be followed by a 1D PhC based on liquid crystals to tune the emitting wavelength of the laser on chip. Afterwards, the graphene modulators and the phase change material memory can be incorporated in order to create different functionalities, such as an optical ROM and RAM memory. Finally different 2D materials can be used as photodetectors, covering the different components in order to give the required functionality needed in a reconfigurable photonic integrated circuit.

References

[1] G. T. Reed, G. Mashanovich, F. Y. Gardes, and D. J. Thomson, "Silicon optical modulators," *Nature Publishing Group*, vol. 4, no. 8, pp. 518–526, 2010.

[2] W. Bogaerts and L. Chrostowski, "Silicon photonics circuit design: methods, tools and challenges," *Laser & Photonics Reviews*, vol. 12, no. 4, p. 1700237, 2018.

[3] D. Thomson, A. Zilkie, J. E. Bowers, T. Komljenovic, G. T. Reed, L. Vivien, D. Marris-Morini, E. Cassan, L. Virot, J.-M. Fédéli, J.-M. Hartmann, J. H. Schmid, D.-X. Xu, F. Boeuf, P. O'Brien, G. Z. Mashanovich, and M. Nedeljkovic, "Roadmap on silicon photonics," *Journal of Optics*, vol. 18, no. 7, p. 073003, 2016.

[4] G. Masini, S. Denton, S. Sahni, A. Mekis, T. Pinguet, J. Balardeta, P. D. Dobbelaere, A. Dahl, B. Weber, B. Chase, B. Welch, D. Foltz, G. McGee, G. Wong, G. Armijo, G. Yastola, G. Hocson, K. Khauv, J. Dotson, J. Schramm, K. Hon, K. Robertson, K. Stechschulte, K. Yokoyama, L. Planchon, L. Tullgren, M. Peterson, M. Eker, M. Mack, M. Musciano, P. Milton, P. Sun, R. Zhou, R. Bruck, S. Fathpour, S. Wang, S. Yu, S. Pang, S. Tran, S. Gloeckner, S. Jackson, W. Putman, W. Li, Y. D. Köninck, Y. Liang, and Y. Chi, "Silicon photonics transceivers for high-speed data communication," in *2017 Conference on Lasers and Electro-Optics Pacific Rim*, p. s2317, Optical Society of America, 2017.

[5] A. Mishra, A. Basu, and V. Tyagi, *Silicon Photonics & High Performance Computing*. Springer, 2018.

[6] Y. Chen, H. Lin, J. Hu, and M. Li, "Heterogeneously integrated silicon photonics for the mid-infrared and spectroscopic sensing," *ACS nano*, vol. 8, no. 7, pp. 6955–6961, 2014.

[7] L. Chrostowski and M. Hochberg, *Silicon photonics design: from devices to systems*. Cambridge University Press, 2015.

[8] J. N. Milgram, J. Wojcik, P. Mascher, and a. P. Knights, "Optically pumped Si nanocrystal emitter integrated with low loss silicon nitride waveguides.," *Optics express*, vol. 15, no. 22, pp. 14679–14688, 2007.

[9] K. Ikeda, R. E. Saperstein, N. Alic, and Y. Fainman, "Thermal and Kerr nonlinear properties of plasma-deposited silicon nitride/ silicon dioxide waveguides," *Optics Express*, vol. 16, no. 17, p. 12987, 2008.

[10] M. Romagnoli, V. Sorianello, M. Midrio, F. H. L. Koppens, C. Huyghebaert, D. Neumaier, P. Galli, W. Templ, A. D'Errico, and A. C. Ferrari, "Graphene-based integrated photonics for next-generation datacom and telecom," *Nature Reviews Materials*, vol. 3, no. 10, pp. 392–414, 2018.

[11] H. Dalir, Y. Xia, Y. Wang, and X. Zhang, "Athermal Broadband Graphene Optical Modulator with 35 GHz Speed," *ACS Photonics*, vol. 3, no. 9, pp. 1564–1568, 2016.

[12] F. J. Rodríguez-Fortuño, A. Espinosa-Soria, and A. Martínez, "Exploiting metamaterials, plasmonics and nanoantennas concepts in silicon photonics," *Journal of Optics*, vol. 18, no. 12, p. 123001, 2016.

[13] M. Liu, X. Yin, F. Wang, and X. Zhang, "Graphene optical modulator," *SPIE Optics 2011*, vol. 8101, pp. 81010J–81010J–6, 2011.

[14] M. Liu, X. Yin, and X. Zhang, "Double-layer graphene optical modulator," *Nano Letters*, vol. 12, no. 3, pp. 1482–1485, 2012.

[15] M. Mohsin, D. Neumaier, D. Schall, M. Otto, C. Matheisen, A. Lena Giesecke, A. A. Sagade, and H. Kurz, "Experimental verification of electro-refractive phase modulation in graphene," *Scientific Reports*, vol. 5, pp. 1–7, 2015.

[16] D. J. Thomson, F. Y. Gardes, J. M. Fedeli, S. Zlatanovic, Y. Hu, B. P. P. Kuo, E. Myslivets, N. Alic, S. Radic, G. Z. Mashanovich, and G. T. Reed, "50-Gb/s silicon optical modulator," *IEEE Photonics Technology Letters*, vol. 24, no. 4, pp. 234–236, 2012.

[17] M. Romagnoli, "Graphene photonics for optical communications," in *Optical Fiber Communication Conference*, pp. M3D–3, Optical Society of America, 2019.

[18] M. R. Jalali Azizpour, M. Soroosh, N. Dalvand, and Y. Seifi-Kavian, "All-optical ultra-fast graphene-photonic crystal switch," *Crystals*, vol. 9, no. 9, p. 461, 2019.

[19] J. Faneca, B. T. Hogan, I. R. Diez, F. Y. Gardes, and A. Baldycheva, "Tuning silicon-rich nitride microring resonances with graphene capacitors for high-performance computing applications," *Opt. Express*, vol. 27, pp. 35129–35140, Nov 2019.

[20] R. Baets, A. Z. Subramanian, S. Clemmen, B. Kuyken, P. Bienstman, N. Le Thomas, G. Roelkens, D. Van Thourhout, P. Helin, and S. Severi, "Silicon photonics: silicon nitride versus silicon-on-insulator," in *Optical Fiber Communication Conference*, pp. Th3J–1, Optical Society of America, 2016.

[21] A. D. Bristow, N. Rotenberg, and H. M. Van Driel, "Two-photon absorption and kerr coefficients of silicon for 850–2200 nm," *Applied Physics Letters*, vol. 90, no. 19, p. 191104, 2007.

[22] H. K. Tsang, C. Wong, T. Liang, I. Day, S. Roberts, A. Harpin, J. Drake, and M. Asghari, "Optical dispersion, two-photon absorption and self-phase modulation in silicon waveguides at 1.5 μ m wavelength," *Applied Physics Letters*, vol. 80, no. 3, pp. 416–418, 2002.

[23] M. Dinu, F. Quochi, and H. Garcia, "Third-order nonlinearities in silicon at telecom wavelengths," *Applied physics letters*, vol. 82, no. 18, pp. 2954–2956, 2003.

[24] D. Pérez, I. Gasulla, P. D. Mahapatra, and J. Capmany, "Principles, fundamentals, and applications of programmable integrated photonics," *Advances in Optics and Photonics*, vol. 12, no. 3, pp. 709–786, 2020.

[25] R. H. Freeman, "Configurable electrical circuit having configurable logic elements and configurable interconnects," Sept. 26 1989. US Patent 4,870,302.

[26] S. M. S. Trimberger, "Three ages of fpgas: A retrospective on the first thirty years of fpga technology: This paper reflects on how moore's law has driven the design of fpgas through three epochs: the age of invention, the age of expansion, and the age of accumulation," *IEEE Solid-State Circuits Magazine*, vol. 10, no. 2, pp. 16–29, 2018.

[27] C. M. Christensen, *The innovator's dilemma: when new technologies cause great firms to fail*. Harvard Business Review Press, 2013.

[28] J. Capmany and D. Pérez, *Programmable Integrated Photonics*. Oxford University Press, 2020.

[29] A. Peruzzo, A. Laing, A. Politi, T. Rudolph, and J. L. O'brien, "Multimode quantum interference of photons in multiport integrated devices," *Nature communications*, vol. 2, no. 1, pp. 1–6, 2011.

[30] B. J. Metcalf, N. Thomas-Peter, J. B. Spring, D. Kundys, M. A. Broome, P. C. Humphreys, X.-M. Jin, M. Barbieri, W. S. Kolthammer, J. C. Gates, *et al.*, "Multiphoton quantum interference in a multiport integrated photonic device," *Nature communications*, vol. 4, no. 1, pp. 1–7, 2013.

[31] A. N. Tait, T. F. De Lima, E. Zhou, A. X. Wu, M. A. Nahmias, B. J. Shastri, and P. R. Prucnal, "Neuromorphic photonic networks using silicon photonic weight banks," *Scientific reports*, vol. 7, no. 1, pp. 1–10, 2017.

[32] A. Ribeiro, A. Ruocco, L. Vanacker, and W. Bogaerts, "Demonstration of a $4\times$ 4-port universal linear circuit," *Optica*, vol. 3, no. 12, pp. 1348–1357, 2016.

[33] A. Annoni, E. Guglielmi, M. Carminati, G. Ferrari, M. Sampietro, D. A. Miller, A. Melloni, and F. Morichetti, "Unscrambling light—automatically undoing strong mixing between modes," *Light: Science & Applications*, vol. 6, no. 12, pp. e17110–e17110, 2017.

[34] D. Pérez, I. Gasulla, and J. Capmany, "Toward programmable microwave photonics processors," *Journal of Lightwave Technology*, vol. 36, no. 2, pp. 519–532, 2017.

[35] L. Chen, E. Hall, L. Theogarajan, and J. Bowers, "Photonic switching for data center applications," *IEEE Photonics journal*, vol. 3, no. 5, pp. 834–844, 2011.

[36] D. A. Miller, "Silicon photonics: Meshing optics with applications," *Nature Photonics*, vol. 11, no. 7, pp. 403–404, 2017.

[37] N. Thomas-Peter, N. K. Langford, A. Datta, L. Zhang, B. J. Smith, J. B. Spring, B. J. Metcalf, H. B. Coldenstrodt-Ronge, M. Hu, J. Nunn, *et al.*, "Integrated photonic sensing," *New Journal of Physics*, vol. 13, no. 5, p. 055024, 2011.

[38] F. Gardes, G. Reed, N. Emerson, and C. Png, "A sub-micron depletion-type photonic modulator in silicon on insulator," *Optics Express*, vol. 13, no. 22, pp. 8845–8854, 2005.

[39] C. Ríos, M. Stegmaier, P. Hosseini, D. Wang, T. Scherer, C. D. Wright, H. Bhaskaran, and W. H. P. Pernice, "Integrated all-photonic non-volatile multi-level memory," *Nature Photonics*, vol. 9, no. 11, pp. 725–732, 2015.

[40] G. T. Reed, G. Mashanovich, F. Y. Gardes, and D. Thomson, "Silicon optical modulators," *Nature photonics*, vol. 4, no. 8, p. 518, 2010.

[41] S. Wang, Y. Kawakami, J. Simpson, H. Stewart, K. Prior, and B. Cavenett, "Znsezncdse quantum confined stark effect modulators," *Applied physics letters*, vol. 62, no. 15, pp. 1715–1717, 1993.

[42] R. Welstand, C. Sun, S. Pappert, Y. Liu, J. Chen, J. Zhu, A. Kellner, and P. Yu, "Enhanced linear dynamic range property of franz-keldysh effect waveguide modulator," *IEEE photonics technology letters*, vol. 7, no. 7, pp. 751–753, 1995.

[43] G. T. Reed and A. P. Knights, *Silicon photonics: an introduction*. John Wiley & Sons, 2004.

[44] L. Chrostowski and M. Hochberg, *Silicon Photonics Design*. 2015.

[45] F. Vogelbacher, S. Nevlacsil, M. Sagmeister, J. Kraft, K. Unterrainer, and R. Hainberger, "Analysis of silicon nitride partial euler waveguide bends," *Optics express*, vol. 27, no. 22, pp. 31394–31406, 2019.

[46] T. D. Bucio, C. Lacava, M. Clementi, J. Faneca, I. Skandalos, A. Baldycheva, M. Galli, K. Debnath, P. Petropoulos, and F. Gardes, "Silicon nitride photonics for the near-infrared," *IEEE Journal of Selected Topics in Quantum Electronics*, vol. 26, no. 2, pp. 1–13, 2019.

[47] Y. A. Vlasov and S. J. McNab, "Losses in single-mode silicon-on-insulator strip waveguides and bends," *Optics express*, vol. 12, no. 8, pp. 1622–1631, 2004.

[48] K. P. Yap, A. Delâge, J. Lapointe, B. Lamontagne, J. H. Schmid, P. Waldron, B. A. Syrett, and S. Janz, "Correlation of scattering loss, sidewall roughness and waveguide width in silicon-on-insulator (soi) ridge waveguides," *Journal of Lightwave Technology*, vol. 27, no. 18, pp. 3999–4008, 2009.

[49] Y. Wang, Z. Lin, X. Cheng, C. Zhang, F. Gao, and F. Zhang, "Scattering loss in silicon-on-insulator rib waveguides fabricated by inductively coupled plasma reactive ion etching," *Applied physics letters*, vol. 85, no. 18, pp. 3995–3997, 2004.

[50] Y. Wang, M. Kong, Y. Xu, and Z. Zhou, "Analysis of scattering loss due to sidewall roughness in slot waveguides by variation of mode effective index," *Journal of Optics*, vol. 20, no. 2, p. 025801, 2018.

[51] D. K. Schroder, R. N. Thomas, and J. C. Swartz, "Free carrier absorption in silicon," *IEEE Journal of solid-state circuits*, vol. 13, no. 1, pp. 180–187, 1978.

[52] Y. Cheng and W. Lin, "Radiation loss in bent step-index slab waveguides," *Optics letters*, vol. 14, no. 21, pp. 1231–1233, 1989.

[53] R. Soref, "The past, present, and future of silicon photonics," *IEEE Journal of selected topics in quantum electronics*, vol. 12, no. 6, pp. 1678–1687, 2006.

[54] R. Soref, "Mid-infrared photonics in silicon and germanium," *Nature photonics*, vol. 4, no. 8, p. 495, 2010.

[55] R. Soref, "Group iv photonics for the mid infrared," in *Silicon Photonics VIII*, vol. 8629, p. 862902, International Society for Optics and Photonics, 2013.

[56] R. B. Wehrspohn, H.-S. Kitzerow, and K. Busch, *Nanophotonic materials: photonic crystals, plasmonics, and metamaterials*. John Wiley & Sons, 2008.

[57] G. T. Reed, *Silicon Photonics: The State of the Art*. 2008.

[58] T. Hu, B. Dong, X. Luo, T.-Y. Liow, J. Song, C. Lee, and G.-Q. Lo, "Silicon photonic platforms for mid-infrared applications," *Photonics Research*, vol. 5, no. 5, pp. 417–430, 2017.

[59] A. Yariv and P. Yeh, *Photonics: optical electronics in modern communications (the oxford series in electrical and computer engineering)*. Oxford University Press, Inc., 2006.

[60] Q. Li, M. Soltani, S. Yegnanarayanan, and A. Adibi, "Design and demonstration of compact, wide bandwidth coupled-resonator filters on a silicon-on-insulator platform," *Optics express*, vol. 17, no. 4, pp. 2247–2254, 2009.

[61] X. Shu, K. Chisholm, I. Felmeri, K. Sugden, A. Gillooly, L. Zhang, and I. Bennion, "Highly sensitive transverse load sensing with reversible sampled fiber bragg gratings," *Applied physics letters*, vol. 83, no. 15, pp. 3003–3005, 2003.

[62] A. M. Armani, R. P. Kulkarni, S. E. Fraser, R. C. Flagan, and K. J. Vahala, "Label-free, single-molecule detection with optical microcavities," *science*, vol. 317, no. 5839, pp. 783–787, 2007.

[63] S. Marquez, M. Alvarez, J. A. Plaza, L. Villanueva, C. Dominguez, and L. M. Lechuga, "Asymmetrically coupled resonators for mass sensing," *Applied physics letters*, vol. 111, no. 11, p. 113101, 2017.

[64] J. Lin, Q. Tong, Y. Lei, Z. Xin, D. Wei, X. Zhang, J. Liao, H. Wang, and C. Xie, "Electrically tunable infrared filter based on a cascaded liquid-crystal Fabry–Perot for spectral imaging detection," *Applied Optics*, vol. 56, no. 7, p. 1925, 2017.

[65] V. Tolmachev, T. Perova, E. Astrova, B. Volchek, and J. Vij, "Vertically etched silicon as 1d photonic crystal," *Physica status solidi (a)*, vol. 197, no. 2, pp. 544–548, 2003.

[66] G. Barillaro, L. M. Strambini, V. Annovazzi-Lodi, and S. Merlo, "Optical characterization of high-order 1-d silicon photonic crystals," *IEEE Journal of Selected Topics in Quantum Electronics*, vol. 15, no. 5, pp. 1359–1367, 2009.

[67] R. St-Gelais, A. Poulin, and Y.-A. Peter, "Advances in modeling, design, and fabrication of deep-etched multilayer resonators," *Journal of Lightwave technology*, vol. 30, no. 12, pp. 1900–1908, 2012.

[68] Y. Yi, P. Bermel, K. Wada, X. Duan, J. Joannopoulos, and L. Kimerling, "Tunable multichannel optical filter based on silicon photonic band gap materials actuation," *Applied physics letters*, vol. 81, no. 22, pp. 4112–4114, 2002.

[69] A. Lipson and E. M. Yeatman, "A 1-d photonic band gap tunable optical filter in (110) silicon," *Journal of Microelectromechanical Systems*, vol. 16, no. 3, pp. 521–527, 2007.

[70] J. Masson, R. St-Gelais, A. Poulin, and Y.-A. Peter, "Tunable fiber laser using a mems-based in plane fabry-pérot filter," *IEEE Journal of Quantum Electronics*, vol. 46, no. 9, pp. 1313–1319, 2010.

[71] Y. Zhao, X. Zhao, and Z. Gu, "Photonic crystals in bioassays," *Advanced Functional Materials*, vol. 20, no. 18, pp. 2970–2988, 2010.

[72] S. Surdo, S. Merlo, F. Carpignano, L. Strambini, C. Trono, A. Giannetti, F. Baldini, and G. Barillaro, "Optofluidic microsystems with integrated vertical one-dimensional photonic crystals for chemical analysis," *Lab on a Chip*, vol. 12, no. 21, pp. 4403–4415, 2012.

[73] R. St-Gelais, J. Masson, and Y.-A. Peter, "All-silicon integrated fabry–pérot cavity for volume refractive index measurement in microfluidic systems," *Applied physics letters*, vol. 94, no. 24, p. 243905, 2009.

[74] V. M. Lavchiev and B. Jakoby, "Photonics in the mid-infrared: challenges in single-chip integration and absorption sensing," *IEEE Journal of Selected Topics in Quantum Electronics*, vol. 23, no. 2, pp. 452–463, 2016.

[75] G. Mazzini, F. Carpignano, S. Surdo, F. Aredia, N. Panini, M. Torchio, E. Erba, M. Danova, A. I. Scovassi, G. Barillaro, *et al.*, "3d silicon microstructures: a new tool for evaluating biological aggressiveness of tumor cells," *IEEE transactions on nanobioscience*, vol. 14, no. 7, pp. 797–805, 2015.

[76] S. Surdo, F. Carpignano, L. Strambini, S. Merlo, and G. Barillaro, "Capillarity-driven (self-powered) one-dimensional photonic crystals for refractometry and (bio) sensing applications," *RSC Advances*, vol. 4, no. 94, pp. 51935–51941, 2014.

[77] T. S. Perova, V. A. Tolmachev, and Baldycheva, "Coupled Silicon-air Fabry-Perot resonators with tunable triplet modes," *Proceeding of the 9th International Conference on "Porous Semiconductors, Science and Technology", PSST-2014*, pp. 306–307, 2014.

[78] B. T. Hogan, S. A. Dyakov, L. J. Brennan, S. Younesy, T. S. Perova, Y. K. Gun'ko, M. F. Craciun, and A. Baldycheva, "Dynamic in-situ sensing of fluid-dispersed 2D materials integrated on microfluidic Si chip," *Scientific Reports*, vol. 7, p. 42120, feb 2017.

[79] S. Surdo and G. Barillaro, "On the performance of label-free biosensors based on vertical one-dimensional photonic crystal resonant cavities," *Optics express*, vol. 23, no. 7, pp. 9192–9201, 2015.

[80] G. Shabtay, E. Eidinger, Z. Zalevsky, D. Mendlovic, and E. Marom, "Tunable birefringent filters—optimal iterative design," *Optics express*, vol. 10, no. 26, pp. 1534–1541, 2002.

[81] O. Aharon and I. Abdulhalim, "Birefringent tunable filter with wide dynamic range," *Opt. Lett*, vol. 34, no. 14, pp. 2114–2116, 2009.

[82] X. Zheng, I. Shubin, G. Li, T. Pinguet, A. Mekis, J. Yao, H. Thacker, Y. Luo, J. Costa, K. Raj, *et al.*, "A tunable 1x4 silicon cmos photonic wavelength multiplexer/demultiplexer for dense optical interconnects," *Optics express*, vol. 18, no. 5, pp. 5151–5160, 2010.

[83] X. Zhao, Y. Yang, Z. Chen, Y. Wang, H. Fei, and X. Deng, "Ultra-wide tuning single channel filter based on one-dimensional photonic crystal with an air cavity," *Journal of Semiconductors*, vol. 38, no. 2, p. 023004, 2017.

[84] X. Hu, Z. Liu, and Q. Gong, "Tunable multichannel filter in photonic crystal heterostructure containing permeability-negative materials," *Physics Letters, Section A: General, Atomic and Solid State Physics*, vol. 372, no. 3, pp. 333–339, 2008.

[85] S.-S. Yun and J.-H. Lee, "A micromachined in-plane tunable optical filter using the thermo-optic effect of crystalline silicon," *Journal of Micromechanics and Microengineering*, vol. 13, no. 5, p. 721, 2003.

[86] M. W. Pruessner, T. H. Stievater, and W. S. Rabinovich, "In-plane microelectromechanical resonator with integrated fabry–pérot cavity," *Applied Physics Letters*, vol. 92, no. 8, p. 081101, 2008.

[87] C. A. Barrios, V. Almeida, R. Panepucci, B. Schmidt, and M. Lipson, "Compact silicon tunable fabry-perot resonator with low power consumption," *IEEE Photonics Technology Letters*, vol. 16, no. 2, pp. 506–508, 2004.

[88] A. Baldycheva, V. A. Tolmachev, K. Berwick, and T. S. Perova, "Multi-channel si-liquid crystal filter with fine tuning capability of individual channels for compensation of fabrication tolerances," *Nanoscale research letters*, vol. 7, no. 1, p. 387, 2012.

[89] T. Asano and S. Noda, "Photonic crystal devices in silicon photonics," *Proceedings of the IEEE*, vol. 106, no. 12, pp. 2183–2195, 2018.

[90] T. Baba, "Slow light in photonic crystals," *Nature photonics*, vol. 2, no. 8, p. 465, 2008.

[91] J. D. Joannopoulos, P. R. Villeneuve, and S. Fan, "Photonic crystals," *Solid State Communications*, vol. 102, no. 2-3, pp. 165–173, 1997.

[92] J. D. Joannopoulos, R. D. Meade, and J. N. Winn, *Photonic crystals*. Princeton, 1995.

[93] A. Shakoor, K. Nozaki, E. Kuramochi, K. Nishiguchi, A. Shinya, and M. Notomi, "Compact 1d-silicon photonic crystal electro-optic modulator operating with ultra-low switching voltage and energy," *Optics express*, vol. 22, no. 23, pp. 28623–28634, 2014.

[94] Z. Wang, J. Zhang, S. Xu, L. Wang, Z. Cao, P. Zhan, and Z. Wang, "1d partially oxidized porous silicon photonic crystal reflector for mid-infrared application," *Journal of Physics D: Applied Physics*, vol. 40, no. 15, p. 4482, 2007.

[95] L.-D. Haret, T. Tanabe, E. Kuramochi, and M. Notomi, "Extremely low power optical bistability in silicon demonstrated using 1d photonic crystal nanocavity," *Optics express*, vol. 17, no. 23, pp. 21108–21117, 2009.

[96] C. Pacholski, "Photonic crystal sensors based on porous silicon," *Sensors*, vol. 13, no. 4, pp. 4694–4713, 2013.

[97] J. Hendrickson, R. Soref, J. Sweet, and W. Buchwald, "Ultrasensitive silicon photonic-crystal nanobeam electro-optical modulator: design and simulation," *Optics express*, vol. 22, no. 3, pp. 3271–3283, 2014.

[98] S. Leonard, H. Van Driel, J. Schilling, and R. Wehrspohn, "Ultrafast band-edge tuning of a two-dimensional silicon photonic crystal via free-carrier injection," *Physical Review B*, vol. 66, no. 16, p. 161102, 2002.

[99] Y. Fu, X. Hu, and Q. Gong, "Silicon photonic crystal all-optical logic gates," *Physics letters A*, vol. 377, no. 3-4, pp. 329–333, 2013.

[100] A. Birner, R. B. Wehrspohn, U. M. Gösele, and K. Busch, "Silicon-based photonic crystals," *Advanced Materials*, vol. 13, no. 6, pp. 377–388, 2001.

[101] M. Belotti, J. F. Galisteo-López, S. De Angelis, M. Galli, I. Maksymov, L. C. Andreani, D. Peyrade, and Y. Chen, "All-optical switching in 2d silicon photonic crystals with low loss waveguides and optical cavities," *Optics express*, vol. 16, no. 15, pp. 11624–11636, 2008.

[102] Y. Ooka, T. Tetsumoto, A. Fushimi, W. Yoshiki, and T. Tanabe, "Cmos compatible high-q photonic crystal nanocavity fabricated with photolithography on silicon photonic platform," *Scientific reports*, vol. 5, p. 11312, 2015.

[103] A. Sayarath and A. W. Poon, "Reconfigurable Demultiplexer Using Feedback- Waveguides Coupled To Microring Resonators," pp. 7–9.

[104] P. Dong, W. Qian, H. Liang, R. Shafiiha, N.-N. Feng, D. Feng, X. Zheng, A. V. Krishnamoorthy, and M. Asghari, "Low power and compact reconfigurable multiplexing devices based on silicon microring resonators," *Opt. Express*, vol. 18, no. 10, pp. 9852–9858, 2010.

[105] E. J. Klein, D. H. Geuzebroek, H. Kelderman, G. Sengo, N. Baker, and A. Driessen, "Reconfigurable optical add-drop multiplexer using microring resonators," *IEEE Photonics Technology Letters*, vol. 17, no. 11, pp. 2358–2360, 2005.

[106] E. J. Klein and A. Driessen, "Densely Integrated Photonic Devices based on Microring Resonators in Access Networks," vol. 17, no. 16, p. 2495, 2007.

[107] L. V. Pavesi and Lorenzo, *Silicon Photonics Handbook of Handbook of.* 2013.

[108] W. Bogaerts, P. De Heyn, T. Van Vaerenbergh, K. De Vos, S. Kumar Selvaraja, T. Claes, P. Dumon, P. Bienstman, D. Van Thourhout, and R. Baets, "Silicon microring resonators," *Laser & Photonics Reviews*, vol. 6, no. 1, pp. 47–73, 2012.

[109] L. Vivien and L. Pavesi, *Handbook of silicon photonics*. Taylor & Francis, 2016.

[110] K. Okamoto, K. Moriwaki, and S. Suzuki, "Fabrication of 64* 64 arrayed-waveguide grating multiplexer on silicon," *Electronics Letters*, vol. 31, no. 3, pp. 184–186, 1995.

[111] D. Dai, J. Wang, and Y. Shi, "Silicon mode (de) multiplexer enabling high capacity photonic networks-on-chip with a single-wavelength-carrier light," *Optics letters*, vol. 38, no. 9, pp. 1422–1424, 2013.

[112] J. Wang, S. He, and D. Dai, "On-chip silicon 8-channel hybrid (de) multiplexer enabling simultaneous mode-and polarization-division-multiplexing," *Laser & Photonics Reviews*, vol. 8, no. 2, pp. L18–L22, 2014.

[113] T. Kita, K. Nemoto, and H. Yamada, "Silicon photonic wavelength-tunable laser diode with asymmetric mach–zehnder interferometer," *IEEE Journal of Selected Topics in Quantum Electronics*, vol. 20, no. 4, pp. 344–349, 2013.

[114] P. Dong, L. Chen, and Y.-k. Chen, "High-speed low-voltage single-drive push-pull silicon mach-zehnder modulators," *Optics express*, vol. 20, no. 6, pp. 6163–6169, 2012.

[115] D. Martens and P. Bienstman, "Study on the limit of detection in mzi-based biosensor systems," *Scientific reports*, vol. 9, no. 1, p. 5767, 2019.

[116] D. Taillaert, P. Bienstman, and R. Baets, "Compact efficient broadband grating coupler for silicon-on-insulator waveguides," *Optics letters*, vol. 29, no. 23, pp. 2749–2751, 2004.

[117] G. Roelkens, D. Van Thourhout, and R. Baets, "High efficiency silicon-on-insulator grating coupler based on a poly-silicon overlay," *Optics Express*, vol. 14, no. 24, pp. 11622–11630, 2006.

[118] F. Van Laere, T. Claes, J. Schrauwen, S. Scheerlinck, W. Bogaerts, D. Taillaert, L. O'Faolain, D. Van Thourhout, and R. Baets, "Compact focusing grating couplers for silicon-on-insulator integrated circuits," *IEEE Photonics Technology Letters*, vol. 19, no. 23, pp. 1919–1921, 2007.

[119] C. R. Doerr, L. Chen, Y.-K. Chen, and L. L. Buhl, "Wide bandwidth silicon nitride grating coupler," *IEEE Photonics Technology Letters*, vol. 22, no. 19, pp. 1461–1463, 2010.

[120] A. Mekis, S. Gloeckner, G. Masini, A. Narasimha, T. Pinguet, S. Sahni, and P. De Dobbelaere, "A grating-coupler-enabled cmos photonics platform," *IEEE Journal of Selected Topics in Quantum Electronics*, vol. 17, no. 3, pp. 597–608, 2010.

[121] D. Andrienko, "Introduction to liquid crystals," *Journal of Molecular Liquids*, vol. 267, pp. 520–541, 2018.

[122] M. Ando and M. Nonaka, "Liquid crystal display device," Jan. 18 2007. US Patent App. 11/478,624.

[123] Y. Utsumi and T. Kamei, "Dielectric permittivity measurements of liquid crystal in the microwave and millimeter wave ranges," *Molecular Crystals and Liquid Crystals*, vol. 409, no. 1, pp. 355–370, 2004.

[124] B. E. Saleh and M. C. Teich, *Fundamentals of photonics*. John Wiley & Sons, 2019.

[125] S. Yu, X. Wu, Y. Wang, X. Guo, and L. Tong, "2D Materials for Optical Modulation: Challenges and Opportunities," *Advanced Materials*, vol. 29, no. 14, 2017.

[126] E. L. Wolf, *Applications of Graphene: An Overview (SpringerBriefs in Materials)*. 2014.

[127] Ricardo A Depine, *Graphene Optics*.

[128] F. Wang, Y. Zhang, C. Tian, C. Girit, A. Zettl, M. Crommie, and Y. R. Shen, "Gate-Variable Optical Transitions in Graphene," *Science*, vol. 320, no. 5873, pp. 206–209, 2008.

[129] C.-F. Chen, C.-H. Park, B. W. Boudouris, J. Horng, B. Geng, C. Girit, A. Zettl, M. F. Crommie, R. A. Segalman, S. G. Louie, and F. Wang, "Controlling inelastic light scattering quantum pathways in graphene," *Nature*, vol. 471, no. 7340, pp. 617–620, 2011.

[130] R. S. Sundaram, M. Engel, A. Lombardo, R. Krupke, A. C. Ferrari, P. Avouris, and M. Steiner, "Electroluminescence in single layer MoS2," *Nano Letters*, vol. 13, no. 4, pp. 1416–1421, 2013.

[131] H. Ramakrishna Matte, A. Gomathi, A. K. Manna, D. J. Late, R. Datta, S. K. Pati, and C. Rao, "Mos2 and ws2 analogues of graphene," *Angewandte Chemie International Edition*, vol. 49, no. 24, pp. 4059–4062, 2010.

[132] M. Wuttig, H. Bhaskaran, and T. Taubner, "Phase-change materials for non-volatile photonic applications," *Nature Photonics*, vol. 11, no. 8, p. 465, 2017.

[133] W. Wełnic and M. Wuttig, "Reversible switching in phase-change materials," *materials today*, vol. 11, no. 6, pp. 20–27, 2008.

[134] C. Rios, M. Stegmaier, Z. Cheng, N. Youngblood, C. D. Wright, W. H. P. Pernice, and H. Bhaskaran, "Controlled switching of phase-change materials by evanescent-field coupling in integrated photonics [Invited]," *Optical Materials Express*, vol. 8, no. 9, p. 2455, 2018.

[135] C. Peng, L. Cheng, and M. Mansuripur, "Experimental and theoretical investigations of laser-induced crystallization and amorphization in phase-change optical recording media," *Journal of Applied Physics*, vol. 82, no. 9, pp. 4183–4191, 1997.

[136] M. Wuttig and N. Yamada, "Phase-change materials for rewriteable data storage," *Nature materials*, vol. 6, no. 11, pp. 824–832, 2007.

[137] W. Wełnic, S. Botti, L. Reining, and M. Wuttig, "Origin of the optical contrast in phase-change materials," *Physical Review Letters*, vol. 98, no. 23, pp. 1–4, 2007.

[138] N. I. Zheludev and Y. S. Kivshar, "From metamaterials to metadevices," *Nature Materials*, vol. 11, no. 11, pp. 917–924, 2012.

[139] M. Stegmaier, C. Ríos, H. Bhaskaran, C. D. Wright, and W. H. Pernice, "Nonvolatile all-optical 1×2 switch for chipscale photonic networks," *Advanced Optical Materials*, vol. 5, no. 1, p. 1600346, 2017.

[140] J. Faneca, T. D. Bucio, F. Y. Gardes, and A. Baldycheva, "O-band n-rich silicon nitride mzi based on gst," *Applied Physics Letters*, vol. 116, no. 9, p. 093502, 2020.

[141] J. Feldmann, N. Youngblood, X. Li, C. D. Wright, H. Bhaskaran, and W. H. Pernice, "Integrated 256 cell photonic phase-change memory with 512-bit capacity," *IEEE Journal of Selected Topics in Quantum Electronics*, vol. 26, no. 2, pp. 1–7, 2019.

[142] P. Xu, J. Zheng, J. K. Doylend, and A. Majumdar, "Low-loss and broadband non-volatile phase-change directional coupler switches," *ACS Photonics*, vol. 6, no. 2, pp. 553–557, 2019.

[143] C. Ríos, M. Stegmaier, P. Hosseini, D. Wang, T. Scherer, C. D. Wright, H. Bhaskaran, and W. H. Pernice, "Integrated all-photonic non-volatile multi-level memory," *Nature Photonics*, vol. 9, no. 11, p. 725, 2015.

[144] N. Farmakidis, N. Youngblood, X. Li, J. Tan, J. L. Swett, Z. Cheng, C. D. Wright, W. H. Pernice, and H. Bhaskaran, "Plasmonic nanogap enhanced phase-change devices with dual electrical-optical functionality," *Science advances*, vol. 5, no. 11, p. eaaw2687, 2019.

[145] E. Gemo, S. G.-C. Carrillo, C. R. De Galarreta, A. Baldycheva, H. Hayat, N. Youngblood, H. Bhaskaran, W. H. Pernice, and C. D. Wright, "Plasmonically-enhanced all-optical integrated phase-change memory," *Optics express*, vol. 27, no. 17, pp. 24724–24737, 2019.

[146] Z. Cheng, C. Ríos, W. H. Pernice, C. D. Wright, and H. Bhaskaran, "On-chip photonic synapse," *Science advances*, vol. 3, no. 9, p. e1700160, 2017.

[147] J. Feldmann, N. Youngblood, C. Wright, H. Bhaskaran, and W. Pernice, "All-optical spiking neurosynaptic networks with self-learning capabilities," *Nature*, vol. 569, no. 7755, pp. 208–214, 2019.

[148] J. Zheng, A. Khanolkar, P. Xu, S. Colburn, S. Deshmukh, J. Myers, J. Frantz, E. Pop, J. Hendrickson, J. Doylend, *et al.*, "Gst-on-silicon hybrid nanophotonic integrated circuits: a non-volatile quasi-continuously reprogrammable platform," *Optical Materials Express*, vol. 8, no. 6, pp. 1551–1561, 2018.

[149] H. Zhang, L. Zhou, B. Rahman, X. Wu, L. Lu, Y. Xu, J. Xu, J. Song, Z. Hu, L. Xu, *et al.*, "Ultracompact si-gst hybrid waveguides for nonvolatile light wave manipulation," *IEEE Photonics Journal*, vol. 10, no. 1, pp. 1–10, 2017.

[150] K. E. J. M. Iller, R. I. F. H. A. J. R, S. M. Haron, and W. Eiss, "Optical phase change materials in integrated silicon photonic devices : review," vol. 8, no. 8, pp. 2415–2429, 2018.

[151] H. Haus, W. Huang, S. Kawakami, and N. Whitaker, "Coupled-mode theory of optical waveguides," *Journal of Lightwave Technology*, vol. 5, no. 1, pp. 16–23, 1987.

[152] B. E. Little, S. T. Chu, H. A. Haus, J. Foresi, and J. P. Laine, "Microring resonator channel dropping filters," *Journal of Lightwave Technology*, vol. 15, no. 6, pp. 998–1005, 1997.

[153] J. K. S. Poon, J. Scheuer, S. Mookherjea, G. T. Paloczi, Y. Y. Huang, and A. Yariv, "Matrix analysis of microring coupled-resonator optical waveguides," *Optics Express*, vol. 12, no. 1, pp. 90–103, 2004.

[154] Y. Wang, J. Flueckiger, C. Lin, and L. Chrostowski, "Universal grating coupler design," in *Photonics North 2013*, vol. 8915, p. 89150Y, International Society for Optics and Photonics, 2013.

[155] T. D. Bucio, A. Z. Khokhar, C. Lacava, S. Stankovic, G. Z. Mashanovich, P. Petropoulos, and F. Y. Gardes, "Material and optical properties of low-temperature nh3-free pecvd sin x layers for photonic applications," *Journal of Physics D: Applied Physics*, vol. 50, no. 2, p. 025106, 2016.

[156] A. Z. Khokhar and C. Lacava, "Material and optical properties of low- temperature NH 3 -free PECVD SiN x layers for photonic applications," 2017.

[157] M. Altissimo, "E-beam lithography for micro-/nanofabrication," *Biomicrofluidics*, vol. 4, no. 2, pp. 2–7, 2010.

[158] Y. Chen, "Nanofabrication by electron beam lithography and its applications: A review," *Microelectronic Engineering*, vol. 135, pp. 57–72, 2015.

[159] M. J. Madou, *Fundamentals of microfabrication and nanotechnology, Three-volume set*. CRC Press, 2018.

[160] U. Fischer, T. Zinke, J.-R. Kropp, F. Arndt, and K. Petermann, "0.1 db/cm waveguide losses in single-mode soi rib waveguides," *IEEE Photonics Technology Letters*, vol. 8, no. 5, pp. 647–648, 1996.

[161] B. Jalali, P. Trinh, S. Yegnanarayanan, and F. Coppinger, "Guided-wave optics in silicon-on-insulator technology," *IEE Proceedings-Optoelectronics*, vol. 143, no. 5, pp. 307–311, 1996.

[162] J. W. Haus, *Fundamentals and applications of nanophotonics*. Woodhead Publishing, 2016.

[163] G. Diankov, M. Neumann, and D. Goldhaber-Gordon, "Extreme monolayer-selectivity of hydrogen-plasma reactions with graphene," *ACS nano*, vol. 7, no. 2, pp. 1324–1332, 2013.

[164] J. Hopwood, H. Search, C. Journals, A. Contact, M. Iopscience, P. S. Sci, and I. P. Address, "Review of inductively coupled," *Plasma Sources Science and Technology*, vol. 1, pp. 109–116, 1992.

[165] J. Lee, J. Kim, A. Efremov, C. Kim, H. W. Lee, and K. H. Kwon, "Etching Mechanisms and Surface Conditions for SiO x N y Thin Films in CF 4 + CHF 3 + O 2 Inductively Coupled Plasma," *Plasma Chemistry and Plasma Processing*, vol. 39, no. 4, pp. 1127–1144, 2019.

[166] K. S. Novoselov, A. K. Geim, S. V. Morozov, D. Jiang, Y. Zhang, S. V. Dubonos, I. V. Grigorieva, and A. A. Firsov, "Electric Field Effect in Atomically Thin Carbon Films," *Science*, vol. 306, pp. 666–669, oct 2004.

[167] X. Li, W. Cai, J. An, S. Kim, J. Nah, D. Yang, R. Piner, A. Velamakanni, I. Jung, E. Tutuc, S. K. Banerjee, L. Colombo, and R. S. Ruoff, "Large-Area Synthesis of High-Quality and Uniform Graphene Films on Copper Foils," *Science*, vol. 324, no. 5932, pp. 1312–1314, 2009.

[168] A. Reina, X. Jia, J. Ho, D. Nezich, H. Son, V. Bulovic, M. S. Dresselhaus, and J. Kong, "Supporting Information Large Area , Few-Layer Graphene Films on Arbitrary Substrates by Chemical Vapor Deposition," *Nano letters*, vol. 9, no. 1, pp. 1–8, 2009.

[169] X. Sun, D. Luo, J. Liu, and D. G. Evans, "Monodisperse Chemically Modified Graphene Obtained by Density Gradient Ultracentrifugal Rate Separation," *ACS Nano*, vol. 4, pp. 3381–3389, jun 2010.

[170] D. Wei, Y. Liu, Y. Wang, H. Zhang, L. Huang, and G. Yu, "Synthesis of N-Doped Graphene by Chemical Vapor Deposition and Its Electrical Properties," *Nano Letters*, vol. 9, pp. 1752–1758, may 2009.

[171] N. Behabtu, J. R. Lomeda, M. J. Green, A. L. Higginbotham, A. Sinitskii, D. V. Kosynkin, D. Tsentalovich, A. N. G. Parra-Vasquez, J. Schmidt, E. Kesselman, Y. Cohen, Y. Talmon, J. M. Tour, and M. Pasquali, "Spontaneous high-concentration dispersions and liquid crystals of graphene.," *Nature nanotechnology*, vol. 5, pp. 406–11, jun 2010.

[172] Y. Hernandez, V. Nicolosi, M. Lotya, F. M. Blighe, Z. Sun, S. De, I. T. McGovern, B. Holland, M. Byrne, Y. K. Gun'Ko, J. J. Boland, P. Niraj, G. Duesberg, S. Krishnamurthy, R. Goodhue, J. Hutchison, V. Scardaci, A. C. Ferrari, and J. N. Coleman, "High-yield production of graphene by liquid-phase exfoliation of graphite.," *Nature nanotechnology*, vol. 3, pp. 563–568, sep 2008.

[173] M. Lotya, P. J. King, U. Khan, S. De, and J. N. Coleman, "High-concentration, surfactant-stabilized graphene dispersions.," *ACS nano*, vol. 4, pp. 3155–62, jun 2010.

[174] A. O'Neill, U. Khan, P. N. Nirmalraj, J. Boland, and J. N. Coleman, "Graphene Dispersion and Exfoliation in Low Boiling Point Solvents," *The Journal of Physical Chemistry C*, vol. 115, pp. 5422–5428, apr 2011.

[175] I. Ogino, Y. Yokoyama, S. Iwamura, and S. R. Mukai, "Exfoliation of Graphite Oxide in Water without Sonication: Bridging Length Scales from Nanosheets to Macroscopic Materials," *Chemistry of Materials*, vol. 26, pp. 3334–3339, may 2014.

[176] J. I. Paredes, S. Villar-Rodil, A. Martinez-Alonso, and J. M. D. Tascon, "Graphene Oxide Dispersions in Organic Solvents," *Langmuir*, vol. 24, pp. 10560–10564, oct 2008.

[177] X. Qi, T. Zhou, S. Deng, G. Zong, X. Yao, and Q. Fu, "Size-specified graphene oxide sheets: ultrasonication assisted preparation and characterization," *Journal of Materials Science*, vol. 49, pp. 1785–1793, feb 2014.

[178] L. Zhang, J. Liang, Y. Huang, Y. Ma, Y. Wang, and Y. Chen, "Size-controlled synthesis of graphene oxide sheets on a large scale using chemical exfoliation," 2009.

[179] L. Peng, Z. Xu, Z. Liu, Y. Wei, H. Sun, Z. Li, X. Zhao, and C. Gao, "An iron-based green approach to 1-h production of single-layer graphene oxide," *Nature Communications*, vol. 6, p. 5716, jan 2015.

[180] D. W. Kim, D. Kim, B. H. Min, H. Lee, and H.-T. Jung, "Sonication-free dispersion of large-area graphene oxide sheets using internal pressure from release of intercalated carbon dioxide," *Carbon*, vol. 88, pp. 126–132, 2015.

[181] Z. Sun, Z. Yan, J. Yao, E. Beitler, Y. Zhu, and J. M. Tour, "Growth of graphene from solid carbon sources," *Nature*, vol. 468, pp. 549–552, nov 2010.

[182] W. Zhang, X. Zou, H. Li, J. Hou, J. Zhao, J. Lan, B. Feng, and S. Liu, "Size fractionation of graphene oxide sheets by the polar solvent-selective natural deposition method," *RSC Adv.*, vol. 5, no. 1, pp. 146–152, 2015.

[183] X. Wang, H. Bai, and G. Shi, "Size Fractionation of Graphene Oxide Sheets by pH-Assisted Selective Sedimentation," *Journal of the American Chemical Society*, vol. 133, pp. 6338–6342, apr 2011.

[184] J. Faneca, T. S. Perova, V. Tolmachev, and A. Baldycheva, "One-Dimensional Multi-Channel Photonic Crystal Resonators Based on Silicon-On-Insulator With High Quality Factor," *Frontiers in Physics*, vol. 6, no. May, pp. 1–9, 2018.

[185] X. Li, W. Cai, J. An, S. Kim, J. Nah, D. Yang, R. Piner, A. Velamakanni, I. Jung, E. Tutuc, *et al.*, "Large-area synthesis of high-quality and uniform graphene films on copper foils," *science*, vol. 324, no. 5932, pp. 1312–1314, 2009.

[186] A. Z. Elorza, A. C. Perez, B. A. Rodriguez, and A. P. Rodriguez, "Method of manufacturing a graphene monolayer on insulating substrates," May 5 2015. US Patent 9,023,220.

[187] A. N. Obraztsov, "Making graphene on a large scale," *Nature Nanotechnology*, vol. 4, no. April, pp. 212–213, 2009.

[188] J. A. Thornton, "Influence of apparatus geometry and deposition conditions on the structure and topography of thick sputtered coatings," *Journal of Vacuum Science and Technology*, vol. 11, no. 4, pp. 666–670, 1974.

[189] P. Pokorný, J. Musil, P. Fitl, M. Novotný, J. Lančok, and J. Bulíř, "Contamination of magnetron sputtered metallic films by oxygen from residual atmosphere in deposition chamber," *Plasma Processes and Polymers*, vol. 12, no. 5, pp. 416–421, 2015.

[190] D. O'Brien, M. Settle, T. Karle, A. Michaeli, M. Salib, and T. Krauss, "Coupled photonic crystal heterostructure nanocavities," *Optics express*, vol. 15, no. 3, pp. 1228–1233, 2007.

[191] K. J. Vahala, "Optical microcavities," *Nature*, vol. 424, no. 6950, pp. 839–846, 2003.

[192] J. Cos, J. Ferre-Borrull, J. Pallares, and L. Marsal, "Tunable fabry–pérot filter based on one-dimensional photonic crystals with liquid crystal components," *Optics Communications*, vol. 282, no. 6, pp. 1220–1225, 2009.

[193] M. Kaliteevskii, "Optical properties of a system of two coupled vertical microcavities," *Technical Physics*, vol. 43, no. 5, pp. 565–568, 1998.

[194] V. A. Tolmachev, V. A. Melnikov, V. Baldycheva, K. Berwick, and T. S. Perova, "Electrically Tunable Fabry-Perot Resonator Based on Microstructured Si Containing Liquid Crystal," *Progress In Electromagnetics Research*, vol. 122, pp. 293–309, 2012.

[195] H. Briggs, "Optical effects in bulk silicon and germanium," *Physical Review*, vol. 77, no. 2, p. 287, 1950.

[196] V. Tolmachev, A. Baldycheva, and T. Perova, "Electrotunable optical filters based on microstructured silicon infiltrated with liquid crystal for mid-infrared range," in *Book of Extended Abstracts of the 8th International Conference on Porous Semiconductors-Science and Technology, ISBN 978-84-370-7693-5*, 2012.

[197] B. Y. Zel'dovich, N. Tabiryan, and Y. S. Chilingaryan, "Fredericks transitions induced by light fields," in *Opticals Effects in Liquid Crystals*, pp. 111–124, Springer, 1982.

[198] V. A. Tolmachev, V. A. Melnikov, V. Baldycheva, K. Berwick, and T. S. Perova, "Electrically tunable fabry-perot resonator based on microstructured si containing liquid crystal," *Progress In Electromagnetics Research*, vol. 122, pp. 293–309, 2012.

[199] J. Faneca, T. S. Perova, V. Tolmachev, and A. Baldycheva, "One-dimensional multichannel photonic crystal resonators based on silicon-on-insulator with high quality factor," *Frontiers in Physics*, vol. 6, p. 33, 2018.

[200] M. Geis, T. Lyszczarz, R. Osgood, and B. Kimball, "30 to 50 ns liquid-crystal optical switches," *Optics express*, vol. 18, no. 18, pp. 18886–18893, 2010.

[201] V. Borshch, S. V. Shiyanovskii, and O. D. Lavrentovich, "Nanosecond electro-optic switching of a liquid crystal," *Physical review letters*, vol. 111, no. 10, p. 107802, 2013.

[202] A. I. Jakli, "Fast switching electro-optical devices using banana-shaped liquid crystals," Aug. 24 2010. US Patent 7,782,438.

[203] A. Jákli, "Liquid crystals of the twenty-first century–nematic phase of bent-core molecules," *Liquid Crystals Reviews*, vol. 1, no. 1, pp. 65–82, 2013.

[204] K. S. Novoselov, V. I. Fal, L. Colombo, P. R. Gellert, M. G. Schwab, K. Kim, V. I. F. Ko, L. Colombo, P. R. Gellert, M. G. Schwab, and K. Kim, "A roadmap for graphene," *Nature*, vol. 490, no. 7419, pp. 192–200, 2013.

[205] A. B. Kuzmenko, E. Van Heumen, F. Carbone, and D. Van Der Marel, "Universal optical conductance of graphite," *Physical Review Letters*, vol. 100, no. 11, pp. 2–5, 2008.

[206] R. R. Nair, P. Blake, A. N. Grigorenko, K. S. Novoselov, T. J. Booth, T. Stauber, N. M. R. Peres, and A. K. Geim, "Fine Structure Constant Defines Visual Transparency of Graphene," *Science*, vol. 320, no. 5881, pp. 1308–1308, 2008.

[207] R. Soref, "Tutorial: Integrated-photonic switching structures," *APL Photonics*, vol. 3, no. 2, 2018.

[208] J. Faneca, T. Perova, V. Tolmachev, and A. Baldycheva, "One-dimensional multi-channel photonic crystal resonators based on Silicon-On-Insulator with high quality factor," *Frontiers in Physics*, vol. 6, no. MAY, 2018.

[209] F. Y. Gardes, G. T. Reed, N. Emerson, and C. Png, "A sub-micron depletion-type photonic modulator in silicon on insulator," *Opt. Express*, vol. 13, pp. 8845–8854, Oct 2005.

[210] D. J. Thomson, F. Y. Gardes, Y. Hu, G. Mashanovich, M. Fournier, P. Grosse, J.-M. Fedeli, and G. T. Reed, "High contrast 40gbit/s optical modulation in silicon," *Opt. Express*, vol. 19, pp. 11507–11516, Jun 2011.

[211] D. J. Thomson, F. Y. Gardes, J. Fedeli, S. Zlatanovic, Y. Hu, B. P. P. Kuo, E. Myslivets, N. Alic, S. Radic, G. Z. Mashanovich, and G. T. Reed, "50-gb/s silicon optical modulator," *IEEE Photonics Technology Letters*, vol. 24, pp. 234–236, Feb 2012.

[212] A. D. Neira, G. A. Wurtz, P. Ginzburg, and A. V. Zayats, "Ultrafast all-optical modulation with hyperbolic metamaterial integrated in si photonic circuitry," *Opt. Express*, vol. 22, pp. 10987–10994, May 2014.

[213] A. S. Shalin, P. Ginzburg, P. A. Belov, Y. S. Kivshar, and A. V. Zayats, "Nano-opto-mechanical effects in plasmonic waveguides," *Laser & Photonics Reviews*, vol. 8, no. 1, pp. 131–136, 2014.

[214] S. Yu, X. Wu, Y. Wang, X. Guo, and L. Tong, "2d materials for optical modulation: Challenges and opportunities," *Advanced Materials*, vol. 29, no. 14, p. 1606128, 2017.

[215] H. Dalir, Y. Xia, Y. Wang, and X. Zhang, "Athermal broadband graphene optical modulator with 35 ghz speed," *ACS Photonics*, vol. 3, no. 9, pp. 1564–1568, 2016.

[216] Y. Ding, X. Zhu, S. Xiao, H. Hu, L. H. Frandsen, N. A. Mortensen, and K. Yvind, "Effective electro-optical modulation with high extinction ratio by a graphene–silicon microring resonator," *Nano Letters*, vol. 15, no. 7, pp. 4393–4400, 2015. PMID: 26042835.

[217] M. Mohsin, D. Neumaier, D. Schall, M. Otto, C. Matheisen, A. L. Giesecke, A. A. Sagade, and H. Kurz, "Experimental verification of electro-refractive phase modulation in graphene," *Scientific reports*, vol. 5, p. 10967, 2015.

[218] M. Romagnoli, "Graphene photonics for optical communications," p. 1, 2019.

[219] C. V. Memory, "Learn more about Volatile Memory Data Hiding Forensics," 2017.

[220] J. Andréasson, U. Pischel, S. D. Straight, T. A. Moore, A. L. Moore, and D. Gust, "All-photonic multifunctional molecular logic device," *Journal of the American Chemical Society*, vol. 133, no. 30, pp. 11641–11648, 2011.

[221] Y. Fu, X. Hu, C. Lu, S. Yue, H. Yang, and Q. Gong, "All-optical logic gates based on nanoscale plasmonic slot waveguides," *Nano Letters*, vol. 12, no. 11, pp. 5784–5790, 2012.

[222] H. Li, Y. Anugrah, S. J. Koester, and M. Li, "Optical absorption in graphene integrated on silicon waveguides," *Applied Physics Letters*, vol. 101, no. 11, 2012.

[223] T. D. Bucio, A. Z. Khokhar, G. Z. Mashanovich, and F. Y. Gardes, "N-rich silicon nitride angled MMI for coarse wavelength division (de)multiplexing in the O-band," *Optics Letters*, vol. 43, no. 6, p. 1251, 2018.

[224] X. Hu and J. Wang, "High Figure of Merit Graphene Modulator Based on Long-Range Hybrid Plasmonic Slot Waveguide," *IEEE Journal of Quantum Electronics*, vol. 53, no. 3, 2017.

[225] Y.-c. Chang, C.-h. Liu, Z. Zhong, and T. B. Norris, "Extracting the complex optical conductivity of true two- dimensional layers by ellipsometry," vol. 261909, no. 1, pp. 3–4, 2014.

[226] Q. Bao and K. P. Loh, "Graphene photonics, plasmonics, and broadband optoelectronic devices," *ACS Nano*, vol. 6, no. 5, pp. 3677–3694, 2012.

[227] C. T. Phare, Y.-H. D. Lee, J. Cardenas, and M. Lipson, "Graphene electro-optic modulator with 30 ghz bandwidth," *Nature Photonics*, vol. 9, no. 8, p. 511, 2015.

[228] P. Gunter, "Electro-optical effects in ferroelectrics," *Ferroelectrics*, vol. 74, no. 1, pp. 305–307, 1987.

[229] W. Zhu, D. Neumayer, V. Perebeinos, and P. Avouris, "Silicon nitride gate dielectrics and band gap engineering in graphene layers," *Nano Letters*, vol. 10, no. 9, pp. 3572–3576, 2010.

[230] K. Luke, Y. Okawachi, M. R. E. Lamont, A. L. Gaeta, and M. Lipson, "Broadband mid-infrared frequency comb generation in a Si_3N_4 microresonator," *Optics Letters*, vol. 40, no. 21, p. 4823, 2015.

[231] C. H. Ng, K. W. Chew, and S. F. Chu, "Characterization and comparison of PECVD Silicon Nitride and Silicon Oxynitride Dielectric for MIM Capacitor-B-0157-20131101.pdf," vol. 24, no. 8, pp. 506–508, 2003.

[232] M. Midrio, S. Boscolo, M. Moresco, M. Romagnoli, C. D. Angelis, A. Locatelli, and A.-D. Capobianco, "Graphene–assisted critically–coupled optical ring modulator," *Opt. Express*, vol. 20, pp. 23144–23155, Oct 2012.

[233] G. Kovacevic, C. Phare, S. Y. Set, M. Lipson, and S. Yamashita, "Ultra-high-speed graphene optical modulator design based on tight field confinement in a slot waveguide," *Applied Physics Express*, vol. 11, no. 6, 2018.

[234] A. Venugopal, L. Colombo, and E. M. Vogel, "Contact resistance in few and multilayer graphene devices," *Applied Physics Letters*, vol. 96, no. 1, 2010.

[235] W. S. Leong, X. Luo, Y. Li, K. H. Khoo, S. Y. Quek, and J. T. Thong, "Low resistance metal contacts to MoS 2 devices with nickel-etched-graphene electrodes," *ACS Nano*, vol. 9, no. 1, pp. 869–877, 2015.

[236] V. Sorianello, M. Midrio, and M. Romagnoli, "Design optimization of single and double layer Graphene phase modulators in SOI," *Optics Express*, vol. 23, no. 5, p. 6478, 2015.

[237] J. K. Lee, C. S. Park, and H. Kim, "Sheet resistance variation of graphene grown on annealed and mechanically polished Cu films," *RSC Advances*, vol. 4, no. 107, pp. 62453–62456, 2014.

[238] R. Ishikawa, Y. Kurokawa, S. Miyajima, and M. Konagai, "Peeling process of thin-film solar cells using graphene layers," *Applied Physics Express*, vol. 10, no. 8, 2017.

[239] K. Cil, "Temperature dependent characterization and crystallization dynamics of ge2sb2te5 thin films and nanoscale structures," 2015.

[240] I. Chakraborty, G. Saha, A. Sengupta, and K. Roy, "Toward fast neural computing using all-photonic phase change spiking neurons," *Scientific reports*, vol. 8, no. 1, pp. 1–9, 2018.

[241] Z. Cheng, C. Ríos, N. Youngblood, C. D. Wright, W. H. Pernice, and H. Bhaskaran, "Device-level photonic memories and logic applications using phase-change materials," *Advanced Materials*, vol. 30, no. 32, p. 1802435, 2018.

[242] W. D. Sacher and J. K. Poon, "Dynamics of microring resonator modulators," *Optics express*, vol. 16, no. 20, pp. 15741–15753, 2008.

[243] C. Rios, P. Hosseini, C. D. Wright, H. Bhaskaran, and W. H. P. Pernice, "On-chip photonic memory elements employing phase-change materials," *Advanced Materials*, vol. 26, no. 9, pp. 1372–1377, 2014.

[244] D. Tanaka, Y. Shoji, M. Kuwahara, X. Wang, K. Kintaka, H. Kawashima, T. Toyosaki, Y. Ikuma, and H. Tsuda, "Ultra-small, self-holding, optical gate switch using ge 2 sb 2 te 5 with a multi-mode si waveguide," *Optics express*, vol. 20, no. 9, pp. 10283–10294, 2012.

[245] M. Rudé, J. Pello, R. E. Simpson, J. Osmond, G. Roelkens, J. J. van der Tol, and V. Pruneri, "Optical switching at 1.55 μ m in silicon racetrack resonators using phase change materials," *Applied Physics Letters*, vol. 103, no. 14, p. 141119, 2013.

[246] C. Ríos, N. Youngblood, Z. Cheng, M. L. Gallo, W. H. P. Pernice, C. D. Wright, A. Sebastian, and H. Bhaskaran, "In-memory computing on a photonic platform," vol. 5, no. February, pp. 1–10, 2018.

[247] J. Feldmann, M. Stegmaier, N. Gruhler, C. Riós, H. Bhaskaran, C. D. Wright, and W. H. Pernice, "Calculating with light using a chip-scale all-optical abacus," *Nature Communications*, vol. 8, no. 1, pp. 1–8, 2017.

[248] Y. Zhang, J. B. Chou, J. Li, H. Li, Q. Du, A. Yadav, S. Zhou, M. Y. Shalaginov, Z. Fang, H. Zhong, *et al.*, "Broadband transparent optical phase change materials for high-performance nonvolatile photonics," *Nature communications*, vol. 10, no. 1, pp. 1–9, 2019.

[249] W. Dong, H. Liu, J. K. Behera, L. Lu, R. J. Ng, K. V. Sreekanth, X. Zhou, J. K. Yang, and R. E. Simpson, "Wide bandgap phase change material tuned visible photonics," *Advanced Functional Materials*, vol. 29, no. 6, p. 1806181, 2019.

[250] A. Redaelli, A. Pirovano, A. Benvenuti, and A. L. Lacaita, "Threshold switching and phase transition numerical models for phase change memory simulations," *Journal of Applied Physics*, vol. 103, no. 11, p. 6, 2008.

[251] K. Kato, M. Kuwahara, H. Kawashima, T. Tsuruoka, and H. Tsuda, "Current-driven phase-change optical gate switch using indium–tin-oxide heater," *Applied Physics Express*, vol. 10, no. 7, p. 072201, 2017.

[252] C. Wu, H. Yu, H. Li, X. Zhang, I. Takeuchi, and M. Li, "Low-loss integrated photonic switch using subwavelength patterned phase change material," *Acs Photonics*, vol. 6, no. 1, pp. 87–92, 2018.

[253] H. Zhang, L. Zhou, L. Lu, J. Xu, N. Wang, H. Hu, B. A. Rahman, Z. Zhou, and J. Chen, "Miniature multilevel optical memristive switch using phase change material," *ACS Photonics*, vol. 6, no. 9, pp. 2205–2212, 2019.

[254] J. Zheng, Z. Fang, C. Wu, S. Zhu, P. Xu, J. K. Doylend, S. Deshmukh, E. Pop, S. Dunham, M. Li, *et al.*, "Nonvolatile electrically reconfigurable integrated photonic switch," *arXiv preprint arXiv:1912.07680*, 2019.

[255] A. A. Balandin, S. Ghosh, W. Bao, I. Calizo, D. Teweldebrhan, F. Miao, and C. N. Lau, "Superior thermal conductivity of single-layer graphene," *Nano letters*, vol. 8, no. 3, pp. 902–907, 2008.

[256] D. E. Sheehy and J. Schmalian, "Optical transparency of graphene as determined by the fine-structure constant," *Physical Review B*, vol. 80, no. 19, p. 193411, 2009.

[257] C. Ríos, Y. Zhang, S. Deckoff-Jones, H. Li, J. B. Chou, H. Wang, M. Shalaginov, C. Roberts, C. Gonçalves, V. Liberman, *et al.*, "Reversible switching of optical phase change materials using graphene microheaters," in *2019 Conference on Lasers and Electro-Optics (CLEO)*, pp. 1–2, IEEE, 2019.

[258] G. Catalogue, "Metals, alloys, compounds, ceramics, polymers," *Composites. Cambridge: GoodfellowMetals*, 1993.

[259] C. D. Wright, M. Armand, and M. M. Aziz, "Terabit-per-square-inch data storage using phase-change media and scanning electrical nanoprobes," *IEEE Transactions on Nanotechnology*, vol. 5, no. 1, pp. 50–61, 2006.

[260] J. T. Gaskins, P. E. Hopkins, D. R. Merrill, S. R. Bauers, E. Hadland, D. C. Johnson, D. Koh, J. H. Yum, S. Banerjee, B. J. Nordell, *et al.*, "Investigation and review of the thermal, mechanical, electrical, optical, and structural properties of atomic layer deposited high-k dielectrics: Beryllium oxide, aluminum oxide, hafnium oxide, and aluminum nitride," *ECS Journal of Solid State Science and Technology*, vol. 6, no. 10, p. N189, 2017.

[261] M. Sadeghi, B. Janjan, M. Heidari, and D. Abbott, "Mid-infrared hybrid si/vo 2 modulator electrically driven by graphene electrodes," *Optics Express*, vol. 28, no. 7, pp. 9198–9207, 2020.

[262] N. Ciocchini, M. Cassinerio, D. Fugazza, and D. Ielmini, "Evidence for non-arrhenius kinetics of crystallization in phase change memory devices," *IEEE transactions on electron devices*, vol. 60, no. 11, pp. 3767–3774, 2013.

[263] S. R. Ovshinsky, "Reversible electrical switching phenomena in disordered structures," *Physical Review Letters*, vol. 21, no. 20, p. 1450, 1968.

[264] L. Yu, Y. Yin, Y. Shi, D. Dai, and S. He, "Thermally tunable silicon photonic microdisk resonator with transparent graphene nanoheaters," *Optica*, vol. 3, no. 2, pp. 159–166, 2016.

[265] J. T. Smith, A. D. Franklin, D. B. Farmer, and C. D. Dimitrakopoulos, "Reducing contact resistance in graphene devices through contact area patterning," *ACS nano*, vol. 7, no. 4, pp. 3661–3667, 2013.

[266] Y. Tamura, H. Sakuma, K. Morita, M. Suzuki, Y. Yamamoto, K. Shimada, Y. Honma, K. Sohma, T. Fujii, and T. Hasegawa, "Lowest-ever 0.1419-db/km loss optical fiber," in *Optical Fiber Communication Conference*, pp. Th5D–1, Optical Society of America, 2017.

[267] Y. Tamura, H. Sakuma, K. Morita, M. Suzuki, Y. Yamamoto, K. Shimada, Y. Honma, K. Sohma, T. Fujii, and T. Hasegawa, "The first 0.14-db/km loss optical fiber and its impact on submarine transmission," *Journal of Lightwave Technology*, vol. 36, no. 1, pp. 44–49, 2018.

[268] J. Tang, T. Hao, W. Li, D. Domenech, R. Baños, P. Muñoz, N. Zhu, J. Capmany, and M. Li, "Integrated optoelectronic oscillator," *Optics express*, vol. 26, no. 9, pp. 12257–12265, 2018.

[269] Y. Okawachi, K. Saha, J. S. Levy, Y. H. Wen, M. Lipson, and A. L. Gaeta, "Octave-spanning frequency comb generation in a silicon nitride chip," *Optics letters*, vol. 36, no. 17, pp. 3398–3400, 2011.

[270] D. Pérez, I. Gasulla, L. Crudgington, D. J. Thomson, A. Z. Khokhar, K. Li, W. Cao, G. Z. Mashanovich, and J. Capmany, "Multipurpose silicon photonics signal processor core," *Nature communications*, vol. 8, no. 1, p. 636, 2017.

[271] J. Wang, H. Shen, L. Fan, R. Wu, B. Niu, L. T. Varghese, Y. Xuan, D. E. Leaird, X. Wang, F. Gan, *et al.*, "Reconfigurable radio-frequency arbitrary waveforms synthesized in a silicon photonic chip," *Nature communications*, vol. 6, no. 1, pp. 1–8, 2015.

[272] X. Li, N. Youngblood, Z. Cheng, S. G.-C. Carrillo, E. Gemo, W. H. Pernice, C. D. Wright, and H. Bhaskaran, "Experimental investigation of silicon and silicon nitride platforms for phase-change photonic in-memory computing," *Optica*, vol. 7, no. 3, pp. 218–225, 2020.

[273] C. Rios, P. Hosseini, C. D. Wright, H. Bhaskaran, and W. H. Pernice, "On-chip photonic memory elements employing phase-change materials," *Advanced Materials*, vol. 26, no. 9, pp. 1372–1377, 2014.

[274] X. Li, N. Youngblood, C. Ríos, Z. Cheng, C. D. Wright, W. H. Pernice, and H. Bhaskaran, "Fast and reliable storage using a 5 bit, nonvolatile photonic memory cell," *Optica*, vol. 6, no. 1, pp. 1–6, 2019.

[275] H. Liang, R. Soref, J. Mu, A. Majumdar, X. Li, and W. Huang, "Simulations of silicon-on-insulator channel-waveguide electrooptical 2×2 switches and 1×1 modulators using a $Ge_2Sb_2Te_5$ self-holding layer," *Journal of Lightwave Technology*, vol. 33, no. 9, pp. 1805–1813, 2015.

[276] Y. Ikuma, Y. Shoji, M. Kuwahara, X. Wang, K. Kintaka, H. Kawashima, D. Tanaka, and H. Tsuda, "Small-sized optical gate switch using $Ge_2Sb_2Te_5$ phase-change material integrated with silicon waveguide," *Electronics letters*, vol. 46, no. 5, pp. 368–369, 2010.

[277] Y. Ikuma, T. Saiki, and H. Tsuda, "Proposal of a small self-holding $2\times$ 2 optical switch using phase-change material," *IEICE Electronics Express*, vol. 5, no. 12, pp. 442–445, 2008.

[278] M. Stegmaier, C. Ríos, H. Bhaskaran, and W. H. Pernice, "Thermo-optical effect in phase-change nanophotonics," *Acs Photonics*, vol. 3, no. 5, pp. 828–835, 2016.

[279] K. Kohary and C. D. Wright, "Electric field induced crystallization in phase-change materials for memory applications," *Applied Physics Letters*, vol. 98, no. 22, p. 223102, 2011.

[280] J. Zheng, S. Zhu, P. Xu, S. T. Dunham, and A. Majumdar, "Modeling electrical switching of nonvolatile phase-change integrated nanophotonic structures with graphene heaters," *ACS Applied Materials & Interfaces*, 2020.

[281] L. Trimby, A. Baldycheva, and C. D. Wright, "Phase-change band-pass filters for multispectral imaging," in *Photonic and Phononic Properties of Engineered Nanostructures VIII* (A. Adibi, S.-Y. Lin, and A. Scherer, eds.), vol. 10541, pp. 148 – 155, International Society for Optics and Photonics, SPIE, 2018.

[282] Q. Wang, E. T. Rogers, B. Gholipour, C.-M. Wang, G. Yuan, J. Teng, and N. I. Zheludev, "Optically reconfigurable metasurfaces and photonic devices based on phase change materials," *Nature Photonics*, vol. 10, no. 1, p. 60, 2016.

[283] J.-Y. Ou, E. Plum, L. Jiang, and N. I. Zheludev, "Reconfigurable photonic metamaterials," *Nano letters*, vol. 11, no. 5, pp. 2142–2144, 2011.

[284] C. R. de Galarreta, A. M. Alexeev, Y. Y. Au, M. Lopez-Garcia, M. Klemm, M. Cryan, J. Bertolotti, and C. D. Wright, "Nonvolatile Reconfigurable Phase-Change Metadevices for Beam Steering in the Near Infrared," *Advanced Functional Materials*, vol. 28, no. 10, 2018.

[285] N. Raeis-Hosseini and J. Rho, "Metasurfaces based on phase-change material as a reconfigurable platform for multifunctional devices," *Materials*, vol. 10, no. 9, p. 1046, 2017.

[286] H. Hu, H. Zhang, L. Zhou, J. Xu, L. Lu, J. Chen, and B. Rahman, "Contra-directional switching enabled by si-gst grating," *Optics Express*, vol. 28, no. 2, pp. 1574–1584, 2020.

[287] B. Shen, H. Lin, S. Sharif Azadeh, J. Nojic, M. Kang, F. Merget, K. A. Richardson, J. Hu, and J. Witzens, "Reconfigurable frequency-selective resonance splitting in chalcogenide microring resonators," *ACS Photonics*, 2020.

[288] Y. Zhang, J. B. Chou, J. Li, H. Li, Q. Du, A. Yadav, S. Zhou, M. Y. Shalaginov, Z. Fang, H. Zhong, C. Roberts, P. Robinson, B. Bohlin, C. Ríos, H. Lin, M. Kang, T. Gu, J. Warner, V. Liberman, K. Richardson, and J. Hu, "Broadband transparent optical phase change materials for high-performance nonvolatile photonics," *Nature Communications*, pp. 1–9, 2019.

[289] K. V. Sreekanth, Q. Ouyang, S. Sreejith, S. Zeng, W. Lishu, E. Ilker, W. Dong, M. ElKabbash, Y. Ting, C. T. Lim, M. Hinczewski, G. Strangi, K.-T. Yong, R. E. Simpson, and R. Singh, "Phase-change-material-based low-loss visible-frequency hyperbolic metamaterials for ultrasensitive label-free biosensing," *Advanced Optical Materials*, vol. 7, no. 12, p. 1900081, 2019.

[290] Z. Cheng, C. Ríos, W. H. P. Pernice, C. D. Wright, and H. Bhaskaran, "On-chip photonic synapse," vol. 2, no. September, pp. 1–7, 2017.

[291] D. Kuzum, R. G. D. Jeyasingh, B. Lee, and H. P. Wong, "Materials for Brain-Inspired Computing," pp. 2179–2186, 2012.

[292] A. Sebastian, M. Le Gallo, G. W. Burr, S. Kim, M. Brightsky, and E. Eleftheriou, "Tutorial: Brain-inspired computing using phase-change memory devices," *Journal of Applied Physics*, vol. 124, no. 11, 2018.

[293] J. Yao and W. Zhang, "Fully Reconfigurable Waveguide Bragg Gratings for Programmable Photonic Signal Processing," *2019 Optical Fiber Communications Conference and Exhibition, OFC 2019 - Proceedings*, no. 2018, pp. 1–9, 2019.

[294] J. Capmany, D. Domenech, and P. Muñoz, "Silicon graphene Bragg gratings," *Optics Express*, vol. 22, no. 5, p. 5283, 2014.

[295] A. Ikhlef, R. Hedara, and M. Chikh-bled, "Uniform Fiber Bragg Grating modeling and simulation used matrix transfer method," *IJCSI International Journal of Computer Science*, vol. 9, no. 1, pp. 368–374, 2012.

[296] R. Boeck, M. Caverley, L. Chrostowski, and N. A. F. Jaeger, "Grating-assisted silicon-on-insulator racetrack resonator reflector," *Optics Express*, vol. 23, no. 20, p. 25509, 2015.

[297] T. Erdogan, "Fiber grating spectra," *Journal of lightwave technology*, vol. 15, no. 8, pp. 1277–1294, 1997.

[298] C. D. Wright, Y. Liu, K. I. Kohary, M. M. Aziz, and R. J. Hicken, "Arithmetic and biologically-inspired computing using phase-change materials," *Advanced Materials*, vol. 23, no. 30, pp. 3408–3413, 2011.

[299] Y. Kim, P. C. Wu, R. Sokhoyan, K. Mauser, R. Glaudell, G. Kafaie Shirmanesh, and H. A. Atwater, "Phase modulation with electrically tunable vanadium dioxide phase-change metasurfaces," *Nano Letters*, vol. 19, no. 6, pp. 3961–3968, 2019. PMID: 31136191.

[300] Y. Lu, M. Wang, S. Song, M. Xia, Y. Jia, X. Shen, G. Wang, S. Dai, and Z. Song, "Multilevel data storage in multilayer phase change material," *Applied Physics Letters*, vol. 109, no. 17, p. 173103, 2016.

[301] N. Youngblood, Z. Cheng, S. Carrillo, H. Bhaskaran, X. Li, W. Pernice, D. Wright, and E. Gemo, "Experimental investigation of silicon and silicon nitride platforms for phase change photonic in-memory computing," *Optica*.

[302] N. Ciocchini, M. Laudato, M. Boniardi, E. Varesi, P. Fantini, A. L. Lacaita, and D. Ielmini, "Bipolar switching in chalcogenide phase change memory," *Scientific reports*, vol. 6, p. 29162, 2016.

[303] F. Xiong, A. D. Liao, D. Estrada, and E. Pop, "Low-power switching of phase-change materials with carbon nanotube electrodes," *Science*, vol. 332, no. 6029, pp. 568–570, 2011.

[304] J. I. Z. Heng, A. M. E. Y. K. Hanolkar, P. X. U. Eipeng, S. H. C. Olburn, S. A. D. Eshmukh, J. A. M. Yers, J. E. F. Rantz, E. R. I. C. P. Op, J. O. H. Endrickson, J. O. D. Oylend, and N. I. B. Oechler, "GST-on-silicon hybrid nanophotonic integrated circuits : a non-volatile quasi- continuously reprogrammable platform," vol. 8, no. 6, pp. 1551–1561, 2018.

[305] A. Sebastian, M. Le Gallo, G. W. Burr, S. Kim, M. BrightSky, and E. Eleftheriou, "Tutorial: Brain-inspired computing using phase-change memory devices," *Journal of Applied Physics*, vol. 124, no. 11, p. 111101, 2018.

[306] J. Hegedüs and S. R. Elliott, "Microscopic origin of the fast crystallization ability of Ge-Sb-Te phase-change memorymaterials," *Nature Materials*, vol. 7, no. 5, pp. 399–405, 2008.

[307] T. Matsunaga and N. Yamada, "A study of highly symmetrical crystal structures, commonly seen in high-speed phase-change materials, using synchrotron radiation," *Japanese Journal of Applied Physics, Part 1: Regular Papers and Short Notes and Review Papers*, vol. 41, no. 3 B, pp. 1674–1678, 2002.

[308] B.-S. Lee, J. R. Abelson, S. G. Bishop, D.-H. Kang, B.-k. Cheong, and K.-B. Kim, "Investigation of the optical and electronic properties of ge2sb2te5 phase change material in its amorphous, cubic, and hexagonal phases," *Journal of Applied Physics*, vol. 97, no. 9, p. 093509, 2005.

[309] T. Tsafack, E. Piccinini, B.-S. Lee, E. Pop, and M. Rudan, "Electronic, optical and thermal properties of the hexagonal and rocksalt-like ge2sb2te5 chalcogenide from first-principle calculations," *Journal of Applied Physics*, vol. 110, no. 6, p. 063716, 2011.

[310] M. Ashanovich and F. R. Y. G. Ardes, "Athermal silicon nitride angled MMI wavelength division (de) multiplexers for the near-infrared," vol. 25, no. 22, pp. 1227–1236, 2017.

[311] I. Friedrich, V. Weidenhof, W. Njoroge, P. Franz, and M. Wuttig, "Structural transformations of Ge2Sb2Te5 films studied by electrical resistance measurements," *Journal of Applied Physics*, vol. 87, no. 9, pp. 4130–4134, 2000.

[312] X. Liu, X. Li, L. Zhang, Y. Cheng, Z. Yan, M. Xu, X. Han, S. Zhang, Z. Zhang, and E. Ma, "New structural picture of the ge2sb2te5 phase-change alloy," *Physical review letters*, vol. 106, no. 2, p. 025501, 2011.

[313] B. Chen, G. H. ten Brink, G. Palasantzas, and B. J. Kooi, "Crystallization kinetics of gesbte phase-change nanoparticles resolved by ultrafast calorimetry," *The Journal of Physical Chemistry C*, vol. 121, no. 15, pp. 8569–8578, 2017.

[314] H. Zhang, L. Zhou, B. M. A. Rahman, X. Wu, L. Lu, Y. Xu, J. Xu, J. Song, Z. Hu, L. Xu, and J. Chen, "Ultracompact Si-GST Hybrid Waveguides for Nonvolatile Light Wave Manipulation Ultracompact Si-GST Hybrid Waveguides for Nonvolatile Light Wave Manipulation," vol. 10, no. 1, 2018.

[315] W. De Cort, J. Beeckman, T. Claes, K. Neyts, and R. Baets, "Wide tuning of silicon-on-insulator ring resonators with a liquid crystal cladding," *Optics letters*, vol. 36, no. 19, pp. 3876–3878, 2011.

[316] A. Farmani, "Graphene plasmonic: Switching applications," *Handbook of Graphene: Physics, Chemistry, and Biology*, p. 455, 2019.

[317] L. A. Shiramin and D. Van Thourhout, "Graphene modulators and switches integrated on silicon and silicon nitride waveguide," *IEEE Journal of Selected Topics in Quantum Electronics*, vol. 23, no. 1, pp. 94–100, 2016.

[318] R. B. Priti, Y. Xiong, and O. Liboiron-Ladouceur, "Efficiency improvement of an o-band soi-mzi thermo-optic matrix switch," in *2016 IEEE Photonics Conference (IPC)*, pp. 823–824, IEEE, 2016.

[319] N. A. Mohammed, H. S. A. Elnasr, and M. H. Aly, "Performance evaluation and enhancement of 2× 2 ti: Linbo3 mach zehnder interferometer switch at 1.3 μm and 1.55 μm," *The Open Electrical & Electronic Engineering Journal*, vol. 6, no. 1, 2012.

[320] M. Zhang, K. Chen, W. Jin, and K. S. Chiang, "Electro-optic mode switch based on lithium-niobate mach–zehnder interferometer," *Applied optics*, vol. 55, no. 16, pp. 4418–4422, 2016.

[321] R. Amin, J. B. Khurgin, and V. J. Sorger, "Waveguide-based electro-absorption modulator performance: comparative analysis," *Optics express*, vol. 26, no. 12, pp. 15445–15470, 2018.

[322] A. Joushaghani, J. Jeong, S. Paradis, D. Alain, J. S. Aitchison, and J. K. Poon, "Wavelength-size hybrid si-vo 2 waveguide electroabsorption optical switches and photodetectors," *Optics express*, vol. 23, no. 3, pp. 3657–3668, 2015.

[323] N. Dupuis, A. V. Rylyakov, C. L. Schow, D. M. Kuchta, C. W. Baks, J. S. Orcutt, D. M. Gill, W. M. Green, and B. G. Lee, "Ultralow crosstalk nanosecond-scale nested 2× 2 mach–zehnder silicon photonic switch," *Optics letters*, vol. 41, no. 13, pp. 3002–3005, 2016.

[324] A. M. Al-Hetar, A. B. Mohammad, A. S. M. Supa'At, and Z. A. Shamsan, "Mmi-mzi polymer thermo-optic switch with a high refractive index contrast," *Journal of Lightwave Technology*, vol. 29, no. 2, pp. 171–178, 2010.

[325] R. B. Priti and O. Liboiron-Ladouceur, "A broadband rearrangable non-blocking mzi-based thermo-optic o-band switch in silicon-on-insulator," in *Advanced Photonics 2017 (IPR, NOMA, Sensors, Networks, SPPCom, PS)*, p. PM4D.2, Optical Society of America, 2017.

[326] J. V. Campenhout, W. M. J. Green, S. Assefa, and Y. A. Vlasov, "Low-power, 2x2 silicon electro-optic switch with 110-nm bandwidth for broadband reconfigurable optical networks," *Opt. Express*, vol. 17, pp. 24020–24029, Dec 2009.

[327] L. Lu, S. Zhao, L. Zhou, D. Li, Z. Li, M. Wang, X. Li, and J. Chen, "16x16 non-blocking silicon optical switch based on electro-optic mach-zehnder interferometers," *Opt. Express*, vol. 24, pp. 9295–9307, May 2016.

[328] L. Qiao, W. Tang, and T. Chu, "Ultra-large-scale silicon optical switches," *2016 IEEE 13th International Conference on Group IV Photonics (GFP)*, pp. 1–2, 2016.

[329] L. Qiao, W. Tang, and T. Chu, "32x32 silicon electro-optic switch with built-in monitors and balanced-status units," *Scientific Reports*, vol. 7, no. 1, p. 42306, 2017.